ENGINEERING - DEVELOPMENT AND INNOVATIONS FOR NEW EMPLOYMENTS 2014

Proceedings of the 4th AMES International Conference, Ljubljana, Slovenia, October 23th, 2014.

EDITORS

IZTOK GOLOBIČ
University of Ljubljana,
Ljubljana, Slovenia.

FRANC CIMERMAN
Plinovodi d.o.o.,
Ljubljana, Slovenia.

CIP - Kataložni zapis o publikaciji
Narodna in univerzitetna knjižnica, Ljubljana

621(082)(0.034.2)

ZVEZA strojnih inženirjev Slovenije. International conference (4 ; 2014 ; Ljubljana)
Engineering - development and innovations for new employments 2014 [Elektronski vir] : proceedings of the 4th AMES International Conference, Ljubljana, Slovenia, October 23th, 2014 / editors Iztok Golobič, Franc Cimerman. - 1st electronic ed. - El. knjiga. - Ljubljana : Association of Mechanical Engineers of Slovenia - AMES, 2015

ISBN 978-961-91393-9-4 (pdf)
1. Gl. stv. nasl. 2. Golobič, Iztok
278006272

Publisher

Association of Mechanical Engineers of Slovenia - AMES

First electronic edition.

Printed in Ljubljana, Slovenia.

PREFACE

This publication is comprised of research papers, presented at the 4th AMES International Conference on Engineering - Development and Innovations for New Employments 2014 held at Ljubljana, Slovenia, October 23th, 2014. The publication as well as the conference was organized by AMES in cooperation with Metal Processing Association (Chamber of Commerce and Industry of Slovenia), Faculty of Mechanical Engineering (University of Ljubljana), and Faculty of Mechanical Engineering (University of Maribor).

The cooperation of academic and industrial partners presents an excellent opportunity: for professional networking and exchange of expert opinions; to present the latest developments and innovations; to emphasize the achievements in the field of sustainable development in Slovenia.

We would like to acknowledge the contribution of the International Advisory Committee for helping us to ensure the quality of the papers presented during the 4th AMES International Conference. Special thanks go to our sponsors, which enabled the realization of the conference and also to the Technical Editors.

Iztok Golobič
University of Ljubljana,
Ljubljana, Slovenia.

Franc Cimerman
Plinovodi d.o.o.,
Ljubljana, Slovenia.

ORGANIZING COMMITTEE

Chairs:

Iztok Golobič, University of Ljubljana, Slovenia

Franc Cimerman, Plinovodi d.o.o., Slovenia

International Advisory Committee:

Cristina H. Amon, University of Toronto, Canada

Bikramjit Basu, Indian Institute of Science, Bangalore, India

Janez Diaci, University of Ljubljana, Slovenia

Jože Duhovnik, University of Ljubljana, Slovenia

Mitjan Kalin, University of Ljubljana, Slovenia

Tassos G. Karayiannis, Brunel University, UK

Džafer Kudumović, University of Tuzla, Bosnia and Herzegovina

Anne Neville, University of Leeds, UK

Niko Samec, University of Maribor, Slovenia

Khellil Sefiane, University of Edinburgh, UK

Brane Širok, University of Ljubljana, Slovenia

Technical Editors & Realization:

Andreja Cigale

Anže Sitar

Žiga Zadnik

Matevž Zupančič

CONTENTS

New generation of viscoelastic granular adaptive damping elements

Marko Bek [a,b*], Nikola Holeček [a], Igor Emri [b]

[(a)] Gorenje gospodinski aparati, d.d., Partizanska 12, 3503 Velenje, Slovenia.

[(b)] University of Ljubljana, Faculty of Mechanical Engineering, Aškerčeva 6, 1000 Ljubljana, Slovenia.

* Corresponding author:
E-mail: marko.bek@fs-uni-lj.si

Abstract

Centre for Experimental Mechanics, Faculty of Mechanical Engineering, University of Ljubljana together with Gorenje gospodinjski aparati d.d., has developed adaptive granular damping elements for damping vibrations and consequently noise. Damping elements consist of flexible tube made out of glass, basalt or carbon fibers and are filled with polymeric granular material under high pressure. Hydrostatic pressure applied on polymeric material (inside damping elements) tunes frequency where material exhibits maximal energy absorptive properties to a frequency of maximum external vibrations. By using this novel idea we can exploit full damping potential of polymeric materials to reduce railway track vibrations and consequently noise. In this paper we present conceptual solution of new granular adaptive dampers.

1 Introduction

Railway transport is considered as one of the most environmentally friendly forms of transportation. In addition, rail transport is safer and more economical in comparison to other forms of transportation. It is expected that in coming years, the role of public transport will increase with the introduction of high-speed trains. It is also expected that cargo carried per kilometer in freight transportation will increase. The European Commission predicts that by the year 2020 the share of passenger traffic will increase by 40% and the share of freight transport by 70% [1].

One of the main problems of railway transportation is the environmental noise pollution. Longer period of exposure to excessive noise increases the risk of various diseases for human beings and negatively affects plants and animals.

There are various sources of noise in railway transportation systems. They can be divided into 5 major groups, which are (i) rolling noise, (ii) noise at turns, (iii) noise on bridges, (iv) aerodynamic noise and (v) noise and vibration of the ground. However, from the literature it is known that at high-speed trains, rolling noise is the governing mechanism. Therefore, it is of key importance to control and reduce rolling noise, as it will reduce vibrations and consequently overall noise [2].

Rolling noise is the consequence of vibrations caused by contact between train wheel and railway track. During the contact, part of the vibrations travels through the track and into the ground (vibrations of ground), second part of the vibrations travels in longitudinal and transverse directions of the track, which causes excessive noise. To prevent travelling of vibrations through the track in longitudinal and transverse directions, damping elements, which absorb mechanical energy of vibrations are used. Majority of solutions provide the use of polymeric materials, since polymers are known for their damping properties [3].

New generation damping elements consisting of viscoelastic granular material encapsulated in fiber reinforced tube made out of glass, basalt or carbon fibers were developed at the Centre of Experimental Mechanics, Faculty of Mechanical Engineering, University of Ljubljana in cooperation with Gorenje gospodinski aparati, d.d. By increasing the hydrostatic pressure within a closed tube one may adjust frequency at which polymeric granular material exhibits its extreme damping properties, and consequently obtain maximum energy absorption of rail vibrations at given frequency. New generation damping elements are designed for positioning along the railway track and underneath, as shown in Figure 1.

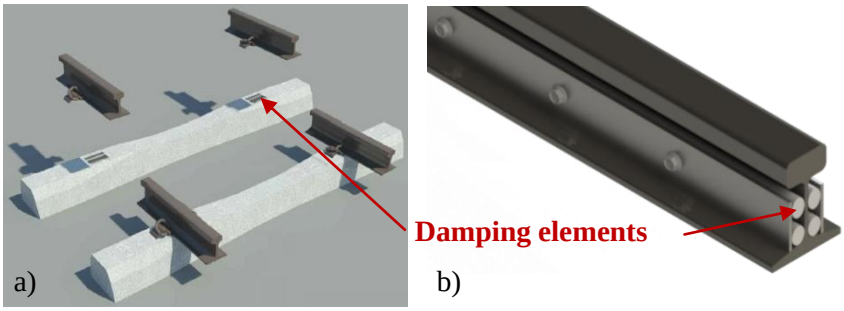

Figure 1: Railway line with polymeric damping elements a) under the railway track and b) along the railway track.

2 Theoretical background

It is known that polymers are good damping materials. Their damping properties are usually presented with a damping factor, $tan\,\delta$, which is profoundly affected by hydrostatic pressure to which material is exposed.

Effect of hydrostatic pressure on damping properties of polymeric materials

Damping factor, $tan\,\delta$ is a frequency-dependent material property, which further on depends on hydrostatic pressure to which material is exposed [4]. When polymeric material is exposed to high hydrostatic pressure, the mobility of molecules is reduced, which is on the macro-scale observed as frequency-dependent shift of damping properties as shown in Figure 2.

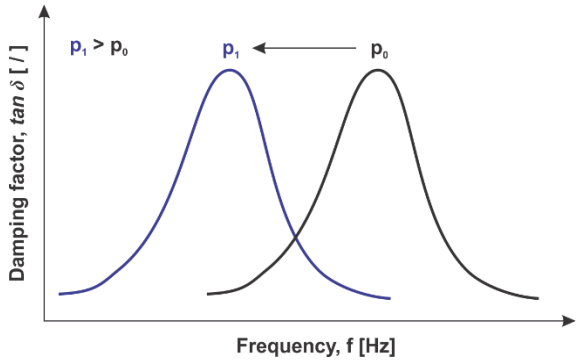

Figure 2: Damping factor of polymeric material, $tan\ \delta$ depending on frequency and pressure.

Effect of average granular size and size distribution on viscosity and sound transmission loss of granular materials

Research on viscoelastic behavior of concentrated suspensions with granular material showed us that appropriate size and size distribution of granules can be used to improve viscosity Figure 3a. Moreover, it was found that granular materials with smaller average particle size and broad size distribution profoundly lower sound transmission and consequently noise, Figure 3b. Therefore, adjusting the particle size distribution of granular materials we can adjust the characteristics required for manufacturing damping elements and their noise reduction capabilities.

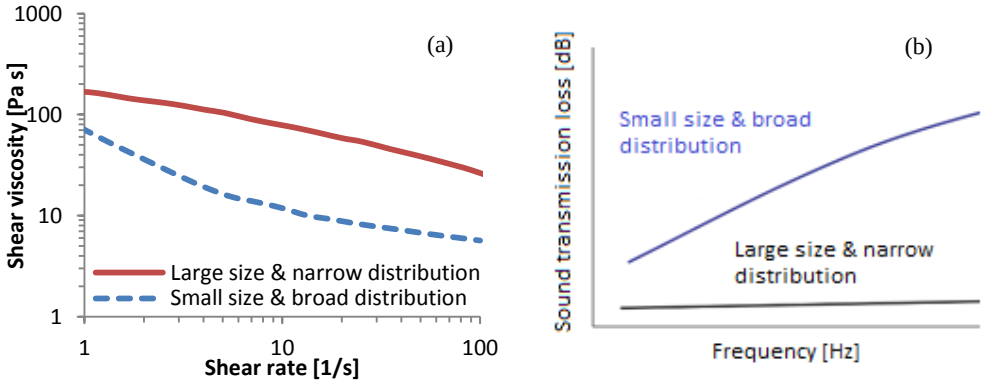

Figure 3: Example of effect of particle size distribution on (a) shear rate viscosity of concentrated suspensions and (b) sound transmission loss of granular materials.

3 Conceptual solution

On the basis of both findings we have developed the new generation damping elements, consisting of flexible tube made out of glass, basalt or carbon fibers filled with pressurized polymeric granular materials, Figure 4. By changing hydrostatic pressure within the flexible tube one can adjust frequency characteristics of material damping properties such so to match the frequency of mechanical vibrations we want

to reduce. Adaptive viscoelastic granular damping elements are protected with two European patents [5,6].

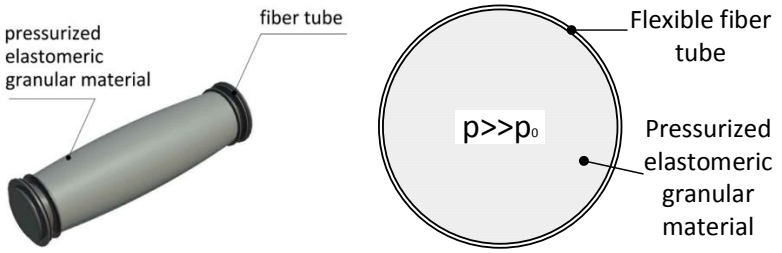

Figure 4: New generation damping elements consisting of fiber tube and pressurized elastomeric material.

Basic principle is schematically presented in Figure 5. Hydrostatic pressure applied on polymeric material within the pressure resistance flexible tube shifts the frequency peak where material exhibits maximal energy absorptive properties such so to match the frequency of maximum rail vibrations. Invented approach allows ultimate exploitation of polymeric material energy absorption properties.

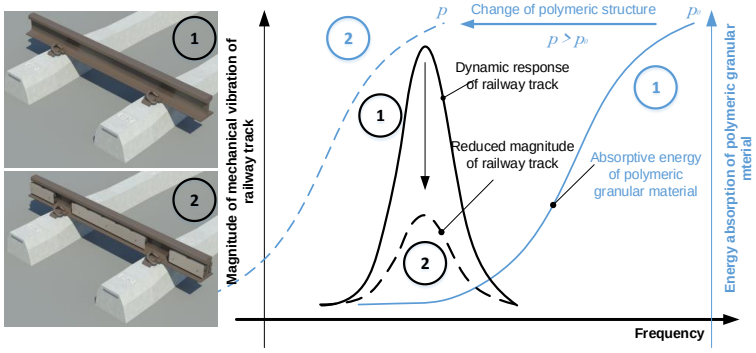

Figure 5: Basic principle for optimizing performance of new generation damping elements.

4 Conclusion

Paper briefly summarizes practical aspects of the research conducted in collaboration between Centre for Experimental Mechanics, Faculty of Mechanical Engineering, University of Ljubljana, and Gorenje gospodinski aparati, d.d.,. The invented damping elements converge research results on the effect of pressure on mechanical behavior of time-dependent polymeric materials, and new findings related to behavior of granular dissipative systems.

5 References

[1] European Commission for Research & Innovation. Transport, from http://ec.europa.eu/research/transport/transport_modes/rail_en.cfm; accessed on 2009-09-07.

[2] Thompson, D. (2009). *Railway noise and vibration: mechanisms, modelling and means of control*; Elsevier, Oxford.

[3] Thompson D. J. *et al*. (2007). A tuned damping device for reducing noise from railway track. *Journal of Applied Acoustics*, vol. 68, no. 1, p. 43-57.

[4] Tschoegl, N.W., Knauss, W.G., Emri, I. (2002). The effect of temperature and pressure on the mechanical properties of thermo- and/or piezorheologically simple polymeric materials in thermodynamic equilibrium -a critical review. *Mechanics of Time-Dependent Materials*, vol. 6, p. 53-99.

[5] Emri, I. *et al*. Sleeper with damping element based on dissipative bulk or granular technology: Anmeldenummer 12006058.7 / EP 12006058 - 2012-08-24. München: Europäisches Patentamt, 2012.

[6] Emri, I., Bernstorff, B.S. von. Dissipative bulk and granular systems technology : Anmeldenummer 12006059.5 / EP 12006059 - 2012-08-24. München: Europäisches Patentamt, 2012.

Nano powder injection mouling tehnology - nPIM

Joamin Gonzalez-Gutierrez [a*], Bernd von Bernstorff [b], Igor Emri [a]

[(a)] University of Ljubljana, Faculty of Mechanical Engineering, Aškerčeva 6, 1000 Ljubljana, Slovenia

[(b)] BASF Societas Europaea, G-CA/MT - J513, D- 67056 Ludwigshafen, Germany.

* Corresponding author:
E-mail: joamin.gonzalez@fs.uni-lj.si

Abstract

Powder injection moulding (PIM) is a versatile technology for manufacturing small parts of complex geometry made of metal or ceramic. In PIM, first a mixture of a polymeric binder and metal or ceramic powder is prepared and then injection moulded. Afterwards the binder is removed and metallic or ceramic powder is fused by sintering.

Despite many advantages of PIM, conventional removal of a polymer binder via melting requires long time. This problem has been partially resolved with the use of polymers, which under appropriate conditions undergo rapid degradation, i.e., sublimate (for example polyoxymethylene – POM). Use of POM as a binder, however, greatly complicates the process of injection moulding due to its high viscosity.

The aim of the collaboration between the Center for Experimental Mechanics (CEM) and BASF is to reduce viscosity of the material used in PIM, and at the same time to maintain the good mechanical properties of the material in the solid state. The paper presents results on viscosity and creep compliance measurements of commercial and feedstock materials developed at CEM.

1 Introduction

Powder injection moulding (PIM) technology combines the advantages of polymer injection moulding with the advantages of powder metallurgy; therefore waste material generated and energy consumption are reduced compared to other techniques such as warm extrusion, casting and machining. The PIM process consists of four steps as shown in Figure 1: (i) Feedstock preparation which consists of mixing a polymeric binder with metal or ceramic powders; (ii) injection moulding to give the feedstock the desired shape; (iii) removal of the polymeric binder or debinding and; (iv) sintering to fuse together the metallic or ceramic powders [1].

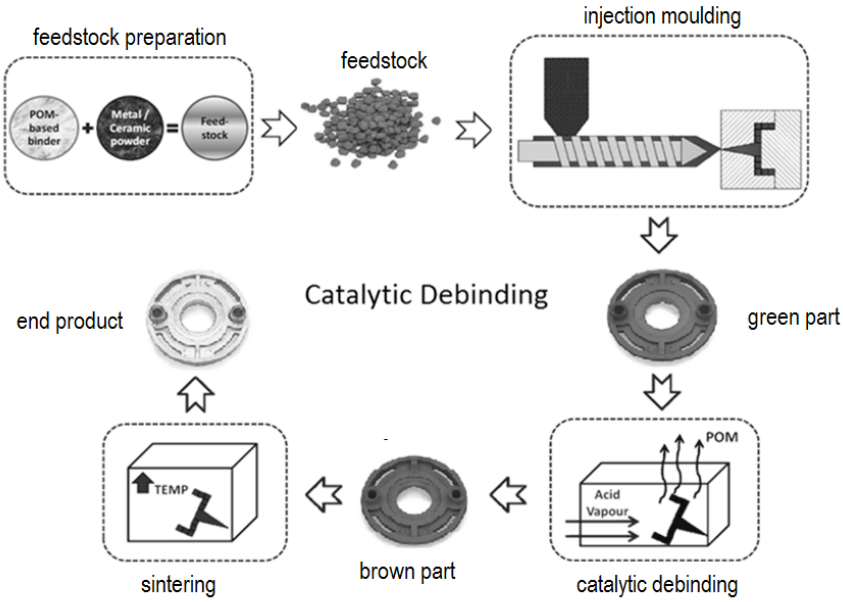

Figure 1: Scheme of PIM process.

When size of the metal and ceramic particles is in the "nano" range we are talking about nano- powder injection moulding technology or nPIM technology. Key benefits of products made with nPIM are their improved mechanical properties (especially fatigue and crack resistance) and their surface quality, which comes into class products with "polished surface". Technology of nPIM is suitable for use in aerospace, automotive, electronic, jewelry and medical industries.

Despite many advantages, some factors significantly inhibit the spread of this technology. One of these is the long time required to remove the polymer binder that is used during the injection moulding phase. This problem has been partially resolved with the use of polymers that undergo rapid degradation under acidic conditions, for example polyoxymethylene POM. This solution was developed and patented by BASF.

In doing so, there are new restrictions: Feedstock material has a higher viscosity, which greatly complicates the production of major products primarily during the injection molding stage. The key problem of nPIM technology are very large processing pressures due to poor flowability of polymer-metal or polymer-ceramic (nano) composite mixtures.

The Center for Experimental Mechanics and BASF corporation are collaboratively investigating "the composition" of POM-based feedstock with the aim of reducing the viscosity of the nano-composite material (feedstock), which is used in PIM and nPIM; while maintaining good mechanical properties of the material in the solid state.

Reduction of the viscosity and good mechanical properties of the material in the solid state can be achieved by (i) manipulating the distribution of the molecular weights of

the polymer matrix, and (ii) selecting the appropriate size distribution of the filler particles in the powder, which contains nano- and micro-sized particles.

2 Materials and methods

In order to estimate flowability of the commercially available feedstock and feedstock developed at CEM, viscosity tests were done, while mechanical properties were estimated via shear creep experiment in the solid state.

Feedstock materials

Two feedstock materials were used in the current investigation: commercial feedstock and experimental feedstock named X92 prepared specially for this investigation. The name of commercial feedstock material is Catamold®, produced by BASF (Germany). Due to confidentiality, information on composition of Catamold® cannot be disseminated; all that can be said is that it consists of a POM binder with an average molecular weight of approximately 92000 g/mol with addition of a polyolefin and approximately 90wt% of 316LW stainless steel powder. Second material, feedstock X92, was composed of a multimodal POM binder with an average molecular weight of around 24000 g/mol and 92 wt% of 316LW stainless steel powder. Particle size distribution of metal powder for observed feedstock is different, but due to confidentially it cannot be published.

Viscosity measurements

Constant rotation viscosity measurements were performed in a Haake MARS II (Thermo Scientific, Karlsruhe, Germany). A plate-plate measuring geometry with a 20 mm diameter was used. The measuring gap was set to 0.2 mm. Measurements were performed in strain-rate-control mode starting at 0.1 s^{-1} and finishing at 100 s^{-1} with 25 steps in between. Each step had duration of 20 s, which was sufficient for the stress to stabilize at all shear rates selected. Measurements were performed at 180°C. Six repetitions on fresh samples were performed for each material. The weight of each sample was approximately 600 mg.

Creep compliance measurements

Shear creep compliance measurements were performed in a HAAKE MARS II controlled stress rheometer fitted with solid clamps. Initial part of the creep measuring procedure started with an annealing phase at high temperature (120 °C for 2 h) to erase mechanical stress–strain history of the material. Annealing was followed by slow cooling to the first measuring temperature, 40 °C at a rate of 0.028 °C/min to minimize the effects of physical aging. After cooling down, shear creep measurements were performed in segmental form at five different temperatures: 40, 60, 80, 100, and 120 °C. Each specimen was loaded in shear with a constant stress of 30000 Pa for 1000 s, once the desired temperature had stabilized for approximately 15 min. The level of applied stress was previously determined to be within the linear viscoelastic regime. The useful segment length was set from 1 to 1000 s. Three repetitions were

performed on different samples for each feedstock material under consideration and their results at a given temperature were averaged. Finally, following the time-temperature superposition principle, averaged segments were shifted along the time-scale in relation to the segment measured at T_{ref} = 80 °C. Shifting was executed by using the closed-form shifting procedure [2].

3 Results

Viscosity of commercial and improved feedstock in dependence of shear rate is presented in Figure 2. Reduction of the average molecular weight of the binder from 92000 g/mol to 24000 g/mol, together with the different particle size distribution, leads to a significant reduction of the viscosity [3].

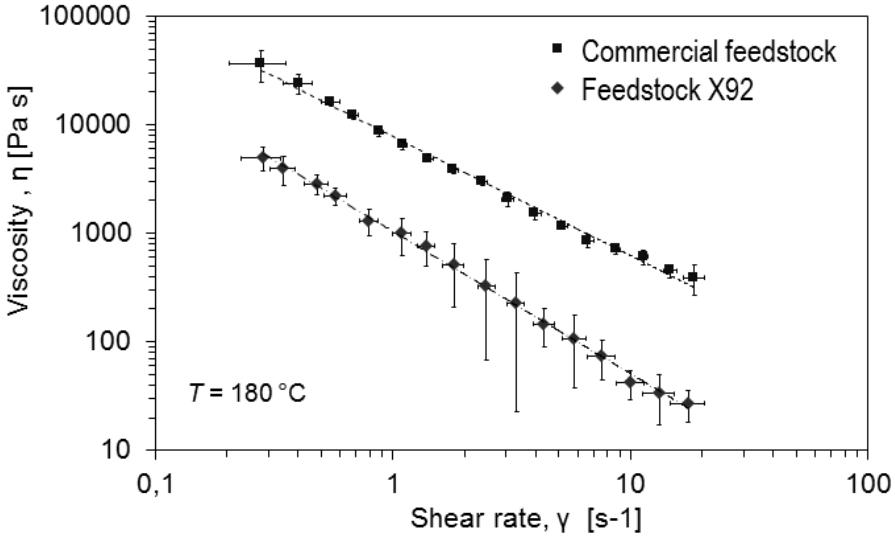

Figure 2: Viscosity of commercial and improved feedstock.

When comparing shear creep compliance of the commercial feedstock and feedstock X92, it can be seen that at short times (t < 100 s at 80 °C), the commercial feedstock and the experimental feedstock creep the same amount and at the same rate. At longer times (t > 1000 s at 80°C), the experimental feedstock actually creeps less than the commercial feedstock, Figure 3 [3].

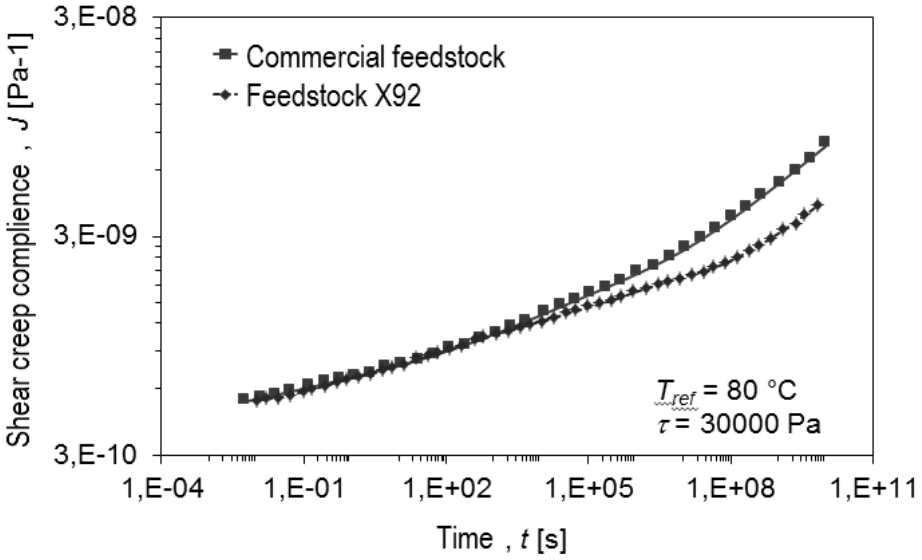

Figure 3: Shear creep compliance of commercial and improved feedstock.

4 Conclusions

- Selection of the appropriate molecular weight and the appropriate particle size distribution leads to a significant improvement in the flowability of the feedstock material without deterioration of its mechanical properties.
- By adding nanoparticles, we expect further improvements.

5 References

[1] Gonzalez-Gutierrez, J., Stringari, G.B., Emri, I. (2012). Powder injection moulding of metal and ceramic parts. *In Some Critical Issues for Injection Moulding*, Wang J. (Ed.), InTech, Rijeka, Croatia, p. 65-88

[2] Gergesova, M., Zupančič, B., Saprunov, I., Emri, I. (2011). *J. Rheol.*, vol. 55, no. 1, p.1-16.

[3] Gonzalez-Gutierrez, J., Stringari, G.B., Megen, Z.M, Oblak, P., & Emri, I. (2014). *Zeitschrift Kunststofftechnik* vol. 10, no. 5, p. 149-164.

The development of high-pressure technology of thermoplastics injection

Pavel Oblak [a*], Vinko Žohar [b], Davorin Dobočnik [b], Igor Emri [a]

[(a)] University of Ljubljana, Faculty of Mechanical Engineering, Aškerčeva 6, 1000 Ljubljana, Slovenia.

[(b)] Odelo Slovenija d.o.o., Tovarniška cesta 12, 3312 Prebold, Slovenia.

* Corresponding author:
E-mail: pavel.oblak@fs.uni-lj.si

Abstract

Injection molding is one of the widely spread methods for producing consumer and industrial goods. However, due to increasing complexity of products, injection molding is becoming more and more demanding and difficult to controll. Consequently manufacturers are often faced with a large amounts of scrap.

Changing pressure and temperature, to which material is exposed during the injection molding, may be drastically reflected through changes in material rheological and mechanical properties. This consequently generates one of the biggest challenges - how to determine the proper settings of processing parameters.

The aim of the collaboration between Center for Experimental Mechanics and ODELO Slovenia is establishment of the methodology for determining ultimate processing parameters utilizing the latest knowledge and theoretical models for predicting pressure and temperature effect on behaviour of polymers. The ultimate goal is to reduce the amount of scrap to the minimum possible level.

1 Introduction

Injection molding is one of the widely spread production methods for consumer and industrial goods. However, combining multiple materials, complex geometry and high dimensional requirements of products make injection molding more and more demanding and difficult to control, consiquently manufacturers are often faced with large amounts of scrap.

In general, procedure of injection molding can be divided into two main phases: (i) material preparation and (ii) material injection stage. In material preparation phase, raw material is filled into the heated barrel, and transported through it by the rotating screw. In material injection phase, prepared melt is further injected into the tempered mold. This phase consists of two steps. In the first step melt is, by controlling the displacement of the piston, i.e., "displacement controlled", injected into the mold. In the second step, additional melt is, by "pressure control", pushed into the mold to compensate shrinkage of the material during the cooling to room temperature.

Properties of polymers strongly depend on temperature and pressure boundary conditions. Change of a pressure or a temperature, to which material is exposed, may be drastically reflected through changes in its rheological and mechanical properties. During the process of injection molding, material is exposed to changing temperature and pressure, shearing caused by the screw rotation, and extensional flow during the injection phase. These complex boundary conditions represent one of the biggest challenges for injection molders today: »How to determine proper processing parameters?«

The aim of the collaboration between Center for Experimental Mechanics and ODELO Slovenia is establishment of the methodology for determing ultimate processing parameters utilizing the latest knowledge and theoretical models for predicting pressure and temperature effects on behaviour of polymers. This methodology will minimise person-dependency of technological process, reduce time required for establishing stable production process, and eliminate scrap due to improper settings of processing parameters.

2 Phases of injection molding process

In general, we can divide injection molding procedure into two main stages: (1) material preparation and (2) material injection stage. In material preparation stage raw material is filled into the heated barrel and transported through it by the rotating screw, Figure 1. At the end of this stage, molted material at selected temperature is packed in front of the screw, ready to be further injected into the mold. This stage is strictly "material dependent"; therefore, changes in set process parameters are not needed if there are no changes in used material.

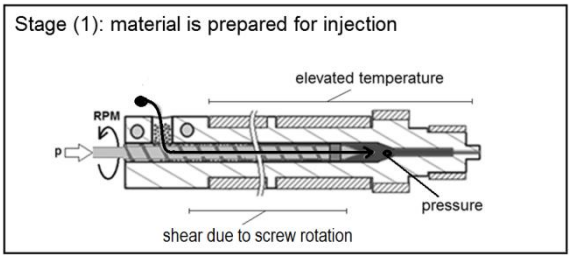

Figure 1: Schematic presentation of material preparation stage and present impacts on the resin.

During material preparation stage, the material is exposed to elevated temperature, shear due rotation of the screw and pressure also caused by the screw, Figure 1.

Second stage of the injection molding process is material injection. In material injection stage, melt prepared in previous, material preparation stage, is injected into the mold. This stage consists of two sub-stages; (2-a) primary or filling stage where melt is injected into the mold, and (2-b) secondary or packing stage where shrinkage of the material in the mold due to cooling is compensated. It is also important to mention that in primary or filling stage screw movement is displacement controlled while in the

secondary or packing stage it is pressure controlled. Mentioned division is schematically presented in Figure 2.

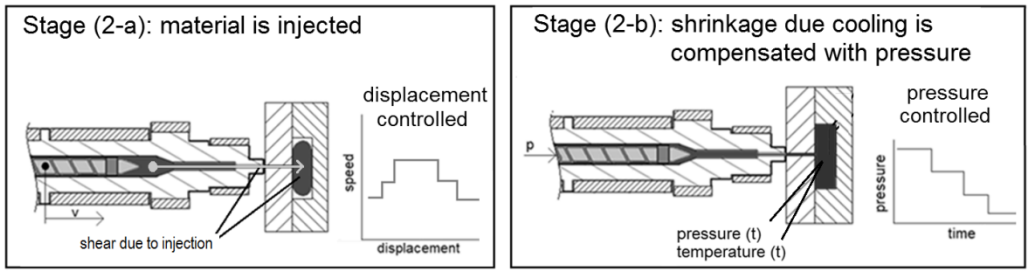

Figure 2: Schematic presentation of primary - filling stage (2-a), left, and secondary – packing stage (2-b), right.

During material injection stage the melt is exposed to elevated temperature, shearing during injection, and high pressure applied to compensate material shrinkage during cooling.

3 Effect of temperature, pressure and shearing rate on PMMA

Polymethyl methacrylate (PMMA) is amorphous polymer, frequently used for manufacturing of lenses for automotive rear lamps. Pressure and/or temperature variation, to which PMMA is exposed during the injection moulding, may be drastically reflected through changes in their rheological and mechanical properties. In addition material is exposed to extensive shearing caused by the screw rotation and elongation flow during the injection. As it will be demonstrated these parameters strongly affect behaviour of PMMA and consequently its processability.

Effect of temperature on rheological properties of PMMA is presented in Figure 3, which shows complex viscosity as function of temperature. For example, if temperature is decreased from 260°C to 240°C, the complex viscosity will double, i.e., increases from 225Pa*s to 500Pa*s. Hence, temperature variation within 20°C will change material flowability twofold, which can seriously affect the moulding process.

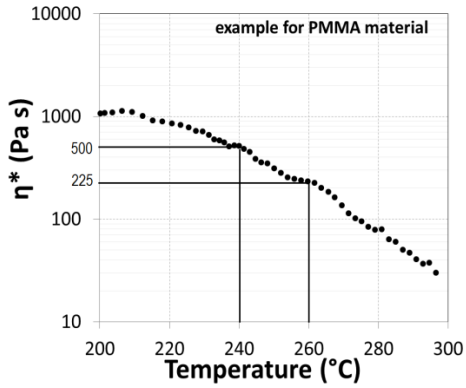

Figure 3: Complex viscosity in dependence of temperature.

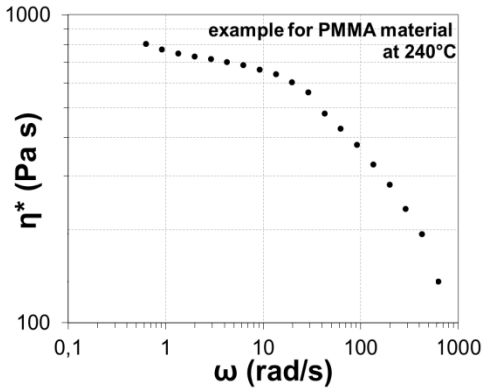

Figure 4: Complex viscosity in dependence of frequency.

Similarly as with increasing of temperature material viscosity is also decreasing with increasing the shear rate. Example for PMMA material is presented in Figure 4. This phenomena is commonly called shear thinning [1].

In addition, temperature and pressure affect volume of the material and its glass transition temperature, Tg. This effect is presented in Figure 5. It can be seen that increasing the pressure lowers specific volume of the material. Further, increasing of pressure shifts Tg towards higher temperatures. Material above the glass transition, in Figure 5 indicated as region A, is in "semi-liquid state" and may be considered to be in thermo-dynamic equilibrium at all times. When the temperature drops below Tg, material becomes rigid and we commonly say that it enters glassy state, in Figure 5 indicated as region B.

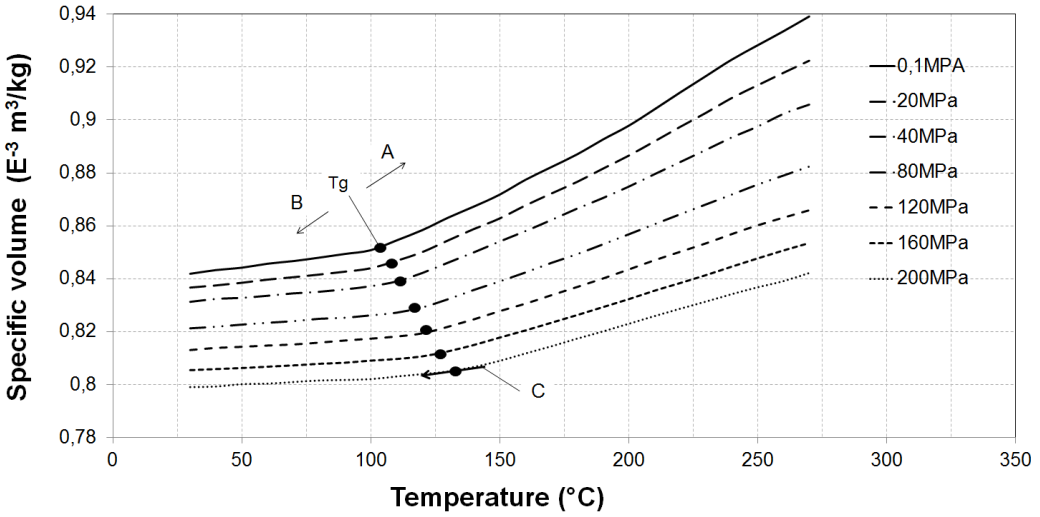

Figure 5: Example of p-V-T relation on case of PMMA material [2].

If the melt is exposed to a certain pressure when it enters the glassy state, for example detail C in Figure 5, this pressure will be "frozen" into the material inherent structure

as internal residual stress. If we open the mold, this internal stress homogenously increases the volume of the injected part. This phenomenon allows us to shorten the technological process by opening the tool at higher than room temperature, which however should be below Tg. Details about this are explained in continuation.

4 Discussion

In a discussion, a method of determining thermal-pressure conditions which lead to the product with prescribed geometry is presented. Presented does not cover the complete injection moulding process, instead it is limited only to the secondary part of material injection stage, i.e. packing stage (2-b) as previously described and presented in Figure 2. The final product contains certain amount of material which occupies certain volume and for the convenience of this discussion we will assume that the volume of the final product is the same as the volume of the mold cavity though in reality molds usually have cavities smaller in comparison to final products.

Product at room conditions (T_{room}, p_0) has an end volume ($\nu_{end\ product}$). This is presented as point (g) in Figure 6. When the product is withdrawn from the tool its temperature is higher than T_{room} and due to temperature expansion also its volume ν (T_{mold}, p_0) increases. This is presented with point (f) in Figure 6.

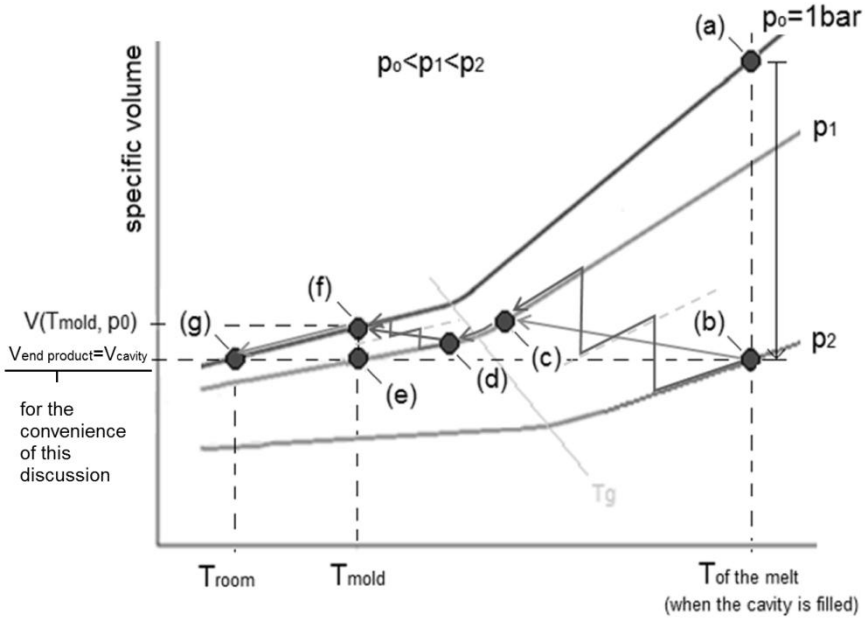

Figure 6: Schematically presented pressure controlled stage.

During cooling down from the temperature of the tool (f) to room temperature (g) in Figure 6, the product shrinks to its end size. In order to compensate this shrinkage (ν (T_{mold}, p_0) - ($\nu_{end\ product}$)), the product needs to be overpressured before mould opens. This is indicated with point (e) in Figure 6. That is how, pressure at which the material needs to be "frozen", mentioned in text above, is determined. This pressure is on

Figure 6 presented as p_1. Material is "frozen" at pressure p1 only if it is subjected to this pressure when entering its glassy region (passing Tg). In line with this we have to pass Tg under the same pressure, i.e. pressure p_1, when cooling the material, that is from point (c) to point (d) in Figure 6.

To repeat, material needs to be solidified (cooled below the Tg) at pressure p_1 since this pressure required to compensate the shrinkage of the material upon cooling from the temperature at which the mold is opened to the room temperature.

If we present the entire process from the beginning; firstly when the temperature of the material is increased to the temperature of the melt, point (a) in Figure 6, its volume will substantially increase. In order to push the required amount/mass of the material into the mold we need to increase its pressure as indicated by arrow in Figure 6. This condition will be achieved at pressure p_2 which is indicated as point (b) in Figure 6. At these conditions material has the same volume and same density as the end product in room conditions. Further when material is cooling down, the pressure should be decreased from p_2 to p_1 because, as previously described, material should pass Tg under pressure p_1 to compensate the shrinkage of the material upon cooling from the temperature at which the mold is opened to the room temperature. Decreasing of pressure from p_2 to p_1 is also presented as a transition from (b) to (c) in Figure 6. Pressure dropping can be continuous or stepwise, depends on machine capabilities, what is the most important is that the material does not pass Tg before reaching pressure p_1. After the material reaches pressure p1 at point (c) it further passes Tg, that is from (c) to (d) and it is further cooled down to the temperature of the mold T_{mold} or point (e) in Figure 6. At point (e), pressure p_1 represents pressure at which material was "frozen" when passing Tg. After mold opens, product volume expands, from (e) to (f) and further shrinks due to cooling from the mold to room temperature, from (f) to (g). Point (g) represents end product at room conditions.

5 Conclusions

It is common practice that manufacturers using injection moulding are trying to stabilize the production via resetting processing parameters. Changes are often done based on experience, sometimes also with trial and error procedure. To assure uniform procedure of setting the processing parameters, universal methodology based on material properties will be established.

The methodology will:

- minimize person (technologist) dependency
- reduce the time for establishment of stable production process
- eliminate a scrap due to improper settings of processing parameters

The methodology can be universally implemented in any process of injection molding.

6 References

[1] R.I.Tanner (1988), *Engineering rheology*, Oxford University press, New York.

[2] http://www.campusplastics.com/campus/en/datasheet/PLEXIGLAS%C2%AE+8N/Evonik+Industries/66/6e68306e/SI?pos=5, accessed on 2014-11-6.

Lifetime prediction of polymeric products in the area of district heating and cooling

Alen Oseli [a*], Andrei Belov [b], Egon Susič [c], Peter Nose [c], Igor Emri [b]

[(a)] Institute for sustainable innovative technologies, Pot za Brdom 104, 1000 Ljubljana, Slovenija.

[(b)] University of Ljubljana, Faculty of Mechanical Engineering, Aškerčeva 6, 1000 Ljubljana, Slovenia.

[(c)] Danfoss Trata, d.o.o., Ulica Jožeta Jame 16, 1000 Ljubljana, Slovenia.

* Corresponding author:
E-mail: alen.oseli@isit.si

Abstract

With implementation of polymeric materials into products of district cooling and heating, the manufacturing process would be cheaper and faster, which represents profound technological and economical breakthrough in this field. These products will be exposed to high temperatures (over100 °C), hydrostatic pressures (over 100 bar) and longer operating periods (more than 25 years). At this environmental and working conditions time- or frequency- dependent mechanical properties of polymeric materials change significantly (by orders of magnitude), which may lead to failure of a product. Therefore prediction of structural lifetime of these products present a major problem. In this paper we present advanced experimental (CMS and DBC setup) and analytical methods (FMT and KE model) used for predicting long-term behaviour of polymeric material and structural lifetime of products exposed to combined temperature and pressure conditions.

1 Introduction

Traditionally, district cooling and heating products (e.g., pipes, pressure regulators etc.) are made out of metallic materials (brass, steel, etc.). The main reason for utilizing metallic materials is that these products are exposed to relatively high temperatures (over 100˚C), hydrostatic pressure (over 100 bar) and longer operating periods (more than 25 years). With implementation of polymeric materials, the manufacturing process of these products will be cheaper and faster, which represents a significant technological and economical breakthrough in this field. Since behaviour of polymeric materials is time- and frequency- dependent, the lifetime prediction of these products through longer operating periods presents a major problem.

Moreover, it is known that environmental conditions, such as temperature, pressure, under which these products will be operating, profoundly affect (in orders of

magnitude) time- and frequency- dependent mechanical properties of polymeric materials [1]. These changes may cause adverse stress-strain response, which can lead to functional (loss of functionality) and structural (large deformations causing leakage, and fracture) failure [2]. Therefore, it is of key importance to understand the effect of temperature and pressure on long-term behaviour of polymeric materials in order to optimize the design and predict lifetime of these products.

Centre for Experimental Mechanics (CEM), at the Faculty of Mechanical Engineering, University of Ljubljana, has developed two unique experimental setups, which allow studying temperature and pressure effects on time- or frequency-dependent mechanical properties of polymeric materials (in shear and bulk). Measured material functions represent an input information for linear and non-linear modelling of long-term behavior of polymeric materials and lifetime prediction of products. Basic analytical tools for these predictions are Fillers-Moonan-Tschoegl (FMT) and Knauss-Emri (KE) model. In this paper we will present unique experimental setups and analytical tools used for long-term characterization of polymeric materials and structural lifetime prediction of products exposed to combined effect of temperature and pressure.

2 Theoretical background

In order to understand the effect of temperature and pressure on long-term behaviour of polymeric materials, one should understand the underlying governing processes that happen on molecular level. Polymeric materials are composed of long molecules or molecular chains. These chains occupy their "own volume", called the "occupied volume." However, between molecules, there is a vast empty space. The sum of this empty areas (holes) is commonly called the "free volume" [1].

By increasing temperature of a bulk material, the free volume will increase due to higher molecular mobility resulting in macroscopic increase of volume, as shown in Figure 1a.

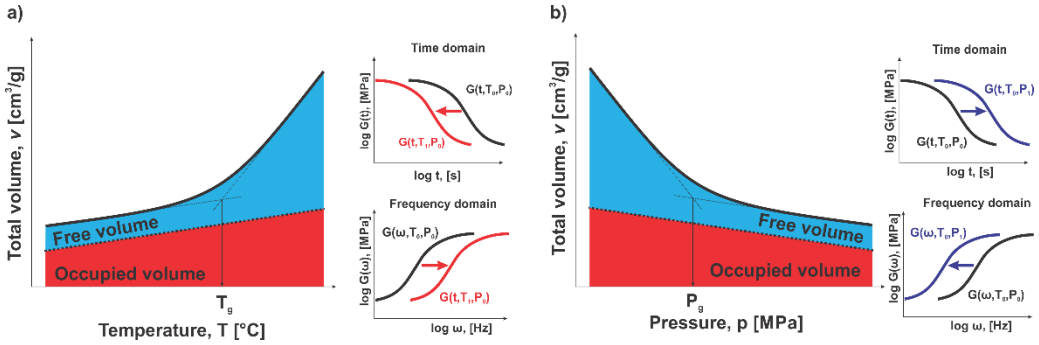

Figure 1: Effect of a) temperature and b) pressure on volume and mechanical properties (shear relaxation modulus) in time and frequency domain.

This will accelerate global molecular rearrangements when material is exposed to an external load, i.e. creep and relaxation processes are accelerated. On the other hand, the

hydrostatic pressure reduces the free volume that hampers mobility of molecules and therefore slows down creep and relaxation processes [1], shown in Figure 1b. On the macro scale, both effects, i.e. temperature and pressure, are manifested via shifting of mechanical properties along the logarithmic time and frequency axis, as presented in Figure 1.

3 Experimental equipment

Effect of temperature and pressure on time- and/or frequency- dependent mechanical properties of polymeric materials and their composites can be studied with the unique experimental setups, developed at CEM.

CEM Measuring System

Experimental setup, called CMS (CEM Measuring System) was developed to study the combined effects of temperature and pressure on mechanical behaviour of polymers, Figure 2 [3, 4]. The measuring system can measure volumetric (bulk) and shear properties of solid polymer specimens through a wide range of temperatures (from -20°C to +120°C) and pressures (from atmospheric to 4000 bar).

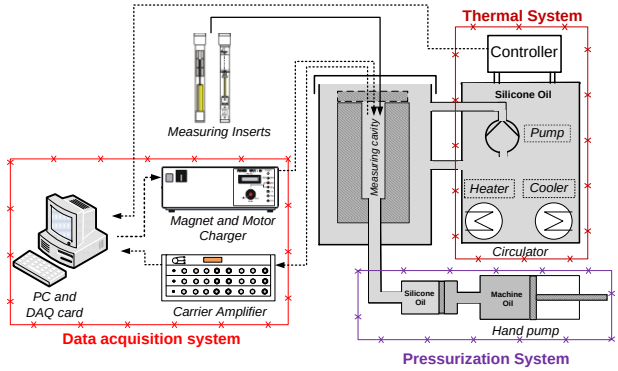

Figure 2: Schematic representation of CMS experimental setup.

For demonstration purpose we show in Figure 3 results on shear relaxation modulus, G(t) of Polyvinyl acetate (PVAc), measured on CMS experimental setup. Measurements were conducted at different temperature and pressure conditions [4]. From these results it is clearly seen that temperature of 100°C accelerates shear relaxation process 10^{11} times, which moves the relaxation curve along the logarithmic time-axis 11 decades to the left, as shown in Figure 3. Similar but opposite effect has pressure of 100 bar that slows the relaxation process and consequently shifts the relaxation curve to the right for approximately 8 decades.

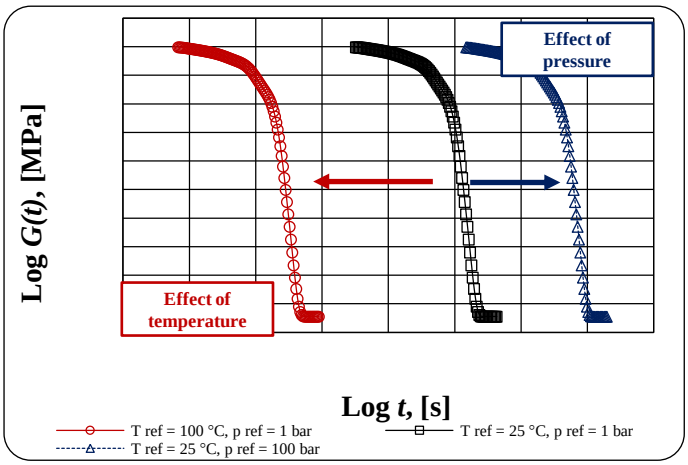

Figure 3: Effect of temperature and pressure on shear relaxation modulus, *G(t)* for PVAc.

Experimental setup for measuring dynamic bulk compliance – DBC experimental setup

Another measuring system developed by CEM is the experimental setup for measuring dynamic bulk compliance, *B*(ω)* also called DBC experimental setup [5]. DBC was developed to study combined effect of temperature and pressure on volumetric (bulk) properties in frequency domain [6, 7], i.e. dynamic bulk compliance *B*(ω)* in wide range of temperatures (from room temperature to 150 °C) and pressures (from atmospheric pressure to 2000 bar). DBC experimental setup is schematically shown in Figure 4.

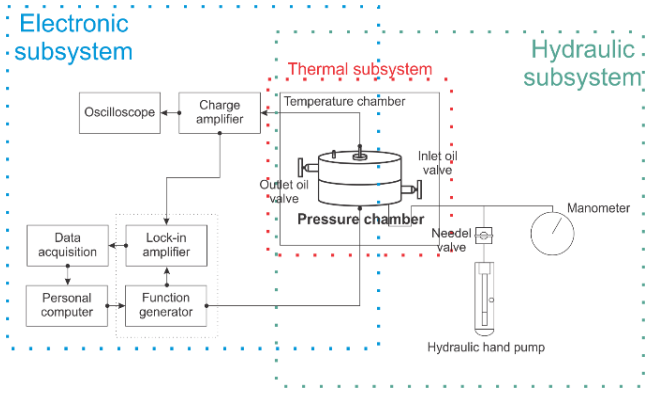

Figure 4: Schematic representation of DBC experimental setup [5]

Dynamic bulk creep compliance, *B*(ω)* is a material function that describes volumetric creep process of polymeric materials under dynamic excitation. When a polymeric sample is loaded with dynamic hydrostatic pressure the response is a dynamic change of volume. Since polymers are generally dissipative systems their response under dynamic excitations is delayed in time or, in other words, phase shifted. This shifted response is mathematically presented with two components, one component is in-phase

with excitation, whereas the second component is out-of-phase with excitation. Dynamic bulk compliance, $B^*(\omega)$ is divided into dynamic bulk storage compliance, $B'(\omega)$, describing average stored energy (elastic component) during one loading cycle, and dynamic bulk loss compliance, $B''(\omega)$, which describes average energy dissipation during one loading cycle.

Examples of the dynamic bulk storage $B'(\omega)$ and loss, $B''(\omega)$ compliance, measured on DBC experimental setup, are presented in Figure 4. Measurements were conducted on polyvinyl acetate (PVAc) through wide range of temperatures and pressures [7]. The results show that temperature affects bulk properties by shifting components of $B^*(\omega)$ to the right in logarithmic frequency axis for app. 4 decades. On the other hand the results show that pressure causes vertical shifting which contradicts the current understanding of the effect of pressure on behaviour of polymeric materials, Figure 5. These findings demand further research of these phenomena.

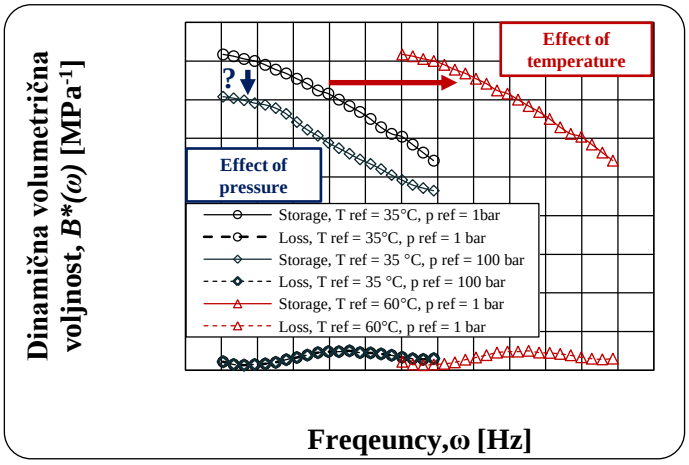

Figure 5: Effect of pressure on master curves obtained through frequency-temperature superposition of dynamic bulk compliance, $B^*(\omega)$ for PVAc [7].

4 Linear and non-linear modelling effect of temperature and pressure

Filler-Moonan-Tschoegl (FMT) model

Today, many models are based on free volume concept for modelling the effect of thermodynamic parameters, such as temperature or pressure, on behaviour of polymeric materials [1]. One of such models is well establish Fillers-Moonan-Tschoegl (FMT) model, which incorporates both parameters, temperature and pressure. FMT model assumes that shifting of mechanical properties in time or frequency domain is related to the effect of temperature and pressure via fractional free volume, caused by temperature, $f_P(T)$, and by pressure, $f_{T0}(P)$ change, respectively. In this model time and/or frequency shifts are modelled with the shift factor, $a_{T,p}$ as

$$\log a_{T,P} = -\frac{B}{2.303\, f_0}\left[\frac{f_P(T)-f_{T_0}(P)}{f_0+f_P(T)-f_{T_0}(P)}\right], \qquad (1)$$

Shift factors can be determined experimentally by shifting segments (measured within experimental window) along the logarithmic time- or frequency- axis in order to construct a master curve at a specified reference temperature, T_{ref} and pressure, P_{ref}, as shown in Figure 6. It has to be stressed that FMT model is valid only for shifting between two thermodynamic equilibrium states. When material is exposed to time-varying temperature and pressure boundary conditions the FMT model can not be used.

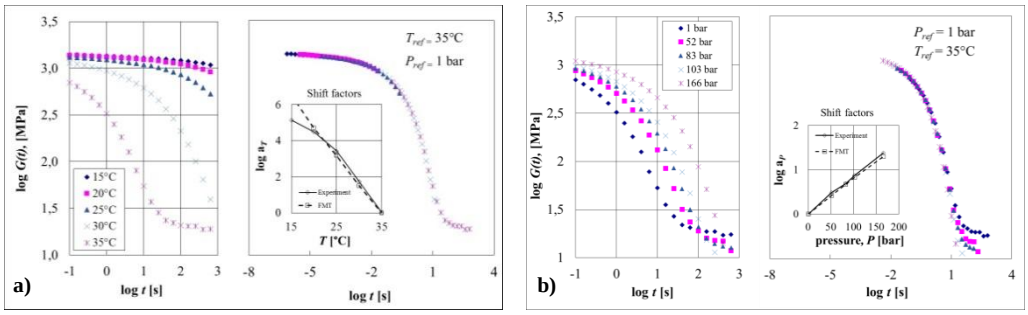

Figure 6: Segments, master curve and shift factors representing a) effect of temperature and b) effect of pressure on time-dependent behaviour of PVAc [4].

Knauss-Emri (KE) model

Effect of temperature, pressure, and mechanically induced stress dilatation on product stress-strain response can be predicted by using non-linear Knauss-Emri (KE) model [2]. Beside mentioned effects, model also incorporates the effect of moisture which is similar to the effect of temperature. KE model is derived from the free volume concept and allows predictions of material time-dependent behaviour in equilibrium as well as in non-equilibrium thermodynamic conditions. Therefore, particular model is most suitable analytical tool for predicting structural lifetime of products, such as products for district cooling and heating systems.

Dilatational and deviatoric forms of the KE model can be expressed as

$$\sigma_{kk}(t) = 3\int_0^t K[t'(t) - \lambda'(t)]\frac{\partial\theta(\lambda)}{\partial\lambda}\mathrm{d}\lambda, \tag{3}$$

$$S_{\mathrm{ij}}(t) = 2\int_0^t G[t'(t) - \lambda'(t)]\frac{\partial e_{\mathrm{ij}}(\lambda)}{\partial\lambda}\mathrm{d}\lambda, \tag{4}$$

where K and G represent bulk and shear relaxation modulus respectively. Internal time, denoted with t', reduced or extended due to the effect of temperature, pressure, induced stress dilatation and moisture, is expressed true integral relation as

$$t'(t) - \lambda'(t) = \int_\lambda^t \frac{\mathrm{d}\xi}{\phi(\xi)}. \tag{5}$$

Where Φ(t) is the shift factor, which encompass the effect of temperature, pressure (and induced stress dilatation) and moisture through their effect on free volume, expressed by f_T, f_θ, *pressure, induced stress dilatation* and f_C respectively,

$$\log \phi(t) = -\frac{B_d}{2{,}303 f_d}\left(\frac{f_T(t)+f_c(t)+f_\theta(t)}{f_d+f_T(t)+f_c(t)+f_\theta(t)}\right), \quad (6)$$

Figure 7 demonstrates the applicability of the KE model for the case of physical aging of PVAc. Diagram shows changing of PVAc specific volume as function of time after exposing material to different temperature jumps from the equilibrium state at 40°C. The end temperatures are indicated above the individual curves. Experimental data obtained by Kovacs [8] are shown as circles, whereas the solid line shows the corresponding analytical predictions. Details on modelling are given elsewhere [2].

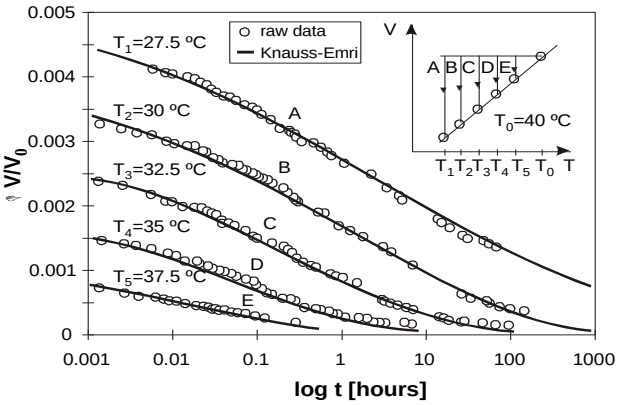

Figure 7: Physical aging of PVAc exposed to different temperature jumps from the equilibrium state at 40°C. The end temperatures are given above the individual curve.

5 Conclusions

Each polymer has unique time-dependent mechanical properties and different susceptibility to temperature and pressure effects. Therefore it is of key importance to measure their mechanical properties at different temperature and pressure conditions in order exploit their full potential, and extend useful range and durability of the products.

Two advance experimental setups were presented, i.e. CMS and DBC experimental setup, capable of measuring shear and volumetric (bulk) properties at different temperature and pressure conditions in time and frequency domain. Measured material functions serve as an input information for linear (FMT) and non-linear (KE) models for predicting long term behaviour of polymeric material and structural lifetime of products made of these materials. These advance experimental approaches and analytical tools are necessary to design durable products in the field of district heating and cooling systems, exposed to various temperature and pressure conditions.

6 Acknowledgement

This paper was prepared in collaboration between Centre for Experimental Mechanics, Faculty of Mechanical Engineering, University of Ljubljana, and company Danfoss Trata, d.o.o., which aim is to establish experimental-analytical approach used for

lifetime prediction of products made out of polymeric materials for district cooling and heating systems.

7 References

[1] Tschoegl, N.W., Knauss, W.G., Emri., I. (2002). The effect of temperature and pressure on the mechanical properties of thermo- and/or piezorheologically simple polymeric materials in thermodynamic equilibrium -a critical review. *Mechanics of Time-Dependent Materials*, vol. 6, p. 53-99.

[2] Knauss, W.G. and Emri I. (1980). Non-linear viscoelasticity based on free volume considoration. *Composites & structures*, vol. 13, p. 123-128.

[3] Kralj A., Prodan T. (2001). An apparatus for measuring the effect of pressure on the time-dependent properties of polymers. *Journal of rheology*, vol. 45, no.4, p. 929-943.

[4] Prodan T., Emri I. (2006). Measuring system for bulk and shear characterization of polymers, *Experimental mechanics*, vol. 46, p. 429-439.

[5] Oseli, A., Emri, I. (2014). Apparatus for measuring dynamic bulk compliance of time-dependent materials. *Journal of Key Engineering Materials*, vol. 601, p. 3-6.

[6] Deng, T.H., Knauss, W.G. (1997). The temperature and frequency dependence of the bulk compliance of Poly(Vinyl Acetate): A re-examination. *Mechanics of Time-Dependent Materials*, vol. 1, p. 33-49.

[7] Sane, S.B., Knauss, W.G. (2001). The time-dependent bulk response of Poly (Methyl Methacrylate). *Mechanics of Time-Dependent Materials*, vol. 5, p. 293-324.

[8] Knauss, W.G., Emri, I. (1987). Volume change and the nonlinearly thermo-viscoelastic constitution of polymers. *Polymer Engineering and science*, vol. 6, p. 86-100.

[9] Kovacs, A.J. (1963). Glass transition in amorphous polymers: A Phenomenological Study. *Fortschr. Hochpolym.-Forch*, vol. 3, p. 394–507.

Alternative solutions for bonding of hand blender housing

Andraž Zupan [a], Joško Valentinčič [a*], Henri Orbanić [b], Izidor Sabotin [a], Andrej Lebar [a,c,] Marko Jerman [a], Nejc Matjaž [a], Mihael Junkar [a]

[(a)] University of Ljubljana, Faculty of Mechanical Engineering, Aškerčeva 6, 1000 Ljubljana, Slovenia.

[(b)] BSH Hišni aparati d.o.o., Savinjska cesta 30, 3331 Nazarje, Slovenia.

[(c)] University of Ljubljana, Faculty of Heath Sciences, Zdravstvena pot 5, 1000 Ljubljana, Slovenia.

* Corresponding author:
E-mail: jv@fs.uni-lj.si

Abstract

Housings of Bosch hand blenders are assembled with screws and it should be replaced by a more suitable for automatic assembly. The housing material is polypropylene (PP). In this paper, two methods of assembly are investigated: adhesive and thermal bonding. The first method utilizes Loctite 770 primer adhesion promoter was used to make low-energy surfaces suitable for bonding and Loctite 406 instant adhesive. In the second method, the housings were locally heated by resistance wire Isachrom 60 and welded together. Simplified crash tests were performed and results indicate both methods can replace assembly by screwing.

1 Introduction

The basic requirement for joining of two halves of hand blender housing is that the joint should sustain a 70 cm fall to the ground to prevent a possible contact of the user with the electrical voltage. Most of hand blenders have assembled housing with one or more screws. Number of screws depends on construction of housing. In the case of B/S/H hand blender, the housing is joined only with one screw (Figure 1), but the producer would like to replace the screwing operation with alternative solution that is easier for automation.

Two possibilities of housing assembly are envisioned. To utilise the adhesive bonding, a suitable adhesive should be selected. It needs to provide sufficient bonding strength, but it also should not contaminate the food when/if it comes in contact with it. In this paper, appropriate primer and adhesive are selected, the housings are assembled and simple crash tests were performed. Additionally, a new method for thermal bonding was tested in the same manner.

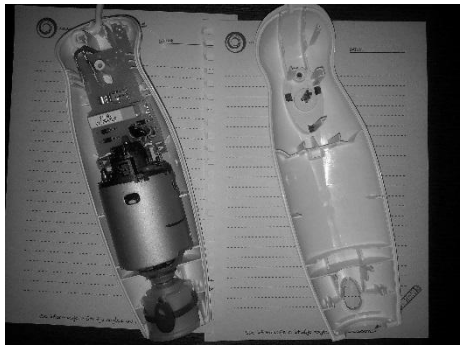

Figure 1. Electric component inside hand blender.

2 Adhesive bonding

The selection of primer and adhesive mostly depends on the housing material. In our case, the base material was polypropylene (PP), which has a low surface energy. When the substrate has a high surface energy, it tends to attract, and the adhesive has a low surface tension, has little resistance to deformation or rupture, a good wetting of the adhesive on the substrate is produced. Improving substrate can be achieved by few methods. Gas plasma is one of the methods. Increases polypropylene surface energy. This is achieved by the addition or substitution of polar chemical groups onto the surface. This process is known as plasma activation. It does not weaken, damage or discolour the polymer surface in any way. [1] Another method is a surface modification technique that uses a low temperature corona discharge plasma to impart changes in the properties of a surface. The corona plasma is generated by the application of high voltage to sharp electrode tips which forms plasma at the ends of the sharp tips. [2] Surface can be treated mechanically with abrasive paper or sponge. In our investigation we used Henkel's primer Loctite 770 to improve adhesion to substrates. Primers are used to improve difficult-to-bond materials such as PP and they can be used with instant bonding adhesives. Therefore the primer Henkel's Loctite 406 was used. Both are presented in Figure 2.

Figure 2. Primer Loctite 770 and Loctite 406.

It has all needed properties. Temperature resistance of chosen adhesive ranges from -40°C to +120°C, which is enough, because operating temperature of appliance reaches approximately 80°C. And there is one other important factor, if this adhesive comes in contact with food in solid state, is not a problem. It can be said that is ″bio-compatibility″. Instant adhesives, are also called cyanoacrylates, cure very quickly when confined between surfaces. Surface humidity on the substrates triggers the cure reaction, which moves from the substrate surfaces towards the middle of the adhesive joint. Due to their limited gap filling capacity they require close fitting surfaces. Their adhesion to most substrates is excellent and the bonding strength in shear and tensile mode is very good. [3] In this case gap between substrates was really minimal, so the adhesive could do its job. In the glued joint we can find two different types of forces: cohesive and adhesive forces. Adhesive are much stronger then cohesive and they appear between two different bodies such as adhesive and substrate. Cohesive appears in adhesive itself. They are much weaker and important is, that layer of adhesive is not too thick. If layer is too thick, forces in the joint are significantly reduced.

Each specimen has to be prepared under certain procedure. Very important is to make sure that the substrate is clean. There must be no small dirt and grease on the substrate. Next step is to coat the housing with primer Loctite 770. We can assist with special brush. It is very important to coat both sides of the housing, to improve adhesion to substrates. It can be applied only one time. In case of several overlays primer does not serve its purpose.

The adhesive can be applied only on one of the substrates. After adhesive is on the surface, the housing must be consists quickly. The final strength of the adhesive bond is not obtained immediately, that is why it is important to compress housing at the beginning to achieve beginner strength of adhesive. After 24 hours the final strength is obtained.

3 Thermal bonding

The main idea is to weld the two parts of housing together by heating the joint with resistance wire. The resistance wire Isachrom 60 with a diameter of 0.5 mm was selected. The specific resistance of the wire *r* is 5.65 Ohm/m. Temperature of the joint need to go beyond polypropylene melting temperature. The length of the wire *l* is 0.5 m and the Ohm resistance of the 0.5 m wire equals to 2.82 Ω. Using 12 V power supply the electric current through the wire is 4.2 A.

$$\boldsymbol{I = \frac{U}{R} = \frac{12\ V}{2{,}825\ \Omega} = 4{,}2\ A} \tag{1}$$

At this current, the temperature above 400°C was reached, therefore the thermal bonding was done in a few seconds. During bonding, both parts of housing were pressed together until the joint material cooled and the housing was assembled. The wire remains in the joint after the process is finished. Components for thermal bonding are given in Figure 3.

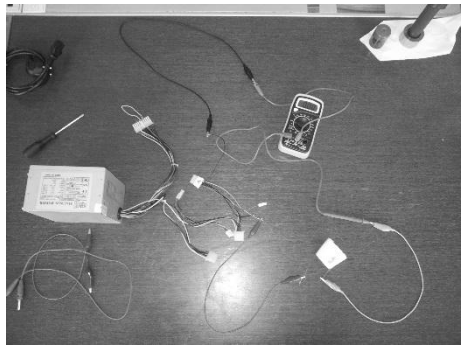

Figure 3. Components for thermal bonding

4 Crash tests

A simple test rig was put in place to provide free fall of the hand blender form the height of 70 cm (Figure 4).

To test the adhesive bonding five specimens were prepared and crash tests were performed at different times after the bonding. Results are gathered in Table 1.

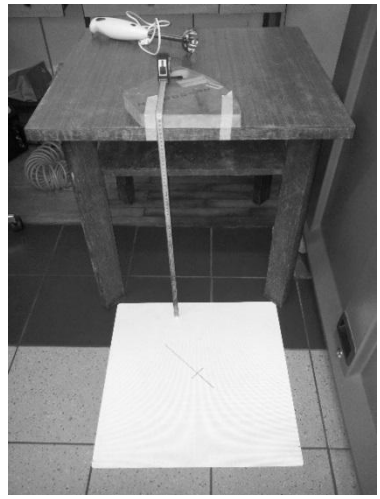

Figure 4. Test rig

Table 1. Test results

Number of specimen (time after bonding)	**Test**	**Result**
1 (1.5 h)	I	√
	II	√
	III	×
2 (18.5 h)	I	√
	II	×
3 (70 h)	I	√
	II	×
4 (45 h)	I	√
	II	√
	III	√
5 (46 h)	I	√
	II	√
	III	√
	IV	√
	V	√
	VI	√

Test specimens were falling on different sides of housing. The first specimen (1) fell horizontally (I). Little damage appeared on the housing. Then it fell on blender foot (II). No extra damage was noticed. The same specimen (1) was used to perform the third crash test (III). It fell on the side where cord exits the appliance. The right side of blender opened (Figure 5).

Figure 5. Test specimen 1, crash test III

Since the fall on the side where the cord exits the housing is critical, in the following crash tests, the specimens were falling on this side. The second specimen suffered some damage on the right side. In the second test, the damage was much bigger (Figure 6).

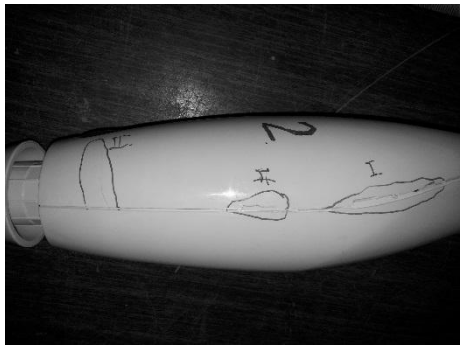

Figure 6. Test specimen 2, test II

No damage occurred in specimen 3, test I. The blender foot was removed and test II was performed where the specimen fell on area where this part is clamped. Housing opened as shown in Figure 7.

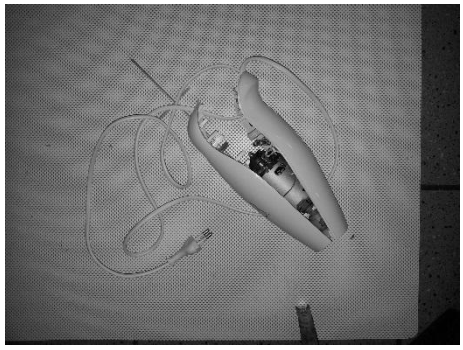

Figure 7. Test specimen 3, test III

The following tests were performed as for the specimen 3 test II. The specimen 4 suffered minimal damage in test 1. In second test (II) the damage was much bigger. There were some cracks, but the housing was still closed. In the third test (III) cracks continued per joint (Figure 8).

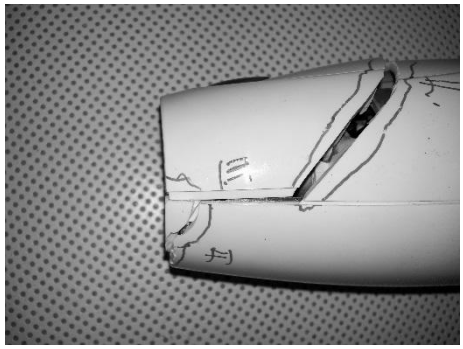

Figure 8. Test specimen 4, test III

The fifth specimen had different construction of housing. The falls were performed on all sides and some cracks appeared. Test was taken six times (Figure 9).

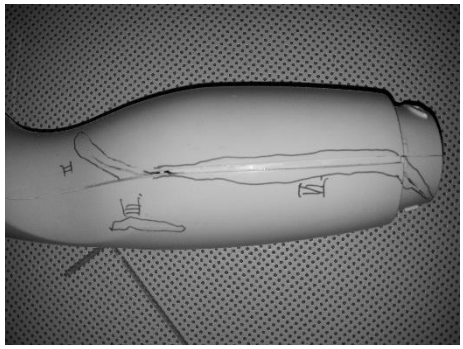

Figure 9. Test specimen 5, test VI

The sixth specimen was thermally bonded. The results of tests are much better than of adhesive bonding. The joint is very strong, even with a screwdriver it is very difficult to separate both parts of housing (Figure10).

Table 2. Test results

Number of specimen	Tests	Results
6 (thermally bonded)	**I.**	**✓**
	II.	**✓**
	III.	**✓**
	IV.	**✓**

Figure 10. Test specimen 6, test IV

5 Conclusions

Construction of housing is very important; housing of specimen 5 is better than housings of specimens 1 to 4. It is of paramount importance that a primer is applied only once. Several applications of primer do not improve adhesion on substrate. This might be the reason that the third specimen opened at second test. Time elapsed between gluing and testing is very important. In order to achieve the highest strength of adhesive it must pass 24 hours. Specimens 1 and 2 were tested in less than 24 hours after bonding and they haven't perform well. The best results were obtained by thermal bonding. This process is recommended to be used.

6 Acknowledgement

This project was funded from Javni sklad republike Slovenije za razvoj kadrov in štipendije, partially from European social fund and Slovenian Research Agency.

7 References

[1] http://www.pvateplaamerica.com/materials/polymers-Polypropylene.php accessed on 2014-7-18.

[2] http://en.wikipedia.org/wiki/Corona_treatment#Pre-treatment accessed on 2014-8-15.

[3] https://asp-cn.secure-zone.net/v2/index.jsp?id=19/80/492&lng=en accessed on 2014-8-20.

[4] http://www.adhesiveandglue.com/adhesive-definition.html accessed on 2014-8-25.

[5] Brent Strong, A. (2005). *Plastics: Materials and processing-3rd ed*. Prentice Hall.

Project driven concurrent realization of orders

Janez Kušar*, Lidija Rihar, Tomaž Berlec, Marko Starbek

University of Ljubljana, Faculty of Mechanical Engineering, Aškerčeva 6, 1000 Ljubljana, Slovenia.

* Corresponding author:
E-mail: janez.kusar@fs.uni-lj.si

Abstract

The market requires that companies continuously reduce their product and process development time and costs, in order not to lose their competitive advantage on the global market. Short product and process development time in combination with low costs and achievement of required quality can be obtained only by integrating project management methods with concurrent engineering elements.

Project management of orders combined with concurrent engineering elements allows for considerable reduction of development time, reduction of costs, and provides for a higher quality of order/product [1].

Order planning phase is very important in integrated product/process development. In the traditional product/process development, on average only 3% of total order development time is used for planning, while at the concurrent concept this time increases to about 20% [2].

The article presents an example of project management implementation in a company, the emphasis being on the concurrent development of planning procedure and project management of orders.

1 Introduction

Mass production was prevailing production concept till the end of the 20th century, while today's companies favour a transition to project type of production [3]. This is not only the case in companies which manufacture special equipment for new investments – this transition can also be seen in companies which have used mass production traditionally, e.g. in automotive industry [4], so the companies nowadays have to deal concurrently with continuous and project processes.

The company deciding for project-driven concurrent realisation of orders has to perform four important steps: (1) training of employees for concurrent engineering and project management, (2) organization and information changes in company operation, (3) creation of system- and operational guidelines for project management of orders, (4) definition of a method for project-driven concurrent realisation of orders.

Prerequisite for a successful project management of concurrent product development requires three levels of strategic management [5], i.e. parallelness, standardisation and integration of product development processes.

2 Sequential and concurrent product realization

The main feature of sequential product realisation is a sequential execution of stages in the product realization processes [8]. The next stage of the product realisation process may begin only after the preceding stage has been completed. Information in a particular process stage is developed gradually and is completed at the end of this stage and is then forwarded to the next stage.

Contrary to the sequential product realisation, the main feature of concurrent product realisation is a concurrent execution of stages in the product realisation processes [1, 5]. In this case, the next stage can begin before its preceding stage has been completed. Information in a particular product development process stage is built gradually and is forwarded continuously to the next stage.

Figure 1 shows a generalised Gantt chart of sequential and concurrent product realisation and information transfer between the stages of product realisation processes.

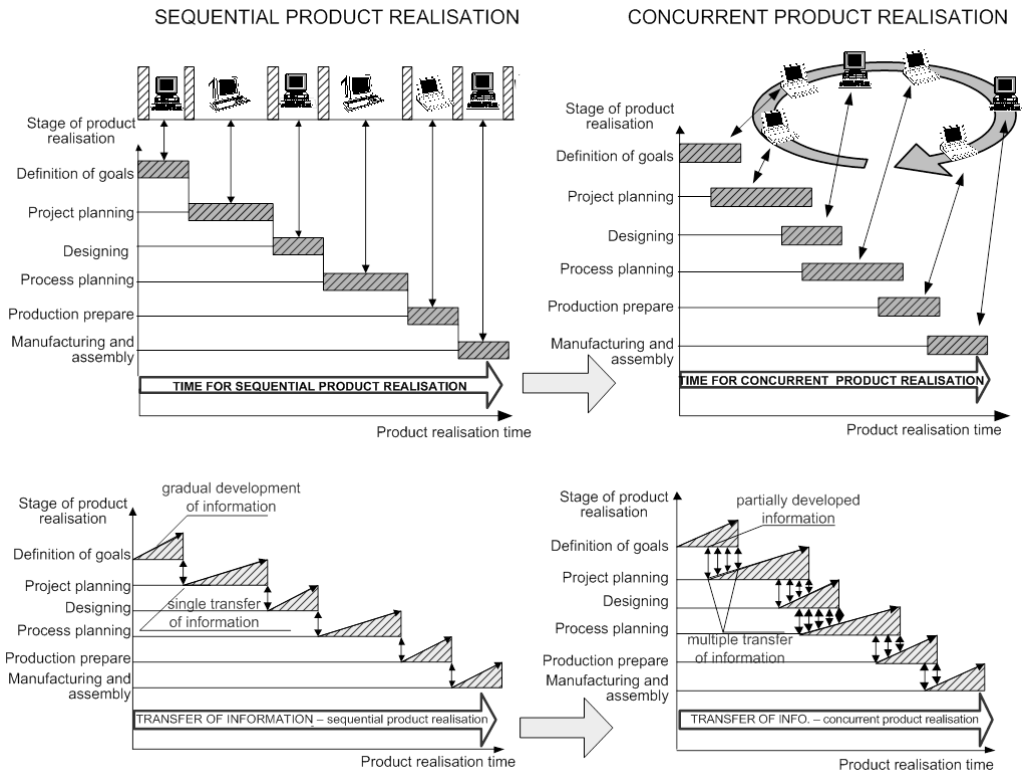

Figure 1. Generalised Gantt chart of sequential and concurrent product realisation processes and information transfer

In concurrent product realisation, there are interactions between individual stages of product realisation processes. Track-and-loop technology was developed for the implementation of these interactions [1, 6]. The type of loop defines the type of co-operation between the overlapping stages of concurrent product realisation processes. Winner [6] suggested that 3-T loops should be used, i.e. interactions exist between three stages of concurrent product realisation processes. A transformation of input to output is made in each loop on the basis of requirements and restrictions [8, 11].

A transition from sequential to concurrent product realisation considerably reduces the time and costs of product realisation [5], as shown in Figure 2.

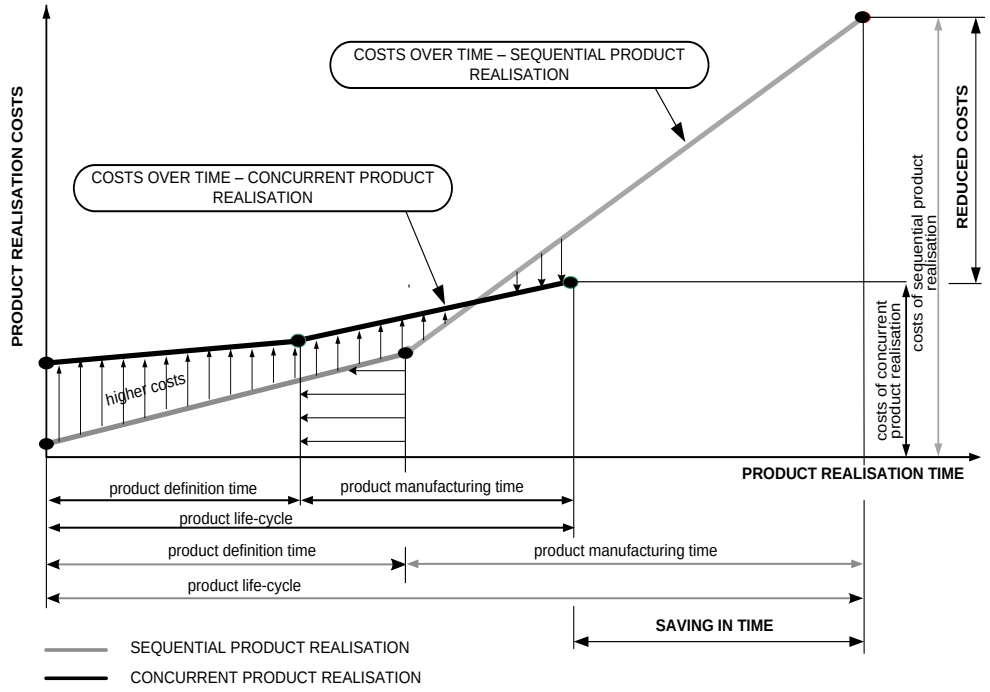

Figure 2. Time and costs of sequential and concurrent product realisation

It can be seen from Figure 2 that product definition costs rise uniformly in sequential product realisation, because of sequential execution of product definition activities (marketing, product draft, product development, elaboration of design documentation, material management), while production costs rise rapidly, due to long iteration loops for carrying out changes or eliminating errors.

The cost of product definition is much higher in concurrent product realisation, due to the concurrent execution of activities (more work is done during this stage), while production costs are much lower than in sequential realisation, due to short iteration loops for carrying out changes and eliminating errors.

3 Project-driven concurrent realization of orders

Project-driven concurrent realisation of orders consists of a logical sequence of all the activities needed for the preparation and implementation of the project [7, 8] extended with track and loops technology and strategies of concurrent engineering [2, 4, 7], as well as the documents resulting from individual activities (Figure 3).

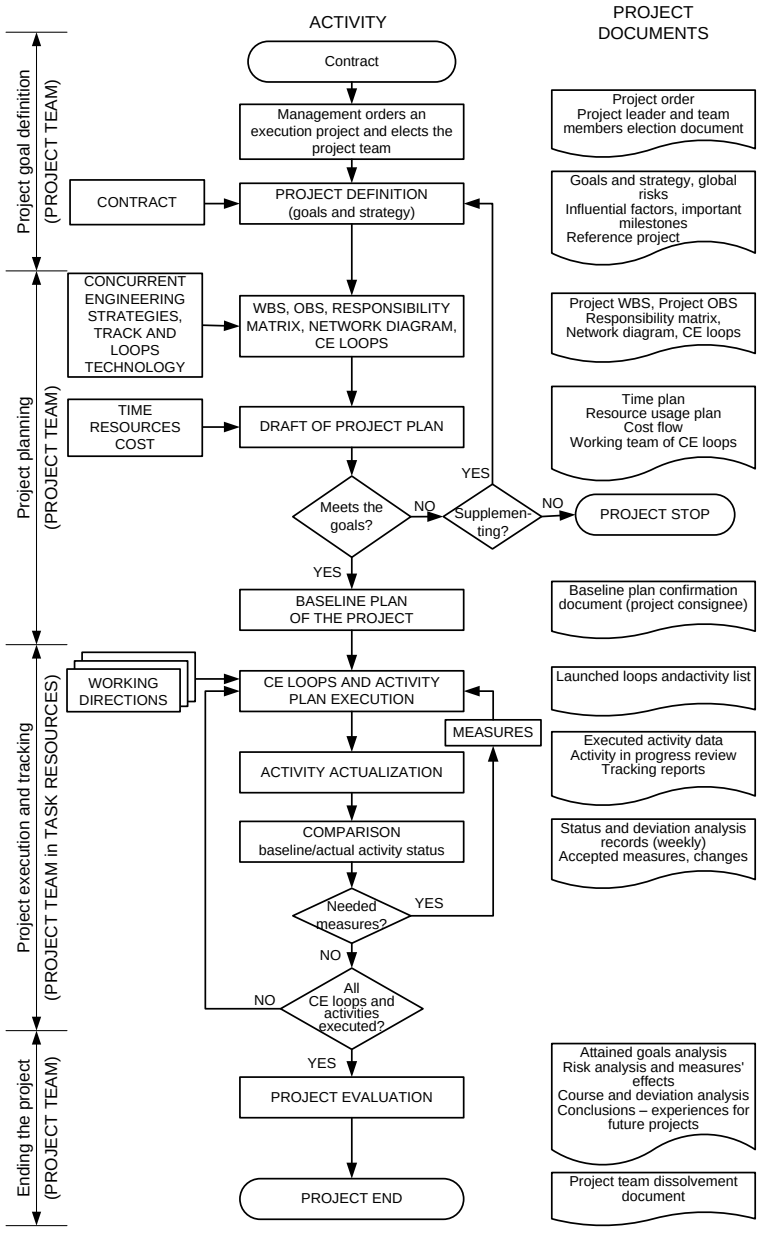

Figure 3. Project-driven concurrent realisation of orders

In small companies, a two-level team structure is planned for execution of 3-T loops of a concurrent product realisation process [1, 5], with a variable structure of core and project teams. The task of the core team is process support and control, while the task of project (working) teams is execution of the CE loops and activity defined within the concurrent product realisation process.

It is obvious that concurrent product realisation of orders is not possible without well-organised teamwork which is the means for organisation integration. It incorporates:

- the formation of a core team,

- project or working teams for realisation of loops,

- the selection of communication tools for the core team and project or working teams and

- definition of a communication matrix between participants of project.

4 Case study of project-driven concurrent realization of order

A company decided to make a case study of project-driven concurrent realisation of order for a pedal assembly (Figure 4).

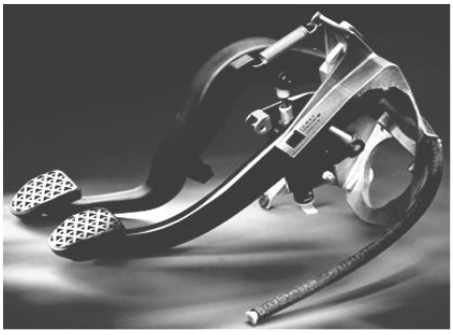

Figure 4. Pedal assembly

The goal of the project was to make a competitive pedal assembly, suitable in terms of quality, reliability, mass, price and realisation time.

There were 280 activities and five loops of simultaneous realisation of the pedal assembly within the six stages and five CE loops of pedal assembly realisation (Figure 5).

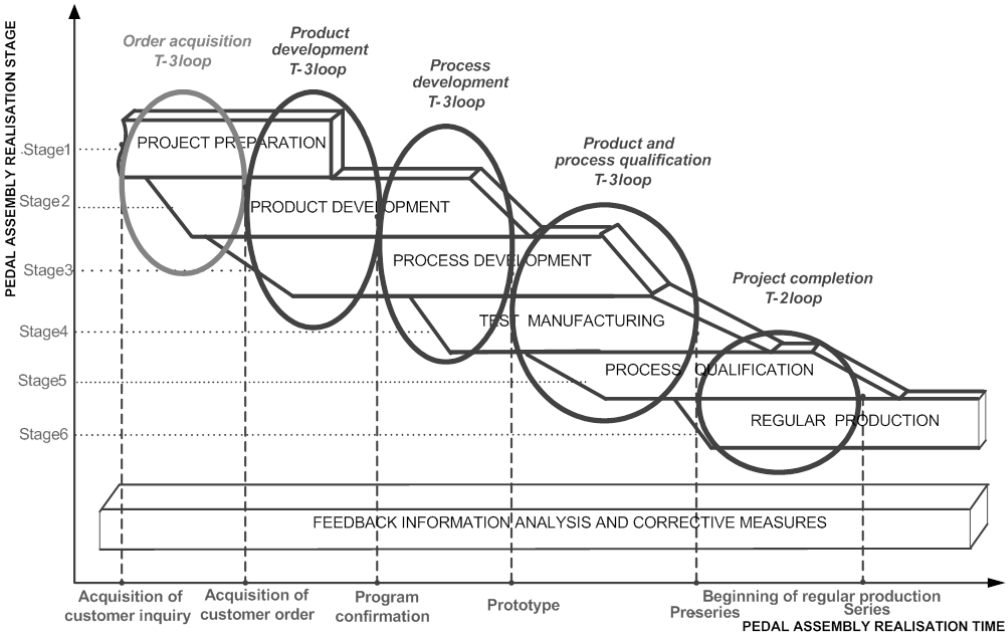

Figure 5. Stages and Loops of concurrent realisation of pedal assembly

Figure 6 presents a part of time schedule of the first loop of concurrent realisation of the pedal assembly named "Order acquisition loop". It contains a WBS of project with activities, duration and start and finish time and graphical presentation of activities in Gantt diagram.

ID	Task Name	Duration	Start	Finish
0	**PEDAL ASSEMBLY**	**139 days**	**7.4.14**	**16.10.14**
1	Preparation project activities	3 days	7.4.14	9.4.14
2	**PREPARATION**	**139 days**	**7.4.14**	**16.10.14**
3	**INQURITY REVIEW**	**11 days**	**10.4.14**	**24.4.14**
4	Receipt of inquires and determination of the status	2 days	10.4.14	11.4.14
5	Review of requirements	5 days	10.4.14	16.4.14
6	Opening the project	1 day	17.4.14	17.4.14
7	Preparation of inquiry	2 days	18.4.14	21.4.14
8	Definition of the project team	1 day	17.4.14	17.4.14
9	Preparation draft of context	5 days	18.4.14	24.4.14
10	Initial meeting 1	0 days	24.4.14	24.4.14
11	**ACQUISITION OF ORDER**	**139 days**	**7.4.14**	**16.10.14**
12	**ACQUISITION OF OFFERS BY THE PURCHASING**	**8 days**	**25.4.14**	**6.5.14**
13	Selection of potential suppliers	5 days	25.4.14	1.5.14
14	Elaboration and launching of inquire	3 days	28.4.14	30.4.14
15	Acquisition of offers	3 days	30.4.14	2.5.14
16	Analysis of offers	2 days	2.5.14	5.5.14
17	Successful offer of investment funds	1 day	6.5.14	6.5.14
18	**ACQUISITION OF OFFERS FOR THE PURCHASE OF**	**6 days**	**7.5.14**	**14.5.14**
19	Selection of potential suppliers	2 days	7.5.14	8.5.14
20	Elaboration and launching of inquiry	3 days	8.5.14	12.5.14
21	Acquisition of offer	2 days	12.5.14	13.5.14
22	Successful offer	2 days	13.5.14	14.5.14

Figure 6. Time schedule of loops of concurrent realisation of pedal assembly (Part of 1st loop)

Complete baseline plan of project of concurrent realisation of an order of pedal assembly consist necessary information for [9]:

- Project scope management.

- Project time management.

- Project resource and cost management.

- Project quality management.

- Project human resource management.

- Project communication management.

- Project risk management.

- Project procurement management.

5 Conclusion

Project-driven concurrent realisation of orders, which is based on project management methodology extended with concurrent management strategies (parallelness, standardisation, information integration) and track and loops technology, allows:

- Systematic and transparent project planning process for realization of orders, because it includes all the tools for managing projects.

- The use of concurrent engineering strategies.

- The use of the track and loops technology for integration of stages, phases and activities of the project.

- Organization of team work on two levels: the core team and working teams of CE loops.

- Continuous and direct communication of all project participants using standard IT communication tools.

- Reduce product and processes development time by 50%, reduce costs by 30% and reduce the number of errors in a test series of up to 40%.

In the paper presented concept of project-driven concurrent realisation of orders was tested and successfully implemented in several Slovenian companies.

6 Acknowledgement

The authors gratefully acknowledge to Slovenian companies: Cimos Koper, Liv Postojna, Iskra MIS Kranj, Iskra PIO Šentjernej, Litostroj Power Lubljana, Polycom Škofja Loka which enabled testing and implementation of system of project-driven concurrent realisation of orders.

7 References

[1] Kušar, J., Duhovnik J., Grum J., Starbek, M. (2004). How to reduce new product development time. *Robotics and Computer-Integrated Manufacturing*, vol. 20, no. 1, p. 1-15.

[2] Prasad, B. (1996). *Concurrent Engineering Fundamentals*, Volume I, Integrated Product and Proces Organization, New Jersey, Printice Hall PTR, p. 216-276.

[3] Kendall, I.G., Rollins, C.S. (2003). *Advanced Project Portfolio Management and the PMO*, J. Ross Publishing, Inc.

[4] Kušar, J., Rihar, L., Duhovnik, J., Starbek, M. (2014). Concurrent realisation and quality assurance of products in the automotive industry. *Concurrent engineering*, vol. 22, no. 2, p. 162-171,

[5] Rihar, L., Kušar, J., Duhovnik, J., Starbek, M.. (2010). Teamwork as a precondition for simultaneous product realization. *Concurrent engineering*, vol. 18, no. 4, p. 261-273.

[6] Winner, R. I. (1988). *The Role of Concurrent Engineering in Weapons System Acquisition*, IDA Report R-338, Alexandrija, VA: Institut for Defence Analysis.

[7] Duhovnik, J., Žargi, U., Kušar, J., Starbek, M. (2009). Project-driven concurrent product development. *Concurrent engineering*, vol. 17, no. 3, p. 225-236.

[8] Kušar, J., Rihar, L., Duhovnik, J., Starbek, M. (2008). Project management of product development, *Strojniški vestnik - Journal of Mechanical Engineering*, vol. 54, no. 9, p. 588-606.

[9] PMBOK Guide (2008). *A guide to the project management body of knowledge*, 5th ed., Newtown Square: Project Management Institute, USA.

The characterization of power-transformer noise

Gregor Čepon [a], Miha Pirnat [b], Janko Slavič [a], Matija Javorski [a], Miha Nastran [b], Peter Tarman [b], Borut Prašnikar [b], Miha Boltežar [a*]

[(a)] University of Ljubljana, Faculty of Mechanical Engineering, Aškerčeva 6, 1000 Ljubljana, Slovenia.

[(b)] KOLEKTOR Etra d.o.o., Šlandrova ulica 10, 1231 Ljubljana, Slovenia.

* Corresponding author:
E-mail: miha.boltezar@fs.uni-lj.si

Abstract

A newly developed calculation scheme for the load and no-load noise of an oil-insulated, three-phase, power transformer is presented. The numerical model is capable of a precise and efficient computation of the electromagnetic field, the mechanical displacement field, as well as the acoustic pressure field of the power transformer. The magnetic field generated by the coils excites the laminated steel core. These coils are exposed to Lorentz forces and the steel in the core is subjected to the magnetostrictive effect. The result of all these is increased vibrations, which are transmitted via the cooling oil to the transformer housing, which radiates the vibrations in the form of acoustic noise to the environment. Finally, the validity of the computer simulations was verified by means of the appropriate measurements.

1 Introduction

For a long time, the energy efficiency of power transformers was by far the most important criteria when developing new products. However, in recent years this has changed as power transformers are frequently being located close to urban areas. For this reason, the sound emissions have to fulfill strict, low-noise standards. Therefore, the prediction and the reduction of power-transformer noise are of increasing interest for the electrical power industry.

The manufacturing process for a power transformer lasts for several months, and only when the transformer is completely assembled can the noise level can be measured. Furthermore, any design changes at the manufacturing stage are demanding and, as a result, can be very expensive. This means that the manufacturer is at significant risk of not achieving the noise requirements and, therefore, can be subject to financial penalties. From the perspective of noise reduction it is essential to identify the sources of the noise and the way in which it is transmitted through the system. A simplified picture reveals that the magnetic field is generated by the coils [1] that are exposed to electromagnetic forces. Then, due to the alternating magnetic field, the core is exposed to the magnetostrictive effect [2], which leads to increased levels of vibration. These

vibrations are transmitted via the cooling oil onto the transformer housing, which then radiates the vibrations in the form of acoustic noise to the environment.

The transformer noise comes mainly from the following sources [1]: (1) the no-load noise caused by the magnetostrictive strain of the core laminations; (2) the load noise caused by the Lorentz forces resulting from the interaction between the stray magnetic field of the current-carrying coil conductors; and (3) the noise produced by the fans and the oil pumps. Since experiment-based investigations of the noise emitted by the core and the coil are lengthy and costly processes, there is an urgent need for an appropriate numerical simulation tool.

Recently, the finite-element method (FEM) and the boundary-element method (BEM) have been effectively applied to model the sound field of an oil-insulated power transformer [3]. Using these methods it is possible to model the multi-physical nature of the power-transformer noise and the effects of different design parameters on this noise. Taking into account the research efforts in this field, here we present a detailed numerical model of a power transformer. The model is capable of predicting the load and the no-load noise, the electromagnetic field, the mechanical displacement field, as well as the acoustic pressure field. The basis of the model is our own experiments, made in connection with original methods for modeling the magnetostriction [4] and the dynamics of a laminated structure [5]. The developed numerical model is implemented in the form of engineering software that enables geometrical, functional and technological optimization analyses.

2 Core vibrations

In order to reduce the eddy currents and, consequently, any overheating, the magnetic core is usually made of a large number of thin electrical sheets. The magnetostriction of electrical steel is a phenomenon accompanying the magnetization process and presents a problem in terms of vibrations. It results in small deformations, where the change in the dimensions is independent of the magnetic flux direction and occurs with double the line frequency.

In order to predict the dynamic response of such structures it is necessary to develop a structural model of the laminated core, including an effective and reliable model of the contact, with friction between the metal sheets. In particular, the contact between the metal sheets (Figure 1), together with the clamping force in the normal contact direction, influences the stiffness and the damping properties of the whole system and hence its dynamic response [5].

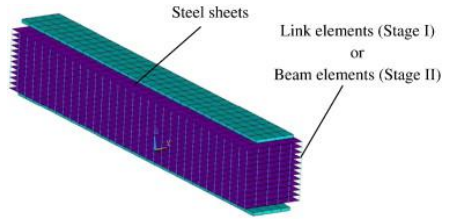

Figure 1: Finite-element model of the laminated structure

A simple, linear, friction contact law was used to model the interactions between the steel sheets, which allowed the use of implicit methods in the framework of linear structural dynamics. The stiffness and the damping parameters of the contact model were identified using an optimization process that was based on a comparison between the experimentally and numerically obtained modal parameters of the laminated stacks. The identified contact parameters were then subsequently used to predict the dynamic response of the laminated, power-transformer core.

The newly developed model of magnetostriction [4] can be integrated with the structural model of the magnetic core. This integration is not straightforward, as different numerical methods are used in order to solve the magnetic and structural problems. The phenomenon of magnetostriction is modeled by introducing the so-called magnetostrictive forces. This process requires the development of the appropriate rheological models and an experimental identification of the relationship between the magnetic flux density and the magnetostrictive deformation. In this context an original experimental test rig was developed that makes it possible to measure the magnetostrictive properties of electrical steel (Figure 2) with a high degree of accuracy. These experimentally obtained results served as the input parameters for the developed magnetostriction model.

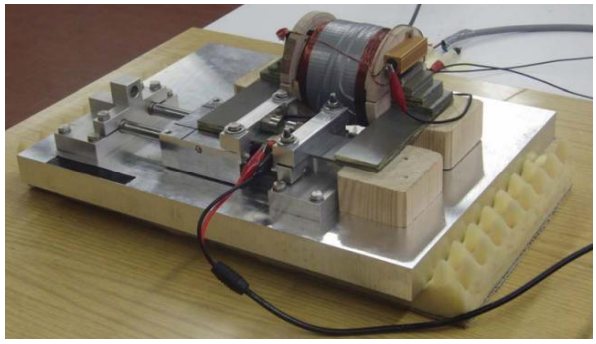

Figure 2: Experimental set-up for measuring the magnetostriction

By using the proposed method it is possible to calculate the vibration of the core by considering the different modes, the complex forces exciting a three-phase transformer, and finally the response of the core due to the magnetostriction (Figure 3).

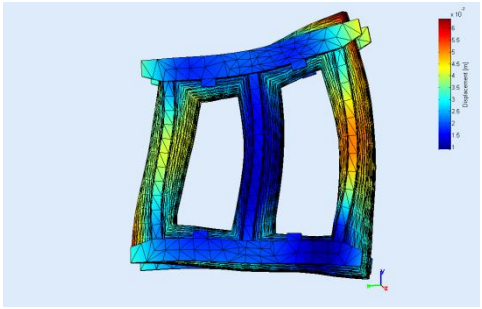

Figure 3: Response of the core to the magnetostriction

3 Coil vibrations

The load-based noise is generated by Lorentz forces that are due to the interaction between the transformer's stray magnetic field and the current-carrying winding loops. The interaction of these magnetic forces with mechanical structures causes vibrations. Because of the asymmetry of the winding set-up in large power transformers (e.g., spiral windings) a full 3D-model has to be established. The windings of power transformers are constructed using several winding technologies, e.g., helix-like layer windings (for LV winding) and spiral-like coil windings (for HV winding), as shown in Figure 4. The analysis of the vibration behavior needs to consider these asymmetries to ensure the correct mechanical behavior. In particular, the position of the natural frequencies of the vibratory structure (Figure 4) with respect to the excitation frequency of 100/120Hz (double the line frequency) is a critical parameter in the amplification of excited vibrations.

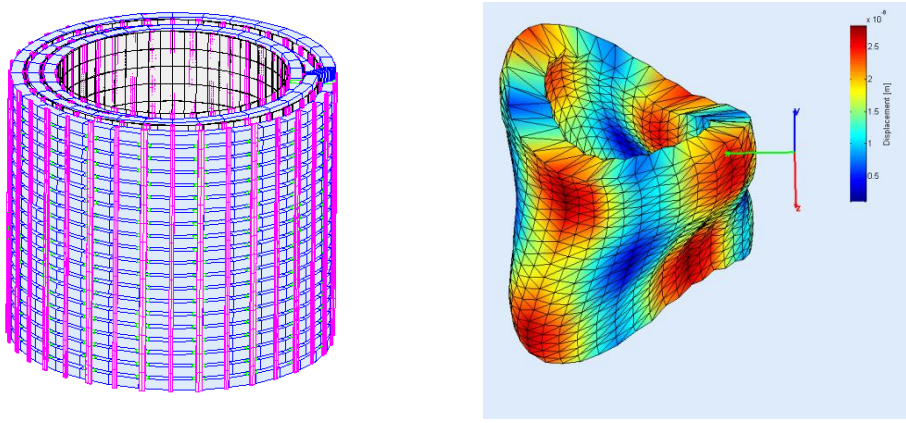

a) b)

Figure 4: LV winding; a) FEM numerical model, b) Response due to the Lorentz forces.

4 Tank vibrations and the radiated sound field

The vibrations generated by the magnetic core and the coil are transmitted through the oil onto the external walls of the transformer tank. This represents a typical problem of the interaction between a flexible structure and a stationary fluid. Such an interaction is complex and influences the dynamic response of the whole system as well as the transmission of vibrations through the core and the coils to the tank of the power transformer. Due to its mass and damping properties, the impact of the surrounding fluid is more pronounced on the dynamic response of the whole system.

In the second step of the developed calculation scheme, the previously calculated core and winding-surface displacement are taken as the mechanical excitation in a 3D acoustic-mechanical FEM of the complete oil-filled tank (Figure 5). Furthermore, in the oil-filled tank model, the 120° phase shift between the three windings is taken into account. The vibrations from the core and the coils are transmitted via the insulation oil to the transformer tank. The thin wall of the tank acts as an acoustic membrane, which causes an amplification and modification of the pressure waves, and especially in the case of resonance, an increased emission of noise. The tank should be designed in such a way as to avoid any unnecessary noise increase due to resonance.

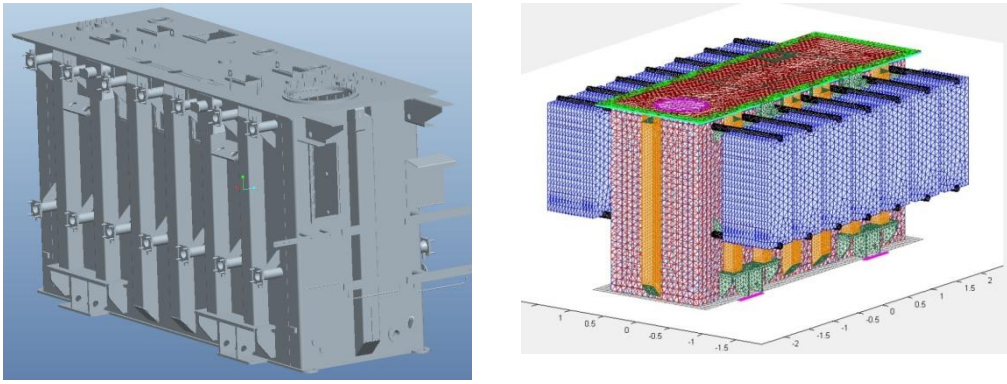

a) b)

Figure 5: Transformer tank; a) CAD model, b) FEM model

In the final step, the previously calculated vibrations of the tank surface are applied as the mechanical excitation in the final acoustic simulation to calculate the radiated transformer noise. For the computation of the free-field sound radiation, the complete structure of the tank was discretized using boundary elements. As the air surrounding the transformer has a negligible effect on the vibrations of the tank, a BEM is well suited to predicting the radiation of transformer noise from the displacement data (Figure 6).

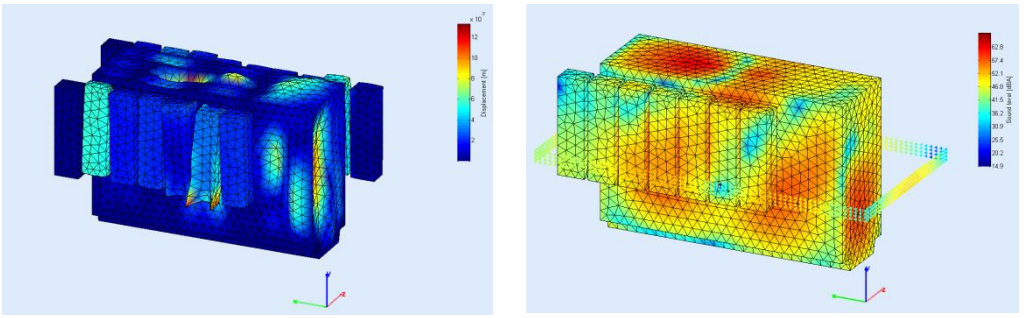

a) b)

Figure 6: Numerical simulation of the response and acoustic field; a) Displacement response, b) Acoustic field

The developed numerical model was validated by comparing the simulation results with the corresponding measured data. The acoustic simulations were verified by full-size measurements based on near-field acoustic holography.

5 Conclusion

In this paper a new numerical scheme is presented for the precise and efficient computer modeling of the load and no-load noise of the power transformers. From the perspective of noise generation, the main sources of noise are identified. Virtual design and the verification of power transformers will replace the time-consuming and very costly experimental testing. The presented computer simulations have been proven to be a useful tool for the prediction, investigation and reduction of power-transformer noise.

6 References

[1] Rausch, M., Kaltenbacher, M., Landes, H., Lerch, R. , Anger, J. , Gerth, J. ,Boss, P. (2001). Combination of finite and boundary element methods in investigation and prediction of load-controlled noise of power transformers, *Journal of Sound and Vibration*, vol. 250, no. 2, p. 323-338.

[2] Javorski, M., Slavič, J., Boltežar, M. (2012), Frequency Characteristics of Magnetostriction in Electrical Steel Related to the Structural Vibrations, IEEE Transactions on Magnetics, vol 48, no. 12, p. 4727-4734.

[3] Ertl, M., Landes, H., Investigation of load noise generation of large power transformer by means of coupled 3D FEM analysis (2001), *The International Journal for Computation and Mathematics in Electrical and Electronic Engineering*, vol 26, p. 788-799.

[4] Javorski, M., Čepon, G., Slavič, J., Boltežar, M. (2013), A Generalized Magnetostrictive-Forces Approach to the Computation of the Magnetostriction-Induced Vibration of Laminated Steel Structures, *IEEE Transactions on Magnetics*, vol 49, no. 11, p. 5446-5453.

[5] Pirnat, M., Čepon, G., Boltežar, M. (2013), Introduction of the linear contact model in the dynamic model of laminated structure dynamics: an experimental and numerical identification, *Mech. mach. theory*, vol. 64, pp. 144-154.

Vibrational ice crushing for kitchen purposes

Vid Resnik [a*], Joško Valentinčič [a], Izidor Sabotin [a], Andrej Lebar [a], Marko Jerman [a], Nejc Matjaž [a], Henri Orbanić [b]

[(a)] University of Ljubljana, Faculty of Mechanical Engineering, Aškerčeva 6, 1000 Ljubljana, Slovenia.

[(b)] BSH hišni aparati d.o.o. Nazarje, Savinjska cesta 30, 3331 Nazarje, Slovenia.

* Corresponding author:
E-mail: vid202@yahoo.com

Abstract

Till now, normal blenders were used for ice crushing purposes, but there were several problems. Blender is not appropriate for ice crushing, thus there are some negative effects on the blender. Likewise, the quality of crushed ice is relatively low. As a possible solution to these problems, a new idea is proposed: ice crushing with vibrations. The goal is to reduce noise and try to maintain control over the crushed ice particles. The design and optimization of a model of ice crusher was performed. The model enables a progressive way of crushing with vibrational mechanism based on two different mechanisms: eccentric shaft and crankshaft mechanisms.

1 Introduction

Project started in cooperation with BSH (Bosch and Siemens Home Appliances) and Laboratory for alternative technologies (LAT) on Faculty of Mechanical Engineering, University of Ljubljana. BSH is a company that produces a large number of house appliances. They are always interested in development of their current products and also support development of completely new products that cannot be found on the market yet.

For the purpose of ice crushing, normal blenders are usually used, but the results are not satisfactory. Blender is not meant for ice crushing, however it is often used for this purpose. A side product of ice crushing with blender is so called snow which is unwanted. Snow is created because of randomly distributed crushing inside the chamber. Blades are rotating at fixed frequency and ice cubes and particles bounce freely in the blender. If small particles of ice are crushed to smaller pieces again and again the final product looks like snow. Also there is a problem with noise, because ice cubes are flying all over the space inside blender and hitting the surrounding wall. The blade is continuously hitting fragile ice cubes, so that they are being hit towards the frame surface. Both processes produce a lot of noise which is not desired for the household appliances. Control over the size of the crushed ice particles is of utmost

importance. Professional cocktail barmans use many different shapes and sizes of ice, so it is desirable to maintain control.

As a possible solution to these problems, a new idea was presented by BSH. They wanted to know, if it is possible to crush ice with vibrations and at the same time reduce noise and try to maintain a bit bigger control over the crushed ice particles. The starting point was first to explore the basic possibilities of vibrational ice cube crushing. Point of interest was also, if this could be appropriate for kitchen use. Because we did not know if similar applications already exist, the market research of current products was performed.

2 Research of appropriate concepts

Currently there are two types of ice crushing principles used, hand powered crushing and electrically powered crushing. Hand powered crushing can be performed using a simple awl, some spiky forks, or with apparatus that uses the same principles with hand powered rotational blades. All electrically driven gadgets for ice crushing work on same basics, that is rotational blade crushing. Differences are in design of individual products, different position of blades, applying the force on cubes from the outside or without etc.

However, none vibrational ice cube crushing mechanisms were found on the market. Because the vibrational mechanism has not been applied to ice crushing before on the market, another research of vibrational mechanisms and their use was needed. Vibration is a very wide term with many accepted meanings, depending on where it is used and what for. For ice crushing only oscillatory movement is reasonable, because our process must run continuously. Short research on how vibrations are commonly created showed that for ice crushing for houshold purposes, only different types of eccentric rotors or combined crankshaft mechanisms should be used.

The next question is, how to apply vibrations to ice cubes in order to achieve actual crushing. So appropriate frame design was the new challenge. After considering all important points of view a final conclusion was still not drawn. A good idea came from the members of LAT, that progressive crushing method should be used. Progressive crushing is mostly known in quarry industry, where they produce different sizes of clay and sand. The principle is appropriate because there is no need to apply high forces, thus minimal forces and minimal movements are sufficient for crushing. Moreover, by adjusting position of one of the plates, the size of crushed particles can be well controlled.

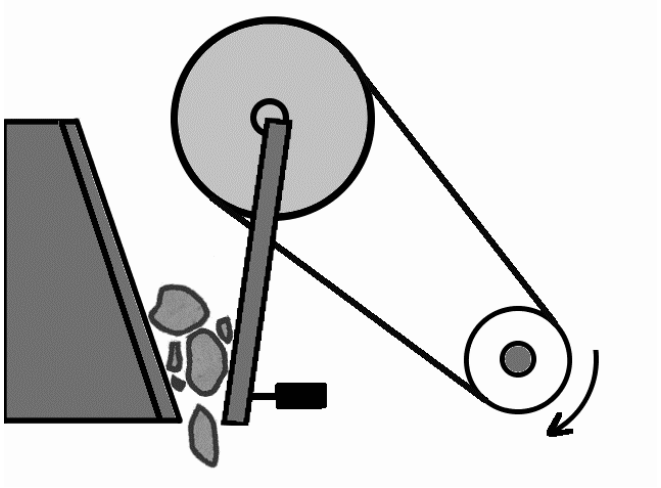

Figure 1. Progressive crushing

3 Conceptual model of the prototype

The next aim was to design and create a 3D model of ice crusher that will contain the progressive way of crushing with vibrational mechanism based on eccentric shaft or crankshaft mechanism. Before the modelling was performed, it was necessary to be sure that vibrations are going to crush the ice. Average sized kitchen ice cube can hold up to 40 Mpa of pressure. By applying basic estimations we concluded that the crushing shouldn't be a problem. Ice cubes can be crushed with vibrations produced by mentioned systems. After some sketching and remodelling first 3D models were created. The model was created intended to be build in a workshop as a prototype, so it was designed modularly. Beforehand it could not be predicted which vibrational mechanism would work better, considering both price and performance, so both versions of mechanisms were designed. It is a rough model which aim is to examine how the mechanism should be placed to work.

The crankshaft mechanism has more parts and it is more complicated than the eccentric shaft mechanism, but you can adjust the stroke of the swinging plate, and after the stroke is determined, the force can be varied by changing the rotational speed of the crankshaft. Good control over parameters can be obtained. With some basic calculations to determine the frames of working area we can later improve the design with try and error method. The stroke of the plate at the joint can be defined as a two-dimensional plate where conrod is mounted to the crankshaft at the center of rotation. The force can be determined as an acceleration of the joint of conrod and swinging plate multiplied with mass of moving objects.

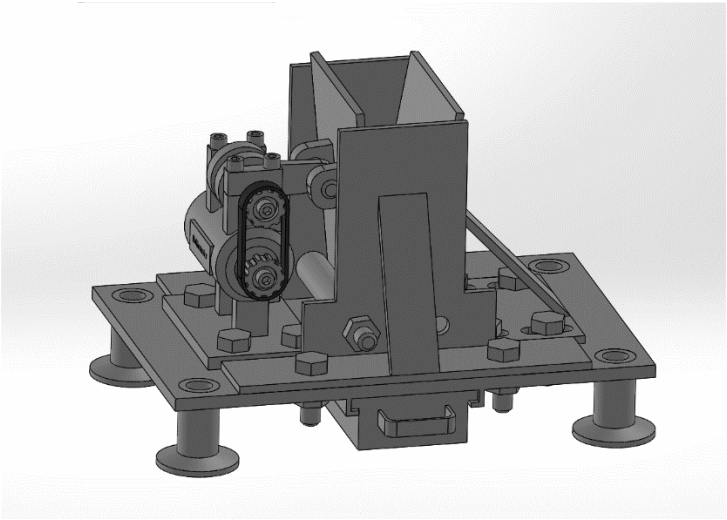

Figure 2. Ice crushing model with crankshaft mechanism

The second mechanism, where eccentric shaft rotor is mounted directly on the swinging plate, has less parts and it is easier to manufacture. Created force can be estimated by taking into account the mass of the rotor, rotational speed of the rotor and distance between mass center and center of rotation. Achieved forces can be very high. It is harder to estimate achieved stroke, because it varies highly depending on the speed of rotation of the rotor, on damping of the plate swinging mechanism, mass of all moving bodies due to oscillations and on the combination of applied springs. Also the transport of the ice cubes should be considered. If we manage to tune-up all components together we can get very good crushing conditions.

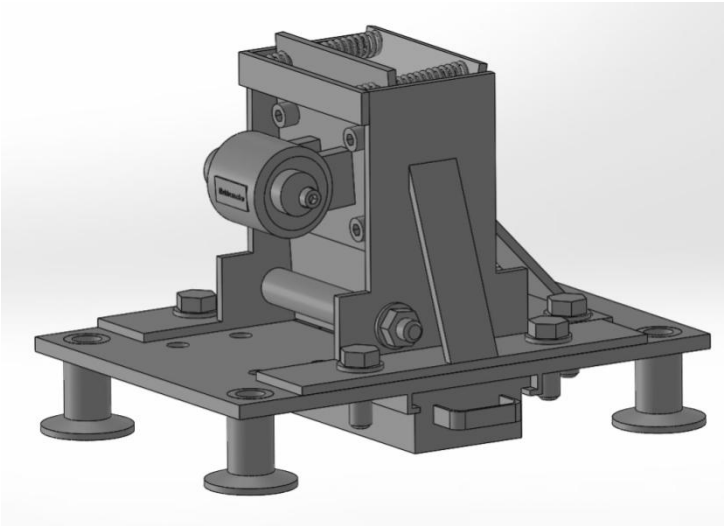

Figure 3. Ice crushing model with eccentric shaft mechanism

To maintain slightly better control over final product of crushed ice, the plate that does not move in the process of crushing, can be adjusted and the slit can be closed or opened depending on the required size of the ice particles.

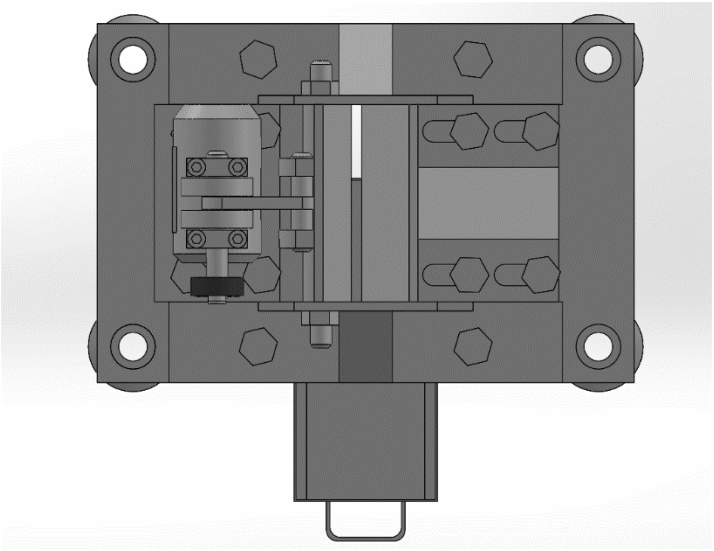

Figure 4. Adjustable slit size, movable plate

After 3D models were examined and some weakneses were pointed out, slightly improved mechanism was packed into user friendly housing. All principles are the same only resized. The new housing is also restricting the mass that can be processed at the time, considering that we usually crush ice only for few drinks at one time. So the forces could be even smaller and also the noise would be reduced, therefore more suitable for everyday use.

Figure 5. Final design

4 Conclusion

Project stopped at this phase. The next step is to continue with building the prototype and start with testing it in the workshop. After trimming all parameters in order to create the wanted conditions for crushing, only housing design and desired processed quantity should be determined and the kitchen ice crusher could be produced. Vibrational ice crusher is not known on the market yet and has good potential. It promises better control over crushed particles size, it is supposed to produce less noise, it should work faster than current crushing appliances and it represents a new product on the market.

Gorenje A+++ tumble dryer

Lovrenc Novak [*], Brane Širok, Marko Hočevar

University of Ljubljana, Faculty of Mechanical Engineering, Aškerčeva 6, 1000 Ljubljana, Slovenia.

* Corresponding author:
E-mail: lovrenc.novak@fs.uni-lj.si

Abstract

Development of the air circulation system of a domestic tumble dryer of the highest energy class A+++ (A-63%) is presented. Requirements for the dryer included maximum energy consumption of 0,21 kWh/kg clothes and maximum drying time of 20 min/kg clothes. These requirements could only be met by increasing air flow through the machine, which was achieved mainly by redesigning the circulation fan. The development process included intensive use of Computational Fluid Dynamics methods on both 2D and 3D models. A squirrel-cage type fan, which consists of a radial impeller with forward-curved blades and a scroll housing, is used in the dryer. The unsteady nature of flow with significant interaction between the impeller and the scroll, which is common for this fan type, required the simulations to be run as transient. The sliding mesh approach was used to model motion of the impeller. The optimized impeller design was manufactured in three versions with different outer diameters and widths. Performance curves and operating points of the prototype impellers were measured by integrating them in an actual tumble dryer. Assessment of the fan versions included their noise characteristics.

1 Introduction

Tumble dryers represent one of the most energy-hungry domestic appliances. In the recent years, a significant reduction of energy consumption has been achieved by replacing the traditional electrical heaters and air-cooled condensers with heat pumps. Tumble dryers of the top A+++ category (EU Energy Label), which are based on heat pump technology, consume less than a third of the energy of a typical condensing tumble dryer with electrical heater (B energy class).

Modern domestic tumble dryers are based on a closed air circulation system, which takes care for transport of moisture from the clothes to the air and from the air to the reservoir or drain. Transfer of moisture to/from air is achieved by changes in air temperature. Heated air with low relative humidity is blown over the clothes to absorb moisture, and then the moist air is cooled to achieve condensation of water from air. Heating and cooling of air takes place in condenser and evaporator of the heat pump.

Circulation of air is provided by a fan, which is typically driven by a fixed-speed motor, also used for drum rotation.

This paper presents a part of the development work done in scope of the Gorenje A+++ tumble dryer project. Our focus was optimization of the air system components with the main goal of increasing the air flow rate. For this purpose a redesign of the fan impeller, scroll and air channels was undertaken. The fan impeller is a radial type with forward-curved blades. Such fans are often called squirrel-cage fans or Sirocco fans and are commonly used for dryers and general HVAC applications due to their relatively high mass flows, size compactness and low noise levels. The main disadvantage is their relatively low efficiency and the need for empirical designing [1].

An existing A++ tumble dryer model was used as a base version for optimization and redesign of the air system components. Restrictions in component size were imposed in some cases by the requirements to not alter production tools. In this respect, the most restricting was the machine back plate design which limited the maximum scroll size.

2 Numerical simulations

CFD simulations were extensively used in the process of fan design. All simulations were performed by using the Ansys Fluent 13 software. A standard engineering approach was chosen by employing the Reynolds Averaged Navier Stokes (RANS) equations. Turbulence was modelled by the SST model which is a proven, robust and accurate model, suitable for turbomachinery applications.

Geometry of the numerical model included fan impeller and casing with air channels up- and downstream. Both 2D and 3D models were designed in several geometrical versions. An example of the 2D model is shown on the left side of Fig. 1. The 3D model, which includes complete impeller and casing geometry with connecting channels, is also shown on Fig. 1 (right side). Model border upstream the fan is placed at the outlet from the evaporator and model border downstream the fan is placed at the drum inlet holes.

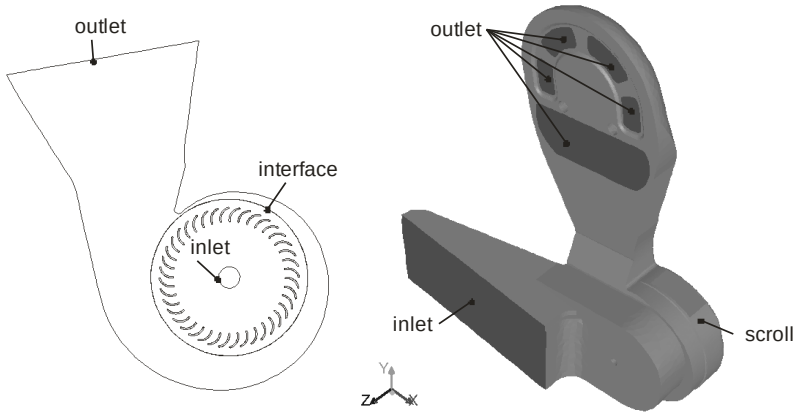

Figure 1. Model geometry and boundary conditions – 2D model (left) and 3D model (right).

Numerical grids were generated by using the ANSYS ICEM CFD 13 software. A stationary and a rotating domain were created separately and later coupled with the sliding mesh interface. Tetra grids with prismatic elements at walls were used. Near wall grid density was chosen for application of wall functions. An average 2D model grid consisted of 27400 cells and the 3D model grid consisted of approximately 2 million cells.

Boundary conditions were set to represent real conditions and be numerically correct. All walls were set as hydraulically smooth walls with no slip. Inlet was set as either pressure inlet or mass flow inlet and was varied to simulate different operating points. Outlets were pressure outlets and were set on all openings that are used for blowing of air into the drum. Rotational speed of the impeller was constant at 2750/min. Working fluid was incompressible air with constant density.

Simulations were initially done as steady-state, but due to convergence problems and indications of flow unsteadiness it was necessary to perform transient (unsteady) simulations. Flow unsteadiness is actually commonly encountered in fans with forward-curved blades, even at design point operation. Besides unsteadiness, flow in these fans is generally complex and includes asymmetric conditions, significant interaction between the impeller and the scroll and a relatively intense backflow through the impeller near the inlet side [3]. Flow separation and recirculation in blade passages and scroll is also common. Consequently, highest efficiencies for such impellers are limited to around 60%, and total efficiencies up to 40% [2], which is inferior to the fans with backward-swept blades. The complex and unsteady nature of the flow prevented proper convergence of steady-state simulations. In our case, it could be achieved only for certain air flow rates on the 2D models and never on the 3D model. Reasonable convergence in residual values could be achieved for unsteady simulations, with only minor oscillations in integral parameters (torque, mass flow) still present.

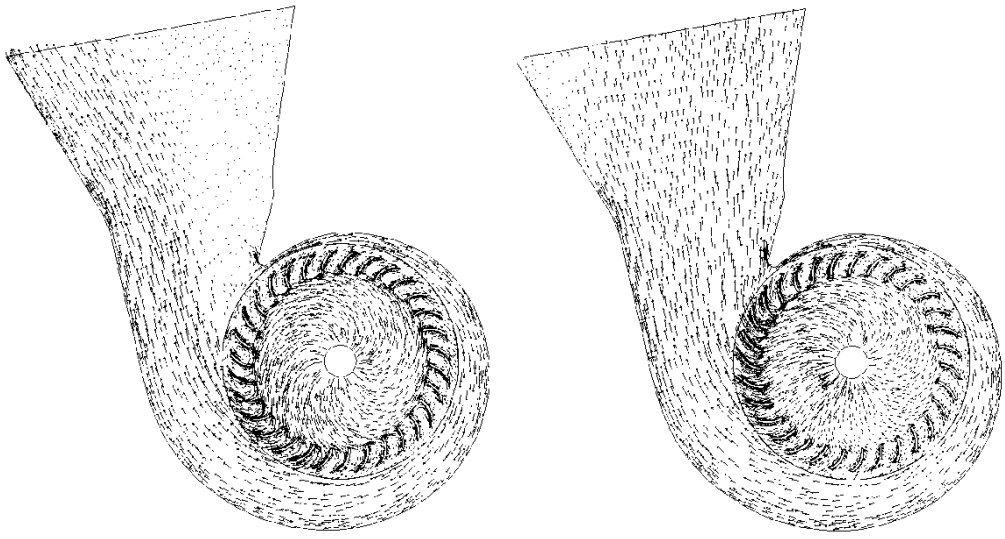

Figure 2. Vector field for steady-state and transient calculation on a 2D model.

Figure 2 shows vector fields computed on one of the 2D geometries. Absolute velocity is shown in the stationary domain and relative velocity is shown in the rotating domain. Vector length is scaled with the velocity magnitude. On the left hand side of Fig. 2 a steady state solution is displayed while on the right hand side an unsteady solution after 6.5 impeller rotations is displayed. Both simulations were set with identical boundary conditions; inlet total pressure was -100 Pa relative to the outlet static pressure of 0 Pa. A significant difference between the steady and the unsteady results can be seen. The steady calculation predicts highly asymmetric conditions in the impeller area with the useful flow being created through a relatively small portion of the total impeller circumference. Consequently, the scroll and the outlet channel are also not optimally sized. On the contrary, the unsteady simulation predicts a more efficient flow through the impeller, the scroll and the outlet channel, which reflects in a significantly higher calculated air mass flow (more than double relative to the steady state prediction).

Optimization of the fan geometry was eventually based on data from literature [1]-[5] and a series of unsteady numerical simulations on a 2D geometry. The resulting impeller design had outer diameter of 144 mm and included 40 forward swept blades. Its maximum efficiency was computed at inlet total pressure of -350 Pa. Subsequent calculations on the 3D model provided a more realistic estimate of conditions in an actual fan with casing. It is evident that geometry of the casing and the channels up- and downstream the impeller causes further reduction of flow uniformity and symmetry. Examination of conditions at several axial cross-sections shows worst conditions at the blade tip. Here, secondary flows form mainly due to asymmetric inflow to the impeller, due to high flow turning (axial to radial direction) and due to backflow at the impeller-casing gap. Flow conditions and effective function of the impeller improve in planes closer to its back plate.

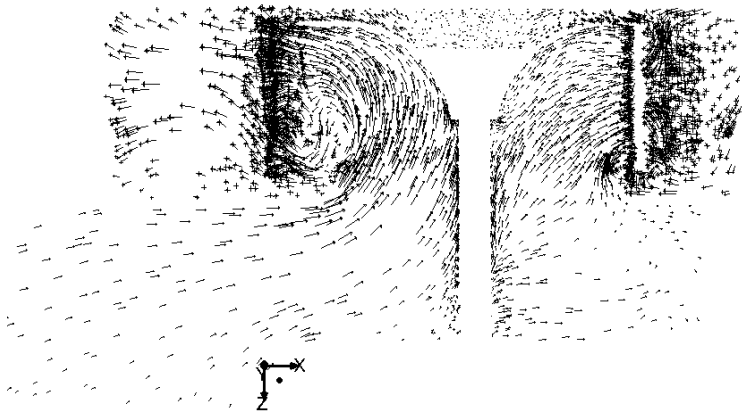

Figure 3. Vector field of absolute velocities at meridional cross-section in horizontal orientation (plane z-x).

Figure 3 shows vectors of absolute velocity in an impeller-centred cross-section, oriented horizontal relative to the actual coordinates. Conditions at impeller inlet are especially unfavourable on the left side, where high redirection of incoming flow is

necessary due to the orientation of the suction and pressure channels. This results in more than half the impeller width being blocked by the recirculating flow. In other parts of impeller circumference the recirculation at blade tip also takes place but is generally within the expected limits.

Reduction of the unwanted 3D flow features was achieved mostly by minimising the impeller-casing gap at the inlet side and by redesigning the fan inlet opening. Increasing the axisymmetry of flow conditions through the fan was highly limited by the fixed layout of the up- and downstream air channels.

3 Measurements

The numerically optimized fan design was created as a 3D printed prototype and subjected to measurements in an actual tumble dryer. A test station (Fig. 4) was built which enabled measuring of the complete fan performance curve. For this purpose the air flow rate, the pressure difference of the fan, the air density and the fan rotational speed had to be measured. In this respect, accurate air flow rate measurement represents the highest challenge due to the complex geometry of the air channels in the actual dryer, which do not provide measuring planes with sufficient flow uniformity. Therefore, an alternative approach was taken by conducting fan performance measurements in an open air system, where air is sucked into the dryer at the filter door upstream the heat exchangers and discharged out of the dryer at the opening, cut in the main door. This opening is connected to the air flow measurement system which is based on the orifice plate method. Downstream the flow rate measurement location an auxiliary fan was installed to help overcome system resistance at the highest air flow rates. The fan operating point was varied by changing system resistance with a damper and by setting the auxiliary fan rotational frequency.

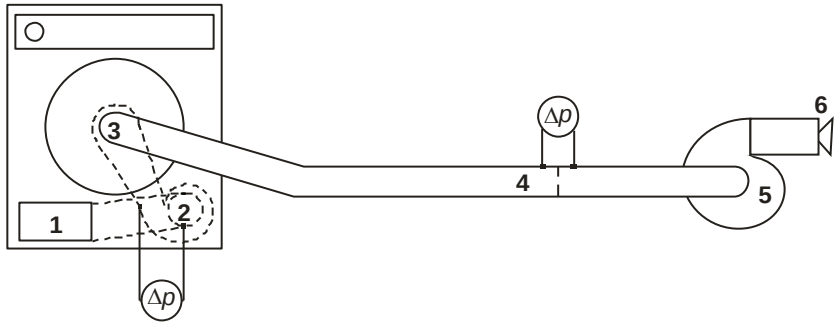

Figure 4. Measurement station: 1 – filter door, 2 – fan, 3 – opening in the main door, 4 – flow measurement (orifice plate), 5 – auxiliary fan, 6 – damper.

Determination of the volumetric air flow was performed on the basis of measured pressure difference at the orifice according to the ISO 5167 standard [6]. The pressure difference was measured by the Endress+Hauser Deltabar PMD235-KUBA1EA1C pressure transducer. Identical transducer type was used to measure static pressure difference between the fan inlet and outlet locations. Signals from the transducers were

led to a data acquisition card connected to a PC and were sampled every second. The fan rotational speed was measured by the Velleman DTO6234 digital tachometer. Air density was determined on the basis of measured ambient temperature, humidity and pressure.

Initial measurements were conducted for the CFD-optimized impeller (labelled V2) and the scaled-up version of the existing fan impeller, used in the A++ dryers (labelled V1). Both impellers are shown on Fig. 5. A further increase in fan performance was attempted by upscaling the impeller V2 to maximum dimensions still acceptable for installation in the existing scroll. Upscaling was done by increasing the impeller outer diameter and width while the inner/outer diameter ratio and number of blades remained unchanged. The new version was labelled as impeller V3. Due to excessive noise emitted by the V3 impeller a fourth impeller version (V4) was made by decreasing the diameter of impeller V3. Basic geometric data for all the impeller prototypes is given in Table 1.

Table 1. Basic data for impeller prototypes

label	**V1**	**V2**	**V3**	**V4**
blade design	**G**	**FS**	**FS**	**FS**
outer diameter [mm]	156	144	155	150
inner diameter [mm]	112	115	125	121
width [mm]	56	56	60	60
number of blades	30	40	40	40

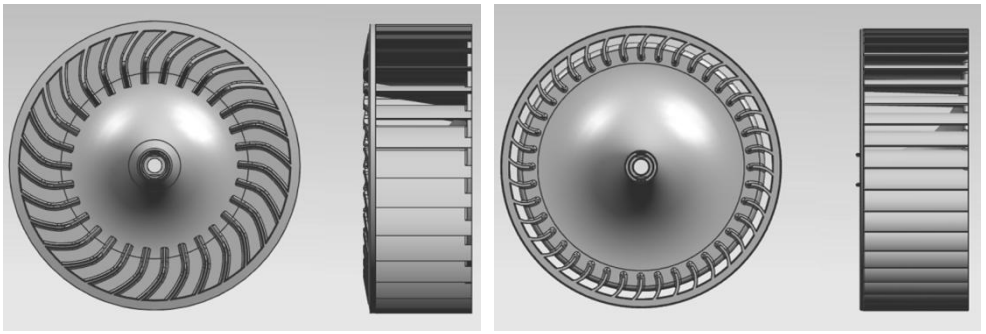

Figure 5. Impeller V1 (left) and impeller V2 (right).

Measurements of fan performance curves were performed with the dryer operating in the ventilation program (heat pump off) and without any clothes in the drum. Presence of clothes in the drum causes undesirable pressure and air flow oscillations; clothes could also enter the pipe leading to the air measurement system and obstruct normal air flow.

The air volumetric flow under normal tumble dryer operation was determined by measuring the fan static pressure difference in the non-modified, closed air circuit. By knowing the fan pressure it was possible to determine the corresponding air flow from the previously determined fan characteristic curve. Operating point was measured both with and without clothes in the drum in ventilation mode. A standardized structure and quantity (7 kg) of dry clothes was used for the measurements.

Measured performance curves and operating points for dryer operation with clothes are presented in Fig. 6. All the measured curves have a saddle-type shape which is typical for the impellers with forward-curved blades. Fan operation should be in the region of stable flow, which is the descending curve region, right from the local curve maximum. Here, lowest performance was measured for impeller V1, which was based on the existing design. Higher parameters were measured for the V2 and V4 impellers and highest for the V3 impeller. With increasing air flow rates, the V2 curve drops faster than the others, while the difference between the V3 and V4 almost disappears. However, the operating points were determined in the range between 250 and 280 m^3/h and here the best performance could be expected from the V3 impeller, which is also largest in size. Disadvantage of the V3 impeller was its noise, with dominant frequency linked to the blade passage frequency. Therefore, the V4 impeller was suggested as the final version for the dryer.

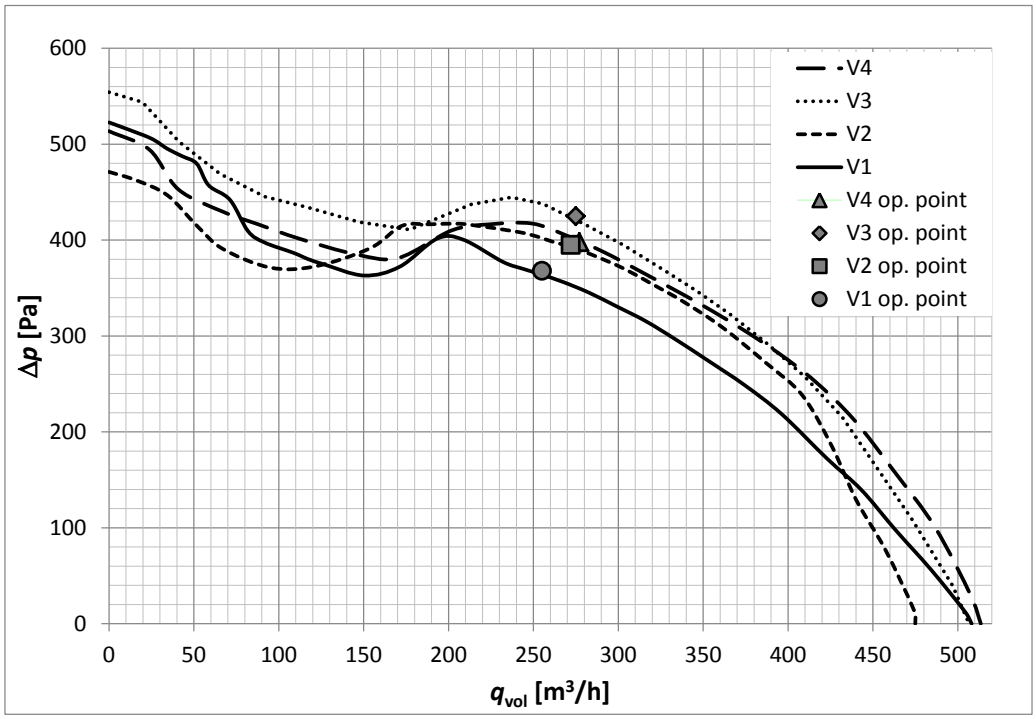

Figure 6. Performance curves for measured impellers.

4 Conclusions

The presented numerical and experimental evaluation of several versions of the tumble dryer circulation fan leads to the following conclusions:

- CFD simulations of the fan with forward-curved blades were affected by the complex and unsteady nature of flow, common for this fan type. Transient calculations had to be performed in order to achieve converged results.
- Newly designed fan impeller has a higher performance curve than the comparatively sized version of the original impeller. Air flow rate at full load operation could be increased by around 8% by using the new impeller. Maximizing the impeller diameter and width without modifying the scroll showed very little improvement in air flow rate at operating point. Differences were within the measurement uncertainty range.
- In addition to impeller re-design it was crucial to perform modifications in casing design. Increase of the fan inlet opening was identified as the most important measure that resulted in the overall 20% higher airflow, relative to the original design from the A++ machine.
- Increasing the impeller outer diameter resulted in increased noise with dominant frequency related to the blade passage frequency.
- Reaching the A+++ energy class requirements for the tumble dryer could only be achieved after further optimization of the heat pump components.

5 References

[1] Frank, S., Darvish, M., Tietjen, B., Stuchlik, A. (2012). Design improvements of Sirocco type fans by means of computational fluid dynamics and stereoscopic particle image velocimetry. *FAN 2012 proceedings*, paper 49.

[2] Guo, E.-M., Kim, K.-Y. (2004). Three-Dimensional Flow Analysis and Improvement of Slip Factor Model for Forward-Curved Blades Centrifugal Fan. *KSME International Journal*, vol 18, no. 2, p. 302-312.

[3] Jung, Y., Baek, J. (2008). A numerical study on the unsteady flow behavior and the performance of an automotive sirocco fan. *Journal of Mechanical Science and Technology*, vol. 22, no. 10, p. 1889-1895.

[4] Carolus, T. (2003). *Ventilatoren*. Teubner Verlag, Wiesbaden.

[5] Velarde-Suarez, S., Guerras Colon, F. I., Ballesteros-Tajadura, R., Gonzalez, J., Argüelles Diaz, K. M., Fernandez Oro, J. M., Santolaria Morros, C. (2012). Evaluation of squirrel-cage fans for HVAC applications in public transport: key parameters and design guidelines. *FAN 2012 proceedings*, paper 5.

[6] ISO 5167-2:2003 (2003). Measurement of fluid flow by means of pressure differential devices inserted in circular cross-section conduits running full – Part 2: Orifice plates. International Organization for Standardization. Geneva.

The potential of heat pumps in sustainable building

Henrik Gjerkeš [a,b*], Gašper Stegnar [a], Marjana Šijanec Zavrl [a]

[(a)] Building and Civil Engineering Institute ZRMK, Dimičeva 12, 1000 Ljubljana, Slovenia.

[(b)] University of Nova Gorica, Vipavska 13, 5000 Nova Gorica, Slovenia.

* Corresponding author:
E-mail: henrik.gjerkes@gi-zrmk.si

Abstract

Directive on the Energy Performance of Buildings Directive (2010/31/EU - EPBD Recast) sets high energy efficiency requirements for nearly zero-energy buildings (nZEB), as defined in Article 313 of the Energy Act EZ-1, which implies that energy needs have to be significantly covered by renewable sources (RES) on site or nearby. By 2020 (public buildings by 2018) all new buildings are going to have to meet the national criteria for the nZEB. Choosing a single family house, energy performance of the buildings was calculated with IDA Indoor Climate and Energy as a whole year detailed and dynamic multi-zone simulation study of indoor climate and energy use. The minimum energy performance requirements are represented by the area of the cost curve that delivers the lowest cost for the end-user and society. The results demonstrate that the minimum requirements set for new single family houses in national building codes in force are more severe than the minimum requirements corresponding to the cost optimal level, mainly due to the national energy and climate policy targets in the building sector. Among systems, heat pumps proved to be important competitors in seeking the cost optimal building performance.

It was shown, that heat pumps are environmentally acceptable and cost effective way of heating with plausible positive social multiplied effects. Heat pumps have support of local economy and are based on well-established technology, their operation is efficient, reliable and are suitable for almost all buildings. In the future it is expected to reach higher coefficient of performance (COP), especially at lower temperatures, which, together with further increase of renewables share in national electrical power system, makes heat pumps important foundation for further development in line with sustainable principles.

1 Introduction

Review of draft nZEB regulations in the Member States has shown that the key issue in the design of nZEB criteria lies in the definition of "nearly" zero-energy requirements [1]. Notwithstanding the open issues, the minimum requirements for the energy performance of buildings is obligated to meet and exceed the cost-effectiveness of life-

cycle perspective [2]. Renewable energy sources (RES) are an integral part of the fight against climate changes and are essential for sustainable growth, job creation and increasing the local energy security, and therefore are essential in the formulation of criteria for the nZEB. Taking into account the sustainability requirements and potential national RES, an analyses has been made, where the potential of various heating systems for residential buildings in the context of the nZEB criteria is being investigated.

By 2020, renewable energy should account for 20% of the EU's final energy consumption. To meet this common target, each Member State (MS) needs to increase its production, use of renewable energy in electricity, heating and cooling, and transport. The renewables targets are calculated as the share of RES consumption to gross final energy consumption. RES consumption comprises the direct use of renewable sources (e.g. biomass, syngas, biofuels) and the part of electricity and heat that is produced from RES (e.g. hydro, biomass cogeneration, solar power plants), while final energy consumption is the energy that households, industry, services, agriculture and the transport sector use. Slovenia started with 16 % in 2005 and has target to reach 25% utilization of RES in final energy consumption by 2020 [3].

In Slovenia the potential of solid biomass is high, with over 55 % of land covered with forests. Secondary wood is used mainly for heating by firing in individual furnaces and is prevailing fuel in household sector. It is local RES and is relatively cheap fuel, but could have also side effects, especially emission of PM10 hard particles, which becomes significant problem for Slovenia. In looking for more appropriate energetic utilization of high potential of wooden biomass, the innovative technologies developing and some already emerging on market (e.g. gasification with poly-generation) seems to be right direction, having in mind district heating systems, local energy self-supply and increase of RES level in national electrical power system. Considering sustainability circumstances, together with regional resources, the potential of heat pumps in residential sector was analysed in context of cost optimal nZEB performance.

2 Cost optimal building performance

The harmonised calculation methodology (Directive 2010/31/EU, article 5 and Annex III a) links energy performance requirements to economic targets in order to achieve cost optimum levels. This methodology supports the objective of minimising costs during a building's lifecycle, while maximising environmental benefits. Including the prognosis of rising energy prices offer even more scope for improving current regulations, as the cost savings from reduced use of energy are higher and can justify higher initial investment. The methodology combines uniform calculation rules with national data to ensure a fair treatment of Member States' national conditions. The definition of reference buildings and technology packages is a crucial part of the process as they affect directly on the assessment and on the possibility of finding cost-optimal solutions that will allow proper benchmarking levels to be compared with existing and planned national minimum energy performance requirements.

In order to investigate the cost optimality of minimum requirements in Slovenian building code the national study was initiated based on the EC comparative methodology framework for calculating cost optimal levels of minimum energy performance requirements for buildings and its elements [4]. The effort at the first stage was focused on the cost optimality at financial level, focusing at definition of cost optimum minimum requirements for new single family houses, which are the most numerous and represent 75% of the residential sector floor area, and 55% of the entire Slovenian building sector.

Single-family house	Multi-family house	Office building
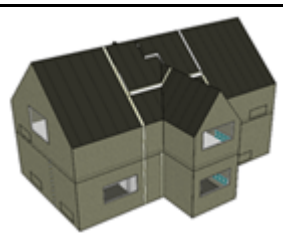		

Figure 1: Examples of the reference buildings

In continuation, Slovenia has established comparative methodology framework on the basis of article 5 of the Directive EPBD – Recast (2010/31/EU) and in accordance with Annex III, differentiating between different categories of buildings (single-family houses, block of flats and office buildings), Figure 1.

Fifteen reference buildings that were taken into study, reflect national building stock, since they are classified into residential and non-residential buildings and adequately cover the age of construction of the building. Reference buildings were chosen on the basis of the EU project IEE Tabula [5], which already dealt with the issue of the reference residential buildings and Registry of Real Estates.

Energy performance of the buildings was calculated with IDA Indoor Climate and Energy as a whole year detailed and dynamic multi-zone simulation study of indoor climate, and energy utilization. From the variety of specific results for the assessed measures (single measures and packages/variants of measures), a cost curve has been derived, shown in Figure 2 andFigure 3. For existing buildings single measures were applied, as well as packages of measures/variants. Single measures represent an improvement of the thermal envelope (either single or multiple components). Packages of measures include improvement of the envelope and replacement of the system for heating and domestic hot water. All combinations were subjected to two types of ventilation – natural and mechanical with heat recovery (AHU – Air Handling Unit).

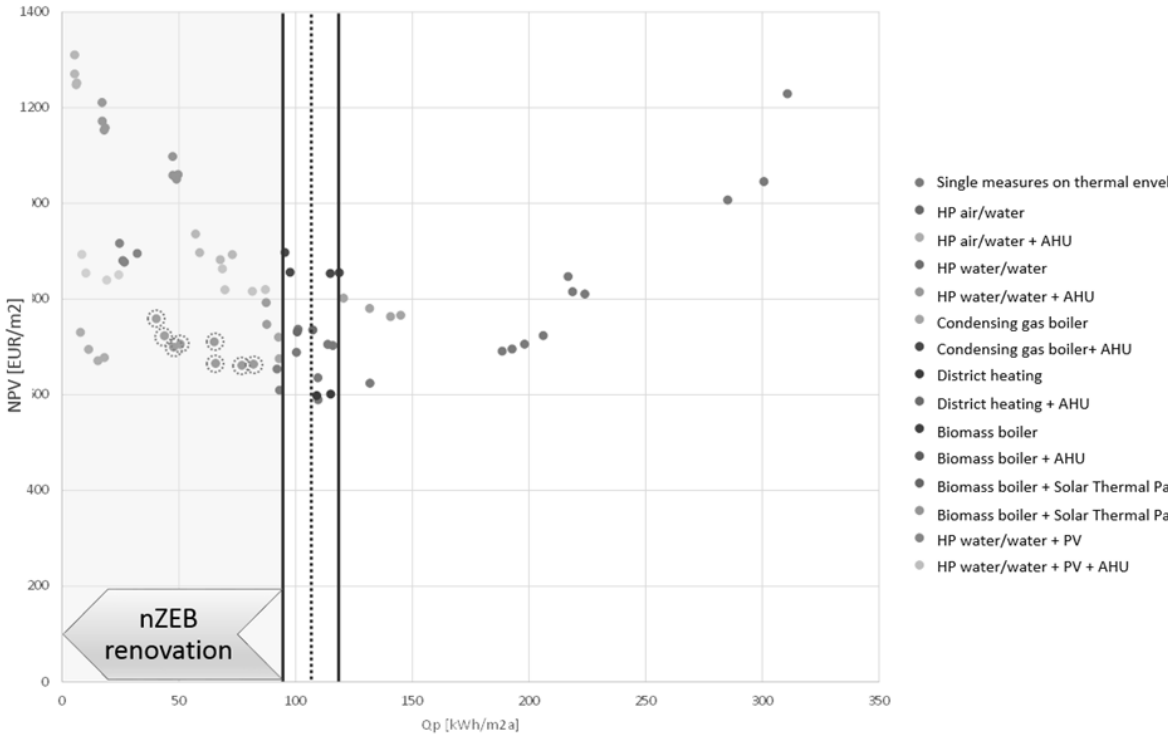

Figure 2: Global energy performance related costs in the reference single family house, built in 1960 and renovated (Qp – Primary energy; NPV – Net present value).

For each building type, cost optimal primary energy use was calculated, based on the feasible solutions leading to minimum net present value within 30 years period (20 years period for public buildings). The net present value calculation included both investment and operation cost using the discount rate of 1,53%. For initial energy prices, the current price data were used from the Statistical Office of the Republic of Slovenia, and includes the prognosis of the energy price trends within the calculation period [6].

The lowest part of the curve in Figures 2 and 3 represents the cost optimal combination of packages. To establish a comprehensive overview, all combinations of commonly used and advanced measures should be assessed in the cost curve. The packages of measures range from compliance with current regulations and best practices to combinations that realise nearly zero-energy buildings [2]. The minimum energy performance requirements are represented by the area of the curve that delivers the lowest cost for the end-user and/or for the company or society. Potentially, these requirements proved to be more effective and efficient than current national requirements, at less or equal cost. The area of the curve to the right of the economic optimum represents solutions that are underperformed in environmental and financial aspect. In Figure 3, the distance to target for new, nearly zero-energy buildings, is made visible on the left side of the cost-optimal levels interval (grey marked area).

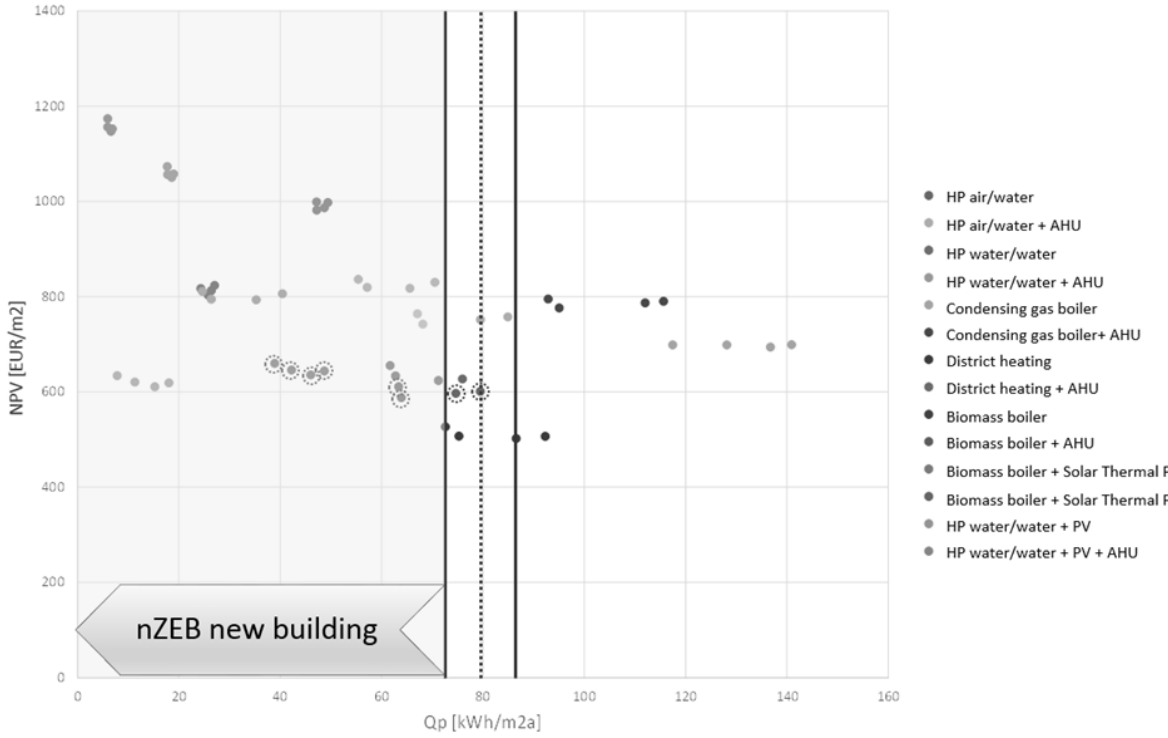

Figure 3: Global energy performance related costs in the reference single family house, new build, (Qp – Primary energy; NPV – Net present value).

The results also demonstrate that the minimum requirements set for residential buildings are more severe than the minimum requirements corresponding to the cost optimal level, mainly due to the national energy and climate policy targets in the building sector. Variants in compliance with the 2010 national building codes are based on the implementation of insulation levels and windows, resulting in the envelope specific heat transfer coefficient bellow 0,4 W/m^{2}K, use of condensing gas boiler and solar collectors for DHW and other systems like heat pump or biomass boilers [7]. Heat pumps (in Figures 2 and 3 marked with a circled dot) in variants with very good envelope insulation (around 20 cm), with various windows glazing and with natural or mechanical ventilation demonstrate a very good cost-optimal performance. Heat pumps proved to be important competitors among nZEB systems and considering other, especially environmental sustainability effects, were chosen for more comprehensive analysis.

3 RES based electricity generation

Renewable based generation share of the electricity fed into the grids increases the cumulative share of RES in heat pump operation. Due to the relatively cold climate (3300 DD) heating is still the main part of energy use in Slovenian building sector. In year 2012, households in Slovenia used 13.804 GWh of energy, most of it, i.e. 11.250

GWh, for heating and domestic hot water (DHW). The most common energy source for heating were wooden fuels with 51 % share, followed by fuel oil with 20 % and natural gas with 12 %. With 11,6 %, electricity becomes important energy source for space heating (652 GWh) and DHW (615 GWh), which together represents 40 % of electricity, used by households [8].

The share of renewable energy sources (RES) in total use of final energy is increasing, especially with different forms of wooden fuels and with rising of the number of district heating systems. The role of heat pumps, which transform renewable energy from environment (sun, ground), is increasing and became important energy source in sector heating. Therefore, from the sustainability point of view, the trends of the share of RES in power generation on national level are very important for meeting the targets of nZEB and sustainable building.

Renewable based generation accounted for 22,3% of the electricity fed into the grids of the European Union in 2012, a year-on-year increase of 7%. By the end of the decade renewables are predicted to be the second largest component of the EU energy mix, accounting for 34% of the total generation, Figure 4 [9].

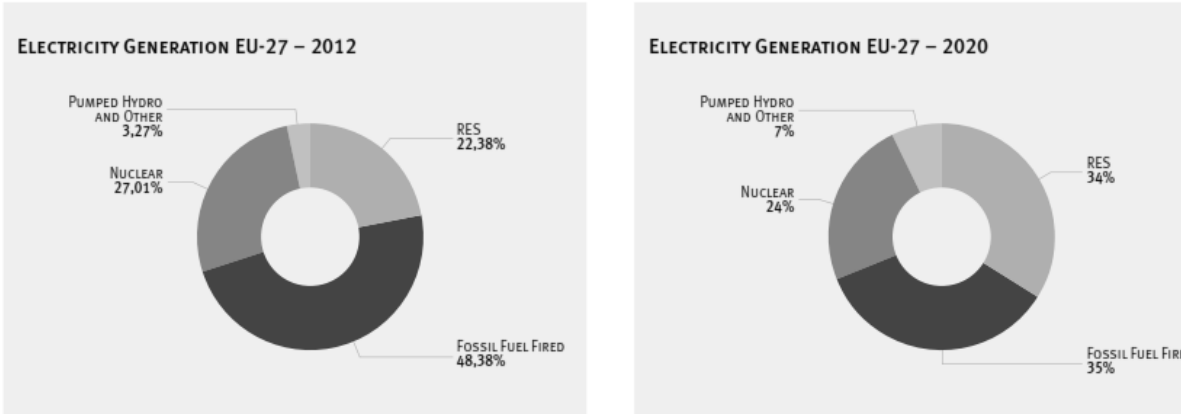

Figure 4: Electricity generation shares in the EU27 countries, 2012 and prediction for 2020 [9].

Increase of RES based electricity generation share in Slovenian energy mix from 2004 to 2012 is shown in Figure 5.

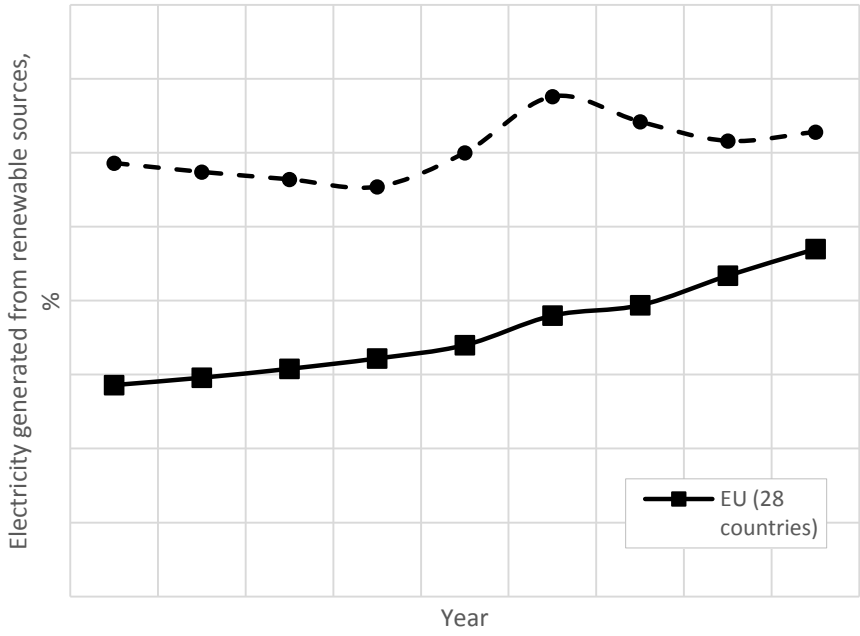

Figure 5: RES based electricity generation share in energy mix

The share of renewables in gross electricity consumption in Slovenia, which as a result of very favourable hydrological conditions in 2009 grew to more than a third, dropped substantially by 2011. In 2009 electricity from renewables accounted for 36.8% of total electricity generated in Slovenia. Even though the hydrological conditions were still relatively favourable, the RES share declined to 33,8 % in 2010 because of higher economic activity and hence higher gross electricity consumption. With much lower water levels of rivers and thus lower hydro-energy production in 2011, the share dropped to 30,8 %. However, it was still above the EU average (21,7 %), where in the past few years the share of renewables in electricity production has been gradually growing.

With the increase in production in hydroelectric power plants and stagnation of gross electricity consumption, in 2012 the share of renewables in electricity production in Slovenia increased to 31,4 % [10]. Slovenia reached 28,50 % share of RES in reference year 2005 and the target in this sector is 39,30 % of RES in electric energy mix by year 2020, which will require more diversification of power generation from RES as well as improved management of electricity use.

4 Cost and environmental efficiency of heat pumps

Heat pumps are an attractive option for reducing GHG emissions caused by buildings. In Slovenia heat pumps have demonstrated that they can provide ample heat in the most challenging environment. Heat pumps exploit primarily the energy of sun,

heating the air, but also from soil, as about 50% of solar energy that falls on the earth's surface is absorbed by it and represent an energy reservoir.

The technology of heat pumps is well developed and their operation is efficient, reliable and are less vulnerable to changes in weather than majority of other low-energy and renewable systems. Heat pumps use the refrigeration cycle to upgrade low-grade environmental energy collected from sources such as air, ground or ground water into energy for use in hot water supply, space heating or cooling.

In Slovenia, an air-source heat pump (a/w) achieves a typical annual average coefficient of performance (COP) of 3,5, which means that 350 % the energy, put into the process in the form of electric energy, is generated as heating energy at appropriate temperature level for low-temperature heating systems in buildings. A soil/water (s/w) and water/water (w/w) heat pumps achieve in Slovenia an annual average coefficient of performance of 4,5 and 5, respectively [11].

In assessment of economic effects of different heating sources, the already presented cost-optimum methodology represent the most comprehensive approach, which was supplemented by direct operational cost comparison for a fast overview about the cost effectiveness of different energy sources systems for building heating.

Operational cost and environmental impact comparison is shown in Figure 6 on the example of single family house with annual consumption of 18,3 MWh of final energy for space heating and domestic hot water. For the analysed systems, typical efficiency data were taken, together with fuel and energy prices from the beginning of 2014.

The comparison of various heating systems relative to the most common fossil-fuel system in Slovenia – boiler utilizing oil – shows that the difference in relative cost efficiency in all of the compared systems is more pronounced than in the relative environmental performance.

It is clearly shown, that comparing the various heating systems, the heat pumps outperforms other systems considerably from the operating cost point of view. Still widely used oil boiler is as much as 188 % more expensive to use as the most common air/water heat pump.

In assessment of environmental effects, the use of primary energy and standard emission of CO_2 were also in compared Figure 6, using the coefficients as determined in the national regulation, i.e. building code PURES 2010. These coefficients imply the actual share of RES in national electric energy mix.

Also in primary energy use and CO_2 emission, the heat pumps outperform other systems, except system on wooden biomass, which, on the other side, contribute to the burning issue in Slovenia with emission of PM10 hard particles from small individual boilers. Comprehensive estimation of effects therefore makes heat pump very competitive heating system also from environmental point of view. Their competitiveness will increase even more with higher COP, especially at lower temperatures, and with increase of the share of renewables in electricity production in Slovenia.

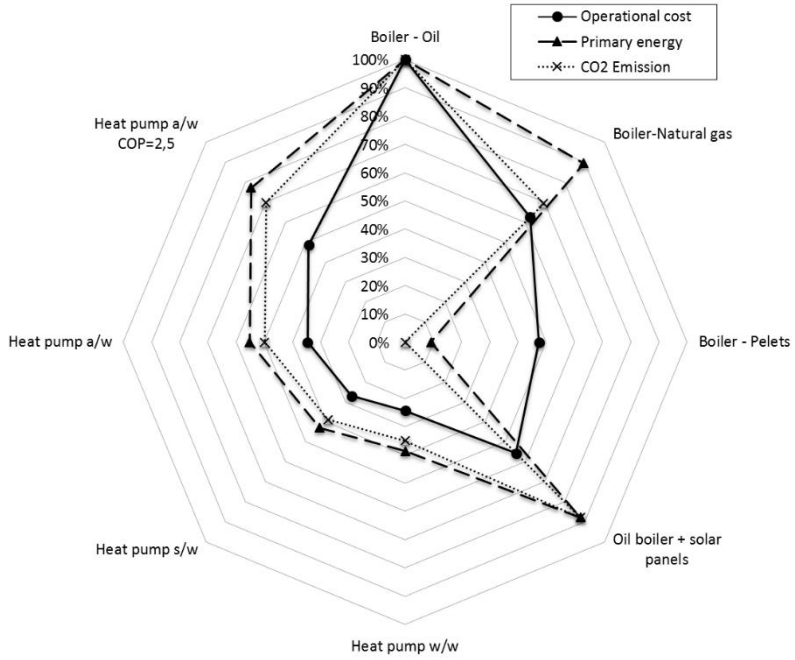

Figure 6: Cost and environmental efficiency of various heating systems relative to oil boiler.

In 2012, in Slovenia, the share of RES in national electric energy mix amounted to 31,4 %, so heat pump with COP of 3,5 utilized 80,4 % of renewable and 19,6 % of non-renewable energy. Reaching the goal in 2020 with 39,3 % share of RES in in national electric energy mix, the same heat pump will utilize 82,7 % of renewable energy.

In general, both the COP and the share of RES in electricity production have impact on the share of renewable energy, utilized by heat pump. Both of these factors will increase with the heat pump technology development and with fulfilment of EU 2020 commitments, which makes heat pump important system not only in cost optimal building performance methodology, but also as an important foundation for further sustainable development, considering that the potential of the Slovenian heat pump industry is growing, having renowned producers with long tradition and competitive products.

5 Conclusions

Slovenia has established comparative methodology framework for the minimum energy performance requirements, differentiating between different categories of buildings. Choosing a single family house, energy performance of the buildings was calculated with IDA Indoor Climate and Energy as a whole year detailed and dynamic

multi-zone simulation study of indoor climate, and utilization of energy. From the variety of specific results for the assessed measures (single measures and packages/variants of such measures), a cost curve has been derived. The minimum energy performance requirements are represented by the area of the curve that delivers the lowest cost for the end-user and/or for the company or society. Potentially, these requirements could prove to be more effective and efficient than current national requirements, at less or equal cost. The results demonstrate that the minimum requirements set for new single family houses in national building codes in force are more severe than the minimum requirements corresponding to the cost optimal level, mainly due to the national energy and climate policy targets in the building sector. Among systems, heat pumps proved to be important competitors in seeking the cost optimal building performance.

In Slovenia, the heat pumps in addition to wooden biomass (and potential waste) represent the greatest potential for sustainable increase of the renewables in the heating and cooling sector. It was shown, that heat pumps are environmentally acceptable and economically efficient way of heating with (potentially) positive social multiplied effects if the domestic manufacturers of equipment and systems will have appropriate conditions for further development. Heat pumps are based on well-established technology, their operation is efficient, reliable, are less vulnerable to changes in weather than majority of other low-energy and renewable systems, and are suitable for (almost) all buildings. Development continues and we can expect even higher COP, especially at lower temperatures. Higher COP, together with further increase of renewables share in the Slovenian electrical power system is making heat pumps important foundation for further development in line with sustainable principles.

6 References

[1] Maldonado E. (2012). Member states approaches EPBD, World Sustainable Energy Days 2012, *Nearly Zero Energy Buildings Conference*, Wels.

[2] Constantinescu T. et al. (2010). *Cost optimality – Discussing methodology and challenges within the recast Energy Performance of Buildings Directive*. Brussels: BPIE.

[3] European Commission, Directorate General for Energy and Transport. (2008). Slovenia – Renewable Energy Fact Sheet.

[4] Šijanec-Zavrl, M., Skubic, M., Rakušček, A., Gjerkeš, H., Potočar, E. (2012). Practical implementation of cost-optimal regulation for establishing national minimum requirements of Slovenia. In: **World Sustainable Energy Days**, [1] Wels, 29 February - 2 March, 2012. Proceedings. Wels: [O. Ö. Energiesparverband, Linz], [13] 3 pp.

[5] Diefenbach, N., Loga, T., Dascalaki, E., Balaras, C., Šijanec Zavrl, M., Rakušček, A., Corrado, V., Corgnati, S., Ballarini, I., Renders, N., Vimmr, T., B. Wittchen, K., Kragh, J. (2012). Application of Building Typologies for Modelling the Energy Balance of the Residential Building Stock – *TABULA Thematic Report N° 2* – ISBN 978-3-941140-23-3.

[6] Capros, P., Mantzos, L., Tasios, N., De Vita, A., Kouvaritakis, N. (2010). *EU energy trends to 2030,* Publications Office of the European Union. Luxemburg.

[7] Šijanec-Zavrl, M., Gjerkeš, H., Tomšič, M. (2012). Integration of nearly zero energy buildings: a challenge for sustainable building stock. V: *World Engineering Forum*, 17-21 September, Ljubljana, Slovenia.

[8] Statistical Office of the Republic of Slovenia. (2013). *Energy consumption in households, Slovenia, 2012 - final data*, http://www.stat.si/eng/novica_prikazi.aspx?id=5803.

[9] EURELECTRIC - Union of the Electricity Industry. (2013). *Power Statistics & Trends*, Brussels.

[10] IMAD – Institute of Macroeconomic Analysis and Development. (2013). Development Report, *Indicators of Slovenia's development*.

[11] Gjerkeš, H., Papler, D., Šijanec-Zavrl, M. (2011). Sustainable development of power generation in Slovenia. In: *Golobič, I. (ed.), Cimerman, F. (ed.). Development and implementation of enhanced technologies 2011 : proceedings of the 3rd AMES International Conference*, Ljubljana, Slovenia, November 29-30.

The effect of nucleation cavities on boiling heat transfer in microchannels

Anže Sitar [*], **Iztok Golobič**

University of Ljubljana, Faculty of Mechanical Engineering, Aškerčeva 6, 1000 Ljubljana, Slovenia.

* Corresponding author:
E-mail: anze.sitar@fs.uni-lj.si

Abstract

The current state of the art in micro heat transfer technologies and the future heat transfer needs are strongly indicating that the forthcoming generations of micro coolers and micro heat exchangers will be forced to exploit the advantages of flow boiling. The employment of two-phase flows allows a more uniform temperature field, lower mass flux of the working fluid, and higher heat transfer coefficients compared to the single-phase flow at an arbitrary heat flux transferred. However, the current knowledge of boiling and its' mechanisms in microchannels is not adequate to overcome some of the challenges which inevitably accompany the boiling process. Boiling instabilities and high temperatures of the onset of boiling (ONB) are two of the insufficiently resolved issues of flow boiling in microchannels. The current study is coping with both issues with an incorporation of flow restrictors and especially potential nucleation cavities to lower the instabilities and enhance heat transfer during flow boiling of water in arrays of microchannels with the hydraulic diameter ranging from 50 μm to 80 μm. The experimental results exhibit not only a lower temperature of the ONB, but also an increased heat transfer coefficient during boiling in microchannels with the potential nucleation cavities etched in sizes from 4 μm to 12 μm. The fabricated nucleation cavities increased the heat transfer coefficient from 3 to 10 times depending on the size of the etched nucleation cavities and the transferred heat flux in microchannels.

1 Introduction

The advances in micro fabrication technologies (micromachining, photolithographic processes, etching, laser drilling, etc.) have enabled the minituarization of devices and their expansion to numerous fields of research and industry. Micro heat exchangers and micro coolers present the next generation of high heat flux removal devices, due to their large surface-to-volume ratio. An efficient heat transfer requires a large available surface, as the convective heat transfer occurs on the solid/fluid interface. The single-phase heat transfer in microchannels has been thoroughly studied in [1-5] and one of the largest heat flux transferred (3 MW/m^2) was presented by Colgan et al. [6]. In macro scaled systems two-phase flow transfers heat substantially more efficient

compared to the single-phase flow, and the same was expected and reported also in micro devices [7-9]. However, condensation and especially boiling in micro systems induce some mechanisms and phenomena, which are not fully understood and in some cases also troublesome. The benefits of two-phase flow compared to the single-phase flow are the additional use of latent heat, the possibility of a uniform temperature field, and lower mass flux of the working fluid. These advantages are hindered by flow instabilities, higher pressure drops and high temperatures of the boiling incipience. A comprehensive review of the heat transfer's current status in microchannels was presented in Kandlikar et al. [10] along with the prediction of the future research needs. Asadi et al. [11] presented a literature review of heat transfer and pressure drops in single and two-phase flows. The single-phase flow can be adequately modelled with the conventional theory. However, the two-phase flow and also the pressure drop in single-phase flow are not utterly supported by the classical theory. Wu and Sunden [12] published a review of heat transfer in single- and two-phase flows in microchannels with an emphasis on possible improvements and further enhancement of heat transfer. One of the most promising improvements is the fabrication of potential nucleation cavities, which lower the temperature of ONB and enhance heat transfer during flow boiling. The sizes of the active nucleation sites were modelled among others also by Hsu [13], Kandlikar et al. [14], and Liu et al. [15]. The scope of the presented study is to experimentally investigate the effect of the potential nucleation cavities on heat transfer during boiling of water in microchannels.

2 Experimental setup

The experimental setup consists of two independent measuring systems with the signal acquisition synchronized with an external trigger. Temperature, pressure, and heat transfer rate were measured with the system comprised from the National Instruments (NI) components, whereas high-speed visualization was enabled with the incorporation of a high-speed camera, microscope and a powerful light source. The NI measurement equipment allowed high frequency data acquisition of up to 250 kHz, which is needed to gain information complementary to the visualization results. The working fluid in all the performed experiments was degassed double-distilled water in order to eliminate the effects of the dissolved gasses and other impurities potentially present in water. The complete scheme of the experimental setup is depicted in Figure 1 and a detailed description of the experimental procedure, measuring equipment and fabrication process of the microchannel test section is given in Sitar et al. [16]. The measurement uncertainties were derived for all the measured quantities, as it is presented in Sitar and Golobic [17].

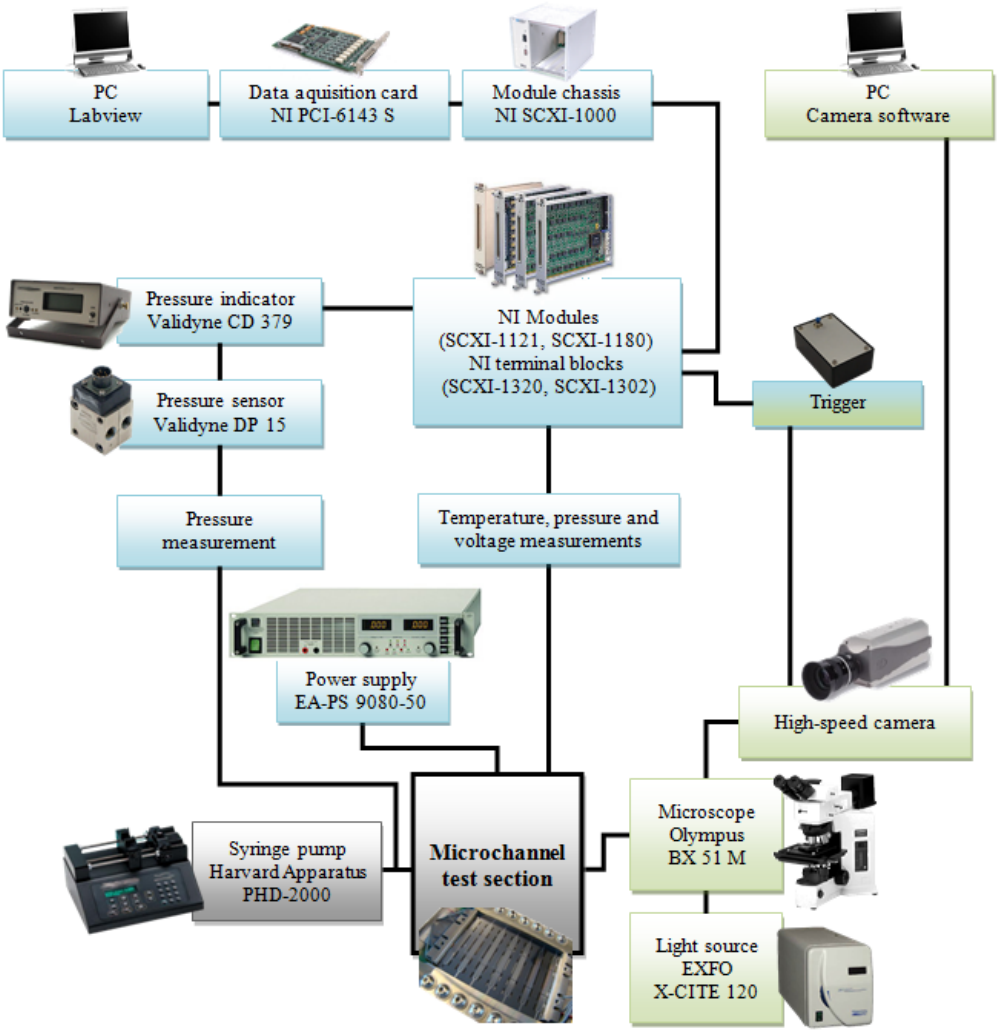

Figure 1: Experimental setup [16]

The fabrication of microchannels in a silicon wafer was divided into 8 steps, as it is shown in Figure 2. The micron sized etched features in silicon require precisely fabricated photomasks and their accurate alignment on the substrate. Bosch process of dry etching was used, as it offers a possibility of a narrow and deep structures in silicon with the depth/width ratio over 20. The deposited platinum and gold on the bottom side of the silicon wafer was 0.1 μm thick for the resistance temperature detectors (RTDs), whereas the thickness of the heaters and connecting wires was 0.5 μm.

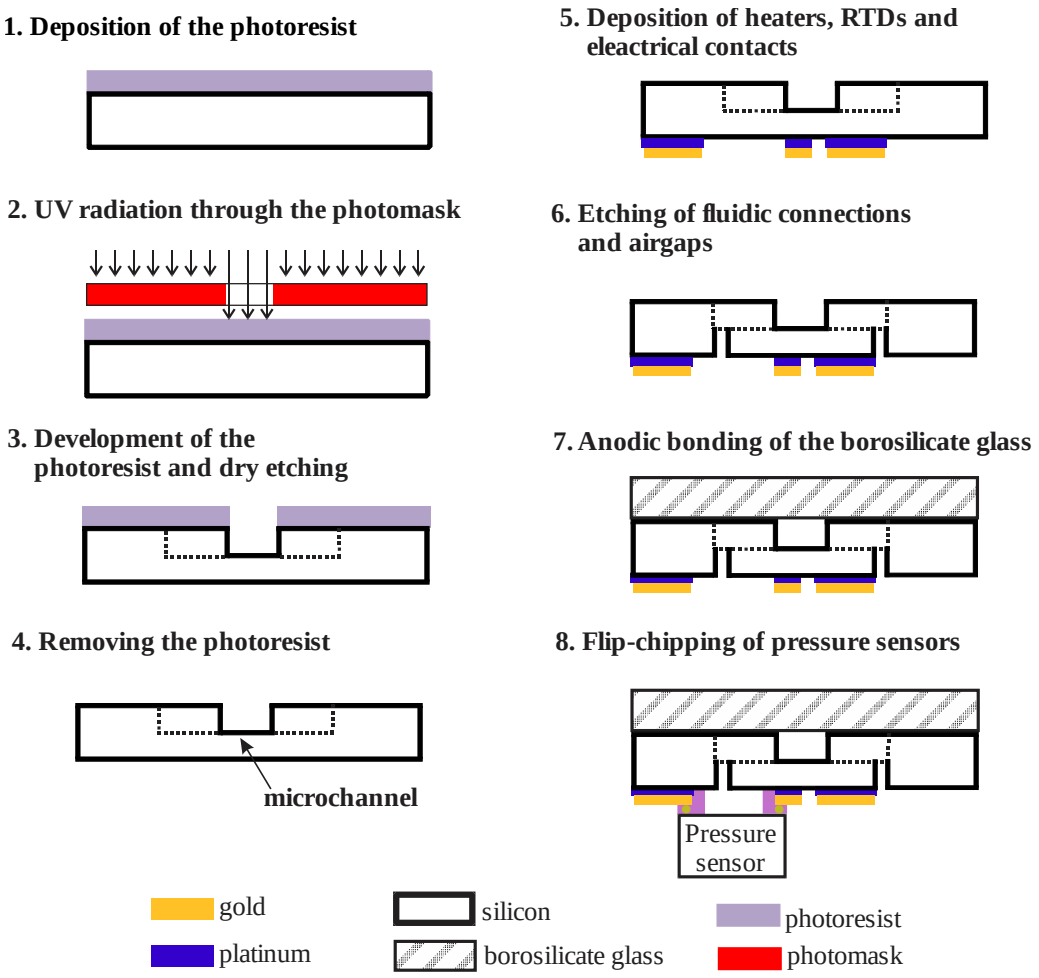

Figure 2: Fabrication of the microchannel test section [18]

3 Results and discussion

Potential nucleation cavities (etched on the microchannel bottom) lower the temperature of the boiling incipience, if the cavities are properly sized. The nucleation sites additionally enhance heat transfer and stabilize the flow during boiling. One of the most important parameters of the cavities activation is their size, thus three different sizes 4 µm, 8 µm, and 12 µm were etched on the bottom of the microchannels. The sizes were modelled and constructed according to the nucleation criterion by Kandlikar et al. [14], which was based on experimental work in minichannels and hereby one of the most appropriate criterion for flow boiling in microchannels.

The activation of the smallest 4 µm cavities in two parallel microchannels with a cross-section 100 × 50 µm is presented in Figure 3. Although, there were several larger

potential nucleation cavities present in the vicinity, only the smallest cavities were activated, which indicates that the optimal size of the cavities is smaller than predicted by the nucleation criteria, which defined the optimal size of the cavities at 10 µm in a 100 × 50 µm microchannel filled with water.

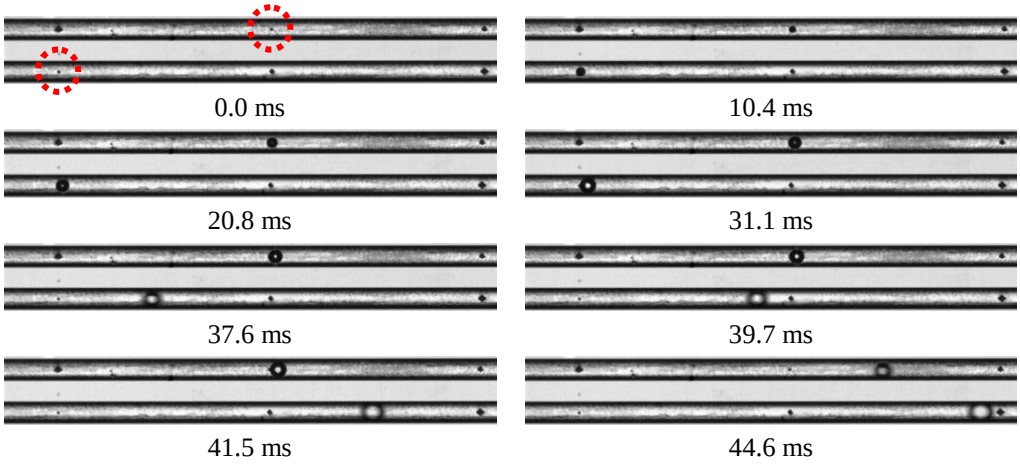

Figure 3: Active 4 µm nucleation sites during boiling of water in two parallel 100 × 50 µm microchannels (4,816 fps)

The nucleation cavities stimulate an earlier transition to flow boiling and also improve the hydrodynamic characteristics of the two-phase flow in the scope of heat transfer. Figure 4 shows a high-speed visualization of a liquid meniscus passing over an active 4 µm cavity in a 200 × 50 µm microchannel. Similarly as in Figure 3, only the smallest etched cavity was active. Nucleation of a vapor bubble is not seen in Figure 4, however the presence of an active nucleation site locally enhanced the heat transfer due to the induced turbulences and improved wettability of the solid silicon walls. The oscillations of the liquid meniscus, presented in Figure 4, are frequently occurring during boiling in small microchannels, as the channels' diameter is smaller than the detaching bubble, which prevents the formation of a bubbly flow. The performed high-speed visualizations revealed that the boiling regime in the manufactured arrays of microchannels was mostly limited to annular flow and oscillations of the meniscus. The etched potential nucleation cavities were not always successful at lowering the temperature of the ONB, as their size was not optimal for boiling incipience of water. However, the nucleation sites were activated at increased temperatures and substantially enhanced the heat transfer during boiling.

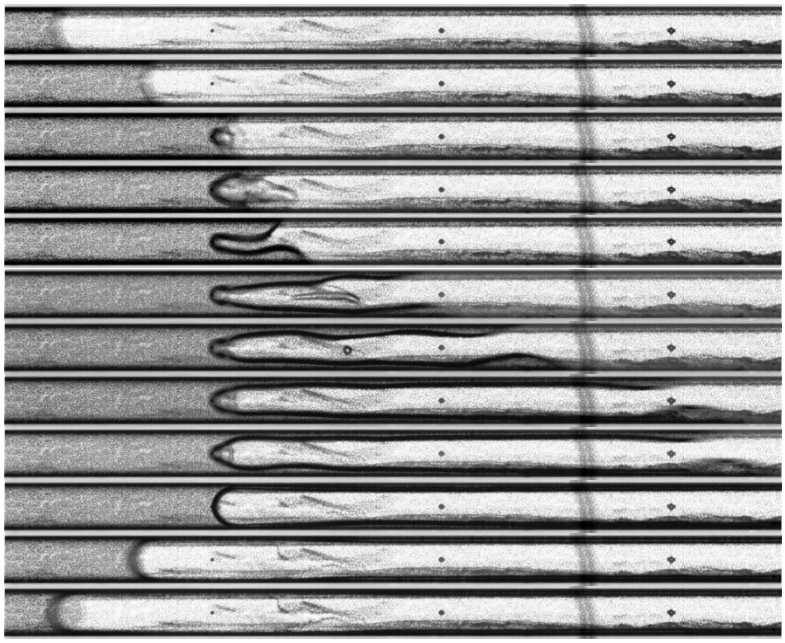

Figure 4: An active 4 μm nucleation site during boiling of water in a microchannel 200 × 50 μm (6,044 fps)

On one hand, the visualizations of boiling provided highly detailed and localized information of the boiling process in microchannels. On the other hand, some precise experimental results of temperatures and heat fluxes are necessary to evaluate the effects of the nucleation cavities on boiling heat transfer. In addition, the experimental results allowed the assessment of the hydraulic diameter and interconnected channels effect on the heat transfer. Figure 5 contains heat flux q_{el} and the achieved temperatures T_w on the bottom of the microchannels at 1 ml/min water flowing through four differently structured arrays of parallel microchannels with their details presented in Table 1. The presented heat flux was calculated as a ratio between the measured heat transfer rate Q_{el} and the heater area A_h, which was identical in all the arrays.

Table 1: Details of the manufactured arrays of microchannels

Label	Hydraulic diameter	Nucleation cavities	Interconnected microchannels
A50 WRN	50 μm	-	No
A50 NRN	50 μm	4 – 12 μm	No
A50 NTC	50 μm	4 – 12 μm*	Yes
A80 NRN	67-80 μm**	4 – 12 μm	No
* an etching error caused an approximately 1 μm nucleation site			
** microchannels of two different widths were etched in the array			

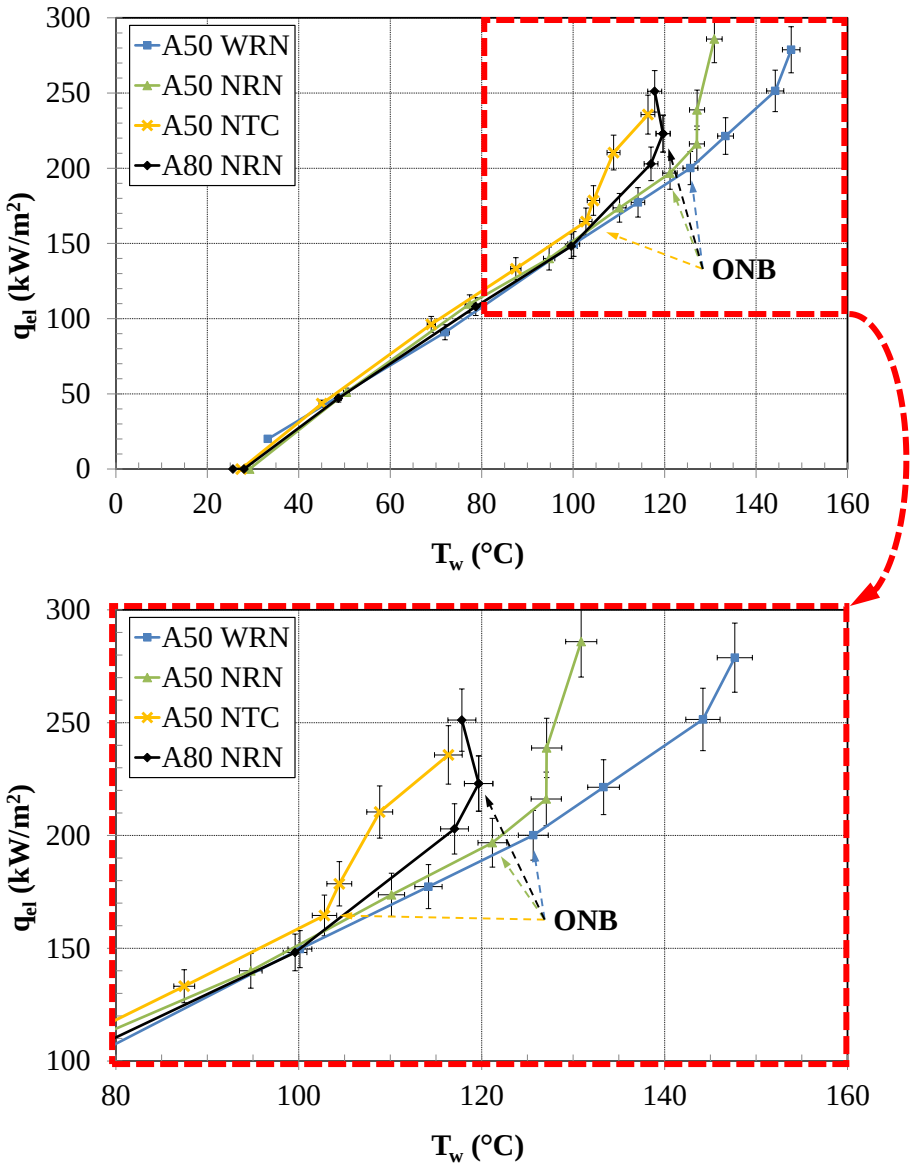

Figure 5: The measured heat flux in arrays of microchannels at 1 ml/min

In the single-phase region the measured temperatures at a certain heat flux differed only slightly between the compared arrays of microchannels, whereas the temperatures in the two-phase boiling region exhibit large differences. The comparison of the arrays A50 WRN and A50 NRN shows the temperatures are up to 17 K lower during boiling of water in A50 NRN, which had the nucleation cavities added on the bottom. The measurements are unambiguously indicating the positive effect of the etched nucleation sites on heat transfer. The microchannel array with the largest hydraulic diameter A80 NRN further improved the heat transfer, due to the faster propagation of

the two-phase flow and a larger surface subjugated to boiling. The array of microchannels labelled with A50 NTC was transferring heat the most efficiently. The origin of the enhanced heat transfer is in the 1 μm nucleation site, which allowed a very early transition to boiling and hence increased the heat transfer coefficient (HTC) substantially. In addition, the parallel microchannels in the array A50 NTC were also interconnected, which insured an instantaneous propagation of the two-phase flow to the entire disposable surface. The temperatures in this array were up to 20 K lower compared to the reference array A50 WRN, in which the microchannels were smooth and not interconnected. Further comparison of the fabricated arrays of microchannels was made with the derivation of the HTC, defined with the Newton's law of cooling as

$$\alpha = q \big/ \Delta T \,. \tag{1}$$

At the single-phase liquid flow a linear temperature gradient is assumed, therefore the local heat transfer coefficient α_{sp} is given with the equation

$$\alpha_{sp} = \frac{q_w}{\eta_0 \left(T_{h,m} - \dfrac{T_{h,i} + T_{h,o}}{2} \right)}, \tag{2}$$

in which the temperatures $T_{h,i}$, $T_{h,o}$ and $T_{h,m}$ are temperatures at the inlet, the outlet and the middle of the microchannels, respectively. The wall heat flux q_w was calculated from the derived fluid heat transfer rate Q_f and the microchannel heated surface A_w

$$q_w = \frac{Q_f}{A_w} \,. \tag{3}$$

The heat rate transferred to the working fluid Q_f is the difference between the measured heat transfer rate Q_{el} dissipating from the electrical heaters and the heat loss Q_{loss} from the active array of microchannels, which was acquired from the "dry" microchannels, as described in Sitar et al. [16]. The heated microchannel surface depends on the number of microchannels in an array N, the width w_{ch}, the height h_{ch}, and the heated length l_h of the microchannels

$$A_w = N \left(w_{ch} + 2h_{ch} \right) l_h \,. \tag{4}$$

The efficiency of the surface between the microchannels η_0 is defined with

$$\eta_0 = 1 - \frac{2h_{ch}}{w_{ch} + 2h_{ch}} \left(1 - \eta_f \right), \tag{5}$$

where the efficiency of a single fin η_f in accordance with adiabatic tip condition is given with the equation

$$\eta_f = \frac{\tanh\left(m h_{ch} \right)}{m h_{ch}} \,. \tag{6}$$

The adiabatic tip condition is assumed due to the low thermal conductivity of the borosilicate glass bonded on top of the microchannels, which transfers a very small amount of heat flux compared to the working fluid. Fin parameter m is defined with equation

$$m = \sqrt{\frac{\alpha \cdot P}{\lambda_{Si} A_c}}, \tag{7}$$

in which heat transfer coefficient α, perimeter of the microchannel P, thermal conductivity of the silicon λ_{Si}, and cross-section area of the channel A_c convert the derivation of the heat transfer coefficient into an iterative method.

The calculation of the local two-phase heat transfer coefficient α_{tp} was accomplished with an assumption, that the bulk fluid temperature is equal to the saturation temperature T_{sat} at the local pressure

$$\alpha_{tp} = \frac{q_w}{\eta_0 \left(T_w - T_{sat} \right)}. \tag{8}$$

The same assumption for derivation of the local two-phase HTC was used in Harirchian [19]. The heat transfer coefficients are presented in Figure 6 in accordance with the previously described procedure of derivation. The structure difference between arrays A50 WRN and A50 NRN is only in the etched nucleation cavities on the microchannel bottom, which considerably increased the HTC during flow boiling, whereas the temperature of the ONB and the heat transfer in the liquid single-phase flow remained almost unaltered. On one hand, the HTC was approximately 3,500 W/m^{2}K in the array A50 WRN in single- as well as in two-phase flow. On the other hand, in the array A50 NRN the heat transfer coefficient increased from 3,500 W/m^{2}K in the single-phase flow to more than 12,000 W/m^{2}K during boiling, which is a direct consequence of the etched nucleation cavities sized from 4 µm to 12 µm. A further improvement of the two-phase HTC is seen in Figure 6 during boiling in the array A80 NRN, which consists of parallel microchannels with the hydraulic diameter ranging from 67 µm to 80 µm. The enhanced heat transfer is attributable to the larger cross-section of the microchannels, which accelerated the propagation of two-phase flow to a larger area, thus increasing the heat transfer coefficient. The heat transfer analysis of the compared microchannel arrays is clearly demonstrating the largest heat transfer coefficient and the lowest temperature of the ONB in the array A50 NTC. The combined cross-section of all the parallel microchannels in the array A50 NTC was half the size of the cross-section of all the other arrays, due to the specific construction of the array, which was considered in the HTC derivation. The visualization of the boiling incipience revealed a micron sized nucleation cavity, which was a results of the etching process error. This nucleation cavity was activated at 104 °C, which is substantially lower compared to all other arrays of microchannels. The almost ideally sized nucleation cavity allowed an early transition to flow boiling with the heat transfer coefficients exceeding 30,000 W/m^{2}K.

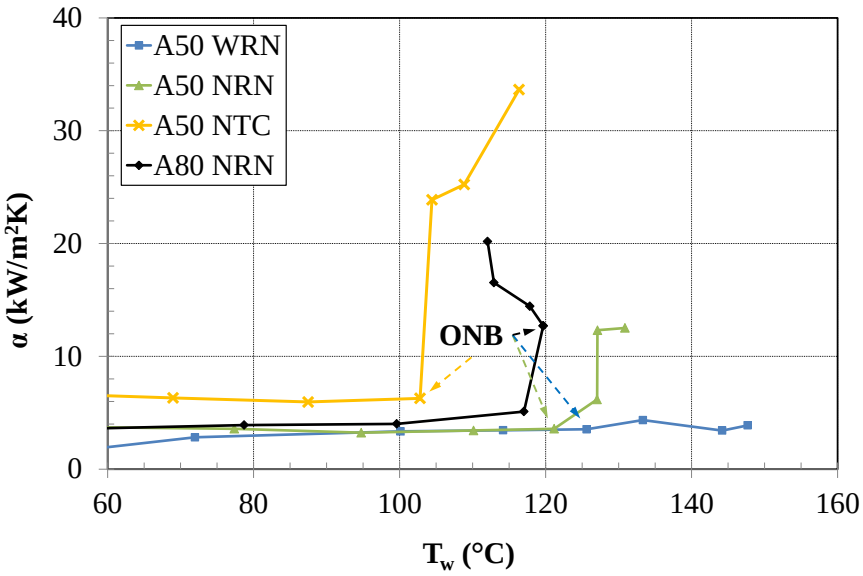

Figure 6: Heat transfer coefficients in both single-phase and two-phase flows at various temperatures

4 Conclusions

Two-phase flow substantially enhanced heat transfer during flow boiling of water in the constructed arrays of microchannels with the hydraulic diameter ranging from 50 to 80 μm. The onset of boiling occurred in a single microchannel and propagated to other parallel channels in the array at increased temperatures. The highest heat transfer coefficient is achieved, when the ONB takes place at the lowest temperature in the largest number of channels, which broadens the surface subjected to boiling. The temperatures of the boiling incipience were lowered with the incorporation of the potential nucleation cavities of appropriate sizes, whereas the surface of boiling was larger at larger hydraulic diameters and in arrays with interconnected parallel microchannels. Consequently, the amount of the boiling liquid was increased and the HTC improved. The combined effect of the interconnected microchannels and the nucleation cavity of an almost ideal size enhanced the HTC in the microchannel array denoted with A50 NTC to more than 30 kW/m^{2}K, which is 10 times higher compared to the array of microchannels with the same hydraulic diameter without any micron sized nucleation sites, denoted with A50 NRN. The heat transfer analysis revealed: (i) the optimal size of the nucleation cavities for water is around 1 μm; (ii) the incorporation of the non-optimally sized cavities increased HTC up to 3 times; (iii) the etched nucleation cavities and the flow restrictors stabilized flow during boiling; (iv) microchannels with hydraulic diameter 80 μm transferred heat more efficiently compared to the 50 μm microchannels due to the propagation of boiling to a larger available surface.

5 References

[1] Harms, T.M., Kazmierczak, M.J., Gerner, F.M. (1999). Developing convective heat transfer in deep rectangular microchannels. *International Journal of Heat and Fluid Flow*, vol. 20, no. 2, p. 149-157.

[2] Morini, G.L. (2004). Single-phase convective heat transfer in microchannels: a review of experimental results. *International Journal of Thermal Sciences*, vol. 43, no. 7, p. 631-651.

[3] Lee, P.-S., Garimella, S.V., Liu, D. (2005). Investigation of heat transfer in rectangular microchannels. *International Journal of Heat and Mass Transfer*, vol. 48, no. 9, p. 1688-1704.

[4] McHale, J.P., Garimella, S.V. (2010). Heat transfer in trapezoidal microchannels of various aspect ratios. *International Journal of Heat and Mass Transfer*, vol. 53, no. 1–3, p. 365-375.

[5] Duryodhan, V.S., Singh, A., Singh, S.G., Agrawal, A. (2015). Convective heat transfer in diverging and converging microchannels. *International Journal of Heat and Mass Transfer*, vol. 80, p. 424-438.

[6] Colgan, E.G., Furman, B., Gaynes, M., Graham, W., LaBianca, N., Magerlein, J.H., Polastre, R.J., Rothwell, M.B., R.J. Bezama, Toy, H., Wakil, J., Zitz, J., Schmidt, R. (2005). A practical implementation of silicon microchannel coolers for high power chips. *Proceedings of the Semiconductor Thermal Measurement, Modeling, and Management Symposium*.

[7] Fu, B.R., Tsou, M.S., Pan, C. (2012). Boiling heat transfer and critical heat flux of ethanol–water mixtures flowing through a diverging microchannel with artificial cavities. *International Journal of Heat and Mass Transfer*, vol. 55, no. 5–6, p. 1807-1814.

[8] Saraceno, L., Celata, G.P., Furrer, M., Mariani, A., Zummo, G. (2012). Flow boiling heat transfer of refrigerant FC-72 in microchannels. *International Journal of Thermal Sciences*, vol. 53, p. 35-41.

[9] Wang, Y., Sefiane, K. (2012). Effects of heat flux, vapour quality, channel hydraulic diameter on flow boiling heat transfer in variable aspect ratio micro-channels using transparent heating. *International Journal of Heat and Mass Transfer*, vol. 55, no. 9–10, p. 2235-2243.

[10] Kandlikar, S.G., Colin, S., Peles, Y., Garimella, S., Pease, R.F., Brandner, J.J., Tuckerman, D.B. (2013). Heat Transfer in Microchannels - 2012 Status and Research Needs. *Journal of Heat Transfer*, vol. 135, p. 091001-091001-091001-091018.

[11] Asadi, M., Xie, G., Sunden, B. (2014). A review of heat transfer and pressure drop characteristics of single and two-phase microchannels. *International Journal of Heat and Mass Transfer*, vol. 79, p. 34-53.

[12] Wu, Z., Sundén, B. (2014). On further enhancement of single-phase and flow boiling heat transfer in micro/minichannels. *Renewable and Sustainable Energy Reviews*, vol. 40, p. 11-27.

[13] Hsu, Y.Y. (1962). On the size range of active nucleation cavities on a heating surface. *Journal of Heat Transfer*, vol. 84, p. 207-216.

[14] Kandlikar, S.G., Mizo, V.R., Cartwright, M.D., Ikenze, E. (1997). Bubble nucleation and growth characteristics in subcooled flow boiling of water. *HTD-Vol. 342, ASME Proceedings of the 32nd National Heat Transfer Conference*, p. 11-18.

[15] Liu, D., Lee, P., Garimella, S.V. (2005). Prediction of the onset of nucleate boiling in microchannel flow. *International Journal of Heat and Mass Transfer*, vol. 48, p. 5134-5149.

[16] Sitar, A., Sedmak, I., Golobic, I. (2012). Boiling of water and FC-72 in microchannels enhanced with novel features. *International Journal of Heat and Mass Transfer*, vol. 55, no. 23–24, p. 6446-6457.

[17] Sitar, A., Golobic, I. (2015). Heat transfer enhancement of self-rewetting aqueous n-butanol solutions boiling in microchannels. *International Journal of Heat and Mass Transfer*, vol. 81, p. 198-206.

[18] Sitar, A., Zupančič, M., Golobič, I. (2014). Nucleation cavities effect on the onset of nucleate boiling in microchannels. Junkar, M. (Ed.) *MIT 2014 : proceedings of the 13th International Conference on Management and Innovative Technologies*, Fiesa, Slovenia.

[19] Harirchian, T. (2010). Two-phase flow and heat transfer in microchannels. Purdue University, USA.

Pool boiling experiments on laser-made biphilic surfaces based on polydimethylsiloxane-silica films

Matevž Zupančič [a*], Peter Gregorčič [b], Miha Steinbücher [a], Janez Možina [a], Iztok Golobič [a]

[(a)] University of Ljubljana, Faculty of Mechanical Engineering, Aškerčeva 6, 1000 Ljubljana, Slovenia.

[(b)] Helios Group, Količevo 2, 1230 Domžale, Slovenia.

* Corresponding author:
E-mail: matevz.zupancic@fs.uni-lj.si

Abstract

In this study we present the development of hydrophobic coating based on polydimethylsioxane resin and hydrophobic fumed silica that become hydrophilic after thermal treatment above 500 °C. By using a pulsed Nd:YAG laser we made patterned biphilic surfaces on thin stainless-steel foils, which were subjected to saturated pool of water. Data analysis of high-speed IR thermographs at different heat fluxes revealed the effect of biphilic patterns, which can provide different densities of active nucleation sites and lower the average wall temperature during boiling. The size of hydrophobic spots also limits the maximal contact diameter of the nucleating bubble, thus delaying the formation of the dried-out area and increasing the CHF. Straightforward production as well as thermal and mechanical stability of biphilic surfaces opens new possibilities for industrial use.

1 Introduction

Due to the large latent heat of the working fluids, phase-change cooling is a promising approach for thermal management of high heat flux applications, such as cooling of nuclear fuel claddings [1], integrated circuits [2], and concentrated photovoltaics [3]. The performance of pool boiling heat transfer is characterized through heat transfer coefficient (HTC) and critical hat flux (CHF), which is the upper limit of nucleate boiling regime. In the last few decades, many techniques have been developed to provide enhanced HTC and CHF [4]. Those techniques are generally based on tailoring the surface and include combinations of micropores, nanopores and tunnels [5, 6]; fins [7]; nanowires and nanotubes [2, 8]; hydrophobic and hydrophilic patterns [9, 10]; and use of nanofluids as a working fluid [11].

Authors Tang, et al. [12] for example showed that during saturated pool boiling of water on nanoporous copper surface (50-200 nm pores), a reduction of 63,3 % in wall superheat and increase of 172,7 % in HTC compared to the plain surface were

achieved. The pores also lowered the temperature of the onset of nucleate boiling by 5 °C. In the study by Dong, et al. [13], the silicon surfaces were covered with lithographically made microfins of diameter ranging from 5 to 100 μm and height varied from 5 to 50 μm. The CHF on structured surfaces was 550-700 kW/m^2, compared to the bare surface, where CHF was only 400 kW/m^2. HTC was increased for at least a factor of two in all cases. Heat transfer enhancement on the structures with diameter of 50 and 100 μm was presumably due to the increased heat transfer effective area. On smaller structures with the diameters of 5 and 10 μm, higher nucleation frequency and increased number of nucleation sites were reported [13] to be the main reasons for HTC and CHF enhancement. Betz, et al. [10] developed superbiphilic (SBPI) surface on silicon substrate, where the contact angles of water reached 0° and 165° on superhydrophilic (SHPI) and superhydrophobic (SHPO) region, respectively. The SHPO spots were around 40 μm in diameter. According to their theory, hydrophobic spots provide active nucleation sites and the size of the spot dictates the contact diameter of evaporating bubble, which also affects the nucleation frequency. The highest CHF (1350 kW/m^2) was achieved on SHPI surfaces and the highest HTC (over 150 kW/m^{2}K) on SBPI surfaces, where superheat at the onset of nucleate boiling was around 1°C. The superheat at the onset of nucleate boiling on SHPO surface was reported to be only 0,1 °C which should in fact drastically improve HTC. However, vapor film covered the heated surface already at low heat fluxes shortly after the onset of boiling.

Therefore, the surfaces that provide enhanced HTC and CHF during nucleate boiling offers at least one of the following improvements: (i) higher density of the active nucleation sites; (ii) higher nucleation frequency; (iii) smaller bubble contact area; and (iv) lower superheat at the onset of nucleate boiling. Biphilic and superbiphilic surfaces show promising results, as the size and the number of hydrophobic (HPO) spots dictate the nucleation site density, onset of boiling, and bubble diameter. On the other hand, the hydrophilic (HPI) region ensures "the suction" of the liquid towards the nucleation sites and prevents bubbles' coalescence. Thus, HPI delays the formation of overheated dried out area and consequentially enhances CHF. However, the mechanical resistance, the thermal stability, and the manufacturing costs are the main drawbacks of biphilic surfaces [4], since fabrication often includes relatively challenging and costly techniques, such as photolithography, etching, sputtering and different sol-gel procedures. Further work is needed in order to develop durable, easy-to-make, and inexpensive biphilic surfaces.

In this work, we present application of hydrophobic coating, based on polydimethylsioxane resin and hydrophobic fumed silica that can be easily air-sprayed on to large surfaces. Since the coating becomes hydrophilic after the localized thermal treatment, we created binary HPO-HPI patterns on thin stainless steel foils by using a Nd:YAG pulsed laser. The so prepared foils have undergone the saturated pool boiling experiments, where high-speed IR and video camera were used to obtain visualization of departing bubbles with the corresponding local wall temperature measurements.

2 Manufacturing of biphilic surface

The procedure of fabricating the hydrophobic surface was as follows. First, the hydrophobic fumed silica was dispersed in polydimethylsioxane resin mixed with an organic solvent (the mass ratio between silica and resin was 1:1). The dispersion was then ball mill grinded to the fineness of 0 μm, according to the ISO 1524. The so prepared coating was air-sprayed on the 25-μm-thick stainless steel foil (S316, Precision Brand) and later heat cured on air for 30 min at 230 °C.

In order to achieve the transition from HPO to HPI, we used a pulsed Nd:YAG laser (Fotona YAG 22 CLASS MARK, λ = 1064 nm) with the spot size on the substrate of 200 μm. The repetition frequency was 3 kHz, pulse duration 340 ns, and energy of the pulse 1.0 mJ. The laser had integrated scanning system with 100 μm resolution, which allowed us to create HPO/HPI patterns. Scanning velocity was set to 150 mm/s.

3 Experimental setup and procedure

Experimental setup for saturated pool boiling experiments on thin metal foils is schematically shown in Fig. 1.The walls of the boiling chamber (170 x 100 x 100 mm^3) were made of double pane glass to enable visualization and at the same time to minimize heat losses during measurements, as the hot air was purged between glasses. The stainless steel foil (17 x 27 mm^2) was glued onto the ceramic base and both were sealed to the bottom of a chamber. The foil was painted at the bottom side with a high emissivity paint (0.9), enabling IR measurements through the borehole in the ceramic base.

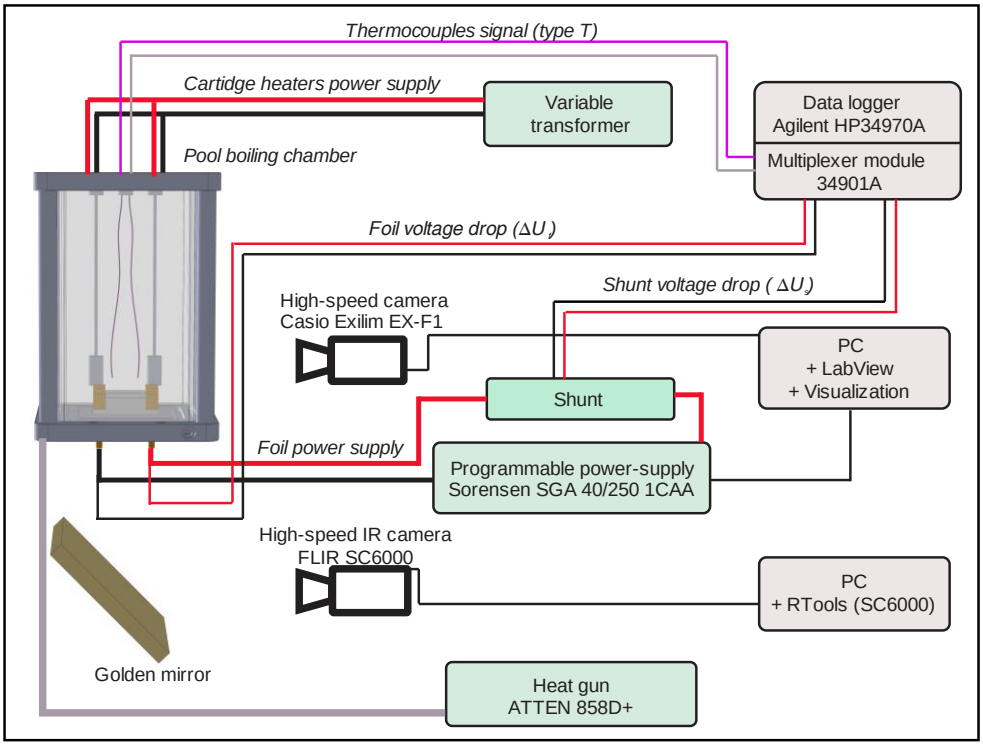

Figure 1. Schematics of pool boiling experiment on thin metal foils.

Double-distilled water was used as a working fluid and was boiled for two hours prior to the experiments to remove most of the potentially dissolved gases. Two immersed cartridge heaters were used for preheating and maintaining the saturation temperature during experiments. The water vapor was converted back to liquid state in the condenser, placed at the top of the chamber (not shown in Fig. 1). T-type thermocouples were used to measure the water temperature. All of the temperature and voltage signals were recorded by an Agilent 34970A and multiplexer module 34901A.

The metal foil was powered by Sorensen SGA 40/250 DC power supply and the electrical current was measured indirectly by measuring the voltage drop (ΔU_s) across the shunt (k_s = 0.333 mΩ). By measuring the voltage drop across the metal foil (ΔU_f), we can calculate the heat flux as

$$q = \frac{\Delta U_f \, \Delta U_s}{A k_s} \tag{9}$$

where A and k_s are foil area and shunts' resistance, respectively. The visualization system consisted of a high-speed CMOS camera (Casio Exilim EX-F1) and high-speed IR camera (FLIC SC6000) both of which recorded at 1200 fps.

4 Results

The basic HPO coating after the heat curing exhibits very low free surface energy, i.e., only 3.19 mJ/m^2, from which the dispersion and polar part of the surface energy are 2.95 and 0.24 mJ/m^2, respectively. Fig. 2 shows the wettability envelope, calculated according to Ownes-Wendt model [14, 15] by measuring the static contact angles (apparatus Krüs DSA 100) between the coated surface and three different fluids: deionised water (139.0°), ethylene glycol (131.1°), and diiodomethane (111.1°). If a fluids' total and polar surface tension falls inside the envelope, the fluid will wet the surface ($\theta < 90°$). Since the surface tension of water is 72.8 mJ/m^2 and its' polar part is 50.7 mJ/m^2, we can conclude that the coating is highly hydrophobic and in fact close to superhydrophobic [10].

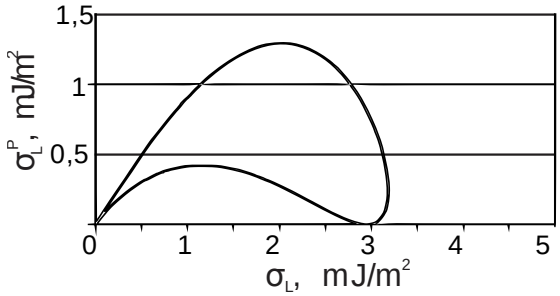

Figure 2. Wettability envelope of the hydrophobic coating. Total and polar free surface energy (or surface tension) are placed on x-axis and y-axis, respectively.

After the localized thermal treatment with pulsed laser, the topology and the chemistry of the surface changes and the coating converts from HPO to HPI/SHPI. The static contact angles on the laser-treated HPI surface are lower than 5°. This way, we were able to produce different biphilic patterns, as shown in Fig. 3. Fig. 3(c) shows that micro surface roughness changes after the laser-treatment. Even though the surfaces are characterized through contact angles measurements, a detailed study including AFM microscopy, IR and Raman spectroscopy, and SEM/EDS analysis is still required in order to explain mechanisms of transition from HPO to HPI.

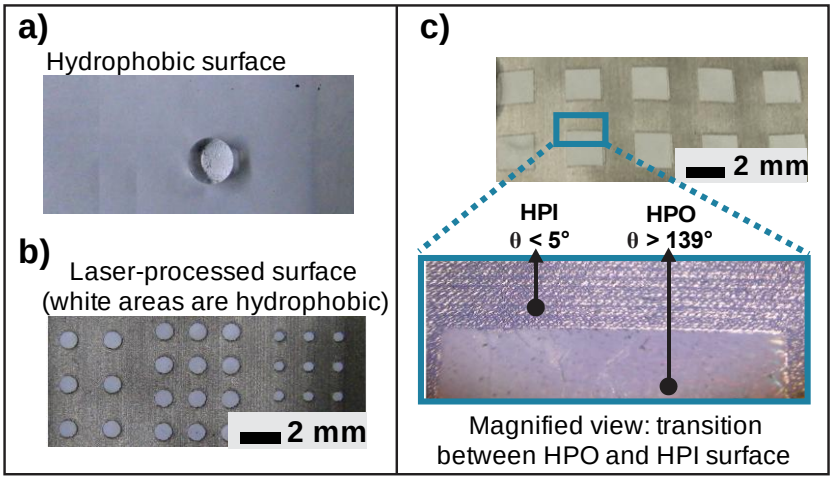

Figure 3: (a) The original hydrophobic coating, (b) laser-processed surface with different circular hydrophobic spots, and (c) rectangular hydrophobic spots and magnified view of the transition between hydrophobic and hydrophilic region.

The pool boiling experiments were conducted on a bare stainless steel foil and on the coated laser-treated surface with square HPO spots of size 0.25 x 0.25 mm^2 and 1.5 mm pitch. Sample IR and video frames during nucleate pool boiling on two surfaces at different heat fluxes are shown on Figure 4. It can be seen that on the biphilic surface the HPO spots dictate the active nucleation sites locations. Increased nucleation site density on biphilic surface is presumably one of the main reasons for lower wall temperature and consequently higher heat transfer coefficient. Average wall temperature on the bare foil at 350 kW/m^2 is 122.1 °C [Fig. 4(c)] and on the biphilic surface only 112.3 °C [Fig. 4(f)].

The size of HPO spot also limits the maximum contact diameter of the nucleating bubble and thus delays the formation of dryed-out area which leads to the burnout. The CHF was increased by almost 260 %, compared to the bare foil. Bubbles, formed on adjacent HPO spots, start to coalescence at a higher heat fluxes, as shown in Fig. 4(f-g). Tailoring a surface to minimize those coalescences, might further improve CHF.

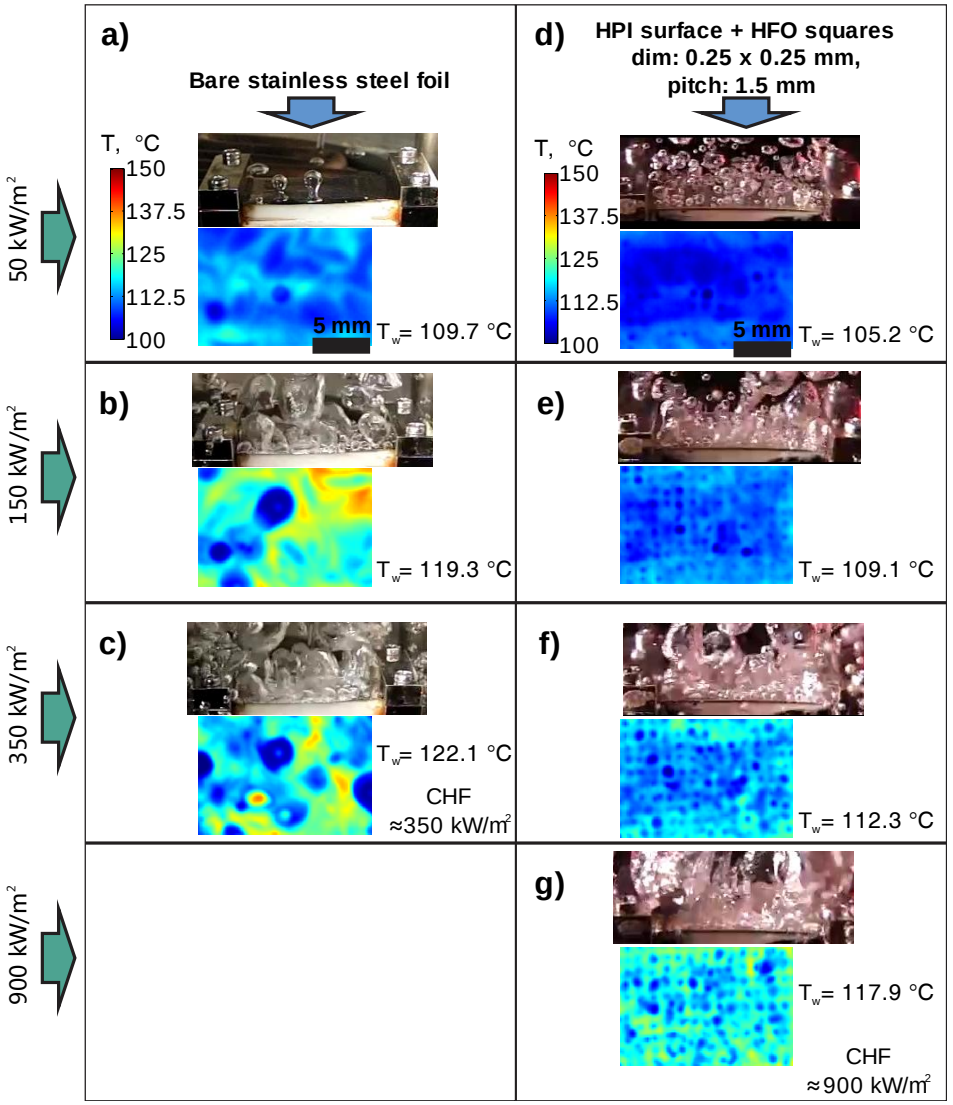

Figure 4: Sample frames from video and IR camera during nucleate boiling (a-c) on a bare stainless steel foil and (d-g) on a biphilic surface with square hydrophobic spots of 0.25 x 0.25 mm^2 and the pitch of 1.5 mm. Average wall temperature is denoted by T_w.

5 Conclusions

We developed hydrophobic (HPO) coating based on polydimethylsiloxane and hydrophobic fumed silica, which can be air-sprayed to large surfaces, such as metal sheets. Contact angle of water on HPO surface was 139° and after the localized thermal treatment with pulsed Nd:YAG laser (above 500 °C), the coating becomes hydrophilic (HPI) with contact angle under 5°, thus enabling production of biphilic surfaces.

The biphilic surface can withstand higher heat fluxes and intensive nucleate boiling and is appropriate for repeatable pool boiling experiments.IR thermography revealed that hydrophobic spots dictate the active nucleation site locations. On the biphilic surface with squared 0.25 x 0.25 mm^2 HPO spots and pitch of 1.5 mm higher nucleation site density was achieved compared to the bare surface. Average wall temperature was decreased from 122.1 °C to 112.3 °C at 350 kW/m^2 during saturated pool boiling of water. CHF on biphilic surface was approximately 260 % higher compared to the bare surface. The coating and experimental setup offers the possibility to further study the heat transfer mechanisms on biphilic surfaces and optimize the patterns to achieve even higher heat transfer coefficients and CHF. Because of the inexpensive and straightforward production, mechanical and thermal stability, our coating also opens new possibilities for industrial use.

6 References

[1] Lee, C., Kim, H., Ahn, H.S., Kim, M.H., Kim, J. (2012). Micro/nanostructure evolution of zircaloy surface using anodization technique: Application to nuclear fuel cladding modification. *Applied Surface Science*, vol. 258, no. 22, p. 8724-8731.

[2] Yao, Z., Lu, Y.-W., Kandlikar, S.G. (2011). Effects of nanowire height on pool boiling performance of water on silicon chips. *International Journal of Thermal Sciences*, vol. 50, no. 11, p. 2084-2090.

[3] Reeser, A.D. (2013). Energy efficient two-phase cooling for concentrated photovoltaic arrays. *Department of Mechanical Engineering*, University of Maryland, Faculty of the Graduate School, College Park.

[4] Lu, Y.-W., Kandlikar, S.G. (2010). Nanoscale surface modofocation techniques for pool boiling enhancement - A critical review and future directions. *8th International Conference on Nanochannels, Microchannels, and Minichannels*, ASME, Montreal, Canada.

[5] El-Genk, M.S., Ali, A.F. (2010). Enhanced nucleate boiling on copper micro-porous surfaces. *International Journal of Multiphase Flow*, vol. 36, no. 10, p. 780-792.

[6] Vemuri, S., Kim, K.J. (2005). Pool boiling of saturated FC-72 on nano-porous surface. *International Communications in Heat and Mass Transfer*, vol. 32, no. 1-2, p. 27-31.

[7] Chu, K.-H., Enright, R., Wang, E.N. (2012). Structured surfaces for enhanced pool boiling heat transfer. *Applied Physics Letters*, vol. 100, no. 24, p. 241603 241601-241604.

[8] Ujereh, S., Fisher, T., Mudawar, I. (2007). Effects of carbon nanotube arrays on nucleate pool boiling. *International Journal of Heat and Mass Transfer*, vol. 50, no. 19-20, p. 4023-4038.

[9] Coyle, C., O'Hanley, H., Phillips, B., Buongiorno, J., McKrell, T. (2013). Effects of hydrophobic surface patterning on boiling heat transfer and critical heat flux of water at atmospheric pressure. *ASME 2013 Power Conference*, Masschusetts, ZDA.

[10] Betz, A.R., Jenkins, J., Kim, C.-J., Attinger, D. (2013). Boiling heat transfer on superhydrophilic, superhydrophobic, and superbiphilic surfaces. *International Journal of Heat and Mass Transfer*, vol. 57, p. 733-741.

[11] Phan, H.T., Caney, N., Marty, P., Colasson, S., Gavillet, J. (2009). Surface wettability control by nanocoating: The effects on pool boiling heat transfer and nucleation mechanism. *International Journal of Heat and Mass Transfer*, vol. 52, no. 23-24, p. 5459-5471.

[12] Tang, Y., Tang, B., Li, Q., Qing, J., Lu, L., Chen, K. (2013). Pool-boiling enhancement by novel metallic nanoporous surface. *Experimental Thermal and Fluid Science*, vol. 44, p. 194-198.

[13] Dong, L., Quan, X., Cheng, P. (2014). An experimental investigation of enhanced pool boiling heat transfer from surfaces with micro/nano-structures. *International Journal of Heat and Mass Transfer*, vol. 71, p. 189-196.

[14] Owens, D.K., Wendt, R.C. (1969). Estimation of the surface free energy of polymers. *Journal of Applied Polymer Science*, vol. 13, p. 1741-1747.

[15] Rulison, C. (2000). Two-component surface energy characterization as predictor of wettability and dispersability, Application note #213. Krüs GmbH, Hamburg, p.

Innovative thermal dispersion mass flow meter

Klemen Rupnik [*], Jože Kutin, Ivan Bajsić

University of Ljubljana, Faculty of Mechanical Engineering, Aškerčeva 6, 1000 Ljubljana, Slovenia.

* Corresponding author:
E-mail: klemen.rupnik@fs.uni-lj.si

Abstract

An innovative thermal dispersion mass flow meter is presented. The originality of the proposed solution is related to the following technical problem. If the measured gas is different to the gas used for the calibration, an appropriate correction has to be applied. To apply such correction in conventional thermal dispersion mass flow meters, the measured gas has to be known. The presented innovative thermal dispersion mass flow meter has, in addition to the measurement of the mass flow rate, the capability to identify the type of gas from a defined set of possible gases and to correct the measurement characteristics. The developed thermal dispersion mass flow meter contains two thermal flow sensors with different constructional parameters, which are required for the implementation of the gas-identification method. If the measurement characteristics for the improper gas are employed, the mass flow readings of two different thermal flow sensors will generally differ. In practical realization of the gas-identification method, the type of measured gas can be identified by means of the objective function, for example the relative difference in the mass flow readings or the normalized measurement error. In the performed validation experiment, air was correctly identified as the proper gas. The developed thermal dispersion mass flow meter could be used in flow systems with different pure, technical or medical gases, for example in medical gas supply system in hospitals.

1 Introduction

Thermal mass flow meters are mostly used to measure the mass flow rate of gases. They can be divided into two types: capillary thermal mass flow meters and thermal dispersion mass flow meters [1, 2]. The thermal dispersion mass flow meter typically comprises a thermal flow sensor, a gas-temperature sensor, a flow pipe (optionally), measurement and control electronics and an enclosure (see its measurement section schematically presented in Figure 1). The measurement principle of the thermal dispersion mass flow meter is based on the effect of gas flow on the heat transfer from the thermal flow sensor. Its resistance temperature sensing element is typically heated for a constant temperature difference ΔT above the gas temperature T_g and the heating electrical power $P = RI^2$ changes with the mass flow rate, where R is the electrical resistance of the sensing element and I is the supplied electrical current. Another option

is to maintain a constant electrical power P and the resulting temperature difference ΔT changes with the mass flow rate. The relationship between the output measurement signal $P/\Delta T$ and the mass flow rate q_m represents the measurement characteristic.

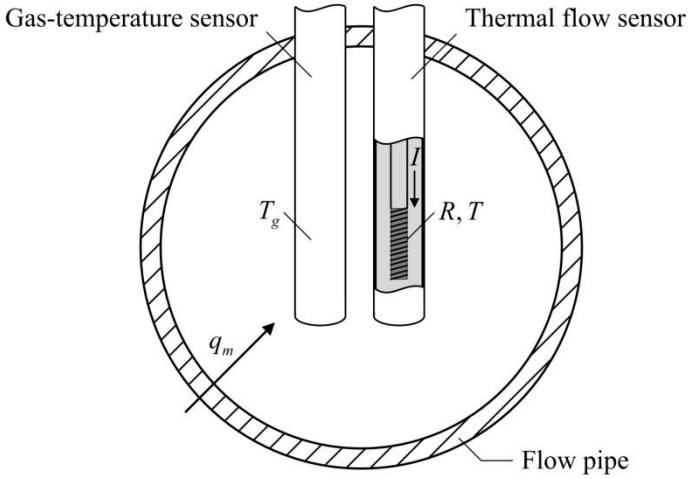

Figure 1. Measurement section of the thermal dispersion mass flow meter.

Because the intensity of the convective heat transfer from the thermal flow sensor to the gas is also affected by the thermodynamic and transport properties of the gas, the measurement characteristic depends on both the type and the composition of the gas. Therefore, if the measured gas is different to the gas used for the calibration, an appropriate correction needs to be applied in order to correctly measure the mass flow rate. Usually, the correction factors are provided or the meter is calibrated for a variety of gases and then the proper measurement characteristic is selected. In both cases, the actually measured gas has to be known.

We set our objective to develop an innovative thermal dispersion mass flow meter that would be capable to identify the type of gas from a defined set of gases and to correct the measurement characteristic. For this purpose we developed a measurement method for identifying the type of gas. To perform the gas-identification method, the thermal dispersion mass flow meter has to contain two thermal flow sensors with different constructional or operational parameters [3-5]. The mass flow readings of such thermal flow sensors will generally differ if the measurement characteristics for the improper gas are employed.

This paper is structured as follows. The realization of the innovative thermal dispersion mass flow meter is presented in Section 2 and the experimental results are presented in Section 3. The conclusions are given in Section 4.

2 Realization of the innovative thermal dispersion mass flow meter

The current realization of the thermal dispersion mass flow meter contains the thermal flow sensors with circular and square cross-sections. The x-ray images of the sensors and schemes of their cross-sections are presented in Figure 2. The square cross-section of the second sensor is obtained with an additional square sheath positioned on the sensor. Each thermal flow sensor comprises a Pt100 resistance temperature sensing element. The thermal flow sensors are connected to the Wheatstone bridges. Input voltage to each Wheatstone bridge is supplied by a DC power supply (National Instruments PXI-4110) and the output voltages are measured with a DAQ board (National Instruments USB-6341). The control of the developed thermal dispersion mass flow meter and the processing of the measurement signals are realized in the LabVIEW programming environment (National Instruments, Ver. 12.0.1). By means of a PI controller, the input voltage to each Wheatstone bridge is being set in such a way that constant temperature difference between the thermal flow sensor and the gas is maintained. The temperature of the gas is determined with the help of an additional temperature sensor.

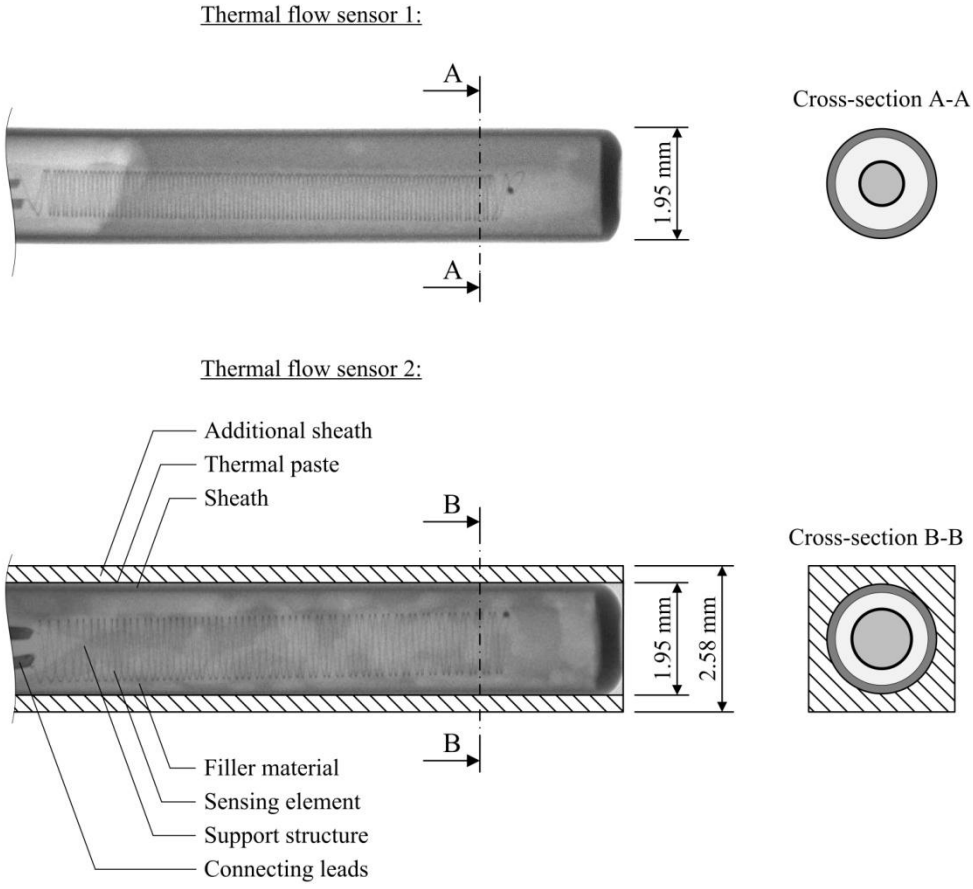

Figure 2. X-ray images of the thermal flow sensors and schemes of their cross-sections.

A block diagram of the gas-identification method, implemented in the developed thermal dispersion mass flow meter, is schematically presented in Figure 3. The measured mass flow rate results in the output measurement signals of the thermal flow sensors 1 and 2, $(P/\Delta T)_1$ and $(P/\Delta T)_2$, respectively. Information regarding the measurement characteristics (e.g. the calibration constants) for each gas from the defined set of gases G_j, $j = 1 \ldots N$, is stored in the database. Mass flow readings of the thermal flow sensors are calculated for each gas and represent inputs for the identification algorithm with the defined objective function.

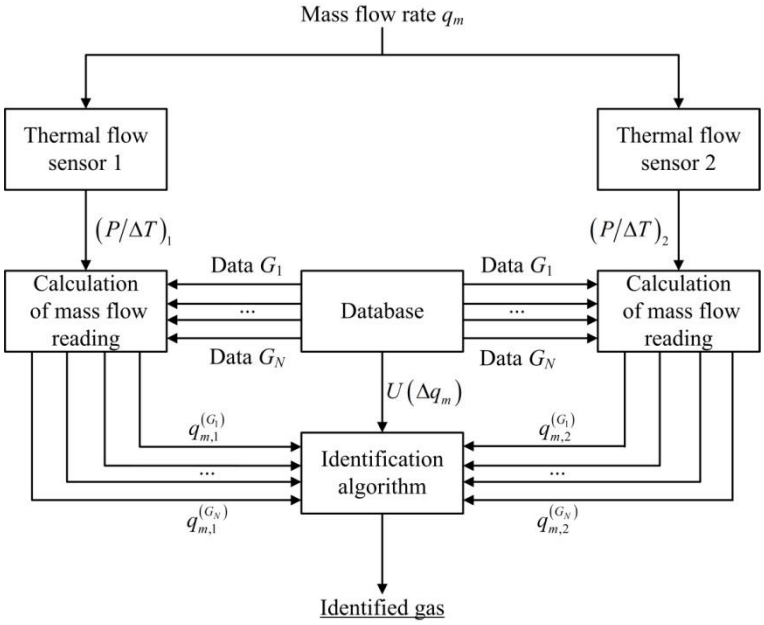

Figure 3. Block diagram of the gas-identification method [3].

The objective function can be defined as the relative difference in the mass flow readings:

$$\varepsilon = \frac{q_{m,2}}{q_{m,1}} - 1, \tag{10}$$

and the identified gas is the gas that minimizes the absolute value of this objective function. An advanced possibility is to define a criterion that accounts for the dispersion that could be reasonably attributed to the difference in the mass flow readings, for example, the normalized measurement error (a similar parameter is used for the evaluation of the results of interlaboratory comparisons [6]):

$$E_n = \frac{q_{m,2} - q_{m,1}}{U\left(q_{m,2} - q_{m,1}\right)}, \tag{11}$$

where $U\left(q_{m,2}-q_{m,1}\right)$ is the expanded measurement uncertainty ($k = 2$) of the difference in the mass flow readings. If $\left|E_n\right|>1$, the difference in the mass flow readings is statistically significant and consequently the particular gas can be identified as improper. In order to identify the proper gas with a sufficient degree of confidence, $\left|E_n\right|>1$ must hold for all but one gas from the defined set of gases.

3 Results

The developed thermal dispersion mass flow meter was calibrated for different gases in the range of mass flow rates between 100 g/min and 350 g/min. The calibration was performed in our ISO/IEC 17025 accredited laboratory by employing the reference mass flow measurement system with critical flow Venturi nozzles. The calibration and measurement capability of this measurement system (expressed as an expanded measurement uncertainty) is $U(q_m)/q_m = 0.16\%$ for air [7] and $U(q_m)/q_m = 0.30\%$ for other gases.

The measurement characteristics of both thermal flow sensors for air and nitrous oxide are given in Figure 4. The results were fitted with the Levenberg-Marquardt method using the following measurement model:

$$\frac{P}{\Delta T}=\frac{1}{c_1+\dfrac{1}{c_2+c_3\,q_m^{\,c_4}}}\,, \tag{12}$$

where c_1, c_2, c_3 and c_4 are the calibration constants (determined for each thermal flow sensor and for each gas).

The experimental validation of the gas-identification method was performed at a reference mass flow rate of 225.10 g/min of air. The output measurement signals of the thermal flow sensors were $\left(P/\Delta T\right)_1 = 10.66\,\mathrm{mW/K}$ and $\left(P/\Delta T\right)_2 = 15.26\,\mathrm{mW/K}$. If the measurement characteristics for air are employed, the mass flow readings of the thermal flow sensors are nearly equal: $q_{m,1}^{(\mathrm{Air})} \approx q_{m,2}^{(\mathrm{Air})}$. In contrast, if the measurement characteristics for nitrous oxide (N_2O) are employed, the mass flow readings differ significantly: $q_{m,1}^{(\mathrm{N_2O})} \neq q_{m,2}^{(\mathrm{N_2O})}$. The relative differences in the mass flow readings are $\varepsilon^{(\mathrm{Air})} = 0.06\%$ and $\varepsilon^{(\mathrm{N_2O})} = -16.0\%$, and the normalized measurement errors are $E_n^{\,(\mathrm{Air})} = 0.04$ and $E_n^{\,(\mathrm{N_2O})} = -9.97$. The minimum value of $\left|\varepsilon\right|$ is achieved for air. Because $\left|E_n\right| \le 1$ holds for only one gas, air is correctly identified as the proper gas.

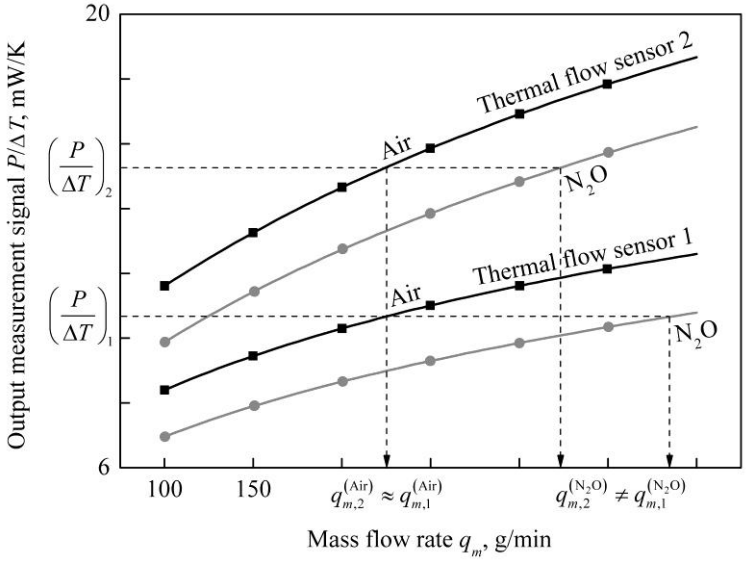

Figure 4. Measurement characteristics of both thermal flow sensors for air and nitrous oxide, and schematically presented results of the performed gas-identification method.

The expanded measurement uncertainty of the difference in the mass flow readings, which was used to calculate the normalized measurement error (eq. (11)), was evaluated in accordance to [8] and estimated to:

$$U\left(q_{m,2} - q_{m,1}\right) = 0.0155\, q_{m,1} + 0.21\,\mathrm{g/min}\,. \tag{13}$$

This measurement uncertainty takes into account the following contributions: the standard errors of estimates of the measurement characteristics, the measurement uncertainties of the heating electrical power and the maintained temperature difference, and the measurement uncertainties due to varying temperatures of both the measured gas and the surrounding air. The measurement uncertainty of the reference mass flow rate was not taken into account, because it does not affect the difference in the mass flow readings.

4 Conclusions

We developed the innovative thermal dispersion mass flow meter with the gas-identification capability. Here, its main characteristics are summarized:

- The thermal dispersion mass flow meter contains two different thermal flow sensors, which are required to perform the gas-identification method.
- The thermal dispersion mass flow meter has to be calibrated for all gases from the defined set of gases with known elemental compositions, i.e. the gases that are expected to flow through the meter.

- The mass flow readings of the thermal flow sensors will generally differ if the measurement characteristics for the improper gas are employed. The objective function, defined on the basis of this difference, is used to identify the type of gas.
- When the gas is identified, the thermal dispersion mass flow meter selects the proper measurement characteristics and then the mass flow rate of the actual gas is correctly measured within the measurement uncertainty.

Results of the performed validation experiment show that it is possible to distinguish between different gases, e.g. between air and nitrous oxide. However, it could happen that the difference in the mass flow readings is statistically insignificant for more than one gas from the defined set of gases, e.g. as presented for air and oxygen in [4, 5]. It was concluded that the gas-identification capability of the thermal dispersion mass flow meter could be improved by optimization of its constructional parameters or by reducing the measurement uncertainty of the difference in the mass flow readings.

The developed thermal dispersion mass flow meter could be used in flow systems with different pure, technical or medical gases. A possible application is in medical gas supply systems in hospitals, where the developed meter could be used to correctly measure the mass flow rate of different gases within the measurement uncertainty and also to detect the improper gas in a particular distribution pipe.

The developed thermal dispersion mass flow meter with the integrated gas-identification method presents a novel advancement in the field of the measurement of mass flow rate and therefore we protected our solution as intellectual property [3].

5 Acknowledgement

This work was supported in part by the Slovenian Research Agency (ARRS).

6 References

[1] ISO 14511:2001 (2001). Measurement of Fluid Flow in Closed Conduits – Thermal Mass Flowmeters. International Organization for Standardization. Geneva.

[2] Baker, R. C. (2000). *Flow Measurement Handbook: Industrial Designs, Operating Principles, Performance, and Applications.* Cambridge University Press, New York.

[3] Rupnik, K., Kutin, J., Bajsić, I. (2013). *Thermal Mass Flow Meter and the Gas-Identification Method*. SI patent application no. P-201300425. Slovenian Intellectual Property Office, Ljubljana.

[4] Rupnik, K., Kutin, J., Bajsić, I. (2014). A method for gas identification in thermal dispersion mass flow meters. *Strojniški vestnik – Journal of Mechanical Engineering*, vol. 60, no. 9, p. 607-616.

[5] Rupnik, K. (2014). *Development of Thermal Mass Flow Meter*. Ph.D. Thesis (mentor: I. Bajsić, co-mentor: J. Kutin). University of Ljubljana, Faculty of Mechanical Engineering, Ljubljana (in Slovene).

[6] ISO 13528:2005 (2005). Statistical Methods for Use in Proficiency Testing by Interlaboratory Comparisons. International Organization for Standardization. Geneva.

[7] *Annex to the Accreditation Certificate LK-015 for the Laboratory of Measurements in Process Engineering* (2013). Slovenian Accreditation, Ljubljana.

[8] JCGM 100:2008 (2008). Evaluation of Measurement Data – Guide to the Expression of Uncertainty in Measurement. Bureau International des Poids et Measures. Sevres.

Rotation generator of hydrodynamic cavitation

Martin Petkovšek [a*], Matevž Dular[a], Brane Širok[a]

[(a)] University of Ljubljana, Faculty of Mechanical Engineering, Aškerčeva 6, 1000 Ljubljana, Slovenia.

* Corresponding author:
E-mail: martin.petkovsek@fs.uni-lj.si

Abstract

Nowadays, due to lack of freshwater resources a sufficient wastewater management is an environmental concern. This global issue is resulting in the rapid growth of technologies for wastewater treatment. One very promising technology is usage of cavitation. In our laboratory, several studies have been made considering treatment of different kind of wastewater with hydrodynamic cavitation. For this purpose a novel machine (rotation generator of hydrodynamic cavitation – RGHC) has been designed, built and tested. RGHC presents a machine, which is based on a modified centrifugal pump and can be used in many different processes. Till now several experiments have been performed using hydrodynamic cavitation as a tool for treating different kind of water, e.g.: use of cavitation for sludge disintegration, for pharmaceuticals removal, for disinfection of swimming pool water and for killing the bacteria Legionella pneumophila.

1 Introduction

Cavitation as a phenomenon is characterized by a formation, growth and collapse of bubbles within a liquid. It forms, when the local pressure drops below the vaporization pressure for which two main reasons are possible. By ultrasonic cavitation, the acoustic waves cause the local pressure fluctuations, which are the cause for local pressure drop, while by hydrodynamic cavitation, the geometry of a system is the reason for velocity fluctuations in a liquid flow, which can cause local drop in pressure.

Locally seen the cavitation is a process of evaporation, gas expansion, condensation and gas compression [1]. The cavitation bubble forms due to evaporation and gas expansion and therefore collects the energy from the surrounding liquid. During the cavitation bubble collapse, where the condensation and gas compression occurs, this energy is released. The energy can be released by: (i) spherical bubble collapse in shape of pressure impulse in an order of several hundred bars [2], (ii) at solid boundary the cavitation bubble collapses asymmetrically, where consequently micro jet is formed, which can reach the velocities in order of 100 m/s [3]. By spherical bubble collapses also very high temperatures of several thousand kelvins occur (theoretically), but these last for very short time – in 1μs the temperature drops to the temperature of

the surrounding liquid [4]. Such extreme conditions are adequate to rupture or kill biological structures or they can cause water molecules to dissociate into OH and H radicals [5].

Till now series of studies have been made using cavitation for treating different kind of wastewaters. The majority of the experiments have been conducted with acoustic cavitation, but also several studies base on hydrodynamic cavitation. To gain the effect on treating wastewater, the acoustic and hydrodynamic cavitation can be combined. Also different kind of hybrid techniques, so called advanced oxidation processes have been developed for even more sufficient treatment, where they use different kind of chemicals like hydrogen peroxide, carbone tetrachloride, Fenton's reagents and others with combination of cavitation. There is no general presumption among the techniques, different types of pollutants demands different treatments and have different optimum conditions, due to different mechanisms of removal or destruction.

In the paper are presented four areas, where our RGHC was successfully used: (i) at municipal wastewater treatment plant (WWTP) the RGHC was used as a tool for sludge pretreatment to improve and accelerate the anaerobic digestion, which benefits in higher biogas production; (ii) RGHC was also used for treatment, removal of different kind of pharmaceuticals from municipal wastewater; (iii) in swimming pool complex or spa, many different chemical compounds can be formed due to combination of chlor and other organic materials, which were successfully removed with RGHC; (iv) also studies with removal of bacteria Legionella pneumophila with hydrodynamic cavitation were performed, where very encouraging results were achieved.

2 Machine presentation

On basis of knowledge and results from the first designed cavitation generator [6], a novel rotation generator of hydrodynamic cavitation (RGHC) was built at Laboratory for Water and Turbine Machines (Faculty of Mechanical Engineering, University of Ljubljana). Based on centrifugal pump design it has a modified rotor and added stator in the housing of the pump (Fig. 1). The RGHC consists of an electric motor (1) with power of 5.5 kW, which drives the modified rotor (2). The stator (3) is placed opposite to the rotor in the axial direction in the housing of the pump. The housing of the pump preserves the original inlet (4) and outlet (5) to retain the possibility of standard installation. The housing, the modified rotor (2) and added stator (3) are forming the cavitation treatment chamber. In addition to treating wastewater with cavitation, the whole RGHC partly still preserves the pumping function, which means that the machine does not require an additional circulation pump to operate.

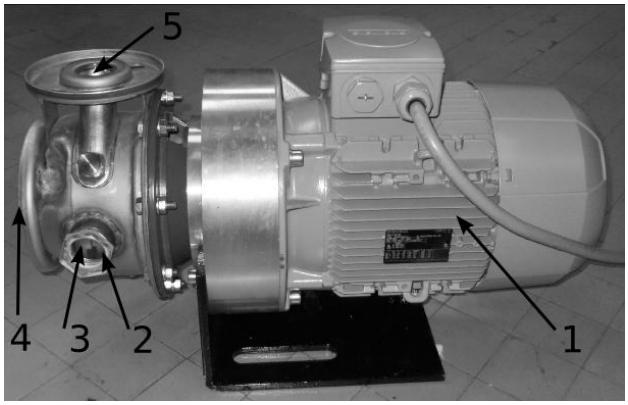

Figure 1: Rotation generator of hydrodynamic cavitation

Modified rotor and added stator have specially designed geometry, which causes periodically repeating pressure oscillations. Alternately low (below the vapor pressure) and high pressure cause the cavity formation. The type of cavitation which is forming inside the treatment chamber is so called shear cavitation, where cavitation structures are formed due to shear forces, which are caused by the relative movement of rotor, stator and the liquid in between them. The rotors geometry "drags" the liquid partially in the tangential and partially in the radial direction. The radial velocity of the liquid gives the machine the suction function, while the tangential velocity of the liquid causes the liquid to rotate in the treatment chamber. The rotor has on its diameter of 190 mm a certain number of grooves. These grooves consequently form the so called teeth, which are sticking out of the main core of the rotor in axial direction. The stator has the same outer diameter and the same number of grooves as the rotor. The difference is at the teeth geometry, where the stator teeth have inclination and they have barriers from three sides of each tooth. The purpose of these barriers is to retain the high pressure outside the cavitation zone, which results in intensification of the cavitation bubble collapse.

The main advantage of the presented RGHC is its double function, which means that it works as a cavitation generator and simultaneously as a pump. In compare with conventional hydrodynamic cavitation generators, such as Venturi restrictions or orifice plates, the presented RGHC does not cause additional pressure drops in consisting system. By restrictions, especially by orifice plates is also a risk of potential obstruction, due to small hole diameter.

Figure 2 presents visualization with high-speed camera of formed cavitation between the rotor and stator of the machine, where the images were taken at 8000 fps. Hatched line presents the stator tooth on the left side of the images (staying still), while on the right side of the images the rotors teeth are moving upwards, due to rotation.

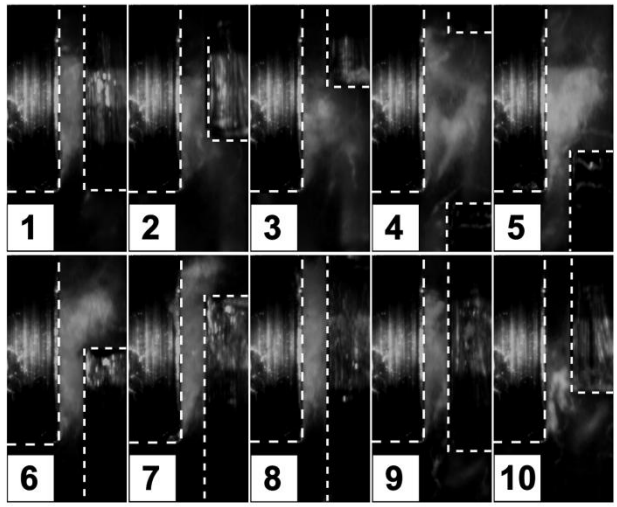

Figure 2: Visualization with high-speed camera of formed cavitation in RGHC

With the distance between the rotor and the stator, teeth geometry and with the frequency of the rotor, we are able to control the size and the aggressiveness of the formed cavitation.

3 Results

Disintegration of waste activated sludge (WAS)

Wastewater treatment plants use the cavitation as a tool for sludge pretreatment to improve and accelerate the anaerobic digestion, which benefits in higher biogas production, mass reduction, pathogen reduction and odour removal. Nowadays, most of commercial technology for sludge treatment, that use cavitation, base on acoustic cavitation (ultrasonication), which is in comparison with hydrodynamic cavitation less complex for implementation, but also less energy efficient. The problem by ultrasonic cavitation devices is that the cavitation effects occur only close to the vibrating surface, which decreases the possibility of the whole sludge to be treated.

With our machine we are able to provide a sufficient disintegration of the sludge, which were confirmed with our experimental work. At the first stage the analysis of hydrodynamics of the RGHC were made with tap water, where the cavitation extent and aggressiveness was evaluated. At the second stage RGHC was used as a tool for pretreatment of a WAS, collected from Wastewater treatment plant Domžale-Kamnik. In case of WAS the disintegration rate was measured, where the soluble chemical oxygen demand (SCOD) and soluble Kjeldahl nitrogen were monitored and microbiological pictures were taken. The SCOD, one of the parameters for disintegration, increased from initial 45 mg/L up to 602 mg/L and 12.7 % more biogas has been produced by 20 passes through RGHC. The results were obtained on a pilot bioreactor plant, volume of 400 liters [7].

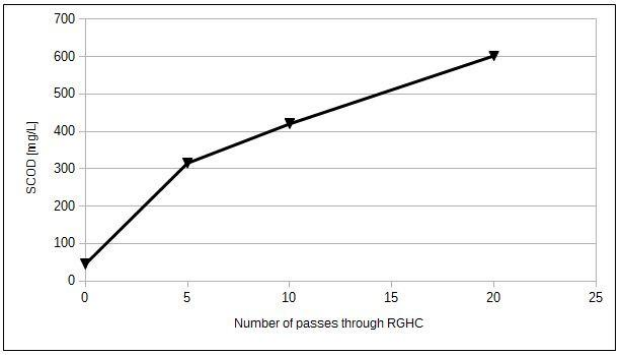

Figure 3: Disintegration rate measured with SCOD by number of passes through RGHC

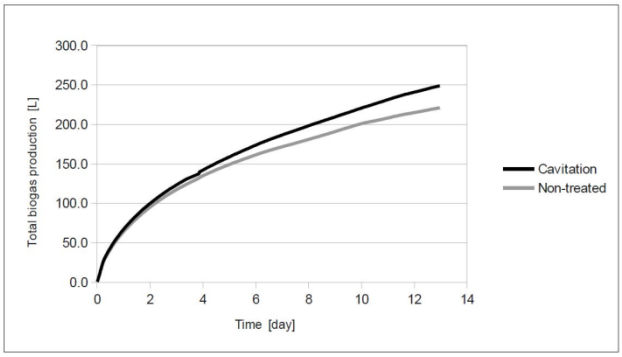

Figure 4: Total biogas production in case of cavitated sludge vs non-cavitated sludge

Pharmaceuticals removal

Pharmaceuticals are an important and indispensable element of modern life but parallel to the continuous rise in their consumption, is the increasing burden on the environment posed by pharmaceutical residues. The main sources of these residues are wastewaters that even after conventional (biological) treatment still contain pharmacologically active compounds. Pharmaceuticals can enter the environment through various routes (hospitals, households, unused medicines, animal excretion, etc.), but generally WWTP effluents are considered the most critical point source. While conventional (biological) treatments are insufficient by most pharmaceutical removal, new, advanced methods are being studied. And one of them is cavitation.

In our studies [6,8,9], the removal of clofibric acid, ibuprofen, naproxen, ketoprofen, carbamazepine and diclofenac residues from wastewater, using a hydrodynamic cavitation, has been systematically studied. The experiments were conducted in deionized water and also in real wastewater, where the results show, that for real wastewater effluents matrix composition reduces removal efficiency. Nevertheless the removal efficiency of the real wastewater effluents, by hydrodynamic cavitation, still reaches form 37% up to 79% for individual selected pharmaceutical.

Removal of trihalomethanes from water in swimming pools

Chemistry of swimming pool water is fundamentally different compared to drinking water. Whilst drinking water is only treated once – if at all – swimming pool water is used and treated repeatedly over extended periods of time. During the use of swimming pools, organic, inorganic and microbial contaminations are continuously introduced into the water by bathers. Additionally, water preparation chemicals as well as their impurities and decomposition products are added to the water, and microbiological activities in parts of the water preparation system may further impair the situation. Trihalomethanes (THMs) are formed as a by-product predominantly when chlorine is used to disinfect water. According to several studies, exposure to THMs may pose an increased risk of cancer. Some THMs have been identified as mutagens, which alerts DNA. Mutagens are considered to affect the genetics of future generations in addition to being carcinogenic. In addition to these risks, THMs are linked to bladder cancer, heart, lungs, kidney, liver, and central nervous system damage.

With our experiments, we showed that cavitation formed in our RGHC could be appropriate for THMs reduction in swimming pools. The results in Fig. 5 are shown for sample volume of 1000L, which could be considered as a pilot experiment.

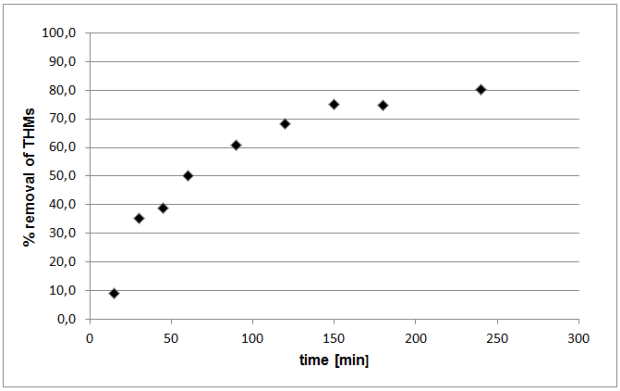

Figure 5: Removal of THMs

Bacteria Legionella pneumophila

Legionella pneumophila is wide spread in all natural fresh water sources in predominantly low concentrations. The bacteria has also frequently been observed in engineered water systems such as warm water distributing systems, cooling towers, humidifiers and fountains. In low concentrations Legionella pneumophila does not represent a significant risk for the health of humans, however the multiplication of the bacteria in water systems poses a potentially fatal (between 15 and 20 % of those infected) human health risk wherever aerosolisation can occur. Especially people with weakened immune system (e.g. cancer patients) are facing with fatal risk. To ensure the safe environment in health institutions, most common, the so called thermal shocks

are used to disinfect water distribution system, which are very energy wasteful and stressful for the plumbing.

In our study [10] we show, that bacteria Legionella pneumophila can be effectively eradicated by hydrodynamic cavitation. We show that it is probably not the pressure peaks or the high local temperatures that cause the eradication of the bacteria, but the rapid pressure decrease which was initiated in supercavitating flow regime. Results of the study show promising ground for further optimization of a methodology for Legionella pneumophila removal by cavitation.

4 Conclusions

Several studies have been made in our laboratory regarding to treatment different kind of water with hydrodynamic cavitation. Due to need for a cavitation machine, which has a simple design, low operating cost and could be easily to scale up or down, a novel Rotation generator of hydrodynamic cavitation has been designed, built and tested. Results of our experiments show, that presented machine is appropriate for several implementations by different processes, where the treatment of different kind of water is needed. With the geometry of some parts of the machine and its kinematics we are able to adjust the properties of the formed cavitation, such as size and aggressiveness.

Our further work is focused to improve the efficiency of the machine and to make an experimental installations on real systems.

5 References

[1] Dular, M., Coutier-Delgosha, O. (2913). Thermodynamic effects during growth and collapse of a single cavitation bubble. *Journal of Fluid Mechanics*, vol. 736, p. 44-66.

[2] Wang, Y.C., Brennen, C.E. (1994). Shock wave development in the collapse of a cloud of bubbles. *Cavitation and Multiphase Flow, FED,* vol. 194, p. 15-19.

[3] Franc, J.P. (2004). *Fundamentals of Cavitation*, Kluwer Academic Publishers.

[4] Fujikawa, S., Akamatsu, T. (1980). Effects of the non-equilibrium condensation of vapor on the pressure wave produced by the collapse of the bubble in a liquid. *Journal of Fluid Mechanics,* vol. 97, p. 481–512.

[5] Braeutigam, P., Franke, M., Schneider, R. J., Lehmann, A., Stolle, A., Ondruschka, B. (2012). Degradation of carbamazepine in environmentally relevant concentrations in water by Hydrodynamic-Acoustic-Cavitation (HAC). *Water Research*, vol. 46, p. 2469-2477.

[6] Petkovšek, M., Zupanc, M., Dular, M., Kosjek, T., Heath, E., Kompare, B., Širok, B. (2013). Rotation generator of hydrodynamic cavitation for water treatment. *Separation and Purification Technology*, vol. 118, p. 415-423.

[7] Petkovšek, M., Dular, M., Mlakar, M., Levstek, M., Stražar, M., Širok B. A novel rotation generator of hydrodynamic cavitation for waste-activated sludge disintegration. Submitted to *Ultrasonic Sonochemistry* in 2014.

[8] Zupanc, M., Kosjek, T., Petkovšek, M., Dular, M., Kompare, B., Širok, B., Blaženka, Ž., Heath, E. (2013). Removal of pharmaceuticals from wastewater by biological processes, hydrodynamic cavitation and UV treatment. *Ultrasonic Sonochemistry*, vol. 20, p. 1104–1112.

[9] Zupanc, M., Kosjek, T., Petkovšek, M., Dular, M., Kompare, B., Širok, B., Blaženka, Ž., Stražar, M., Heath, E. (2014). Shear-induced hydrodynamic cavitation as a tool for pharmaceutical micropollutants removal from urban wastewater. *Ultrasonic Sonochemistry*, vol. 21, p. 1213–1221.

[10] Šarc, A., Oder, M., Dular, M. (2014). Can rapid pressure decrease induced by supercavitation efficiently eradicate Legionella Pneumophila bacteria?. *Desalination and Water Treatment*.

Heat exchanger tube sampling in nuclear power plants

Matic Resnik [a], Joško Valentinčič [a*], Izidor Sabotin [a], Andrej Lebar [a,b], Marko Jerman [a], Nejc Matjaž [a], Mihael Junkar [a]

[(a)] University of Ljubljana, Faculty of Mechanical Engineering, Aškerčeva 6, 1000 Ljubljana, Slovenia.

[(b)] University of Ljubljana, Faculty of Health Sciences, Zdravstvena pot 5, 1000 Ljubljana, Slovenia.

* Corresponding author:
E-mail: jv@fs.uni-lj.si

Abstract

In this work, a new device is developed for cutting stainless steel tubes from heat exchangers in nuclear power plants. Tubes are cut from inside out because they can not be accessed from outside. The process of dry EDM (Electrical Discharge Machining) is identified as the most appropriate. The work comprises of design development, manufacturing, testing and optimization of the developed dry EDM cutting head, selection of suitable electrical generator and optimization of cutting process parameters by performing design of experiments using the Taguchi method. The final product of this research is a portable device used for cutting the heat exchanger tube inside a Romanian nuclear power plant Cernavoda.

1 Introduction

Nowadays nuclear power plants contribute an important part of electrical energy all over the world. Maintenance is crucial to avoid power losses, break downs and other unnecessary costs. Therefore, maintenance intervals are carefully planned and maintenance should always be on schedule. One of the things that must be inspected is tubes inside a heat exchanger. Damaged tube samples are taken to determine the state of degradation and study the wear mechanisms. Furthermore, they help us predict problems and improve the design of heat exchangers. Main problem that occurs on site is limited access and difficult working environment, often inside the radioactive zone in the nuclear power plant. Our goal is to design a portable device for tube sampling in nuclear power plants.

2 Technology determination

An extensive review of solutions with similar field of application is conducted. Several solutions have been protected by patents [1-7]. It is followed by a SWOT (Strengths, Weaknesses, Opportunities, Threats) analysis of mechanical, thermal and electro

thermal processes, that also considered all of our customer demands [8]. After the requirements for working in nuclear power plants are also taken under considerations, the process of dry EDM cutting is identified as the proper technology to be used. Its main attributes are cutting at any desired depth, precision, absence of tube wall deformation and debris of insignificant dimensions.

3 Preliminary testing

To determine if dry EDM can be used for cutting stainless steel tubes from inside out a plan of preliminary experiments is made. Firstly a cutting head with simplified principle of centrifugal force opening is designed. Secondly an electric power source and source of rotation for the cutting head are chosen. First experiment is unsuccessfully conducted on the EDM machine due to short circuit prevention of the machine itself. Therefore a new electrical source is introduced in form of a portable welding machine. Rotation of the cutting head on the other hand is provided by a bench drilling machine again with intent of simplification for the preliminary experimentation. Numerous improved designs of cutting heads are designed and tested with the combination of tungsten and electrolytic copper electrodes. Tungsten proves to have better temperature resistance but limits our options when it comes to electrode design. The performance of electrolytic copper is on the other hand satisfactory, and allow us to manufacture different designs of electrodes. After defining parameters of the cutting process and achieving sufficient repeatability the next step is to build a portable cutting system.

4 Portable cutting system

Main difference introduced to make the cutting system portable is a standard three phase electric motor and flexible cable for the rotation of the cutting head. Welding machine is still used as a portable electric power source. Ability of the system being easy to assemble and disassemble is emphasised. Safety is also considered due to danger of electric shock for the operator, fire danger or the danger of parts of equipment falling into the heat exchanger. In order to know when the cutting process is finished an oscilloscope is attached on the system. It allows us to monitor the process that is happening deep inside the tube and cannot be visually monitored.

5 Optimization of the cutting parameters

Only when the portable cutting system is designed, the optimization of the cutting parameters can be made. The Taguchi method of designing the experiments is used. Only the most influent parameters are optimised. Those parameters are the electric current intensity, the cutting head rpms (revolutions per minute) and the length of the spring on which the electrodes are mounted. The range of each parameter was determined beforehand during preliminary testing. Criteria for assessing the best combination of parameters is the material removal rate, in other words cutting speed.

To achieve comparable and repeatable results each experiment duration is 7 minutes and each experiment is completed three times.

To evaluate each experiment, tube samples are cut in half transversely to the cuts from experiments. Tube samples are cut twice, once on the left side and once on the right, hence they are separated in upper and bottom part of the tube (Figure 1). The depth of the cut is than measured with a linear laser profilometer and an average of upper and bottom side cut is calculated to nullify the influence of gravitational force. Furthermore, results of all three experiment repetitions are also averaged and inserted in a computer program Design Management. This program provides users with optimal parameter values by establishing the influence of each parameter and their mutual dependence.

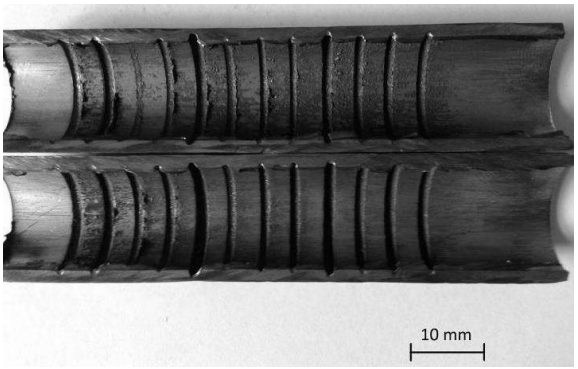

Figure 1. Tube samples cut in half.

Verification experiment was made and the parameter values from Design Expert gave better result than any other tested during experiments.

6 Testing on a scale model

In order to get approval to use the developed portable cutting system in the nuclear power plant Cernavoda, Romania, testing on a scale model is needed. This particular model is 6 meter long and has 19.05 x 1.65 mm tubes (outer radius is 19.05 mm, tube wall is 1.65 mm, and inner radius 15.75 respectively). After testing is successfully finished the person responsible for the heat exchanger maintenance at Cernavoda nuclear power plant approves the technology.

7 Heat exchanger in Cernavoda

When one of the reactors in Cernavoda is shut down due to regular planned inspection and maintenance we get an opportunity to cut and extract a tube from a real nuclear power plant heat exchanger. Heat exchanger inspection starts by inspecting every tube along entire length of the tube with eddy current probes. Results give information on how deeply damaged certain tube is. The depth of the damage is expressed in percent of tube wall damaged. If this percent reaches the critical value tube must be sealed. On

this occasion, instead of plugging one of this tubes we got to cut it and extract it from the heat exchanger with intent of analysing wear mechanisms. While extracting it with a special tool, we had to cut the tube into smaller samples because of the limited space of the chamber we worked in. This cutting was done by an outer tool cutter that produces no debris. Every sample was carefully labelled. Furthermore we plugged the holes that were left in the support plates on both sides of the heat exchanger. They were plugged with special purpose plugs and air tight welded onto support plates. After testing the welds we were done. Corrosion damage on inner tube walls was visually inspected by borocsope (Figure 2). Tube samples were send to detailed analysis afterwards.

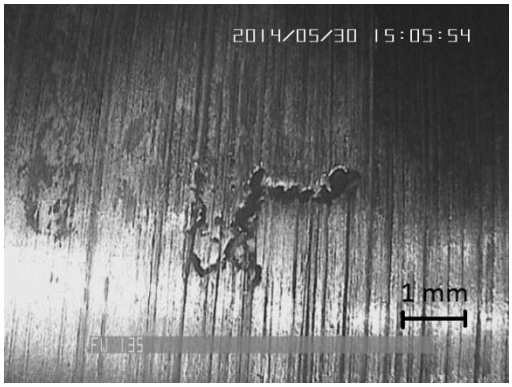

Figure 2. Corrosion damage on inner wall of the tube.

8 Conclusions

A patentable device for heat exchanger stainless steel tube cutting from inside out has been developed. Dry EDM can be used for the purpose of cutting and feedback gap control can be avoided due to centrifugal force and proper adjustment of parameters. The technology of tube sampling is commercially interesting and provides our customer with an important advantage. Additional uses of the developed cutting system are also to be investigated.

9 Acknowledgement

This work was supported by Ministry of Education, Science and Sport and company Numip Ltd. (grant agreement 93 823/LAT).

10 References

[1] Chamming's, P., Cartry, J.P. (1990). Device for cutting the wall of the tubular piece by electrical discharge machining. *Google Patents*, US 4916282 A.

[2] Cole, W.G., Hydeman, J.E., Gunsallus, J.M., Le, Q. (1996). Electron discharge machining apparatus and method. *Google Patents*, US 5543699 A.

[3] Dudden, D.E. (1976). Apparatus for electric discharge machining of holes. *Google Patents*, US 3995134 A.

[4] Evans, D.M., Candee, C.B. (1988). Tube cutting apparatus and method. *Google Patents*, US 4779496 A.

[5] Louis, D.M.S. (1991). Portable device for cutting the inside wall of a tube by a continuous arc. *Google Patents*, US 5077456 A.

[6] Braswell, S.P. (1966). Inside pipe cutting tool. *Google Patents*, US 3283405 A.

[7] Cammann, F.W. (1960). Internal tube cutter. *Google Patents*, US 2942092 A.

[8] Valentinčič, J., Resnik, M., Frankovič, M. (2013). Technologies for tube sampling in nuclear power plant heat exchangers. *Proceedings of the 12th International Conference on Management of Innovative Technologies & 4th International Conference on Sustainable Life in Manufacturing*, p. 189-192.

Methodology for evaluation of tribological mechanisms and quality of sliding bearings

Mitjan Kalin [a*], Blaž Žugelj [a], Andraž Rant [b], Aljoša Močnik [b]

[(a)] University of Ljubljana, Faculty of Mechanical Engineering Aškerčeva 6, 1000 Ljubljana, Slovenia.

[(b)] Domel d.o.o., Otoki 21, 4228 Železniki, Slovenia.

* Corresponding author:
E-mail: mitjan.kalin@tint.fs.uni-lj.si

Abstract

Sintered bearings with lubricant in pores are used in several machines and devices e.g. electric motors. They are widely used because they can run without usage of additional lubricant and by comparison with rolling bearings they are quieter and have simpler design. The sustainability and the quality of sintered bearings are contingent upon wear and friction of sintered bearings which at the same time also affect the working temperature. The usage of reliable and quality bearing in adequate load conditions is crucial for the quality and reliability of the devices in which bearings are installed. We have thus carried out research on tribological properties of several sliding bearings from various series, i.e. bearings delivered from industrial bearing producers through different time periods. First we focused on finding the causes and mechanisms, which lead to a damage and a failure of sliding bearings. Furthermore, the test methodology based on the model tribological experiments was developed to enable relatively fast, simple and reliable pre-mounting quality control of different series of sliding bearings. Consequently, savings due replacement of the demanding test methods with simpler and inexpensive method have been achieved. At the same time the new test methodology will increase the understanding of installed component's behavior and provide guarantee for quality and reliability of electric motors.

1 Introduction

Because of economic and technical advantages the usage of P/M materials is currently employed in many mechanical parts such as gears, camshafts, bearings etc. Many of these components are exposed to the severe cycling loading during its operation and mostly fail by contact fatigue wear [1].

Sintered metal self–lubricating sliding bearing presents one of the products which are based on powder-metallurgy technology. Because sintered metal self–lubricating bearing are economical, suitable for high production rates and can be manufactured in precision tolerances they are widely used in home appliances, small motors, machine tools, aircraft and automotive components etc. [2].

One of the main advantages of self–lubricating porous sliding bearing is that there is no necessity for certain lubricating equipment such as oil pipes, pumps, etc. Moreover, porosity can act as oil reservoir in which oil or lubricant can be stored. In this case lubricant comprise about 25 % of material volume [3, 4]. Since the lubricant is stored in pores there is no need for external supply of lubricant [5]. In the initial stages of their lifetime, when pores are filled with lubricant, the sintered bearings operate under hydrodynamic lubrication conditions. However, when starting and stopping or after a certain period of time, when the bearings run short of lubricant due to leakage and evaporation, they operate under mixed and boundary lubrication conditions [6, 7]. While porous sliding bearings are operating, oil will come out from the pores to lubricate the sliding surface and upon unloading or shut-down of the operation it will penetrate back into the pores [6, 8]. This process repeats until all amount of lubricant is removed from pores. It is when the material from the sintered bearings can either be transferred to the shaft or it can get embedded in the pores, which cause pore closure [9]. Consequently high wear rate occurs, which leads to the failure of the bearings.

Among all sintered bearings, sintered bronze bearings are very common and most widely used [4]. By internal industrial testing protocols using complex devices, it is found that in some series (bearings delivered by producers on different delivery occasions/times) bearings experienced frequent failures prior the expected time, i.e. prior the test conclusion. To find out the reasons why some bearings fail the tests analysis were carried out to compare tribological mechanisms and surface damage of tested adequate and unsuitable bearings. Furthermore the test methodology based on the model tribological experiments was developed, which proved relatively fast, simple and reliable pre-mounting quality control of sliding bearings.

2 Experimental

In the first part of our research we analyzed bearings from different series which were previously tested in accelerated dynamic real-scale test rig. Some of them were adequate (the bearings were operational by the end of the test) and some were unsuitable (the bearings prematurely failed).

For porosity, wear, surface analyses and wear mechanisms investigations, several analytical methods were used. We used 3D optical interferometry (Bruker Contour GT-K0), optical microscopy (Nikon, LV150) and scanning electron microscopy SEM (Jeol JSM T330A).

The surfaces of the bearings were first analyzed using Bruker Contour GT-K0 3-D optical profilometer. Namely, topographies of the inner surfaces were used to determine the topography and porosity of the surfaces. Porosity was determined by at least 5–6 measurements performed at different locations on each sample.

SEM analysis was performed to analyze microstructure of new bearings where purposely fractured surfaces were investigated. Moreover, a key part of the work was to observe the tribological mechanisms and compare different worn and unworn

surfaces of the bearings. By using the SEM we scanned the whole inner surface of the bearings' direction along the axis as well as circumferentially.

In addition to above surface damage analyses, we set the test methodology for faster and reliable pre-mounting quality control. First, tribological tests were performed on several series of bearings. All the tests were carried out with a tribometer shown in Figure 1. For each test new (un-used) bearing and shaft were used. Both components were prepared before the tests with respect to the specific requirements of the testing. The shaft was held stationary, while the bearing has been cut on half, placed on the shaft and slid against the shaft in a reciprocating motion (Figure 1).

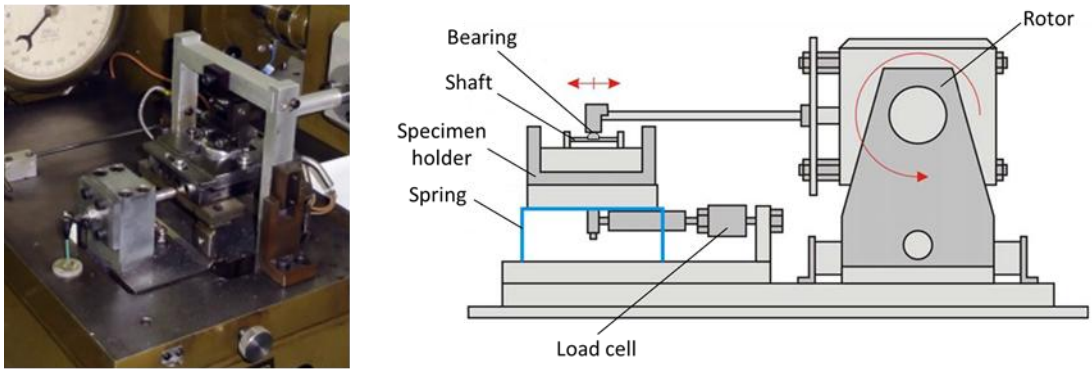

Figure 4: Tribometer TE77 on which tribological tests of the bearings were performed (left) and schematic demonstration of the tribological test rig (right).

Before and after each test the weight of the shaft and the bearing were measured. The difference in bearing's weight was used to determine the wear rate. For weighing the shafts and bearings, precision digital scale (Radwag XA210/X) was used.

Porosity, surface analyses and wear mechanisms were investigated after each test with the help of 3-D optical interferometer, optical microscope and SEM.

With all the sliding tests the same frequency, stroke and consequently the sliding velocity were used. The variables in testing were time (duration of the tests) and normal load. The test matrix of the parameters used for tests with all bearing is presented in Table 1.

Table 1: Test conditions for the sliding tests performed on all bearings

Frequency [Hz]	20
Stroke [mm]	10,5
Velocity [mm/s]	420
Normal load [N]	200
Time [h]	4

3 Results and discussion

SEM analysis

First we performed SEM analysis on the sliding surfaces of bearings which were previously tested under the conditions of real-scale application. Figure 2 presents the surface of a bearing which passed the tests and are therefore considered of adequate quality. On the other hand Figure 3 shows surface of unsuitable bearing e.g. bearing which did not passed the test.

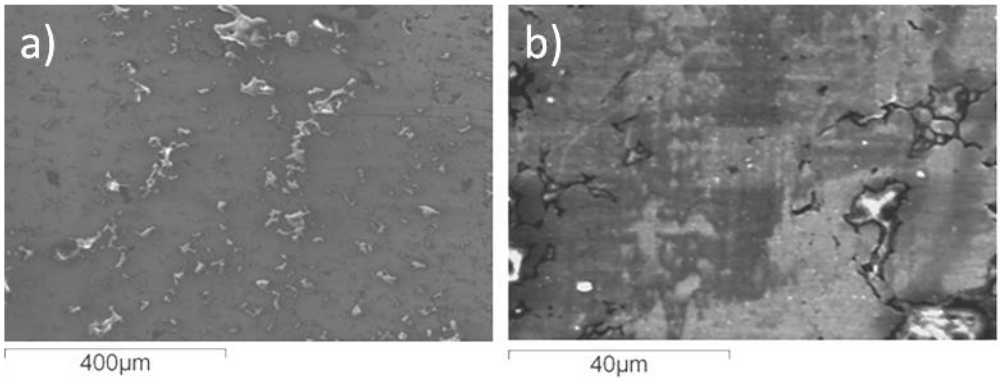

Figure 5: Sliding surface of adequate bearing tested in real-scale test rig, obtained by SEM at a) 150x and b) 1500x magnification.

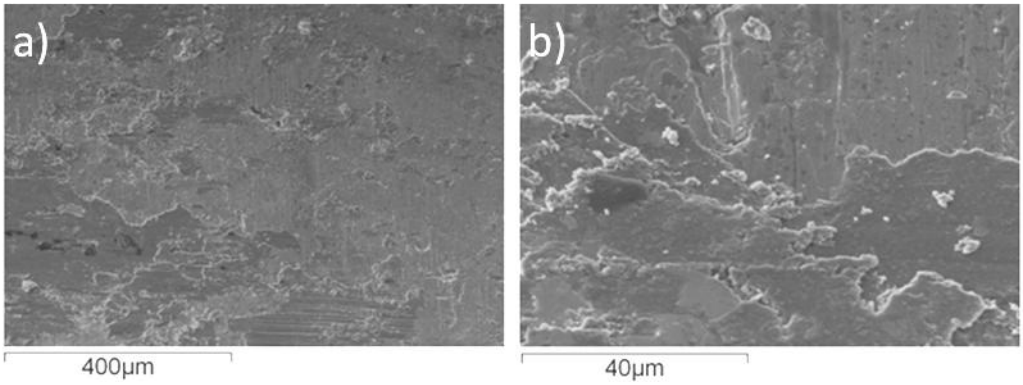

Figure 6: Sliding surface of unsuitable bearing tested in real-scale test rig obtained by SEM at a) 150x and b) 1500x magnification.

These SEM results were later compared with the results of SEM images obtained on the sliding surfaces, which were tested under corresponding test conditions on model tribological tests in a tribometer. They are presented in Figure 4 and 5. Figure 4 shows the sliding surface of adequate bearing while Figure 5 presents sliding surface of unsuitable bearing.

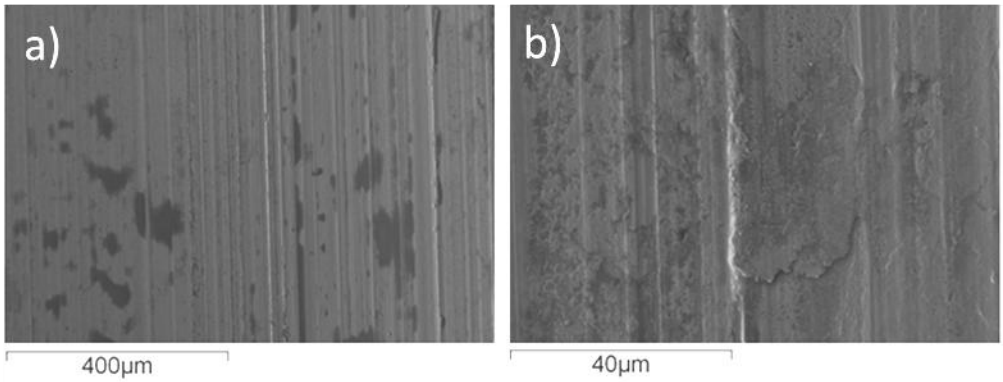

Figure 7: Sliding surface of adequate bearing tested in model tribological test, obtained by SEM at a) 150x and b) 1500x magnification.

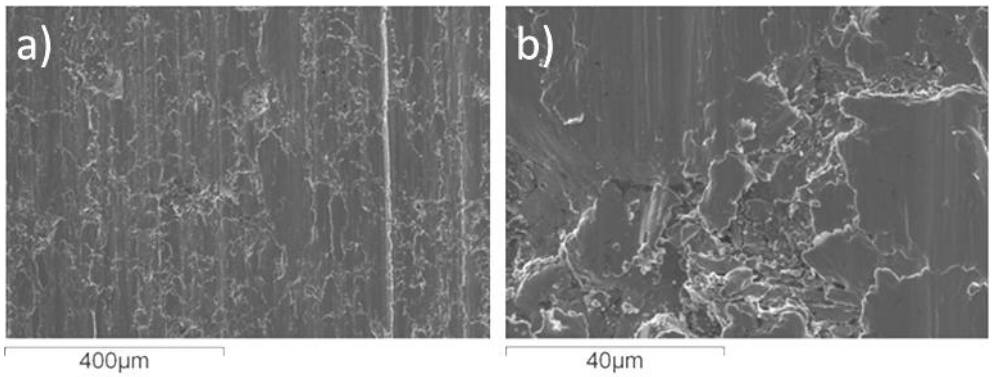

Figure 8: Sliding surface of unsuitable bearing tested in model tribological test, obtained by SEM at a) 150x and b) 1500x magnification.

As can be seen on Figures 2, 3, 4 and 5 wear mechanisms on the sliding surfaces of the bearings tested in real-scale and model tests are similar. On the surfaces of unsuitable bearings from both tests we did not detect any traces of oil. Furthermore, on all surfaces of unsuitable bearings brittle layers and debris were detected. On the other hand surfaces were smoothed out and oil was detected on the surfaces of the adequate bearings. By observing this similarity in wear mechanisms, it can be claimed at sufficient statistical verification that model tribological tests can simulate the conditions which bearings are exposed in real-scale applications.

Once the right test conditions were set we performed other analysis, which could additionally distinguish between the adequate and unsuitable bearings.

Porosity of the sliding surfaces

Figure 6a shows the example of porous sliding surface of the bearing which was reported to be sufficient for further usage. The sliding surface of unsuitable bearing is presented in Figure 6b. Percent share of the porosity for both examples is presented in Figure 7.

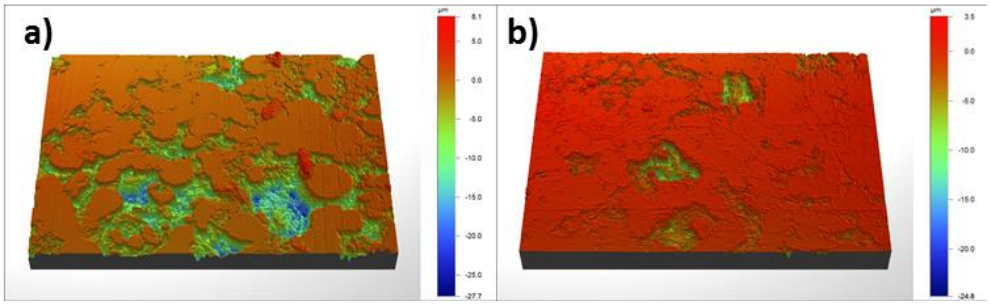

Figure 9: Porous sliding surface of a) adequate and b) unsuitable bearing

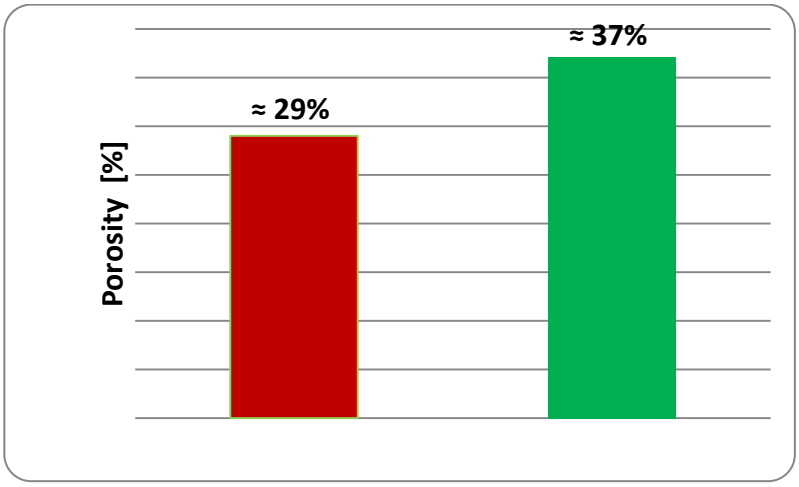

Figure 10: Average porosity of sliding surfaces of the adequate (right column) and unsuitable (left column) sintered bearings.

As can be seen from Figures 6 and 7, sliding surface of an adequate bearing is much more porous. Consequently, more oil can be stored in the bearing which ensures longer lubrication of the contacting parts.

Wear

As reported earlier, the wear of each bearing was determined as the difference in mass before and after the test. The wear results for sliding bearings are shown in Figure 8. The results can clearly tell, which bearings are adequate (denoted as good) and which are not (denoted as bad).

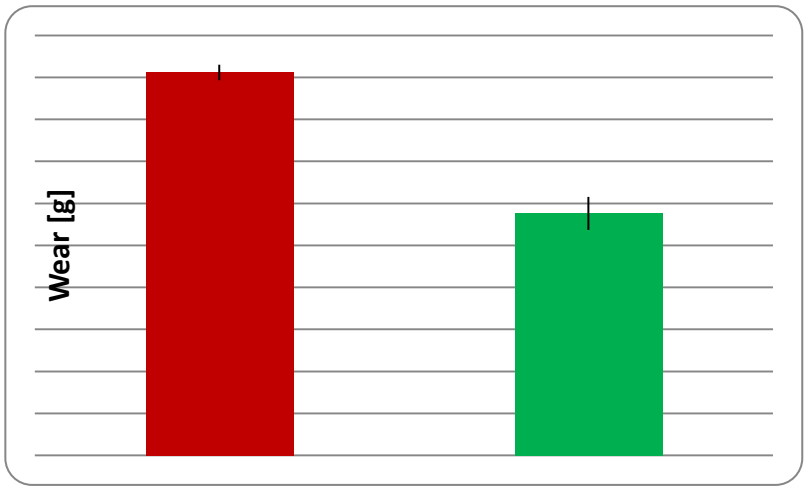

Figure 11: Wear measured on adequate (right column) and unsuitable (left column) bearings.

Figure 8 shows that the wear measured on the unsuitable bearing is much higher than on the adequate bearing. Wear rate can be referred to the porosity of the bearings. In the case of adequate bearings sliding surfaces are more porous and the wear rate in this case is lower. On the other hand sliding surfaces of unsuitable bearings have lower porosity and higher wear rate. Bearings with more porous material, which can store more oil, provide longer lubrication which prevents wear of the sliding surfaces. Lower the porosity is, less lubricant can be stored in pores and less lubricating sites are present at the surface. Consequently, bearings quickly run out of oil and sliding surfaces start to heat and wear. It is what causes the failure of unsuitable bearings.

4 Conclusions

In our research a test methodology based on the model tribological experiments was set. With its help we can simulate the same wear mechanisms as are presented on the sliding surfaces of the porous sintered bearings in real-scale application. The test methodology enables relatively fast, simple and reliable pre-mounting quality control of different series of sliding bearings. Based on the obtained results, the following conclusions can be drawn:

- Failure of sintered bearings is primarily caused by the absence of lubricant. Consequently, severe brittle fracture on sliding surfaces of the bearings occurs.
- Results show that the wear rate of the bearings from unsuitable series is almost 60 % higher than in case of the bearings from adequate series.
- Average porosity of the sliding surfaces in the case of adequate series of the bearings was approximately 8 % higher than in case of unsuitable bearings.

5 Acknowledgement

The authors wish to thank dr. R. Simič for porosity measurements and dr. J. Kogovšek and F. Kopač for help in various aspects related to the testing during this study.

6 References

[1] Govindarajan, N., Gnanamoorthy, R. (2007). Rolling/sliding contact fatigue life prediction of sintered and hardened steels. *Wear*, vol. 262, no. 1, p. 70-78.

[2] Ertuğrul, D., Fazh, D. (2008). Tribological and fatigue failure properties of porous P/M bearing. *International Journal of Fatigue*, vol. 30, no. 4, p.

[3] Eisen, W., Ferguson, B., German, R., Iacocca, R., Lee, P., Madan, D., Moyer, K., Sanderow, H., Trudel, Y. (1998). Powder metal technologies and applications. vol., p.

[4] Tavakoli, A., Liu, R., Wu, X. (2008). Improved mechanical and tribological properties of tin–bronze journal bearing materials with newly developed tribaloy alloy additive. *Materials Science and Engineering: A*, vol. 489, no. 1, p. 389-402.

[5] Naduvinamani, N., Hiremath, P., Gurubasavaraj, G. (2001). Squeeze film lubrication of a short porous journal bearing with couple stress fluids. *Tribology international*, vol. 34, no. 11, p. 739-747.

[6] Durak, E. (2003). Experimental investigation of porous bearings under different lubricant and lubricating conditions. *KSME international journal*, vol. 17, no. 9, p. 1276-1286.

[7] Raman, R., Chennabasavan, T. (1998). Experimental investigations of porous bearings under vertical sinusoidally fluctuating loads. *Tribology international*, vol. 31, no. 6, p. 325-330.

[8] Kaneko, S. (1993). Porous oil bearings. *Japanese Journal of Tribology*, vol. 38, no. 9, p. 1141-1150.

[9] Gnanaraj, S.D., Raman, R. (1992). Experimental studies on wear in oil-impregnated sintered bearings. *Wear*, vol. 155, no. 1, p. 73-81.

Evaluating tribological properties of polymer materials for gears in tribological and gear tests

Aljaž Pogačnik [a], Mitjan Kalin [b*]

[(a)] Iskra Mehanizmi, Lipnica 8, 4245 Kropa, Slovenia.

[(b)] University of Ljubljana, Faculty of Mechanical Engineering, Aškerčeva 6, 1000 Ljubljana, Slovenia.

* Corresponding author:
E-mail: mitjan.kalin@tint.fs.uni-lj.si

Abstract

The use of polymer materials for gears has increased significantly in the last decade, especially because of their advantages over classical gear materials like steel and brass. The advantages of using polymer materials for gears are mainly low cost for serial production, good vibration damping, good tribological properties even without lubrication and low gear mass. The main disadvantages are lower allowable operating temperatures and also lower allowable gear stresses.

One of the biggest challenges when designing gear drives from polymers is the determination of the operating temperature of the gears. There are theoretical models available, however they all require coefficient of friction as the input parameter.

In the literature, the amount of data regarding the tribological properties of polymer materials (friction, wear, mechanisms …) is very limited. And the data that is available, is often very unreliable as not all testing conditions are known and well controlled. In order to determine the coefficient of friction and to reliably calculate operating gear temperatures for different material combinations, it is necessary to perform tribological evaluation prior to gear testing.

This paper discusses results obtained from tribological evaluation of polyamide 6 (PA6) and polyacetal (POM) in tribological as well as in model (gear) testing. For the purpose of gear testing, test gears were injection moulded and tested on a purpose built test rig. The results from tribological as well as gear testing show, that very similar tribological phenomenon occur at both types of tests. The results also show that it is possible to predict gear behaviour based on tribological testing. In addition, a precise gear calculation of gear operating temperature is possible based on the measured coefficient of friction from tribological testing.

1 Introduction

Plastic gears have been in use for over 50 years and their importance is growing every year. The main advantages of plastic gears are low manufacturing costs, no need for

external lubrication, low mass and also good noise damping properties. There are also some disadvantages that prevent plastic gears from certain fields of use; plastic gears have inferior mechanical and thermal properties compared to steel, lower operating temperatures, lower manufacturing tolerances, water absorption, ... [1-3].

Mass production of plastic gears with injection moulding processes and new plastic materials with improved technical characteristics have also accelerated the use of plastic gears. A wide variety of different types of polymer materials, different reinforcements and internal lubricants can be used for polymer gears [1, 2]. However, with a vast amount of different combinations available, it is very hard to determine the optimal material combination for a gear drive design, especially when taking into consideration also noise and vibrations properties.

In spite of the growing use of plastic gears, there hasn't been a lot of systematic scientific research. The standard most widely used for strength calculation of cylindrical plastic gears is the VDI 2545 [4], which is a simplified version of metal gear standard DIN 3990. But the VDI 2545 was introduced in 1981 and was retracted in 1996. In 2014 a new VDI 2736 [5] was released; however it is very similar to the old VDI 2545. The number of data for different material combinations is still very limited.

The fact that polymer materials have much lower operating temperatures, lower thermal conductivity and higher coefficient of thermal expansion makes them highly sensitive to temperature changes. It is thus very important to calculate gear operating temperatures precisely [6-8].

An engineer therefore needs to know how to design plastic gears successfully without the use of valid standards and also without much material data. One way to overcome this problem is to rely on the knowledge gained from past gear design experiences. It also seems that for a reliable and optimal gears design, preliminary gear testing is necessary.

The basis for temperature calculations is coefficient of friction [6-8]. In the literature, the amount of data regarding the tribological properties of polymers (friction, wear, mechanisms …) is very limited. And the data that is available, can often be very unreliable as not all testing conditions are known. In order to determine the coefficient of friction and to reliably calculate operating gear temperatures for a certain material combination, it is necessary to perform tribological evaluation prior to gear testing.

Gear testing is a very time consuming and expensive option that tests different material combinations under different operating conditions on a gear test rig. This way, an engineer gains much deeper understanding of the operation of the polymer gears.

The goal of the research is to see, if it is possible to predict tribological behaviour of polymer materials in gears based only on simple tribological testing of the same material combination. This paper discusses results obtained from tribological evaluation of polyamide 6 (PA6) and polyacetal (POM) in tribological as well as in model (gear) testing. The material combinations used for evaluation were POM/PA6, POM/POM and PA6/PA6.

2 Experimental

Tribological testing

The tribological tests were performed on a pin-on-disc machine under dry sliding conditions. The testing machine consists of a turntable, which holds the lower disc specimens and is driven by a servomotor (Figure 1). The upper pivoting arm is fixed to the frame of the machine through bearings, so that normal loads can be applied to the upper specimens. The upper specimen, having a flat circular contact area of 7 mm^2, is fixed to the pivoting arm via a special holder and the loads are applied with weights being placed directly on top of the holder fixing point. The tangential forces are measured with an LVDT sensor, which is measuring the deformation of the loading arm. In addition, two weights are attached to the loading arm to counter-balance the arm before the tests. The radius on which all the tests were performed was 18 mm. The CSEM software was used to control the apparatus. During the tests the coefficient of friction was measured together with the sliding distance and the time.

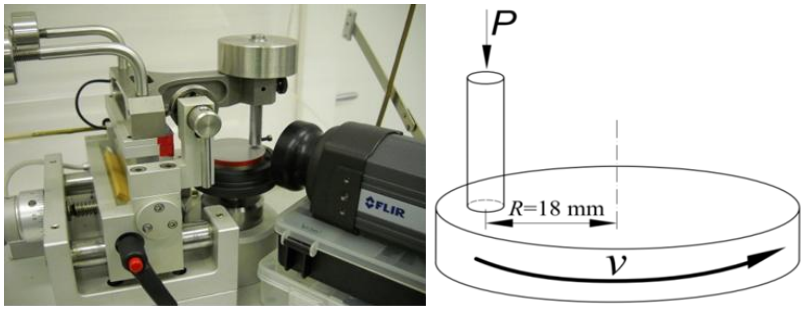

Figure 1. Pin-on-disc machine for tribological testing

The materials used for the upper (pin) specimens and lower (disc) specimens were unreinforced polyamide (PA6, Ultramid® B3S, BASF, Germany) and unreinforced polyacetal (POM, Delrin® 500, DuPont, Germany). The upper specimens were cylindrical pins of Φ 3 mm x 14 mm. The raw material was produced in granular form and then injection moulded to the desired form on a BOY 35M machine (BOY limited, UK). The lower specimens were discs manufactured in dimensions of Φ 50 mm x 17 mm. Raw material was also produced in granular form and then injection moulded to the desired form using the same injection-moulding machine as for the pins. Due to the uneven shrinkage of the material, the polymer discs were additionally machined so that the top and bottom surfaces were parallel and of controlled roughness.

The controlled surface roughness of disc specimens was achieved with different abrasive papers. The surfaces were then measured using a stylus-tip profilometer (T8000, Hommelwerke GmbH, Schwenningen, Germany). The surface roughnesses of the discs were R_a = 0.30 µm ± 0.05 µm.

Gear testing

For the purpose of this research, an open-loop gear testing rig was used. The scheme of the test rig is shown on Figure 2a. The driver test gear (Figure 2b) is mounted on the "power" shaft, which is connected (via coupling) to the electric motor with the maximum torque output of 1 Nm at 4000 rpm. The driven gear is mounted to the "brake" shaft, which is connected (via coupling) to the hysteresis magnetic brake.

Each bearing unit, that enables the precise rotation of the shaft, consist of two roller bearings, which are pre-tensioned in order to eliminate the effect of bearing backlash. The design of the test rig allows precise positioning of the test gears in *x* and *y* directions. Centre distance can be adjusted between 5 mm and 50 mm with the precision of 0.002 mm. The test rig is computer controlled and enables the measurements of the test torque and the number of cycles to failure.

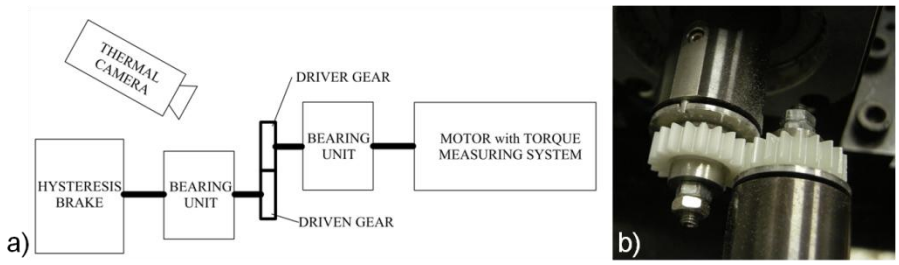

Figure 2: a) Scheme of the gear test rig and b) polymer gear pair (driver (left), driven (right)).

The temperature of the driver gear was measured using a thermal camera (Flir A320, Flir, USA). The maximum temperatures were measured from the side of the gear, as shown on Figure 3, immediately after the end of engagement with the driven gear. The emissivity of the gear materials was measured prior to the tests and was set to a constant value throughout the duration of the test.

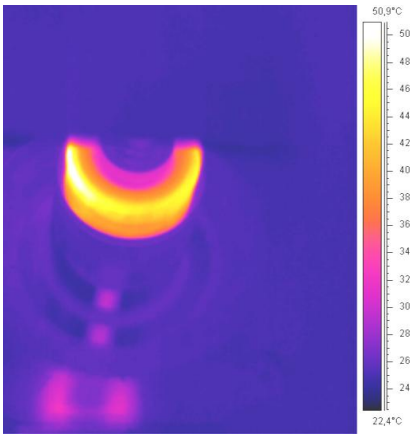

Figure 3: Thermographic measurement of the test gears.

Envolute gear geometry was selected for the test gears due to its common use in modern gear drives. A standard pressure angle of $\alpha = 20°$ was used when designing the geometry. No profile shift was applied to the geometry, while the rounding of the tip of the teeth was 0.1 mm. The specification of the test gears is presented in Table 1. Due to the injection moulding, the quality of the test gears was 10 according to ISO standard.

Table 1: Specification of the test gears

Module	1 mm
Number of teeth	20
Diameter of tip circle	22 mm
Pressure angle	20°
Face width	6 mm
ISO gear quality	10

Two different polymer materials were used for polymer gears moulding. The first material was unreinforced polyamide 6 (PA6, Ultramid® B3S, BASF, Germany). The second material was unreinforced polyacetal (POM, Delrin® 500P, DuPont, Germany). Both materials used were produced in granular form and then injection moulded to the desired gear geometry on a BOY 35M machine (BOY limited, UK).

Materials were selected due to their good tribological performance [9] and their common use in plastic gear drives [1]. We decided to use unlubricated conditions, as it is a favourable contact in automotive industry due to cost reduction and process simplification.

The theoretically calculated center distance was 20.00 mm. However, due to expected thermal expansion of the gears, the center distance was for all tests set to 20.05 mm.

3 Results

Material combination POM/PA6

Figure 4 shows max. gear temperature in gear testing for combination POM/PA6 at 0.3 Nm and 2305 rpm. It can be seen that gear temperature very quickly reaches 80 % of the max. operating temperature. After 20 hours, the temperature stabilises at 100°C and is constant throughout the whole duration of the test.

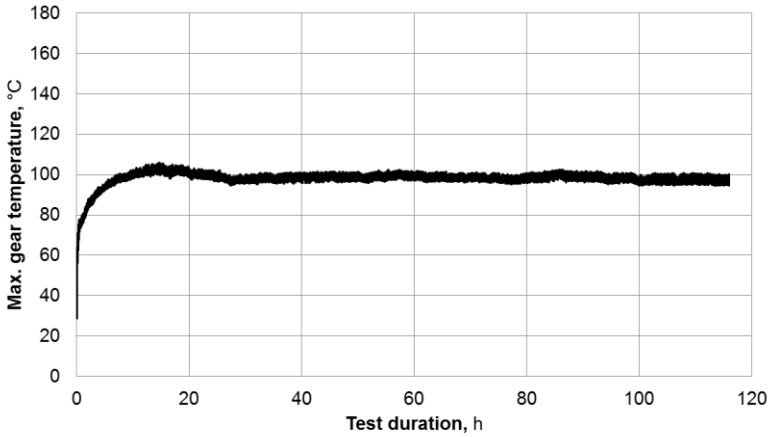

Figure 4: Max gear temperature during gear testing at 2305 rpm and 0.3 Nm.

Coefficient of friction measured during tribological testing for combination POM/PA6 is shown in Figure 5. The measurement was performed at 0.85 MPa and 0.7 m/s. It can be seen, that coefficient of friction rapidly increases at the beginning of the test to around 0.6. After the running in phase is completed (after 10 km), the coefficient of friction stabilises at 0.5 and is stable during the rest of the test.

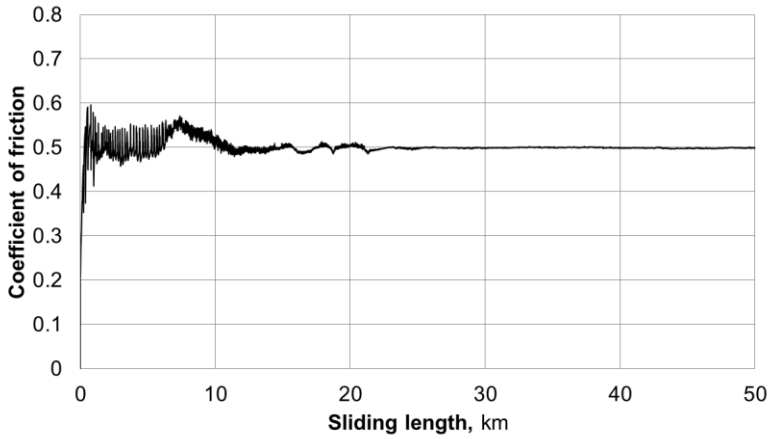

Figure 5: Coefficient of friction during tribological testing at 0.85 MPa and 0.7 m/s.

Material combination POM/POM

Figure 6 shows the operating gear temperature for material combination POM/POM at 0.42 Nm and 1176 rpm. In the running in phase, the gear temperature peaks at around 90 °C and then slowly decreases to around 70 °C. After the first 6 hours of testing, the running in phase is completed. The gear temperature is stable throughout the rest of the gear test.

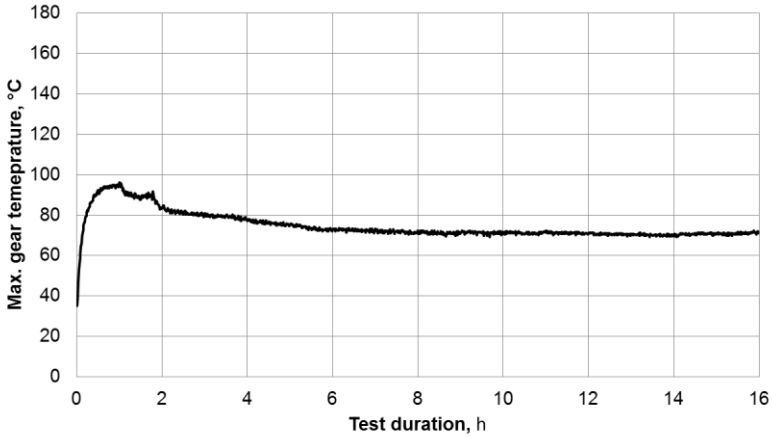

Figure 6: Max gear temperature during gear testing at 1176 rpm and 0.42 Nm.

The results from tribological testing of POM/POM materials combination at 0.55 MPa and 0.4 m/s are shown in Figure 7. It can be seen that the coefficient of friction quickly increases to around 0.4 and is stable during the remainder of the test.

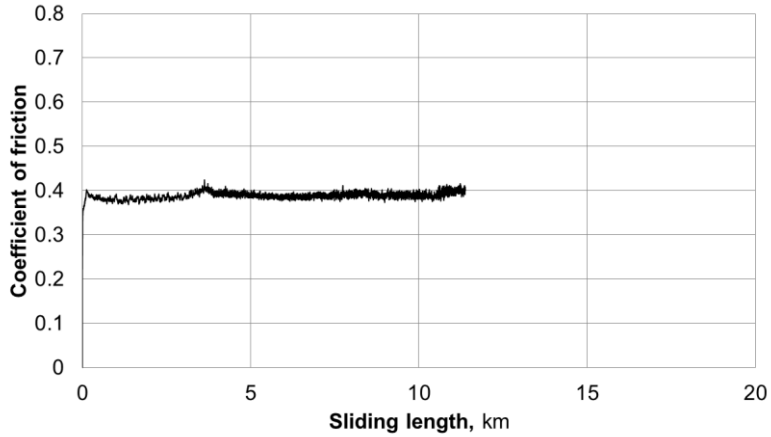

Figure 7: Coefficient of friction during tribological testing at 0.55 MPa and 0.4 m/s.

Material combination PA6/PA6

Max. gear temperature for combination PA6/PA6 at 0.42 Nm and 600 rpm is shown in Figure 8. In the first hour of the test, the temperature increases to around 140 °C and then slowly decreases to around 110 °C. At the end of the tests, additional peaks in the temperature occur. The operation of the gears is unstable, as the temperature measurement scatter is as high as 20 °C.

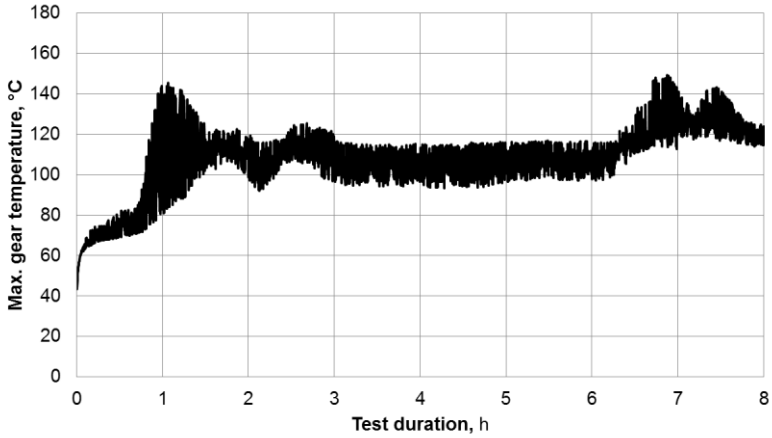

Figure 8: Max gear temperature during gear testing at 600 rpm and 0.42 Nm.

Coefficient of friction for the PA6/PA6 combination at 0.7 m/s and 0.55 MPa is shown in Figure 9. It can be seen that the coefficient of friction quickly increases to around 1.1. During the remainder of the test, the coefficient of friction is very unstable. The scatter of the measured data is very high, which indicates a non-compatible material combination.

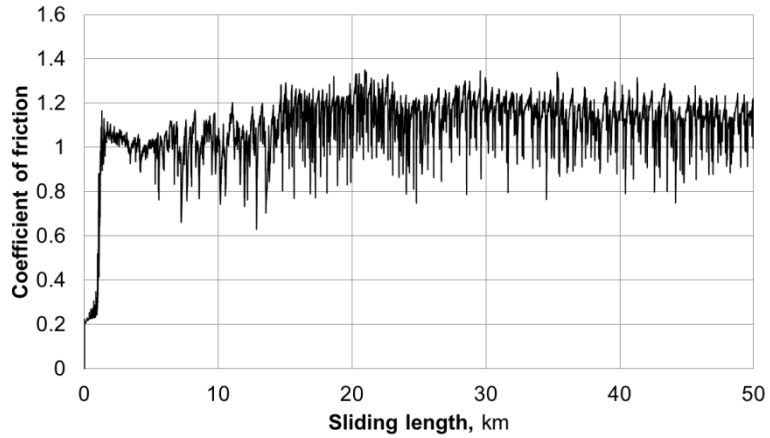

Figure 9: Coefficient of friction during tribological testing at 0.7 m/s and 0.55 MPa.

4 Discussion

For the material combination POM/PA6, curve for the gear temperature (Figure 4) as well as coefficient of friction (Figure 5) show very stable behaviour. As the coefficient of friction for this material combination is moderate (around 0.5, Figure 5), the temperatures at gear testing are also moderate (around 100°C, Figure 4). The wear of the specimens in tribological testing was around $1.1 \cdot 10^{-5}$ mm^3/Nm, which is not significant for polymer material. As can be seen from Figure 10, wear on the tooth

flanks was minimal. This is a result of a good tribological compatibility of POM and PA6 materials.

Figure 10: Fatigue of the tooth for POM/PA6 combination after 16.000.000 cycles.

The tribological investigation of POM/POM combination showed coefficient of friction around 0.4 (can be seen on Figure 7) but at the same time also very high wear $2.0 \cdot 10^{-5}$ mm^3/Nm, which is 10 times higher compared to material combination POM/PA6. The temperatures at gear testing were around 80°C, which is lower compared to the material combination POM/PA6. Lower temperatures are a result of lower coefficient of friction. The operation at both types of testing is very stable (Figure 6 and 7). As can be seen from Figure 11, the wear of the gear teeth is very high (the top of the tooth is completely worn out). For both types of testing, very similar trends can be observed.

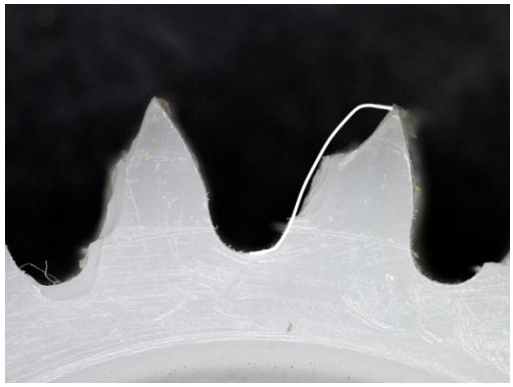

Figure 11: Teeth wear for POM/PA6 combination after 2.000.000 cycles.

Material combination PA6/PA6 resulted in very high coefficient of friction (around 1.2, Figure 9) and had very unstable operation (coefficient of friction not constant at the test. Despite high coefficient of friction, the wear was low - $2.4 \cdot 10^{-5}$ mm^3/Nm. At gear testing, the operating temperatures were very high (120°C, Figure 8) and also the operation was very unstable. High gear temperatures are a result of high coefficient of

friction, which was observed at the tribological testing. No wear was observed on PA6 gears after the test.

5 Conclusions

Based on the experimental results, the following conclusions can be drawn:

- Based on the tribological testing, it is possible to predict the behaviour of materials in gear application.
- The material combination POM/PA6 resulted in moderate coefficient of friction and moderate gear temperatures, stable operation as well as low material wear.
- The material combination POM/POM resulted in moderate coefficient of friction and moderate gear temperatures, stable operation but also very high wear occurred.
- The material combination PA6/PA6 resulted in high coefficient of friction and high gear temperatures, unstable operation but also very low wear was observed.

6 References

[1] Adams, C.E. (1986). *Plastics gearing: selection and application*. M. Dekker, New York.

[2] Campo, E.A. (2006). *Complete Part Design Handbook - For Injection Molding of Thermoplastics*. Hanser Gardner Publications, Cincinnati.

[3] Brydson, J.A. (1999). *Plastics materials, Third ed*. Butterworth-Heinemann, Oxford.

[4] VDI 2545 (1981). Zahnräder aus thermoplastischen Kunststoffen. VDI.

[5] VDI 2736 Blatt 1-4 (2014). Thermoplastische Zahnräder. VDI.

[6] Mao, K. (2007). A new approach for polymer composite gear design. *Wear*, vol. 262, p. 432-41.

[7] Hachmann, H., Strickle, E. (1966). Polyamide als Zahnradwerkstoffe. *Konstruktion*, vol. 959, no. 18, p. 81-94.

[8] Blok, H. (1963). The flash temperature concept. *Wear*, vol. 6, p. 483-494.

[9] Pogačnik, A., Kalin, M. (2012). Parameters influencing the running-in and long-term tribological behaviour of polyamide (PA) against polyacetal (POM) and steel. *Wear*, vol. 290-291, p. 140-148.

Tribological properties of advanced sliding electrical contacts

Dejan Poljanec [a], Mitjan Kalin [b*], Rok Simič [b], Ludvik Kumar [a]

[(a)] Kolektor Group, Vojkova 10, 5280 Idrija, Slovenia.

[(b)] University of Ljubljana, Faculty of Mechanical Engineering, Aškerčeva 6, 1000 Ljubljana, Slovenia.

* Corresponding author:
E-mail: mitjan.kalin@tint.fs.uni-lj.si

Abstract

Sliding contacts with conduction of electrical current have been investigated many times because of their significant importance in many electrical machines and devices. Custom made tribological testing rig with a capacity up to 17 m/s sliding speed and 20 A electrical current was developed and is described in this study. The testing rig was used to perform tribological study of different material combinations, normal contact pressures, electrical currents and surface polarity on wear, friction, contact resistance and temperature. Long-term tests (240 h) were performed to reduce measurement error effect on wear rate evaluation. Positive effect of electrical current passing on coefficient of friction was noted. At sufficient contact pressures electron donating surface (negative bias) exhibited higher wear rate in comparison to positively biased contact surface. On the other hand, arcing in contact usually appears at low contact pressures, which severely increases wear of the contacting materials. Both, friction and contact resistance contribute to contact temperature rise. Therefore, the contact material pairing is of significant importance for efficient electrical and tribological properties of the sliding electrical contacts.

1 Introduction

Almost every machine in the industry, transport or household, consists of some electrical device and almost each of these require conduction of electrical current from a rotating to a stationary part. Accordingly, the challenges in further development of these sliding electrical contact systems are cost-related, and what is even more desirable - related to technical advancements, such as improving the quality, performance, life-time, reducing maintenance, as well as enabling greener technologies, using renewable materials and reducing overall life-cycle emissions. The sliding electrical contacts that conduct current from a rotating to a stationary part in electrical devices must be designed to transmit as much of the current as possible with high electrical efficiency, but they are also tribological systems that must provide low friction to ensure mechanical efficiency and low wear due to maintenance and durability reasons. Therefore, the materials used in slip ring-brush electrical sliding systems must simultaneously provide satisfactory electrical and tribological operation.

Carbon brushes on copper rings are used and studied for many decades [1-6]. It is surprising that this system has not been changed dramatically for the last 60 or more years and remains unchanged in many major characteristics, both in terms of materials and design. Copper is used mainly due to its excellent electrical properties [7], however due to the strong metallic bonds and adhesive interactions cannot be used in self-mated pairs. Therefore, graphite with also very good electrical properties [8] is used for brushes to form graphite-copper interaction, primarily due to the tribological suitability, providing low friction with its basal-plane lamellar structure and relatively poor adhesive interactions with metals [3]. While the slip ring-brush design has remained almost the same over the decades, there have been many studies in the past that were related to various aspects of electrical and tribological behaviour in the graphite-copper electrical contacts. This has influenced modifications in materials and improvements, mainly in specific applications and environments [9-11]. For example, several types of graphitic materials can nowadays be used for brushes: natural, synthetic, electro graphite, polymer-impregnated, metallic-impregnated and metallic-coated [12-15]. On the other hand, copper and its alloys are usually used in mass production of rings. Besides, noble and more expensive materials with their alloys based on silver, bismuth, mercury, gold, etc. or galvanic coatings can be used as well [16-21]. These materials primarily improve electrical performance compared to copper-based rings, but unfortunately, experience higher friction and wear. There have been some attempts also to increase current density and reduce contact resistance by using all-metal contacts with brushes from metallic fibres [9,22,23], however, also in this case the brush wear was too high and temporary current instabilities were too large [22]. As evident from the state of the art, due to simultaneous electrical, mechanical, as well as thermal effects, the properties and parameters of the interface boundary films in the electrical sliding contacts are quite complex and even interfaces in contacts of today's design are not sufficiently understood. Accordingly, to achieve better performance of the electrical sliding contacts, modifications of the contact conditions, design and materials are needed. Therefore, to fully understand the influencing parameters and contact mechanisms and to enable tailoring and optimisation of the system, the experimental tests in real contact conditions and with anticipated optimal materials need to be carried out.

2 Experimental test rig

A custom tribological testing rig was designed and made for the purpose of examination of the tribological and electrical properties of sliding electrical contacts. Tribological test rigs in some other electrical sliding contact studies [9,10,24-26] were initial design guidelines, however, because of some other sliding contact specificities in this case, custom design was necessary. On the testing device the following properties can be evaluated: sliding friction or coefficient of friction by measuring frictional torque and normal contact load, bulk temperatures of stationary specimens, sliding contact voltage drop or contact resistance, wear of the contact materials and relative environment humidity can also be monitored during the tests. Testing rig was designed to enable testing of electrical sliding contacts in wide range of mechanical

and electrical loads and even to operate in climate chamber to alter environmental temperature and humidity. Tests can be performed in the following range of conditions:

- Sliding speed: 0 – 17 m/s;
- Normal contact load: 0 – 50 N;
- DC electrical current: 0 – 20 A.

The testing rig (Figure 1) consists of a test shaft driven by 1.1 kW electromotor via belt transmission. Electromotor is driven with frequency inverter enabling sliding speed adjustments. On each end of the test shaft is one rotating test sample, which is electrically insulated from the shaft with a plastic holder. Both rotating test samples are electrically connected with conductor guided through the hollow shaft. Two stationary test samples are pressed against the rotating test samples – one on each side of the shaft. The stationary test specimen is placed on multi-component sensor with plastic insolating holder. Both stationary specimens are connected to DC source. With such arrangement electrical circuit is assured. Multi-component sensors measure normal force in a range between 0 – 50 N and frictional torque in a range between 0 – 0.5 Nm. A coefficient of friction can be calculated from these two parameters. The stationary test specimen with multi-component sensor is placed on a slider and pressed against the rotating test sample with an adjustable tension spring. The contact resistance of each sliding contact is measured independently. Voltage tap wires are attached to both stationary specimens and third voltage tap wire is connected to additional slip ring-brush system in the middle of the rotating shaft. The electrical sliding contact resistance is calculated using Ohm's Law with voltage drop and conducted electrical current over the contact. For bulk temperature measurement two K-type thermocouples are placed into each stationary specimen, one approximately 1.2 mm under the sample's contacting surface and another about 2.4 mm deep. Data acquisition is performed with National Instruments' analog input modules and LabVIEW software.

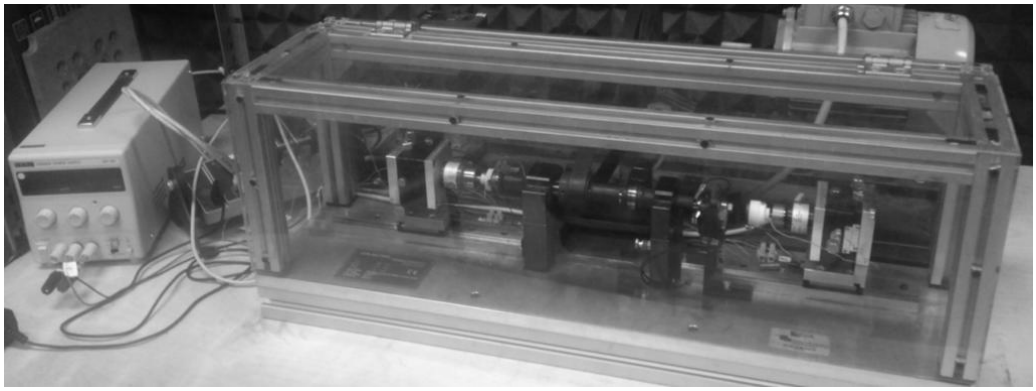

Figure 1. Tribological testing rig.

3 Experiments and results

Two sets of experiments were performed. The first set of experiments included 240-hour durability tests, which were performed to evaluate the effect of normal contact load and electrical current on tribological properties. These tests served for the evaluation of the contact stability over time and to reduce the error effect on the wear rate evaluation. In this set of experiments two different contact materials were used: A and B. Tests were performed at a constant sliding speed of 5 m/s, environment temperature of approximately 30 °C and electrical current of 6 A. Reference tests with no electrical current were performed as well. Before and after each test the amount of material removed due to wear was evaluated by measuring the height of the samples using a micrometer. The difference in height is represented as a linear wear. The average linear wear for the positively and negatively biased surfaces at different normal loads is presented in Figure 2.

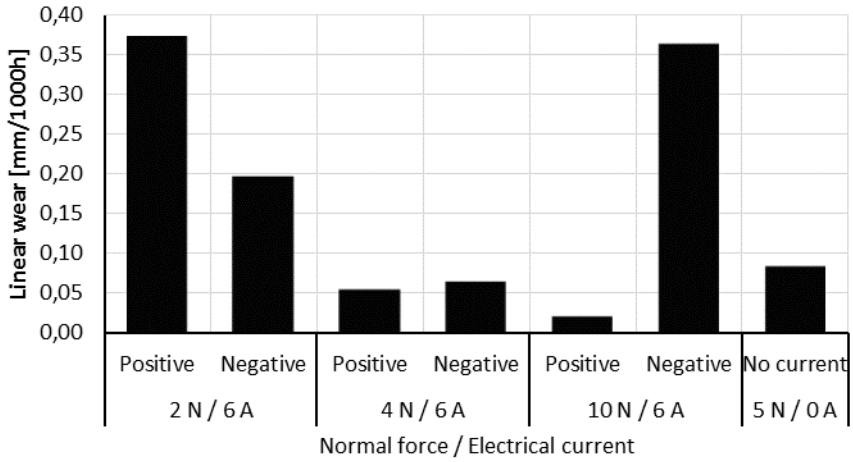

Figure 2. Linear wear for positively and negatively biased surfaces at different loads.

The lowest wear was measured on the samples tested at a normal force of 4 N and at the tests without any electrical current. At 10 N of load, a very large difference in wear was observed for positively and negatively biased surfaces. Since the wear of the "positive" surface in this tests was a bit lower than at 4 N load, some material transfer from negative to positive contact surface is considered. At 2 N of load, the contact pressure was too low to assure a steady electrical contact. Therefore, arcing in the contact was observed, which resulted in changed wear mechanism and overall higher wear. Although "negative" surface normally suffers of higher wear, "positive" surface showed more wear at this testing conditions, as positive surface was from material A, which seems to have lower wear resistance to arcing. While material B was used for negatively biased surface.

In test with no electrical current higher coefficient of friction was measured in comparison to tests with electrical current. While no significant effect of normal

contact pressure on coefficient of friction has been noted. Considering electrical resistance (e. g. Figure 3), results show lower electrical resistance for material combination A/B in comparison to B/B. As expected, at higher normal load there is also slightly lower electrical contact resistance. Temperatures measured during the tests (Figure 4) show increasing trend with increasing normal load. Meanwhile, the temperatures were the lowest in the test without the electrical current, which shows considerable contribution of electrical current to the bulk temperature rise.

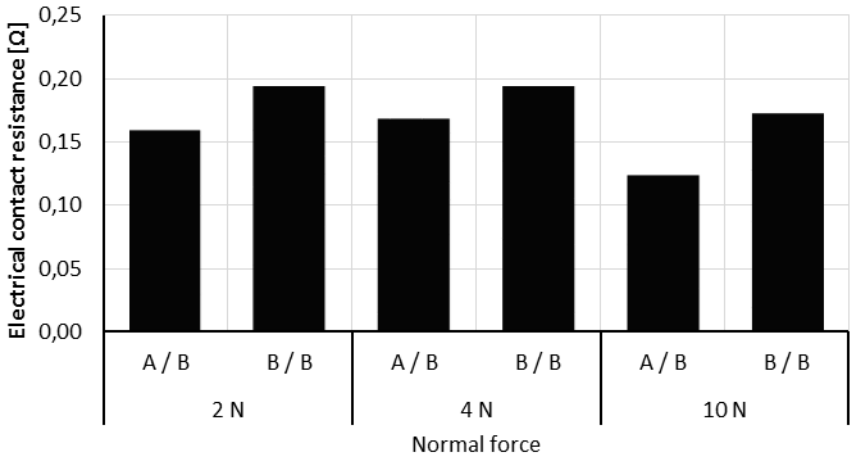

Figure 3. Electrical contact resistance for contact material combinations.

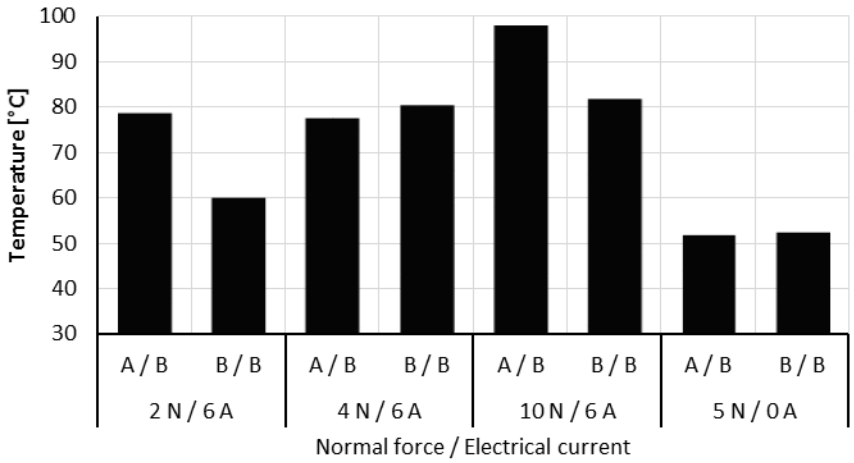

Figure 4. Bulk contact temperatures for contact material combinations.

In the second set of experiments, a shorter 5-hour test were performed to evaluate the effect of different material combinations on tribological and electrical parameters. Tests were performed at following constant parameters: 5 m/s sliding speed, 5 N

normal load and 2 A electrical current. In these tests three different contact materials were used: A, B and C. The measured contact voltage drop and the coefficient of friction during testing for two different material combinations is presented in Figure 5 and 6. It can be seen, that not only values for material combination B/C are higher than for A/B, but also variations of both parameters throughout the test are much higher. It can be seen in Figure 7 that the bulk material temperature is affected by the contact voltage drop and friction. Namely, higher voltage drop and higher friction in case of the B/C combination compared to the A/B combination most probably resulted in higher bulk temperatures shown in Figure 7.

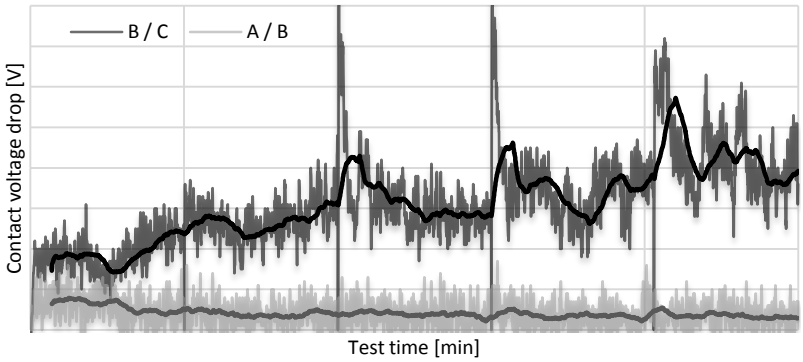

Figure 5. Contact voltage drop for two different material combinations.

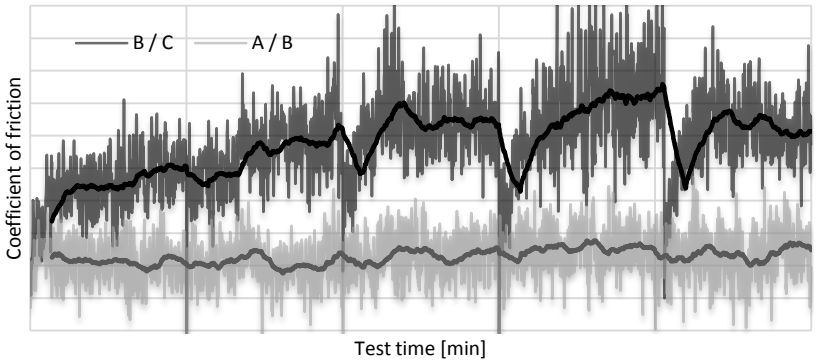

Figure 6. Coefficient of friction for two different material combinations.

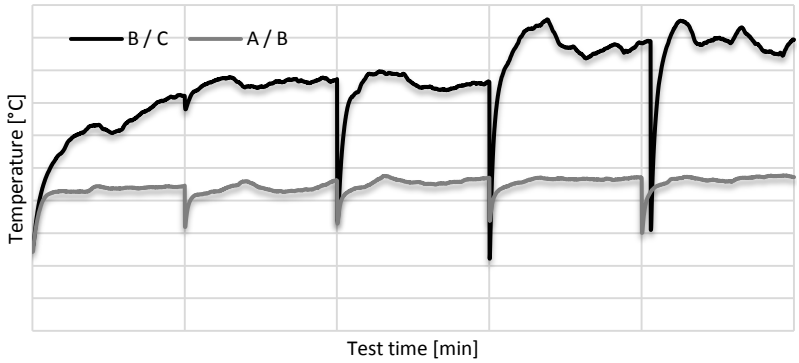

Figure 7. Bulk temperatures for two different material combinations.

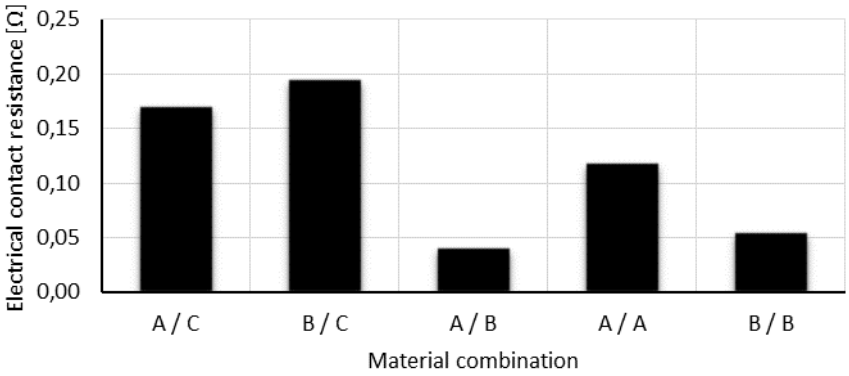

Figure 8. Electrical contact resistance for different material combinations.

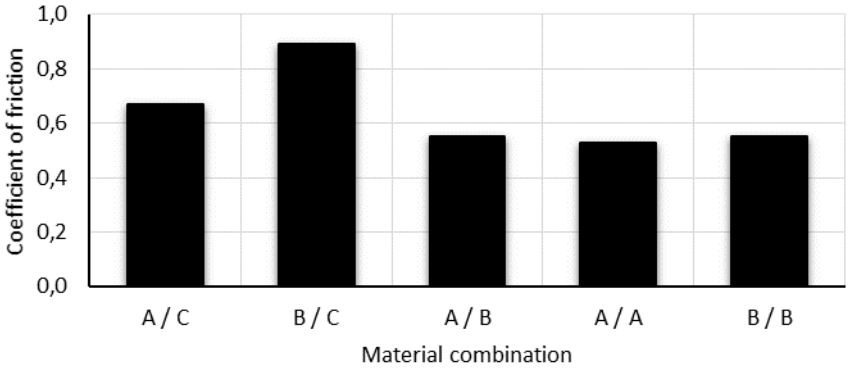

Figure 9. Coefficient of friction for different material combinations.

Considering all tested material combinations, those that include material C exhibit higher electrical contact resistance (Figure 8) and higher coefficient of friction (Figure 9). As mentioned before, temperature rise for those material combinations is consequently higher as well, as seen in Figure 10. Tests show that not only contact materials but also contact material combinations have a significant effect on the electrical and tribological properties of the electrical sliding contacts.

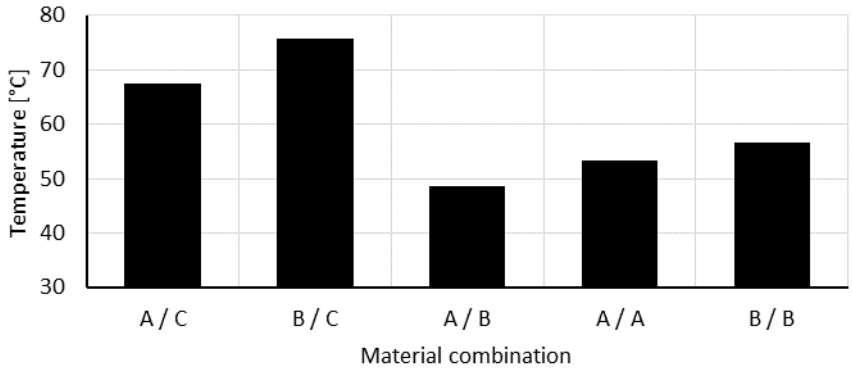

Figure 10. Bulk material temperatures for different material combinations.

4 Conclusions

A custom tribological testing rig was designed and manufactured to evaluate the effect of contact materials, electrical current and normal contact load on the contact material wear, contact resistance, friction and temperature. Two sets of experiments were performed: long-term and short-term. From the obtained results the following conclusions can be made:

1. Higher contact resistance and higher contact pressure increase temperature in the contact.
2. Contact surface polarity influences the contact material wear rate. At sufficient contact loads that enable no arching, the positively biased contact surface showed lower wear than the negatively biased one.
3. At insufficient loads arcing may appear, which can cause a severe increase in the wear rate. This was especially true for the material A, which obviously possesses low arcing wear resistance.
4. The presence of an electrical current in the sliding contact decreases the coefficient of friction.
5. The electrical and tribological properties of the electrical sliding contacts are crucially dependent on the contacting materials as well as on contact conditions.

5 Acknowledgement

This research was cofounded by Slovenian Research Agency under project number L2-5487.

6 References

[1] Shobert, E.I. (1954). Electrical Resistance of Carbon Brushes on Copper Rings. *Power Apparatus and Systems, Part III. Transactions of the American Institute of Electrical Engineers*, vol. 73, p. 788-799.

[2] Holm R. (1958). *Electric contacts handbook*. Springer Verlag, Berlin, p 14.

[3] Senouci, A., Frene, J., Zaidi, H. (1999). Wear mechanism in graphite–copper electrical sliding contact. *Wear*, vol. 225–229, p. 949–953.

[4] Takaoka, M., Aso, T., Sawa, K. (2001). A commutation performance and wear of carbon-fiber brush in gasoline. *Proceedings of the Forth-Seventh IEEE Holm Conference on Electrical Contacts*, p. 44-49.

[5] Takaoka, M., Sawa, K. (2000). An influence of commutation arc in gasoline on brush wear and commutator. *Proceedings of the Forty-Sixth IEEE Holm Conference on Electrical Contacts*, p. 211-215.

[6] Hu, Z.L., Chen, Z.H., Xia, J.T. (2008). Study on surface film in the wear of electrographite brushes against copper commutators for variable current and humidity. Wear, vol. 264, p. 11–17.

[7] Brady, G.S., Clauser, H.R., Vaccari, J.A. (2002). *Materials handbook 15-th ed*. McGraw-Hill Handbooks.

[8] Mitchell, B.S. (2004). *An introduction to materials engineering and science for chemical and materials engineers*. John Wiley & Sons, Inc., Hoboken, New Jersey.

[9] Argibay, N., Bares, J.A., Sawyer, W.G. (2010). Asymmetric wear behavior of self-mated copper fiber brush and slip-ring sliding electrical contacts in a humid carbon dioxide environment. *Wear*, vol. 268, p. 455–463.

[10] Argibay, N., Bares, J.A., Keith, J.H., Bourne, G.R., Sawyer, W.G. (2010). Copper–beryllium metal fiber brushes in high current density sliding electrical contacts. *Wear*, vol. 268, p. 1230–1236.

[11] Wang, Y.A., Li, J.X., Yan, Y., Qiao, L.J. (2012). Effect of surface film on sliding friction and wear of copper-impregnated metallized carbon against a Cu-Cr-Zr alloy. *Applied Surface Science*, vol. 258, p. 2362– 2367.

[12] Shobert, E.I. (1976). Carbon, Graphite, and contacts. *IEEE Transactions on Parts, Hybrids, and Packagine*, vol. 12, no. 1, p. 62-74.

[13] Lancaster, J.K., Pritchard, J.R. (1980). On the 'dusting' wear regime of graphite sliding against carbon. *Journal of Physics D: Applied Physics*, vol. 13, no. 8, p. 1551-1564.

[14] Chung, D.D.L. (2004). Electrical applications of carbon materials. *Journal of Materials Science*, vol. 39, p. 2645 – 2661.

[15] Lu, C.T., Bryant, M.D. (1994). Simulation of a carbon graphite brush with distributed metal particles. *IEEE transactions on components, packaging, and manufacturing technology*, Part A, vol. 17, no. 1, p. 68-77.

[16] Ben Jemaa, N., Morin, L., Jeannot, D., Hauner, F. (2000). Erosion and contact resistance performance of materials for sliding contacts under arcing. Electrical Contacts - 2000. *Proceedings of the Forty-Sixth IEEE Holm Conference on Electrical Contacts*, p. 73-78.

[17] Holzapfel, C., Heinbuch, P., Holl, S. (2010). Sliding electrical contacts: Wear and electrical performance of noble metal contacts. *Proceedings of the 56th IEEE Holm Conference on Electrical Contacts*, p. 978-985.

[18] Bares, J.A., Argibay, N., Mauntler, N., Dudder, G.J., Perry, S.S., Bourne, G.R., Sawyer, W.G. (2009). High current density copper-on-copper sliding electrical contacts at low sliding velocities. *Wear*, vol. 267, p. 417–424.

[19] Cho, K. H., Hong, U. S., Lee, K. S., Jang, H. (2007). Tribological Properties and Electrical Signal Transmission of Copper–Graphite Composites. *Tribology Letters*, vol. 27, no. 3, p. 301–306.

[20] Holzapfel, C. (2008). Nanoindentation studies of contact materials used for sliding electrical contacts. *Proceedings of the Annual Holm Conference on Electrical Contacts*, p 90-97.

[21] Talmage, G., Mazumder, S., Brown, S.H., Sondergaard, N.A. (1995) Viscous and Joulean power losses in liquid-metal sliding electrical contacts with finite electrically conducting electrodes. *IEEE Transactions on Energy Conversion*, vol. 10, no. 4, p. 634-644.

[22] Makel, D.D., Kuhlmann-Wilsdorf, D. (1992). Improved sliding electrical brush performance through the use of water lubrication. *Proceedings of the Thirty-Eighth IEEE Holm Conference on Electrical Contacts*, p. 149-155.

[23] Argibay, N., Sawyer, W.G. (2012). Low wear metal sliding electrical contacts at high current density. *Wear*, vol. 274–275, p. 229– 237.

[24] Bares, J.A., Argibay, N., Dickrell, P.L., Bourne, G.R., Burris, D.L., Ziegert, J.C., Sawyer, W.G. (2009). In situ graphite lubrication of metallic sliding electrical contacts. *Wear*, vol. 267, p. 1462–1469.

[25] Shin, W.G., Lee, S.H. (2010). An analysis of the main factors on the wear of brushes for automotive small brush-type DC motor. *Journal of Mechanical Science and Technology*, vol. 24, p. 37-41.

[26] El Mansori, M., Paulmier, D., Ginsztler, J., Horvath, M. (1999). Lubrication mechanisms of a sliding contact by simultaneous action of electric current and magnetic field. *Wear*, vol. 225–229, p. 1011–1016.

Gradient Implants and Solid-State Drug Delivery Systems

Alexandra Aulova [a*], Crispulo Gallegos [b], Igor Emri [a]

[(a)] University of Ljubljana, Faculty of Mechanical Engineering, Aškerčeva 6, 1000 Ljubljana, Slovenia.

[(b)] Fresenius Kabi AG, Else-Kröner-Straße 1, 61352 Bad Homburg, Germany

* Corresponding author:
E-mail: alexandra.aulova@fs.uni-lj-si

Abstract

From previous experience, we know that PA6 materials with different initial kinetics (i.e., different molecular weight distributions) exhibit extremely nonlinear behavior [1]. By exposing them to properly selected temperature-pressure history during solidification and cooling below T_g, we can vary their percentage of crystallinity, size of crystals and amount of free volume present in bimodal PA6 [2,3]. Moreover, at proper temperature-pressure conditions during solidification these materials will form gradient structure with mechanical properties different throughout the length of the specimen.

Based on these findings and utilizing also osseointegrative, absorptive and biodegradable properties of PA6 we have introduced gradient implants and solid-state drug delivery system concept. The main advantage of these products is their extreme osseointegrativity, which means that once installed into a bone they will be "consumed" by the body (bone will grow through the specimen) within a certain time, and will not require surgery for removal. Possibility to vary gradient properties mimics real bone structure, while free volume in the material allows storing drug substances that will be released into the body through desorption and osseintegration processes. Osseointegration rate will depend on the structure of the polymer drug-delivery container or implant as well and can be influenced by changes in temperature-pressure conditions during solidification of the end product.

Investigation of mechanical properties of sample implants was conducted via speckle interferometry, while absorptive properties were checked via submerging PA6 samples to distilled water and saturated solutions of salt and sugar. Liquid absorption was measured gravimetrically and presence of ions of sodium and chloride was detected via EDS (Energy-dispersive X-ray spectroscopy, while glucose molecules were identified by means of NMR (nuclear magnetic resonance) technique.

Biological compatibility and osseointergrativity were confirmed by tests *in vivo.*

1 Introduction

Biocompatibility, osseointegrativity and gradient structure are very important properties for bone implants, because biocompatible implants are not rejected by body as foreign materials. Osseointegrative implants are consumed by the body and do not require surgery for their removal, while gradient structure of the implant maximally mimics structure of our bones which are softer in the core. Possibility to store medical substances inside make such an implant an ultimate solution for the solid-state drug delivery systems, that can be used for treating bone diseases, for example osteosarcoma.

It is known that intravenous injections of radioactive iodine (I-131) reduce or even reverse the apparent growth of tumors in bones[4] in case of osteosarcoma. However, healthy tissues might be damaged and injection might be useless, especially if the affected area is not accessible for bloodstreams. As an ultimate solution we propose solid-state drug delivery system, carriers of which will be placed into the hard tissues/bones and will provide appropriate treatment for the areas that are hard to access for conventional intravenous medicaments. Multimodal polyamide 6 is proposed as a drug carrier material due to its outstanding osseointegrative and biocompatible properties.

The developed solid drug delivery system due to its localized application and osseointegrative properties will tremendously improve treatment of bone cancer. Gradient mechanical properties of the proposed system might be utilized as orthopedic and dental implants.

2 Theoretical background

Polyamide 6 (PA6), also known as Nylon is widely used in variety of applications including automotive, textile, medicine and engineering solutions. Great mechanical properties, resistivity to abrasion and chemicals are the main properties of PA6. In addition, modification of its molecular composition proved to result in highly non-linear behavior of this material. Particularly changes of molecular weight distribution [1] and well-defined temperature-pressure conditions resulted in formation of gradient structure of PA6.

Figure 1 demonstrates molecular weight distribution of monomodal and bimodal PA6 and images of their crystalline structure obtained via optical microscopy[3]. Structures of the two materials are vividly different and consequently they exhibit orders of magnitude different time-dependent properties. This is demonstrated in Figure 2, which shows comparison of the shear creep compliance of a monomodal and a bimodal PA6. The diagram speaks by itself – the relaxation process of the bimodal PA6 is in initial stage close to 100 times slower than that of monomodal material.

This non-linear behavior may be explained by the **“free-volume” theory**. Free volume is an inherent intermolecular empty space formed in a material structure during cooling below the glass transition temperature. Free volume formation is determined by

temperature-pressure conditions during transition of material from molten to solid state, and further on below the glass transition. The first transition determines the amount of crystalline phase whereas the second transition the size of the free volume in the remaining amorphous phase. Cooling rate directly affects the free volume: the faster the cooling is (higher cooling rate) the larger the free volume is[5].

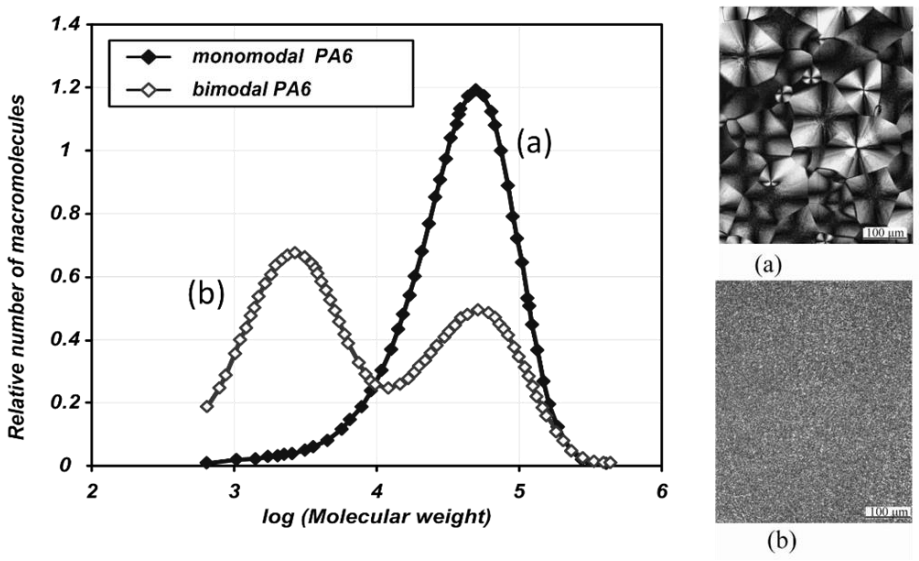

Figure 1. On the left: Molecular weight distribution of monomodal and bimodal PA; on the right: (a) Morphology of monomodal PA6, and (b) bimodal I-PA6; Axioskop 2 MAT (Carl Zeiss), polarized transmitted light, 200x

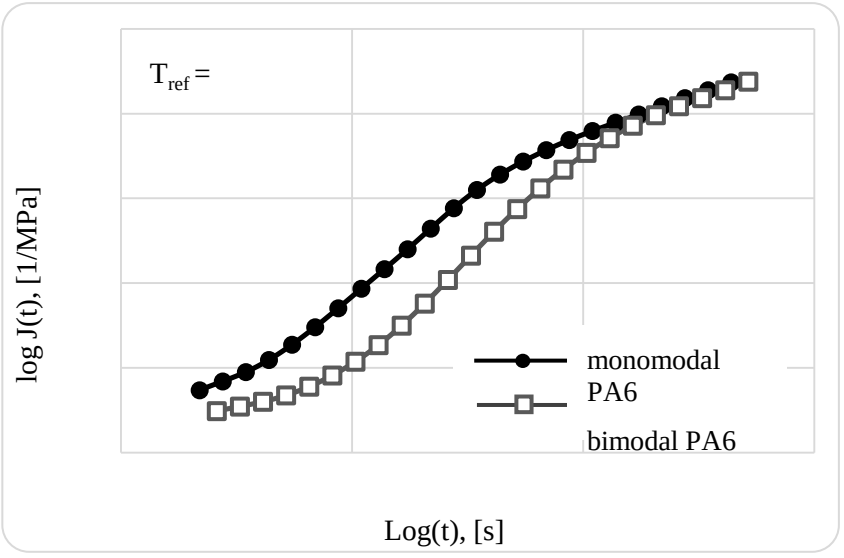

Figure 2. Comparison of the shear creep compliance of a monomodal PA6 and a bimodal PA6.

An increase of temperature will increase Brownian motion of molecules and consequently the amount (size) of free volume, which further increases molecular mobility when material is exposed to an external load. Hence, the larger free volume is (or the higher the temperature is) the faster molecules move and rearrange when loaded with an external load. Applied pressure reduces amount of free volume and, therefore reduces mobility of molecules. This means that increasing the temperature will speed up all processes in the material including its reaction to external loads, while increasing pressure will slow down these processes. Macroscopic properties are directly dependent on molecular mobility of the material and, consequently on the amount of free volume present in the observed material.

Absorption properties of a material will be also determined by the amount of free volume in it, since it is the only available space to store molecules of water and other substances.

Figure 3 represents changes of volume of a polymeric material with temperature at two constant pressures $p_1 < p_2$. According to the principle described above, with an increase of pressure all inherent processes slow down, this is why the graph corresponding to p_2 is moved to the right.

For semicrystalline polymers, such as PA6 there are two transitions during cooling from the liquid state. The first one, solidification, is characterized by melting temperatures $T_{m1}(p_1)$ and $T_{m2}(p_2)$. During this transition temperature of the material does not change, while its volume reduces. The second transition appears at temperatures $T_{g1}(p_1)$ and $T_{g2}(p_2)$, commonly called "glass-transition temperature", where material properties change from rubber-like to brittle-like behavior.

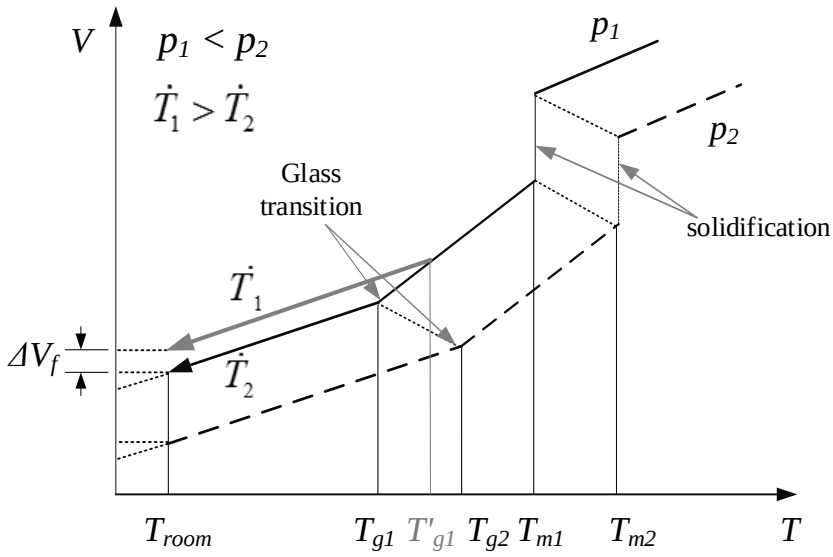

Figure 3. PVT diagram demonstrating free volume control principle

This transition is a second order transition, which means that it is rate-dependent. Hence, when polymeric material is cooled below T_g infinitely slow all molecules will have sufficient time to find their optimal topological arrangements, meaning that material will reach its state of thermodynamic equilibrium in which molecules occupy minimal volume at a given temperature. Whereas, if polymer is cooled fast, molecules will not have enough time to reach their optimal arrangements and consequently there will be some "frozen-in" free volume in the material. Hence, the faster we cool the material the larger will be the "frozen-in" free volume, as it is demonstrated in Figure 3 by ΔV_f.

These theoretical observations allowed us to develop methodology of production of implants with gradient structure, which were characterized in respect to their mechanical, biocompatibility and absorptive properties. The results are shown in continuation.

3 Mechanical properties of implants with gradient structure

Implants were tested in uniaxial compression, using speckle interferometry to measure local deformations along the axial direction. Speckle interferometry or electronic speckle pattern interferometry is a technique that uses laser light, together with video detection, recording and processing to visualize static and dynamic displacements of components with optically rough surfaces. Deformation measurements of object surfaces is possible with sensitivity below fractions of the wavelength of light. The idea is to superimpose original laser beam and the one reflected by the surface of the tested sample. Their interference creates speckle pattern on a video camera, which is analyzed before and after deformation.

Speckle interferometry was used to determine strain-stress relations at three different locations on a sample implant exposed to uniaxial compressive load. The results are shown in Figure 4.

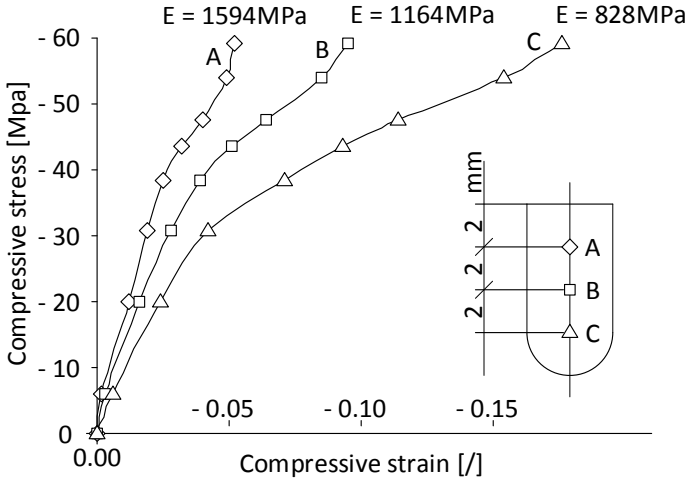

Figure 4. Local stress-strain properties of an implant with gradient structure

Results presented in Figure 4 reveal gradient structure of the implant. The modulus of the tested sample measured at three different locations separated merely for 4 mm differs more than 2 times, and the corresponding deformation almost 4 times!

4 Biocompatibility of implants with gradient structure

Biocompatibility and osseointegrativity of samples were tested in vivo on pigs. Samples were placed in front leg bone of pigs and investigated after certain time period (Figure 5). Histological investigation showed that bone grew into the implants, which proves that they are fully biocompatible and can be consumed by the body.

Figure 5. Result of biocompatibility tests performed in-vivo in pig bones

5 Absorption properties of implants

The underlying process of absorption is diffusion. It may be governed by mechanical interaction of particles with surface and, consequently by size of the particles, and/or by interaction of electromagnetic forces and, consequently by polarity of the particles.

In order to check absorptive properties of PA6 implants and their ability to store molecules of different size and polarity, the absorption tests were performed. Since it is well known that PA6 absorbs water molecules, it was decided to test distilled water solutions of different substances with different particle size and polarity. Distilled water was taken as reference. Solutions of glucose with neutral large molecules and salt with small ions of calcium and chloride were prepared. Solution concentration was chosen in way to prevent floating of samples.

Several of gravimetrically casted cylindrical PA6 samples with diameter 4mm and length approximately 8mm were submerged into the solutions with characteristics presented in Table 1 and the rest of them were left dry as reference.

Table 1. Basic information on media/solutions used for investigation of PA6 absorption properties

Substance	Distilled water	Sodium chloride		Glucose
Molecular formula	H_2O	NaCl		$C_6H_{12}O_6$
Molar mass, g/mol	18	58.44		180.16
Size of particle	278 pm	Na^+ R=97 pm	Cl^- R=181 pm	700 pm
Molar mass of particle, g/mol	18	23	35.5	180.16
Solution concentration	-	18.4%wt		30%wt
Solution density, g/ml	1	1.14		1.13

Measurements were performed at room temperature that was kept in range of 25±5 °C (measurements were performed during summer period). Samples were submerged in the substances for 33 days.

Absorption process was observed gravimetrically: specimens were taken out of solution, dried with a tissue and weighted. During the first day of measurements weighting of the samples was performed every two hours. Starting from the second day number of measurements per day was reduced to 3 times and in a week to 2 times per day.

Figure 6 shows relative mass changes of samples immersed into three different solutions in respect to their initial mass. It is visible that specimens in all solutions did not reached saturation during measurements period. As expected, the highest mass gain obtained implants immersed in distilled water, followed by specimens in sugar and in salt solutions.

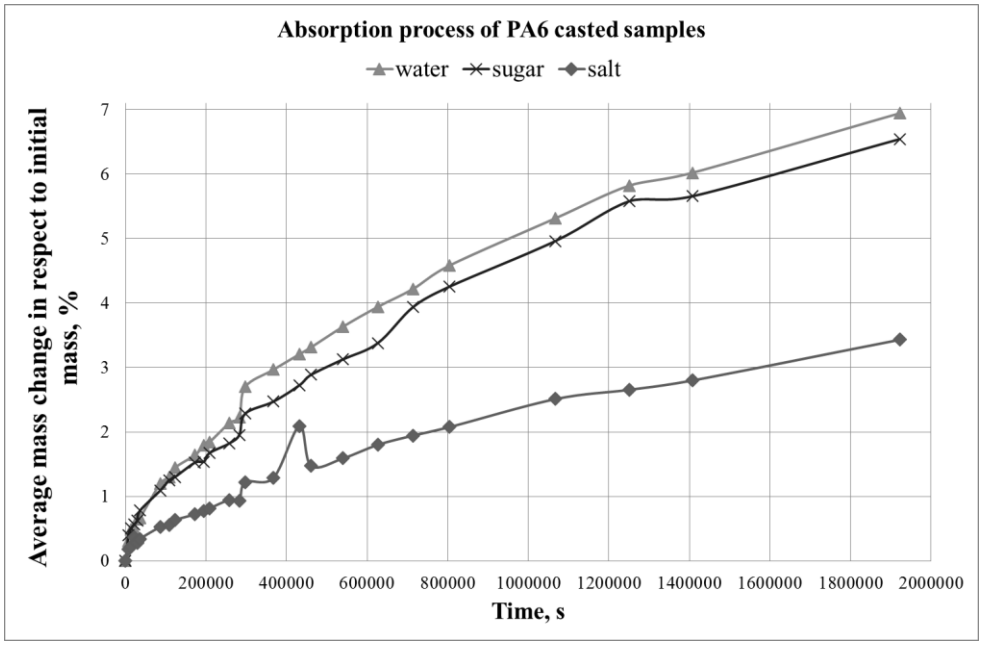

Figure 6. Change of mass of PA6 during absorption process

In order to determine presence of the absorbed ions of chloride and sodium in PA6 samples energy dispersive X-ray analysis, also known as EDS, EDX or EDAX was used. Unfortunately, this technique is not appropriate for determination of presence of glucose molecules in polymers since it consists of the same molecules of C, H and O, which are light elements and cannot be quantitatively defined. Therefore, Proton Nuclear Magnetic Resonance analysis (NMR) was used in order to determine if glucose molecules penetrated into PA6.

The following samples were tested via EDS: dry PA6, submerged in distilled water and PA6 submerged in salt solution.

For the samples of dry PA6 and PA6 submerged to distilled water, presence of Na and Cl ions was not detected, while for the sample that was kept in water solution of NaCl the peaks appeared for Na and Cl ions (Figure 7a). Based on the "mapping analysis" it is evident that Na and Cl are homogeneously dispersed within PA6 (Figure 7b). However, it is necessary to mention the fact that EDS does not provide analysis of depth, X-rays reach the depth of only few millimeters.

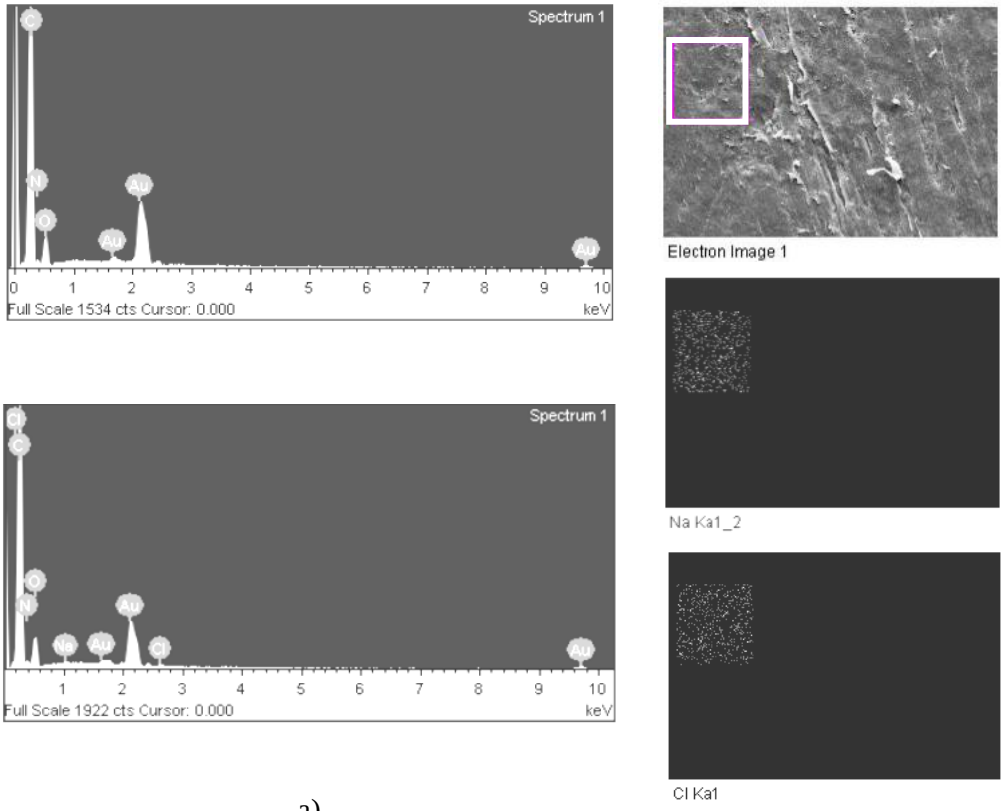

Figure 7. Results of EDS (a), SEM images (b) of sample surface subjected to NaCl solution – particles are evenly spread

The Proton NMR measurements were performed at room temperature at Larmor frequency of ν_L = 500 MHz on Bruker Avance 500 MHz NMR Spectrometer. Typical $\pi/2$ pulse width was 6 μs. The spectra were measured by free-induction decay, spin-lattice relaxation times by inversion-recovery technique, and spin–spin relaxation time by the Hahn-echo technique. The Larmor frequency of the protons within the sample is affected by their local surrounding. Hence, from the NMR (frequency distribution) spectrum one may be able to distinguish the signals from protons in different local environments.

The following samples were tested via NMR: dry PA6, submerged in distilled water and PA6 submerged in sugar solution.

Proton signal of dry sample (dry PA6) was significantly weaker in comparison to the other two types of samples immersed in H_2O and sugar-water solution. This clearly shows presence of H_2O in the samples PA6 that were submerged into the water and sugar-water solution. Besides this, the difference in the signals of the latter two confirms that the sample (PA6 in sugar-water solution) did not absorbed only water but also sugar, which gave different 1H NMR response. However, since the molecules of

sugar in the PA6 influence also the 1H NMR response of the PA6 itself, the accurate estimation of how much of this signal belongs to PA6, how much to H_2O, and how much to sugar, was disabled. Results are shown in Figure 8.

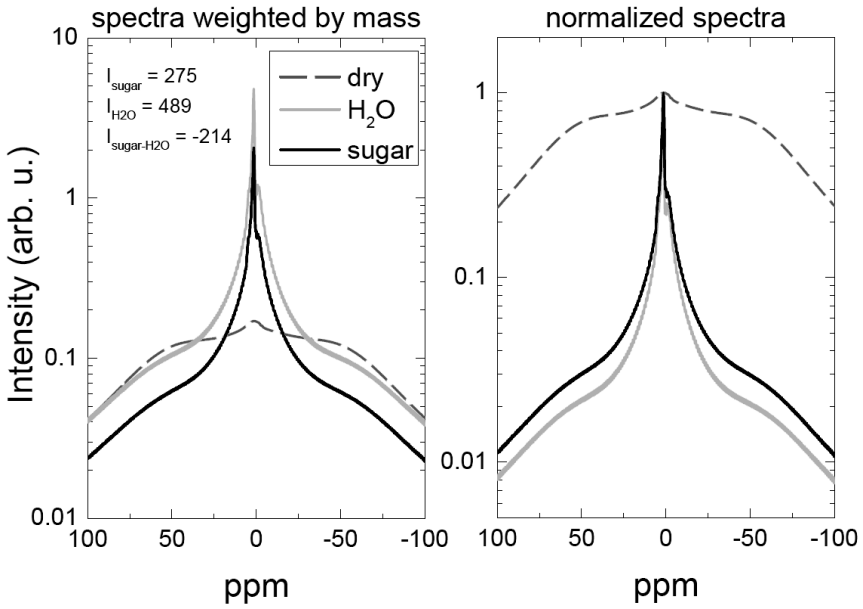

Figure 8. Results of NMR test

6 Conclusions

Presented methodology for manufacturing osseintegrative, biocompatible PA6 implants with gradient structure based on varying temperature-pressure history during manufacturing indicates to be appropriate for medical applications such as drug delivery in treatment of bone diseases.

It was shown that developed technology allows production of implants that mimic gradient structure of bones.

Preliminary biocompatibility and osseointegrativity tests showed that multimodal PA6 with gradient structure could be successfully used for solid state drug delivery containers, as well as for orthopedic and dental implants.

Preliminary tests on absorptive properties and abilities to store ions of sodium, chloride and molecules of glucose were positive, showing potential for delivery of different medicaments with different size of molecules.

In conclusion, investigation of possibilities to vary free volume in order to store substances proved that nano-structured PA6 implants with gradient structure offer an option and opportunity for Fresenius Kabi corporation to develop the new approach in treatment of bone cancer.

7 Acknowledgement

Authors would like to thank Barbara Zupančič and Joamin Gonzalez-Gutierrez as well as team of Jožef Stefan Institute that greatly helped with EDS and NMR measurements. Special thank you to professor Michael Sutton from the University of South Carolina for assistance in speckle interferometry tests.

8 References

[1] Emri, I., Bernstorff, B.S. von (2006). The effect of molecular mass distribution on time-dependent behavior of polyamides. *Journal of Applied Mechanics*, vol. 73, no. 5, p. 752-757.

[2] Emri, I., Bernstorff, B.S. von (2002). In: Rauschenberger and H. Horn, *Multimodale Polymermischungen: Patentanmeldung*. USA Patent PCT. O.Z.: 0050/052586/CI.

[3] Kubyshkina, G., Zupančič, B., Štukelj, M., Grošelj, D., Marion, L., Emri, I. (2011). The influence of different sterilization techniques on the time-dependent behavior of polyamides. *Journal of biomaterials and nanobiotechnology*, vol. 2, no. 4, p. 361-368.

[4] Schlumberger, M. (1994). Radioactive iodine treatment and external radiotherapy for lung and bone metastases from thyroid carcinoma. *Journal of Nuclear Medicicne*, vol. 37, no. 4, p. 598-605.

[5] Tschoegel, N., Knauss, W., Emri, I. (2002). The Effect of Temperature and Pressure on the Mechanical Properties of Thermo- and/or Piezorheologically Simple Polmeric Materials in Thermodynamic Equilibrium - A Critical Review. *Mechanics of Time-Dependent Materials*, vol. 6, no.1, p. 53-99.

Laser supported implantology

Georgije Bosiger [a*], Tadej Perhavec [a], Marko Marinček [a], Janez Diaci [b]

(a) Fotona d.d., Stegne 7, 1000 Ljubljana, Slovenia.

(b) University of Ljubljana, Faculty of Mechanical Engineering, Aškerčeva 6, 1000 Ljubljana, Slovenia.

* Corresponding author:
E-mail: georgije.bosiger@fotona.com

Abstract

This paper presents a feasibility study of implant bed preparation using adaptive guided laser beam, consisting of an Er:YAG laser, a laser scanner and detection system for monitoring the depth and shape of the bed during preparation. The key emphasis is placed on the development of new reliable and accurate optodynamic methods for monitoring laser treatment based on piezoelectric detection of shock waves that propagate in the air above the tissue during the laser ablation process. Characteristics of the shock waves are analyzed, and the suitability of Sedov-Taylor point explosion model is confirmed. A model that provides a theoretical description of the measured signals and a new optodynamic method for accurate and reliable source localization were developed. Functional prototype of adaptive laser medical system is made, which simulates practical conditions. First *in vitro* studies show that bed preparation could be achieved with sufficient precision and reliability.

1 Introduction

Er:YAG laser is a well-established tool for tissue removal in the field of dentistry where various treatments benefit from the advantages of ablative Er:YAG laser tissue interaction over the conventional methods. Key advantages are: smaller heat-affected zone, absence of mechanical vibrations and noncontact intervention. To this day, numerous medical treatments have been developed to benefit from these advantages that lead to faster recovery and reduced pain. Clinical and feasibility studies have been conducted to show that implant bed preparation using Er:YAG laser has the potential for use in practice.

On one side, clinical studies on animals show that oseointegration, characterized by bone to implant contact (BIC), is in the case of Er:YAG laser implant bed preparation at least comparable [1-3] or even significantly better [4, 5] compared to the conventional method using mechanical drills. Histological analysis [2, 6], measurements of implant stability quotient (ISQ) [1] and removal torque [3] support

these conclusions. Oseointegration is also faster in case of Er:YAG laser, which leads to faster increase in implant stability and treatment recovery [4].

Numerous feasibility studies were performed in order to solve technical and scientific challenges that need to be solved for practicable laser implant bed preparation. Studies in this research area show that modern techniques of treatment planning, using 3D computer tomography and stereolitographic surgical guides, can ensure proper bed preparation in terms of deviations in the position and inclination between the planned and prepared implant beds [7]. Efforts were made to ensure proper shape and depth of the implant bed using laser, however viable and reliable solutions are still not available. As it turned out [5, 7], proper shape can not be obtained by hand guided laser hand-piece, despite the tracking systems that control laser output energy during the preparation [8]. In terms of implant depth control, usage of simplified theoretical models, that predict the depth [9], and laser focus navigation to stop the treatment with occurrence of nonablative interaction beyond the laser focus [10], were first proposed. Further work in this direction has not been made, likely to the fact that Er:YAG laser ablation is a complex mechanism, as ablation efficiency depends on numerous factors [11, 12], and the fact that nonablative interaction of the laser can cause unwanted heating that could lead to tissue carbonization with negative effects on the healing times [2]. Methods of laser ablation monitoring that would enable on-line implant bed depth measurement were also proposed, for example using laser triangulation [13] or optical tomography [14], but to this day no practicable solution was found.

To our view, an adaptive medical laser system with scanning Er:YAG laser and piezoelectric detection of optodynamic (OD) phenomena is a promising solution that could enable laser implant bed preparation in practice. Figure 1 demonstrates our idea: hand-piece is upgraded with a laser scanner that allows precise and computer controlled bed preparation in XY plane, one or more broadband piezoelectric sensors are mounted on the laser handpiece to detect shock waves that propagate in the air above the tissue and allow depth control in Z axis. Considering typical conditions (geometry of the handpiece and sensor, focal length of the focusing optics, laser pulse energy, etc.) it is reasonable to assume that the shock waveform is nearly hemispherical as it impinges onto the sensor and its amplitude has decreased to the intermediate to weak-shock level.

2 Optodynamic monitoring of Er:YAG laser ablation of biological tissue

The most challenging task for implant bed preparation using laser is to prevent the laser to make hole deeper than needed, because in the mandible or maxilla, where implant bed is usually prepared, there are very sensitive soft tissues, i.e. nerve and blood vessels [15], underlying more compact hard bone structure, which should not be damaged by laser ablation. Because of that fact and because of the fact that the compact bone structure is not homogeneous, the laser ablation process has to be monitored all the time during bed preparation.

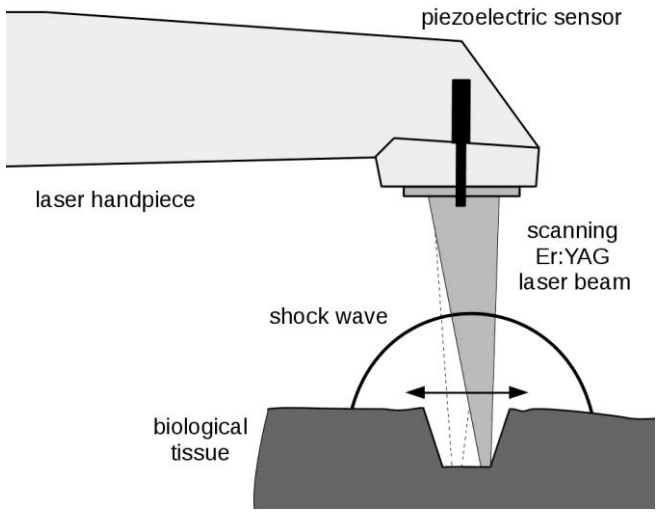

Figure 1: Schematic representation of the idea: laser handpiece supports scanning Er:YAG laser and piezoelectric detection forming the proposed adaptive laser system for implant bed preparation.

Several methods and sensors have been used to monitor laser ablation process outcome, i.e. confocal microscopy [16], laser triangulation method [13, 17, 18], optical coherence tomography (OCT) [14], and others. These methods have two main disadvantages: first, the devices are composed of relatively large and/or expensive components, in most cases not being able of using them for *in vivo* medical treatments, and second, most of them need complex computer processing, that makes these methods very time consuming.

During pulsed Er:YAG laser irradiation of biological tissue shock waves are generated, originating at the laser-tissue interaction point, and expanding into surrounding air and tissue. Detection of shock waves in air has two main advantages over detection of shock waves in tissue, first, the air in contrast to tissue does not have to be prepared for sensor fixation (i.e. removing soft tissue that overlays the bone and provide a reliable contact with sensor [19]), and second, the air is homogeneous medium in respect to tissue, and the shock wave is expanding more smoothly and predictably, and the propagation can be well approximated using theoretical model.

Several OD sensors and methods have been used for monitoring shock waves [20]. Microphone [21], for example, can detect acoustic frequencies up to few 100 kHz, but cuts off shock discontinuities, that are important for shock wave interpretation. Laser deflection probe is also used [22], which has wide frequency bandwidth [23] limited only by the electrical components used in the set-up.

In order to study shock waves with spatial resolution a shadowgraph or schlieren method can be used. For this work, an improved double-exposure shadowgraph method was developed, which allows visualization of an expanding shock wave in two time instances on a single image [24]. The method has been developed to study shock waves generated in air during interaction of Er:YAG laser light with water and biological tissues. The shock wave is illuminated by pulsed green laser light coupled into two optical fibers of different lengths to establish two illumination flashes separated by a fixed time delay. An image of the shock wave region, acquired by a digital still camera, exhibits two distinct shock wavefronts. In Figure 2 there are sample images of shock waves propagating in air during Er:YAG laser ablation of water surface at different time delays between ablation and illumination laser pulse.

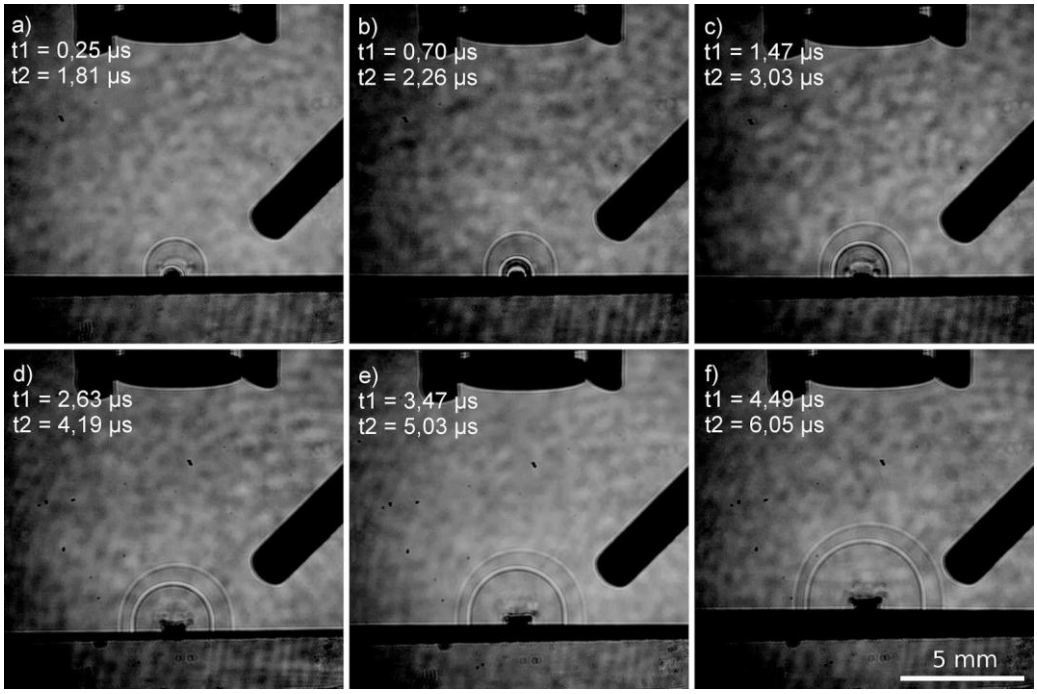

Figure 2: Illustration of ablative shock wave evolution: images of 6 expanding shock waves in air above the water surface. Time delays of the two illumination laser pulses are indicated in each image. Black shadows on the upper and on the right hand side represent handpiece ending, from which the laser beam propagates perpendicularly to the water surface, and used piezoelectric sensor, respectively.

The obtained results have demonstrated that the propagation of shock waves can be approximated using Sedov-Taylor point explosion model [24]. By fitting the wavefront locations from acquired shadowgraph images onto the space-time function from point explosion model, called trajectory, it has been shown that shock waves are located in strong and intermediate shock region only few millimeters above water surface.

Afterwards, quasi-hemispherical and weak shock waves arise, which simplify their detection and theoretical treatment.

While most of described OD techniques represent useful research tool within controlled laboratory experiments, only a few of them exhibit the potential to be used for the on-line process monitoring in practice. Here additional factors come into prominence with environmental influences in particular. Existing OD methods of shock wave characterization mostly rely on empirically selected signal features where their relationships to other influencing factors (sensor characteristics, its orientation and distance from the source, released shock energy, etc.) are not known, thus limiting the applicability of these methods to the strictly controlled conditions.

If appropriate theoretical models are used, OD characterization of laser ablation with independent process characterization is possible [25]. In previous research on this subject, using Sedov-Taylor point explosion model, Diaci and Možina estimated shock energy from shock time of flight and positive pressure phase [22]. The latter proposed characteristic gave better results as it has greater sensitivity to released shock energy and only slight sensitivity to the distance from the source [23].

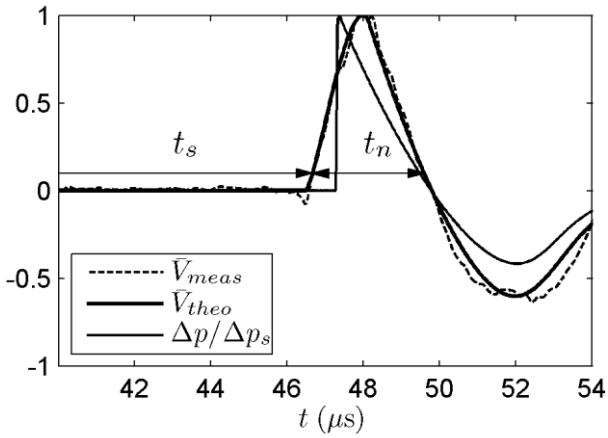

Figure 3: Measured signal, theoretical signal and pressure waveform. Two selected signal characteristics t_s and t_n defined on 10% of the normalized amplitude are also indicated.

We use similar approach to the problem of OD source localization (estimation of distance between the OD source on the ablated surface and sensor above it) using piezoelectric detection. To our view, a small piezoelectric sensor could be incorporated in a small tool, such as dental handpiece, and is capable of detecting pressure fluctuations in air in ultrasound region typical for shock waves [26]. First experiments using this sensor in quasi-ideal half-space, formed by water surface which serves as a tissue phantom, have shown that measured signals waveforms do not correspond to the

pressure waveforms using the point explosion model (Figure 3). This indicates that the employed piezoelectric sensor (CA-1135, Dynasen inc.) can not be treated as an ideal point sensor.

A new model piezoelectric sensor has been developed that takes into account finite aperture as well as the electric and mechanical characteristics [27]. We treat the sensor as a one-dimensional element where current generating (pure elastic) deformations occur only in its axial direction. A transfer function for a force sensing element is obtained and validated on an impedance analyzer. Neglecting the effects of changed acoustic impedance (weak incident shocks), assumption that measured voltage for the given resistive load of the recording device is proportional to the force of axial excitation and finally with employing linear spherical wave propagation theory, during the propagation of the shock over the sensor aperture, a finite sensor size is taken into account where a theoretical signal waveform can be conveniently found with the convolution of the pressure waveform at a point in the center of the aperture (given by the point explosion model) and impulse response of the sensor surface [27].

The model allows us to tackle the problem of on-line monitoring of implant bed preparation by OD source localization [28]. The employed method of OD source localization employs shock trajectory, which is a function of released shock energy and distance from the source. Theoretical analysis of OD signals leads to determination of two functions that describe the dependence of the characteristics t_s and t_n as functions of estimated distance h_0 and released shock energy E_h (Figure 3). These functions then enable simultaneous estimation of distance h_0, with approx. absolute errors around 1% at heights between 10 and 20 mm, and independent estimation of shock energy E_h, which can also be a valuable process characteristic.

3 Results of *in vitro* experiments

Our experimental set-ups, briefly described in previous section, enable detailed study of OD phenomena within controlled conditions which lead to development of appropriate theoretical models and OD methods for laser ablation monitoring. In order to test novel approach to the laser supported implantology, it is reasonable to carry out feasibility studies on a system that simulates real conditions as much as possible. For this purpose, a prototype of adaptive laser system was developed.

The developed prototype set-up is shown on Figure 4. A laser scanner, developed by Fotona d.d., is mounted on an existing Er:YAG medical device (Lightwalker AT, Fotona d.d.). An appropriate laser handpiece has also been developed. Three piezoelectric sensors that enable OD monitoring are attached to the handpiece. Similar to the experimental system from previous section, OD signals are digitized using oscilloscope and sent to a PC where they are saved and processed. Laser output is also controlled from the same PC as well as set of laser positions for the laser scanner. It should be noted that this system is acceptable only for the execution of *in vitro* studies

where requirements for biocompatibility of used materials and other practical and safety aspects can be neglected.

Nonetheless, the prototype is designed and constructed for the execution of the target application in mind. It enables preparation of implant beds with max. 6 mm in diameter whereas smallest diameter equals to a spot size of 0.9 mm. At the end of the handpiece, a water spray enables cooling of the tissue during the ablation and thus prevents tissue carbonization. Water spray also cleans the handpiece output window and sensor surfaces from ejected material during ablation.

While *in vitro* experiments are performed, handpiece of adaptive laser system is attached to the holder. Treated bone is placed on appropriate (working) distance of 12 mm from the output window. Red laser diode scans the contour of the implant bed onto the tissue before the ablation with Er:YAG laser is started so that it facilitates positioning of the bone. Different diameters and depths of the implant beds can be prepared *in vitro* using this set-up (Figure 4).

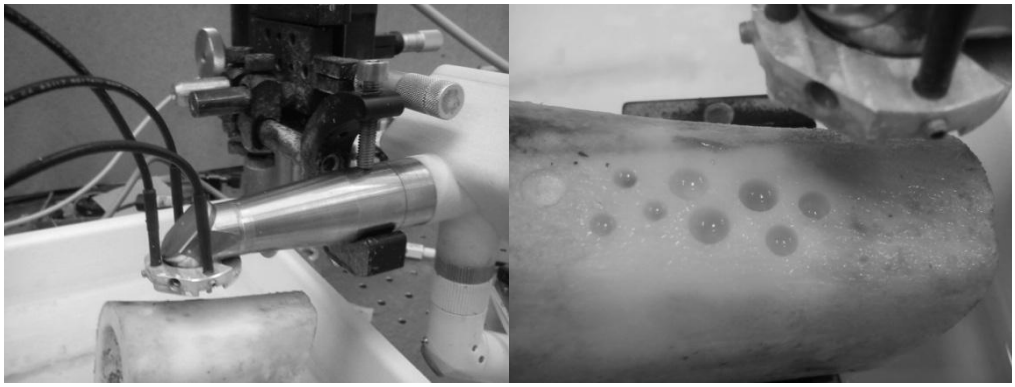

Figure 4: Experimental set-up for *in vitro* studies using a functional prototype of adaptive laser medical system, that allows Er:YAG laser scanning and simultaneous OD monitoring of implant bed preparation.

Preliminary *in vitro* experiments are intended to answer two key questions. First question refers to the accuracy of the proposed detection system. In this scope, experiments are conducted in order to test and adapt developed methods for OD monitoring in terms of accuracy. Second question relates to the feasibility and reliability of the proposed adaptive laser system. In this case experiments are conducted to test if implant bed shape can be reconstructed during the preparation despite disturbances that can occur in practice (presence of water spray, accumulation of the ejected material on sensor surfaces, etc.). Detailed description about this work is presented elsewhere [29], whereas here only short summary is provided.

For the purpose of accuracy, holes of 4 mm in diameter and depths of 5, 10 and 15 mm are drilled in a bovine bone using mechanical drills. Each hole is then placed under the scanning Er:YAG laser with the OD measurement set-up integrated into the handpiece. Energy output is set just to such extent (3.14 mJ) that tissue ablation occurrs, so that necessary shock waves are generated, but the tissue surface modifications still remain negligible, thereby multiple independent experimental repetitions on the prepared bone are executable.

In order to compare measured and drilled hole depths, the half-space OD method described in section 2 is extended to the case of cylindrical holes. In this case the following assumptions are accepted: trajectory of the shock front, that generates electric charge on the sensor, corresponds to the shortest path from interaction point, inside the measured hole, to the center of the sensor above the tissue, effect of confined space on shock velocity is neglected; and mean released energy of the interaction points inside the measured hole corresponds to the mean released energy of the interaction points surrounding the measured hole.

Using this method, mean absolute values of relative errors between measured and drilled hole depths for six repetitions equal to 5 %, 3 % and 1 % for heights 5, 10 and 15 mm, respectively. Although this OD method is highly simplified, estimated errors exceed expectations. However, further testing shows that these errors do increase in case of holes with smaller diameters. Based on previous experiments, we attribute this observation to the effect of confined space, formed by hole walls [26].

To check whether OD monitoring with piezoelectric detection also exhibits the potential practical value during the execution of target application, we apply the method to monitor the shape of the implant bed during the preparation with a scanning Er:YAG laser.

We use two different modes of laser operation: ablative and measuring mode. In the ablative mode output energy is set to 500 mJ, pulse duration to 175 μs and pulse repetition rate to 20 Hz. In this mode, the use of a water spray for tissue cooling and cleaning of the output window of the handpiece is necessary to avoid tissue carbonization and window damage. Measurements during this mode of operation are not possible. For the purpose of measurement, it is necessary to stop the water spray and change the parameters of the laser pulses. In this case output energy is set to 3.14 mJ, pulse duration to approximately 1 μs (so that it generates only one shock wave) and pulse repetition rate to 1 Hz (due to the limited speed of data acquisition from the oscilloscope to a PC). An example of the result of laser ablation with on-line monitoring of the implant bed preparation is shown in Figure 5, where the shape of the implant bed is reconstructed in several steps.

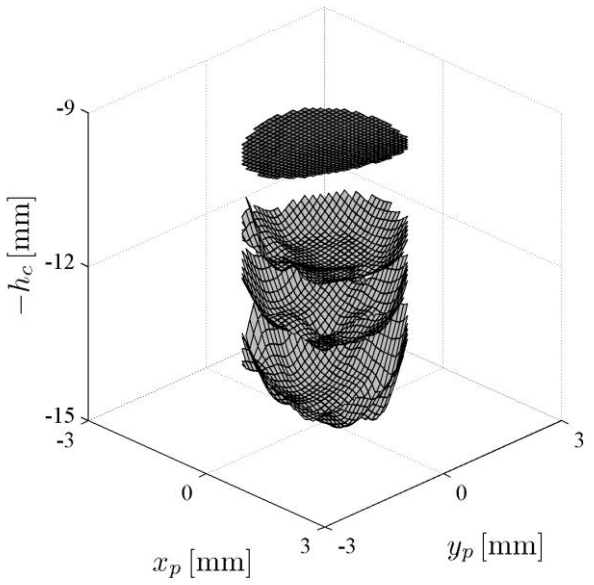

Figure 5: OD implant bed reconstruction using piezoelectric detection during its preparation using scanning Er:YAG laser.

4 Conclusions

Our work towards new approach to laser supported implantology is presented in this contribution. First, we report on preliminary experimental studies that led to confirmation of suitability of Sedov-Taylor point explosion model for the description of optodynamic phenomena during Er:YAG laser ablation of biological tissue. we demonstrate that already few millimeters from interaction point weak shock waves are developed. For this purpose an improved double-exposure shadowgraph method has been employed. Observations obtained using this experimental set-up are of great importance in later theoretical interpretation. Further experimental research using piezoelectric sensors confirms their practicable value for monitoring ablation process with scanning Er:YAG laser. Theoretical studies lead to development of a new sensor model that takes into account finite sensor size and its electrical and mechanical properties, as well as novel practicable method for precise optodynamic source localization that enables simultaneous distance and energy estimation. Obtained results have allowed progress in dealing with complex cases such as optodynamic implant bed reconstruction. In order to test our approach we develop a functional prototype of adaptive laser medical system, which simulates practical conditions. Preliminary *in vitro* studies show that bed preparation could be achieved with sufficient precision and reliability. Further actions are still necessary in order to carry out first clinical trials.

5 References

[1] Lee, S.-Y., Piao, C., Heo, S.-J., Koak, J.-Y., Lee, J.-H., Kim, T.-H., Kim, M.-J., Kwon, H.-B., Kim, S.-K. (2010). A comparison of bone bed preparation with laser and conventional drill on the relationship between implant stability quotient (ISQ) values and implant insertion variables. *The Journal of Advanced Prosthodontics*, vol. 2, no. 4, p. 148–153.

[2] Salina, S., Maiorana, C., Iezzi, G., Colombo, A., Fontana, F., Piattelli, A. (2006). Histological evaluation, in rabbit tibiae, of osseointegration of mini-implants in sites prepared with Er:YAG laser versus sites prepared with traditional burs. *Journal of Long-Term Effects of Medical Implants*, vol. 16, no. 2, p. 145–156.

[3] Stübinger, S., Biermeier, K., Bächi, B., Ferguson, S. J., Sader, R., Rechenberg, B. von (2010). Comparison of Er:YAG laser, piezoelectric, and drill osteotomy for dental implant site preparation: a biomechanical and histological analysis in sheep. *Lasers in Surgery and Medicine*, vol. 42, no. 7, p. 652–661.

[4] Kesler, G., Romanos, G., Koren, R. (2006). Use of Er:YAG laser to improve osseointegration of titanium alloy implants--a comparison of bone healing. *The International Journal of Oral & Maxillofacial Implants*, vol. 21, no. 3, p. 375–379.

[5] Schwarz, F., Olivier, W., Herten, M., Sager, M., Chaker, A., Becker, J. (2007). Influence of implant bed preparation using an Er:YAG laser on the osseointegration of titanium implants: a histomorphometrical study in dogs. *Journal of Oral Rehabilitation*, vol. 34, no. 4, p. 273–281.

[6] Stübinger, S., Ghanaati, S., Saldamli, B., Kirkpatrick, C. J., Sader, R. (2009). Er:YAG laser osteotomy: preliminary clinical and histological results of a new technique for contact-free bone surgery. *European Surgical Research. Europäische Chirurgische Forschung. Recherches Chirurgicales Européennes*, vol. 42, no. 3, p. 150–156.

[7] Seymen, G., Turgut, Z., Berk, G., Bodur, A. (2012). Implant Bed Preparation with an Erbium, Chromium Doped Yttrium Scandium Gallium Garnet (Er,Cr: YSGG) Laser Using Stereolithographic Surgical Guide. *Journal of Lasers in Medical Sciences*, vol. 4, no. 1, p. 25–32.

[8] Wolff, R., Weitz, J., Poitzsch, L., Hohlweg-Majert, B., Deppe, H., Lueth, T. C. (2011). Accuracy of navigated control concepts using an Er:Yag-laser for cavity preparation. *Conference Proceedings: ... Annual International Conference of the IEEE Engineering in Medicine and Biology Society. IEEE Engineering in Medicine and Biology Society. Annual Conference*, *2011*, p. 2101–2106.

[9] Stopp, S., Svejdar, D., Kienlin, E. von, Deppe, H., Lueth, T. C. (2008). A new approach for creating defined geometries by navigated laser ablation based on

volumetric 3-D data. *IEEE Transactions on Bio-Medical Engineering*, vol. 55, no. 7, p. 1872–1880.

[10] Stopp, S., Deppe, H., Lueth, T. (2008). A new concept for navigated laser surgery. *Lasers in Medical Science*, vol. 23, no. 3, p. 261–266.

[11] Niemz, M. H. (2002). *Laser-Tissue Interactions: Fundamentals and Applications.* 2nd ed. Springer-Verlag Berlin and Heidelberg GmbH & Co. K.

[12] Vogel, A., Venugopalan, V. (2003). Mechanisms of pulsed laser ablation of biological tissues. *Chemical Reviews*, vol. 103, no. 2, p. 577–644.

[13] Quest, D., Gayer, C., Hering, P. (2012). Depth measurements of drilled holes in bone by laser triangulation for the field of oral implantology. *Journal of Applied Physics*, *111*(1), 013106. doi:10.1063/1.3676219

[14] Fuchs, A., Schultz, M., Krüger, A., Kundrat, D., Díaz, D. J., Ortmaier, T. (2012). Online measurement and evaluation of the Er:YAG laser ablation process using an integrated OCT system. *Biomedical Engineering / Biomedizinische Technik*, Vol. 57, p. 434–437.

[15] Schroeder, A., Belser, U. (1996). *Oral implantology*. Thieme.

[16] Kahrs, L. A., Burgner, J., Klenzner, T., Raczkowsky, J., Schipper, J., Wörn, H. (2010). Planning and simulation of microsurgical laser bone ablation. *International Journal of Computer Assisted Radiology and Surgery*, Vol. 5, no. 2, p. 155–162.

[17] Perhavec, T., Gorkič, A., Bračun, D., Diaci, J. (2009). A method for rapid measurement of laser ablation rate of hard dental tissue. *Optics & Laser Technology*, vol. 41, no. 4, p. 397–402.

[18] Jezeršek, M., Grad, L., Požar, T., Cencič, B., Bačak, I., Možina, J. (2011). Optodynamic monitoring of laser tattoo removal. *Proc. SPIE 8092, Medical Laser Applications and Laser-Tissue Interactions V.* Vol. 8092, p. 809214–809214–8.

[19] Rupprecht, S., Tangermann-Gerk, K., Wiltfang, J., Neukam, F. W., Schlegel, A. (2004). Sensor-based laser ablation for tissue specific cutting: an experimental study. *Lasers in Medical Science*, vol. *19, no.* 2, p. 81–88.

[20] Možina, J., Diaci, J. (2011). Recent advances in optodynamics. *Applied Physics B*, vol. 105, no. 3, p. 557–563.

[21] Grad, L., Možina, J., Šušterčič, D., Funduk, N., Skalerič, U., Lukač, M., Cencič, B., Nemeš, K. (1994). Optoacoustic studies of Er:YAG laser ablation in hard dental tissue. SPIE proc. *Laser Surgery: Advanced Characterization, Therapeutics, and Systems IV,* vol. 2128, p. 456–465.

[22] Diaci, J., Možina, J. (1994). A study of energy conversion during Nd :YAG laser ablation of metal surfaces in air by means of a laser beam deflection probe. *Le Journal de Physique IV,* vol. 04, no. C7, p. C7-737–C7-740.

[23] Diaci, J. (1992). Response functions of the laser beam deflection probe for detection of spherical acoustic waves. *Review of Scientific Instruments*, vol. 63, no. 11, p. 5306–5310.

[24] Perhavec, T., Diaci, J. (2010). A novel double-exposure shadowgraph method for observation of optodynamic shock waves using fiber-optic illumination. *Journal of Mechanical Engineering*, vol. 56, no. 7-8, p. 477–482.

[25] Diaci, J. (1990). *Mehanski pojavi pri lasersko induciranih transformacijah snovi*. PhD Thesis.

[26 Perhavec, T. (2010). *Optodinamski nadzor ablacije bioloških tkiv z laserjem Er:YAG*. PhD Thesis.

[27] Bosiger, G., Perhavec, T., Diaci, J. (2014). A method for optodynamic characterization of Erbium laser ablation using piezoelectric detection. *Strojniški Vestnik - Journal of Mechanical Engineering*, vol. 60, no. 3, p. 172–178.

[28] Bosiger, G., Perhavec, T., Marinček, M., Diaci, J. (2013). Method for optodynamic source localization during Er:YAG laser ablation. *Journal of Biomedical Optics*, vol. 18, no. 10, p. 100505-1–100505-3.

[29] Bosiger, G. (2014). *Ablacija bioloških tkiv z adaptivno vodenim laserskim snopom*. PhD Thesis.

Development and manufacturing of guide template for pedicular screw placement

Tomaž Brajlih [a*], Matjaž Merc [b], Gregor Rečnik [b], Igor Drstvenšek [a], Tomaž Irgolič [a], Matej Paulič [a], Jože Balič [a], Franc Čuš [a]

[(a)] University of Maribor, Faculty of Mechanical Engineering, Smetanova 17, 2000 Maribor, Slovenia.

[(b)] University Medical Centre Maribor, Ljubljanska ulica 5, 2000 Maribor, Slovenia.

* Corresponding author:
E-mail: tomaz.brajlih@um.si

Abstract

Use of pedicle screw systems for vertebral fusion has become increasingly common in spine surgery. It is routinely used for stabilization between two or more spinal levels in degenerative, traumatic, oncogenic or preoperatively deformed vertebrae. Although the method is generally safe it carries some risks connected with accurate screw placement. For this reason, we can find on the market many computer-assisted surgical systems that are highly accurate. However, these devices are expensive, learning curve is steep and the procedure takes longer in comparison with "free-hand" technique. We have developed a method of pedicle screw placement in lumbar and sacral region using drill guide template created with rapid prototyping technique and are validating it in clinical study.

1 Introduction

Use of pedicle screw systems for vertebral fusion has become increasingly common in spine surgery. It is routinely used for stabilization between two or more spinal levels in degenerative, traumatic, oncogenic or preoperatively deformed vertebrae [1]. In pedicle screw insertion, it is important both to select the correct size of screw and to place it properly within the pedicle to ensure good anchoring. Free-hand technique has a high associated rate of unplanned perforation, which is the major specific complication of pedicle screw placement and causes a high risk of bone weakening or lesions of the spinal cord, nerve roots, or blood vessels [2]. The principle of image guidance (navigation) is to register the patient's pre-operative computed tomography (CT) scans, thus permitting the surgeon to navigate simultaneously within the patient and the CT scan volume. Such navigation systems have shown good clinical results [3–5]. There are, however, several disadvantages associated with navigation systems. In cases where screws are to be placed in more than one vertebra, it is necessary to perform a separate registration step for each vertebra. Intraoperative registration of bone structures takes

up to several minutes, and thus the time taken for the overall procedure is increased
Materials and methods

The objective of our study was to evaluate the accuracy of a drill-guide template technique for lumbar and first sacral pedicle screw insertion. A clinical trial was performed on 10 subjects, implanting minimal 50 pedicular screws using drill guide template and 50 screws using free-hand technique under fluoroscopy surveillance. The study was classified according to the National Institute of Child Health and Human Development (NICHD) criteria.

2 Design of the drill guide template

A CT scan was performed on a lumbar and sacral spine with 0.5 mm slice thickness. The images were stored in DICOM format and transferred to a workstation running EBS ver. 2.2.1 (Ekliptik, Slovenia) software (Figure 1) to generate a 3D reconstruction model for the targeted lumbar or sacral vertebra. The 3D spine model was exported in STL format, and then opened in a workstation running SolidWorks 2011 (SolidWorks Corp., USA) for the optimal screw size and orientation. First, the 3D model was opened and the image of the pedicle was exposed. Second, the pedicle circumference and direction was investigated. Lastly, a circle was found whose diameter was the least diameter of this ellipse. The centre of this circle was then virtually connected with the vertebra and the facete joint to obtain the optimal pedicle screw trajectory (Figure 2A, 2B). Then, a 3D vertebral model was reconstructed with a virtual screw placed on both sides and on different levels. The optimal screw length was also determined so that the end of the screw has reached 50-80% of vertebral diameter for lumbar vertebra and the frontal cortex for first sacral corpus (Figure 2A). We have used Click´X stabilisation system (Synthes, Swiss) with 6.25 mm diameter screws.

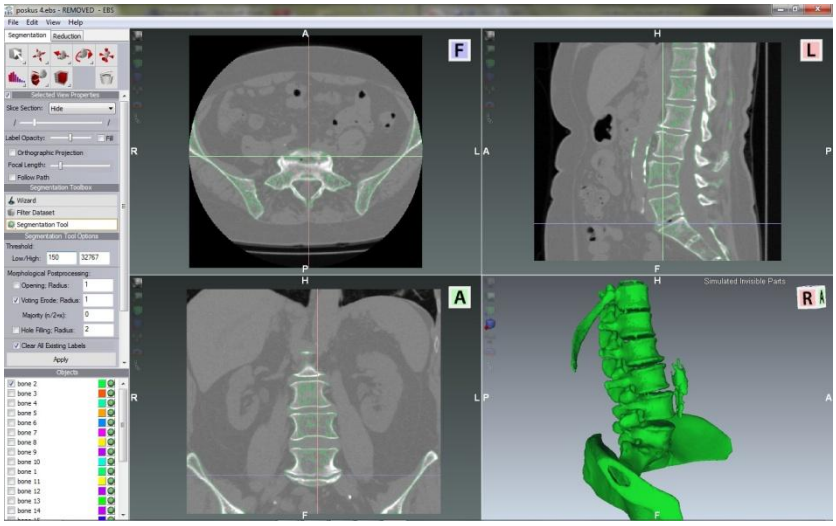

Figure 1. Ekliptik EBS ver. 2.2.1 software

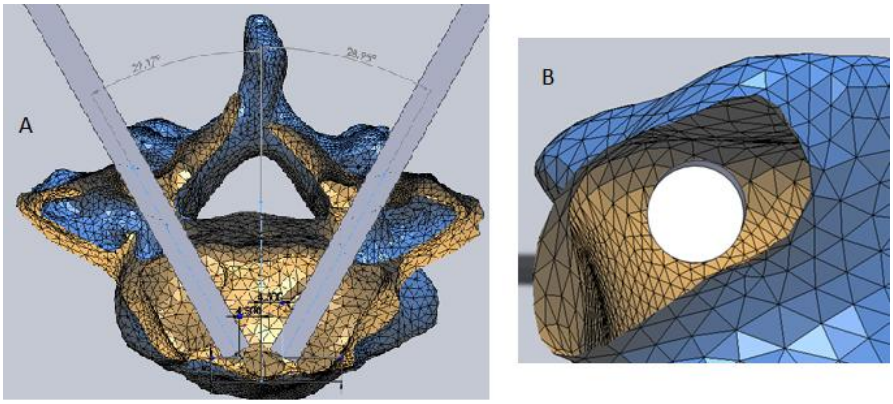

Figure 2. Projecting virtual screws direction. Screws end between 50-80% of vertebral corpus diameter (A). Screw trajectory is exactly in the centre of pedicle (B) (Solidworks).

Once this had been done, a drill guide template was constructed with a surface designed to be inverse of the dorsal part of facete joint. That was meant to enable a lock-and-key structure with 0.1 mm accuracy fitting dorsal part of facete to achieve minimal overlap. The parts of template for each pedicular screw were connected between each other in sagittal and transversal plane to achieve maximal stability of template.

A drill guide template was afterwards exported in STL format and manufactured out of polyamide powder, using the EOS Formiga P100 selective laser sintering machine (Figure 3). In first investigated case also a vertebral bio model was manufactured for more exact surgical planning and conception.

Figure 3. Drill guide template.

3 Clinical application

In 2011 and 2012, 10 patients with lumbar or lumbo-sacral spinal pathology requiring spinal fusion underwent posterior instrumentation of the affected spine. In each case, a personalized drill guide template was sterilized and used intraoperatively to navigate the insertion of pedicle screws. Intraoperative fluoroscopy was always used for surveillance. Postoperative a CT scanning was used to assess the accuracy of the pedicle screw placement.

In the same period free-hand technique under fluoroscopy surveillance was performed on 10 patients for control group. The entry point and the direction for pedicle screw were determined according to the free-hand technique guidelines. The entry point for the screw was intersection between the midline of facete joint and the midline of the processus transversus. Direction of the screw trough the pedicle was determined using special introduction tool [6]. Length of the screw was estimated using fluoroscopy.

All screws were implanted by one surgeon (Rečnik G.).

4 Postoperative evaluation

Postoperatively all patient underwent CT scan. First, an analysis was made comparing accuracy between projected virtual screws direction and actual direction of screws in-vivo using drill guide templates (Figure 4). Second, comparison between accuracy and level of violence in control group and a "template" group was performed. The accuracy was measured using EBS ver. 2.2.1 (Ekliptik, Slovenia) software and was defined as eccentric position of screw according to the least diameter of the ellipse of the pedicle. Displacement was measured in millimetres for all three planes. Inclination from optimal angle was measured in degrees. Level of violence was estimated according to the adopted thoracic screw placement score, using 4 Grade scoring system. Grade 0: no misplacement, whole screw is in pedicle, Grade 1: <2 mm and <1/2 diameter of screw is out of pedicle, Grade 2: >2 mm and <4 mm or <1 screw diameter is out of pedicle, Grade 3: >4 mm or whole screw diameter is out of pedicle [7].

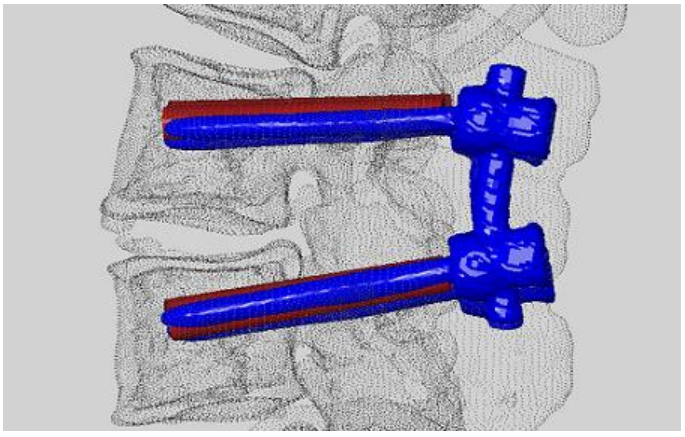

Figure 4. Designed position of screws (red). Actual position of screws (blue).

5 First results and discussion

Ten patients were treated using a drill guide template system. More than 50 pedicle screws were inserted and no pedicle perforation or major violation was observed by postoperative CT scan. According to these first results, this method is promising and the concept of a template fitting dorsal elements of facete joint is precise enough to be routinely used in selected cases with severe spinal deformation where free-hand technique could be challenging.

During the operation, the best fit for positioning the template was easily found by hand, because no significant free motion of the template occurred when it was pressed against the dorsal facete surface. Thus, the navigational template could be used as an in situ drill guide.

Individual vertebral templates eliminate the need for complex equipment and time-consuming procedures in the operating room if using navigation [8]. These templates are a simple and low-cost solution that provides exact, safe and fast implementation of elective surgery on bone structures [9, 10]. A preoperative CT scan is mandatory both to generate the individual templates and to establish a precise spatial correspondence between the individual bone structure in situ and the intended position of the tool guide. The goal of this study was to evaluate the practicability and accuracy of image-based individual templates and to design an effective multi-level guide for lumbar or sacral spinal level.

The technique also has potential sources of error. Because the 3D model of each vertebra is constructed manually or automatically, there is a potential for error in the procedure. Furthermore, the RP model could deviate from the computer 3D model, but existing RP technology can control deviation to 0.1 mm [11].

6 First conclusions

Our study showed that using a template with a drill guide can simplify the surgical act and may at the same time enhance the accuracy of pedicle screw positioning, even when using multi-level template. We have also successfully implanted pedicular screws using drill guide in the first sacral vertebra. Nonetheless, several caveats remain, and this method has not yet replaced free-hand technique and navigation systems.

7 Acknowledgement

Authors are truly grateful for all help and collaboration by usage of program Ekliptik EBS.0 product of Ekliptik d.o.o. company.

8 References

[1] Mattei, T.A., Meneses, M.S., Milano, J.B., Ramina, R. (2009 "Free-hand" technique for thoracolumbar pedicle screw instrumentation: Critical appraisal of current "state-of-art". *Neurology India*, vol. 57, no. 6, p. 715–721.

[2] Zeiller, S.C., Lee, J., Lim, M., Vaccaro, A.R. (2005). Posterior thoracic segmental pedicle screw instrumentation: Evolving methods of safe and effective placement. *Neurology India*, vol. 53, no. 4, p. 458–465.

[3] Berlemann, U., Langlotz, F., Langlotz, U., Nolte, L.P. (1997). Computer-assisted orthopedic surgery. From pedicle screw insertion to further applications. *Orthopade*, vol. 26, no. 5, p. 463–469.

[4] Richards, P.J., Kurta, I.C., Jasani, V., Jones, C.H., Rahmatalla, A., Mackenzie, G., Dove, J. (2007). Assessment of CAOS as a training model in spinal surgery: A randomised study. *European Spine Journal*, vol. 16, no. 2, p. 239 –244.

[5] Youkilis, A.S., Quint, D.J., McGillicuddy, J.E., Papadoupoulos, S.M. (2001) Stereotactic navigation for placement of pedicle screws in the thoracic spine. *Neurosurgery*, vol. 48, no. 4, p. 771–778.

[6] Mattei, T.A., Meneses, M.S., Milano, J.B., Ramina R. (2009) "Free-hand" technique for thoracolumbar pedicle screw instrumentation: Critical appraisal of current "state-of-art". *Neurology India*, vol. 57, no. 6, p. 715–721.

[7] Youkilis, A.S., Quint, D.J., McGillicuddy, J.E., Papadoupoulos, S.M. (2001). Stereotactic navigation for placement of pedicle screws in the thoracic spine. *Neurosurgery*, vol. 48, no. 4, p. 771–778.

[8] Hughes, S.P., Anderson, F.M. (1999). Infection in the operating room. *The Bone & Joint Journal*, vol. 81, no. 5, p. 754–755.

[9] Lu, S., Xu, Y.Q., Zhang, Y.Z., Li, Y.B., Xie, L., Shi, J.H., Huo, H., Chen, G.P., Chen, Y.B. (2009). A novel computer-assisted drill guide template for lumbar pedicle screw placement: A cadaveric and clinical study. The International Journal of Medical Robotics and Computer Assisted Surgery, vol. 5, no. 2, p. 184–191.

[10] Ma, T., Xu, Y.Q., Cheng, Y.B., Jiang, M.Y., Xu, X.M., Xie, L., Lu, S. (2012). A novel computer-assisted drill guide template for thoracic pedicle screw placement: a cadaveric study. *Archives of Orthopaedic and Trauma Surgery*, vol. 132, no. 1, p. 65–72.

[11] Drstvensek, I., Ihan Hren, N., Strojnik, T., Brajlih, T., Valentan, B., Pogacar, V., Zupancic Hartner, T. (2008). Applications of rapid prototyping in cranio-maxilofacial surgery procedures. *International Journal of Biology and Biomedical Engineering*, vol. 2, no. 1, p. 29–38.

Handheld 3D optical apparatus for head-to-trunk orientation measuring

Urban Pavlovčič [a*], Janez Diaci [a], Janez Možina [a], Zvezdan Pirtošek [b], Matija Jezeršek [a]

[(a)] University of Ljubljana, Faculty of Mechanical Engineering, Aškerčeva 6, 1000 Ljubljana, Slovenia.

[(b)] University Medical Centre, Department of Neurology, Zaloška cesta 2, 1000 Ljubljana, Slovenia.

* Corresponding author:
E-mail: urban.pavlovcic@fs.uni-lj.si

Abstract

System for a head-to-torso orientation measuring is presented. It is based on a 3D measuring of the shape of head and upper trunk. Handheld 3D optical apparatus, based on digital DSLR camera, was developed for quick and accurate measuring. In front of the camera's build-in flash we position projection system, which projects structured light pattern onto the measured surface. Its shape is reconstructed from deformation of the light pattern on the acquired image and known geometry between projection system and camera. Reconstructed surfaces of head and trunk are than registered to the reference surface. From both rotations, required for the registration, orientation of the head with respect to the trunk is calculated.

Method was verified by *in-vitro* and *in-vivo* verification. First was conducted using mannequin with movable head and reference orientation tracker, and the latter by measuring a person, rotating head left and right. Results show, that accuracies are 2° *in-vitro* and 3° *in-vivo*, which is satisfactory for measuring orientation of the head in patients with cervical dystonia.

1 Introduction

Known orientation of the head is important in many technical fields, such as development of natural user interfaces, face recognition systems, monitoring systems and different medical systems. Researchers usually use a combination of different gyroscopes, accelerometers and electronics compasses. Those sensors are attached to the measured head via frame of glasses, cap or helmet. [1-3] Although those systems achieve high levels of measuring uncertainty, our concerns are mostly related to the rigidness of the junction between head and attached sensor. If the sensor moves during the measuring procedure, results are not representative. Weight and size of the sensors can also present a problem since they can influence the kinematics of the head movement and in that manner alter the results.

That is why we developed a method, which does not require any attachments to the head, since it bases on the registration of the 3D surfaces. The rotation of the trunk is "subtracted" of the rotation of the head, required for the registration, and difference is defined as the head-to-trunk orientation.

The system was developed with a view to measure the orientation of the head in rest posture and cervical range of motion in patients with cervical dystonia (CD). It is a movement disorder which result in abnormal head position and hampered movement. Using our measuring system we want to objectively assess it's severity before and after the treatment.

2 Methods

The method requires two 3D measurements: measurement, acquired in the reference position and measurement in position, we want to characterize. The reference measurement must be captured in position where all body planes of the head and trunk are parallel.

Figure 12. Handheld 3D optical apparatus.

People cannot stand still for longer periods of time and that is why data acquisition time must be as short as possible, otherwise the measuring precision is lowered. To be able to acquire 3D measurement quickly, but with satisfactory precision, we developed a handheld 3D optical apparatus (HOA), which acquires the measuring image in 0.05 s, has measuring range 750×750×500 mm, and measuring uncertainty of 1.5 mm. It is

based on the commercial DSLR camera and custom made projection system (PS), which is fixed in front of the camera's build in flash. In order to capture measuring image, measured surface is photographed with engaged flash. At that moment the grating in the PS is illuminated by the flash from behind. At front side a light pattern is formed and projected to the measured surface by lens of the PS. Image of deformed pattern is captured by the camera. Degree of deformation of the pattern, which consists of 67 parallel lines, depends on the shape of illuminated surfaces and geometry between camera and PS. Surface is reconstructed based on a Fourier transform profilometry [4] and triangulation [5] principles.

Once the surface of head and upper trunk is measured, it is divided into subsurfaces of head and trunk. Parts of the surfaces, where high degree of the deformation during the movement is expected, must not be included in neither subsurface. The divided surfaces are than registered to the reference surface, which was previously aligned to the coordinate system. During the registration required rotations are monitored. In that manner we obtain a pair of rotations: rotation of the head $\mathbf{R}_h$ and rotation of the trunk $\mathbf{R}_t$. Trunk rotation between reference and processed measurement is caused by the movement of measuring equipment or measured person as a whole. We define the orientation of the head with respect to the trunk $\mathbf{R}$ as:

$$\mathbf{R} = \mathbf{R}_h \cdot \mathbf{R}_t^{-1} \ . \tag{14}$$

Euler angles, which describe the rotation in each body plane, are calculated by the matrix decomposition procedure [6].

3 Verification

Proposed method was verified by *in-vitro* and *in-vivo* verification. The first was conducted using a mannequin with movable head. Orientation of the head was measured by proposed method in combination with two different 3D measuring systems: presented HOA and laser scanner (LS), which has measuring accuracy of 0.3 mm, but is inappropriate for *in-vivo* measuring due to long data acquisition time. In addition we measured the orientation by orientation tracker, which was fixed to the mannequin's head.

Results showed that the accuracy of measured orientation using proposed method in combination with the LS was 0.3°, while in combination with the HOA was 2.0°. These results indicate that the method works, but its accuracy depends on the accuracy of the measured surfaces.

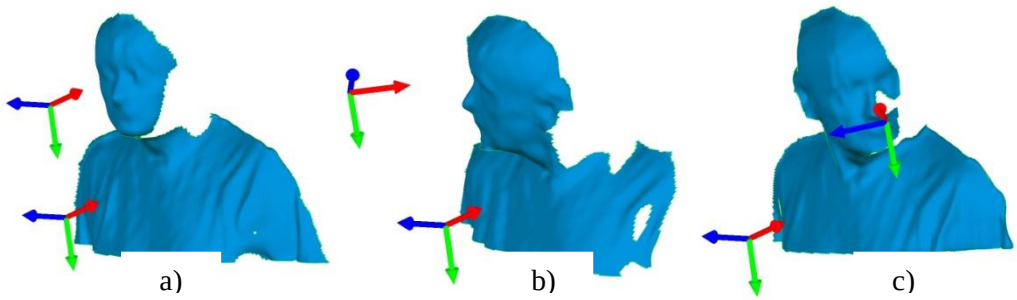

Figure 13. Measurements of patient in reference position (a), right (b) and left rotation (c).

In-vivo verification was conducted by measuring the patient with diagnosed CD. He was instructed to rotate the head left and right as far as possible. The move was repeated for 13 times with one minute brakes in-between. Scatter between measured orientations was 3°, but it must be emphasized, that it also includes the scatter caused by unrepeatable movement of the patient.

4 Conclusions

The non-contact method for measuring head-to-trunk orientation is based on 3D surface acquisition. The method is quick, accurate, causes little stress for the operator or measured person and enables compensation of the rotation of the measuring equipment or measured person during the measuring procedure. Orientation is calculated from rotations, required for the alignment of head and trunk surfaces to the reference surface. Results of the verification showed the accuracy of the measurement is about 2° *in-vitro* and 3° *in-vivo*.

Presented measuring system is used in cooperation with Clinical Medical Centre, Department of Neurology, Ljubljana, Slovenia, to objectively assess the severity of the CD and effect of the botulin toxin therapy. As part of that research orientation of rest posture and cervical range of motion of about 100 patients were measured between December 2011 and April 2014.

5 Acknowledgement

Research was conducted as a part of the project Laser triangulation in medicine (LASTRIM-l7-4274), financed by the Slovenian Research Agency.

6 References

[1] Ohayon, S., Rivlin, E. (2006). Robust 3d head tracking using camera pose estimation. *18th International Conference on Pattern Recognition, 2006. ICPR 2006.* , IEEE.

[2] Kim, J., Nam, K.W., Jang, I.G., Yang, H.K., Kim, K.G., Hwang, J.-M. (2012). Nintendo Wii remote controllers for head posture measurement: accuracy, validity, and reliability of the infrared optical head tracker. *Investigative Ophthalmology & Visual Science*, vol. 53, no. 3, p. 1388-1396.

[3] Lian, E., Hachadorian, J., Hoan, N.T., Toi, V. (2010). A Novel Electronic Cervical Range of Motion Measurement System. *The Third International Conference on the Development of Biomedical Engineering in Vietnam*, Springer.

[4] Takeda, M., Mutoh, K. (1983). Fourier transform profilometry for the automatic measurement of 3-D object shape. *Applied optics*, vol. 22, no. 24, p. 3977-3982.

[5] Jain, R., Kasturi, R., Schunck, B.G. (1995). *Machine vision.* McGraw-Hill New York.

[6] Spong, M.W., Hutchinson, S., Vidyasagar, M. (2006). *Robot modeling and control*. John Wiley & Sons New York.

Development of manufacturing technology for integrated micro-optics

Jaka Pribošek [*], **Janez Diaci**

University of Ljubljana, Faculty of Mechanical Engineering, Aškerčeva 6, 1000 Ljubljana, Slovenia.

* Corresponding author:
E-mail: jaka.pribosek@fs.uni-lj.si

Abstract

In this paper we present the development of manufacturing technology for integrated micro-optics, with the main focus on refractive microlens arrays for measurement applications. The development of three state-of-the-art manufacturing concepts is presented: the use of printing technology, replication techniques and lithography. First we exploit off-the-shelf printhead for selective deposition of photosensitive resists on glass substrates. Next, we develop a computer controlled microforging apparatus to fabricate the microlens arrays moulds, which are exploited in hot embossing procedure of polymethylmethacrylate (PMMA) to fabricate microlens array. Last, we use laser direct imaging lithography to fabricate the microlenses in thin film photoresist coatings on glass substrates. We use a prototype device for laser illumination developed by LPKF Laser & Electronics AG. By employing the above three techniques, we have successfully developed microlenses with diameters between 30 and 1000 μm. The conducted experimental study presents practical findings and comparison of individual technologies in terms of relevance and use in measurement applications.

1 Introduction

Recent advances of semiconductor technology gave rise of micro-optics which represents an important milestone in optics. The diversity of applications, that emerged on account of microoptics,require micro-optical elements with completely different properties. For some application, including beam steering, light homogenization and Bessel beam generation microlens arrays with diameters of several hundred micrometers and sags exceeding 50 μm are required. On the other hand, significant smaller microlenses with diameter of only few tenths of micrometers are demanded for measurement applications. Despite of similar purpose considering measurement applications, there are huge differences in required focal lengths and diameters. No single fabrication technique is able to cover the fabrication of microlenses with diameter ranging from 10um to 10mm and focal lengths from 10um to 100mm. Smaller micro-optical elements are nowadays fabricated exclusively by lithography. Lithography is found unsuitable for microlenses with diameters of several hundred micrometers. Such lenses are mostly fabricated by replication techniques, such as hot-

embossing and injection molding technologies with metal molds, offering low-cost large-scale production capabilities while maintaining micron accuracy, good repeatability and high quality surfaces without subsequent treatments [1]–[3]. One of the main challenges that remain unresolved is the manufacture of molds for injection molding or hot embossing of microoptics. Daly has experimented with micromilling and subsequential polishing [4]. The alternative technology is pressing the steel balls in a pre-polished surfaces. In this way it is possible to produce lenses of larger diameters and very controlled focal lengths [4]. Nowadays, the single-point diamond machining with Fast Tool Servo is used to machine the mold [5], [6] meeting the needs of fast and accurate fabrication. The complexity and lack of access to such technology leads us to seek alternative routes to manufacture the mold to use it with replication technologies. There are also other alternative techniques of fabrication, such as inkjet printing [7], [8] Today's printing technology enables precise and quick deposition of drops of ink with volume lower than 10 pL, speeds of several meters per second and the repetition of a few thousand droplets per second. The use of inkjet technology has recently spread to the field of bioengineering [9], a variety of additive manufacturing technologies, manufacturing of decorative ceramics as well as printing of textiles. Recently patented technology allows one to print the optics of complex 3D shapes [10]. In the following paper, we present the development of three different manufacturing technologies, capable of covering the fabrication of wide variety of microlenses. The manufacturing technologies are adapted to the available equipment to maintain low-cost.

2 Inkjet technology

We followed the idea of [8] to selective deposit drops of UV curable photoresist, which form a spherical shape due to surface tension. After the deposition, the drops of photoresists are polymerized with UV light and act as a microlenses. We built a selective deposition system shown in Figure 14

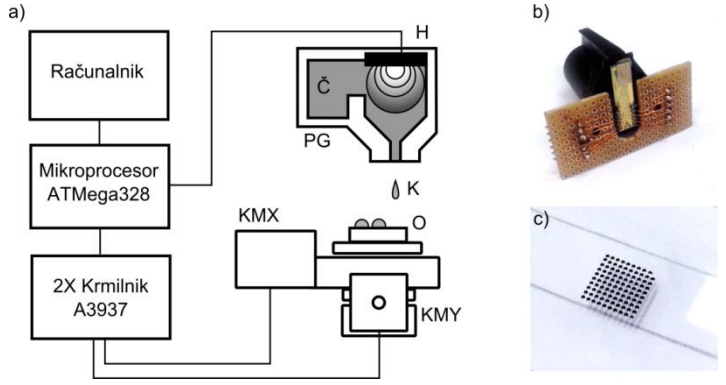

Figure 14: a) a System for printing microoptics b) Commercial thermal printhead with improvised electric contacts c) Printing lens array

In our experiments we exploit off-the-shelf thermal inkjet printhead HP51604A. In the head, heating element (H) instantly heats up a small amount of the ink until

evaporation, whereby the increased pressure pushes the ink through the nozzle, producing a small droplet one at a time. For each cycle it is necessary to generate a 5 μs wide 20V pulse. The delay time between the firing of individual nozzles must be at least 10 μs. We exploited only one printhead nozzle. Initially we tried printing with the existing ink. The form of the lens is determined by the number of drops fired, in our case, each lens is composed of one thousand drops. Promising results have stimulated us to a further experiment with photosensitive resist SU-8. The ink was drained out and entire head was cleaned in an ultrasonic bath removing any traces of ink. After cleaning, we poured in photosensitive polymer SU-8 2000. This photoresist offers good optical properties and extremely low viscosity, similar to the original applied ink. Photoresist is based on Gamma-butyrolactone solvent which turned out to be extremely aggressive and melted plastic print head, which prevented further printing. However, during preliminary tests it was also found that wetting properties of photoresist SU-8 do not allow effective formation of microlens spherical shape. Researchers throughout the world use superhydrophobic coatings prepared by using the sol-gel processes to increase the wetting angle [11]. These sol-gel procedures are usually complex and time consuming. Further work regarding the use of existing setup would make sense especially in the direction of the selective deposition with a simultaneous polymerization, similar to the techniques described in patents owned by LuxExcel AG [10].

3 Replication techniques

We present the manufacturing of such molds by computer-controlled microforming apparatus. In general, the apparatus proves to be repeatable enough for microlens mold fabrication. The whole setup is represented in the Figure 15. Optical cross-tables SMX and SMY ensure a precise positioning of the workpiece in a plane, with the typical movements of the order of a few 100 micrometers. At each position the cam-driven-lever strikes the workpiece. The cam angular position is controlled by the stepper motor SMZ. A hammer consists of a simple lever and the holder of the bearing steel balls T. The depth of the resulting cavities depends on the potential energy introduced by lifting the lever. The level of introduced potential energy can be precisely adjusted by adjusting the heights h1, h2 and h3.To provide a perpendicular strike of the lever the condition h2 = h3 + h4 must be maintained. The apparatus is controlled from a PC running an interface made in MathWorks Matlab environment. All the necessary movements calculated from the input geometry are passed from computer through serial communication to a microprocessor unit. The microprocessor unit is based on Atmel ATmega 328 microcontroller and decodes the serial commands into step/direction signals required for each motor. The stepper motor driver is based on an A3937 integrated circuit, capable of micro-stepping to assure maximal positioning precision.

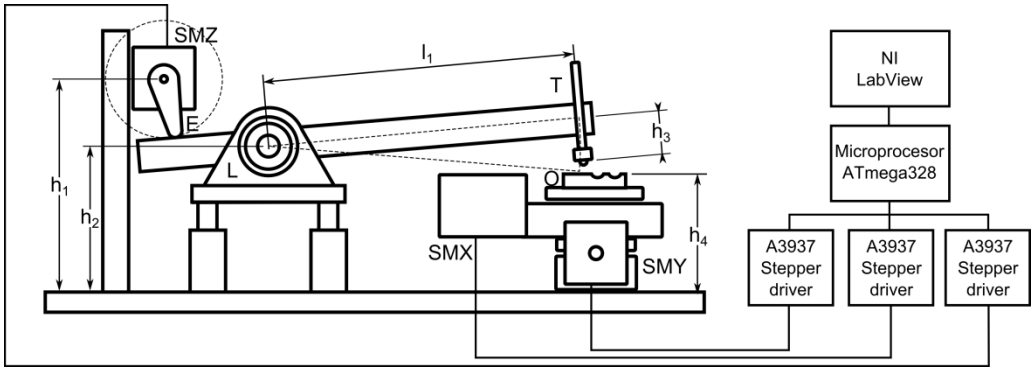

Figure 15: Microforging apparatus

The whole operation of fabrication a cavity takes few seconds. The fabrication of a mold for 100 x 100 microlens lasts about 8 hours. We have inspected 400 hundred cavities with optical microscope, measured their diameters and found good homogeneity and repeatability of the microforging process ($d = 332$ μm, $\sigma = 14$ μm). Next, the hot embossing process is employed to fabricate the microlens arrays. Sheet of Polymethylmethacrylate (PMMA) of 2 mm thickness was cut to size and heated in a conventional kitchen oven over glass transition temperature of PMMA. Small hole was drilled in the sheet where thermocouple was placed to control the temperature in the sample. Heated sheet was then inserted onto mold and covered with 8 mm thick glass substrate to ensure smooth back-surface. Whole composition is then pressed together in a small manual press while cooled down to room temperature. The mold, and the embossed microlens array can be seen in the Figure 16.

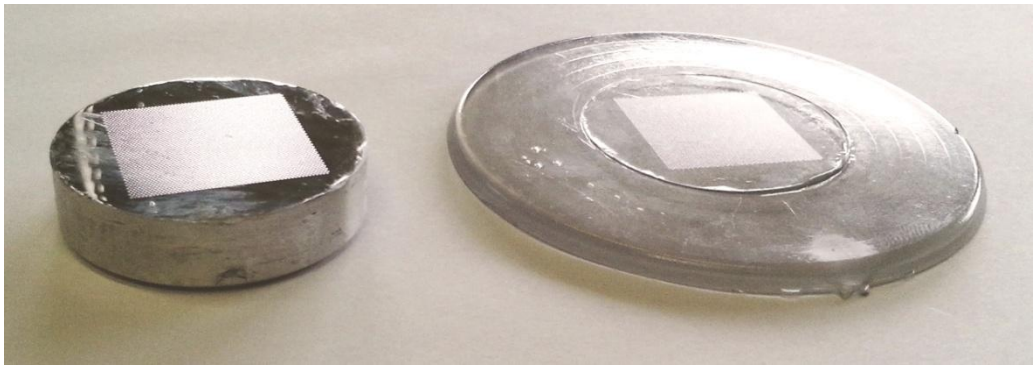

Figure 16: The mold (left) and embossed microlens array(right)

4 Lithographical procedures

The manufacturing chain of the integrated optics consists of a number of successive steps (Figure 10), first demonstrated by Popovic et al [12] and employed by several authors [4], [13]. First, the substrate on which we intend to integrate micro-optical structures is appropriately cleaned. For this purpose we clean them in ultrasonic bath –

first in 10% soaping solution, followed by successive alcohol bath. After that, the substrates are blasted with compressed nitrogen and dehydrated on a heating plate at 150 °C. After cooling down, thin layer of photosensitive polymer is then coated on the upper side of the substrate. This is done by the use of spin-coater, where the glass substrate is mounted in a vacuum chuck and spun to evenly spread out the drop of applied photoresist. The thickness of such thin layer can be controlled by varying both solvent concentration and speed of the spin coater.

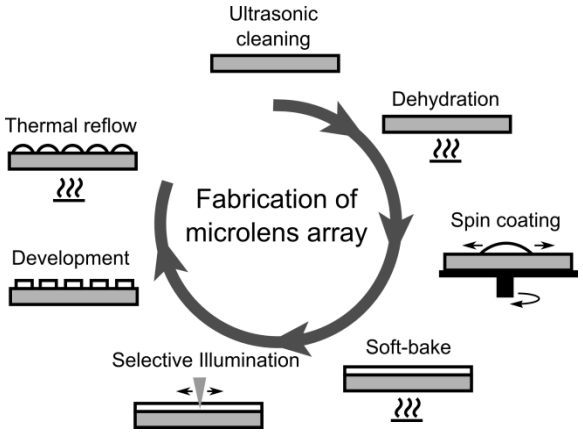

Figure 17: Fabrication of microlens array by the means of laser direct imaging lithography

After spin-coating, the thin layer is baked on a heating plate to evaporate the solvent. In our study, we used positive photoresist AZ9260, diluted with PGMEA and empirically tuned spin-coating process to produce 1 and 10 µm thick layer of photoresists. Next, the substrate is let to cool down until it is ready for selective illumination. This is in our case done by laser, with the prototype device ProtoLaser LDI (LPKF, AG). We illuminated cylindrical structures. Laser fluencies around 140 mJ/cm^2 were found ideal for 1 µm thick and 280 mJ/cm^2 for 10 µm thick layer of photoresist. After the illumination, the exposed photoresist is chemically developed, so only cylindrical structures remain on the substrate. Cylindrical structures are then heated above the glass transition temperature of photoresists, which lie at (100 °C).

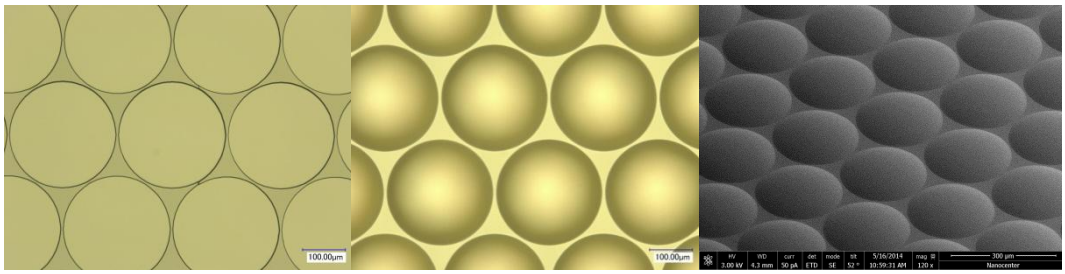

Figure 18: Left: cylindrical structures after photoresist development, Middle: Spherical shapes after thermal reflow of photoresists, Right: SEM of the hemispherical shapes

Surface tension forms the cylindrical structures of photoresists to hemispherical shape, which work as microlenses. These lenses can be used as is, however additional manufacturing steps such as ion beam milling or LIGA (Lithographie Galvanik, Abformung), might be applied to improve the optical and scratch-resistance properties. As noted by Daly [33] in case height/diameter ration does not exceed 3.4%, the surface tensions are too low for successful shape formation (Figure 19).

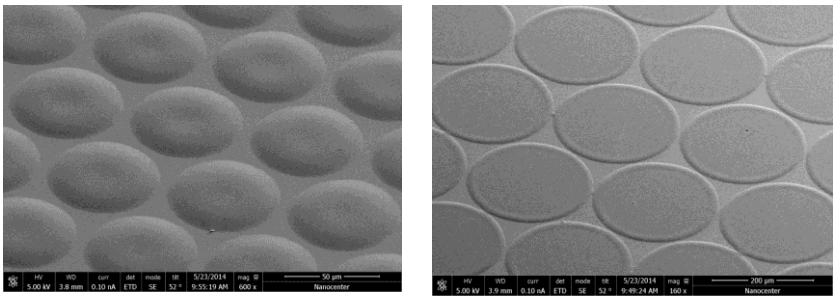

Figure 19: The: a) Dip in the center of the lenses occurred due to insufficient surface tension (height/diameter=3%) b) extreme example in case of height/diameter= 0.4%.

5 Discussion

For metrology applications, we require the microlenses of diameter ranging from 30-300 μm and both very short and very long focal lengths, thus required F-number lies in the range 1 – 50. The initial experiments carried in our study, show distinctive benefits and drawbacks of each presented technology. The printing technology offers very elegant solution of precise determination of photoresist volumes. In addition to that different shapes are feasible (oval, square etc) while negative photoresists, exhibiting superior optical quality can be used. The main drawback is difficult control of F-number, for which superhydrophobic surface treatments are required.

The mold fabrication method, along with hot embossing technique shown here, is easy to use with almost no fabrication costs and is capable of large scale production. Additional benefit is the use of optical grade polymers. This technique is appropriate mainly for larger micro lenses (300 μm – 5 mm), with focal lengths from hundreds of microns up to several tenths of millimetres. Except for larger size, those lenses are suitable both for illumination and measurement purposes, such as wave-front sensing.

Among demonstrated, the lithography technique is clearly the most accurate technique, but tied to small scale micro-optics with diameters between 20 to 300 μm and F-numbers from 3 to 5. The main advantage of lithography is flexibility regarding fabrication of complex shapes and the possibility of both creating refractive and diffractive optics. However, no large focal length refractive micro-optics can be fabricated by the presented techniques without additional manufacturing steps. Additional drawback is use of positive photoresist, which exhibit poor optical performance. Fabricated lenses are suitable for optical metrology where short focal lengths and small sizes are desired, such as confocal microscopy.

6 Conclusions

We present the development of three promising state-of-the art techniques of microlens fabrication. Inkjet technology shows great potential for fabrication of microlenses of good optical quality, however process control is tightly related to the hydrophobic surface treatments. We developed the microforging apparatus capable of manufacturing molds with cavities diameters between 300 μm and 2000 μm. Fabricated molds were successfully used in hot embossing replication technique to produce microlens array. The Direct laser illumination lithography was found successful for fabrication of smaller microlenses with diameters of 20 - 250 μm. The presented technologies cover the fabrication of wide variety of microlenses regarding their focal lengths and sizes which may be incorporated in various micro optical measurement systems.

7 Acknowledgement

We would kindly like to thank dr. Anže Jerič (LPKF AG) for fruitful collaboration and provided support. Special thanks go to Ivana Jud from LPKF AG for help with the laser direct imaging lithography and acquisition of SEM images.

8 References

[1] Chang, C.-Y., Yang, S.-Y, Huang, L.-S., Chang, J.-H. (2006) Fabrication of plastic microlens array using gas-assisted micro-hot-embossing with a silicon mold. *Infrared Physics & Technology*, vol. 48, no. 2, p. 163–173.

[2] Pan, C. T., Wu, T. T., Chen, M. F., Chang, Y. C., Lee, C. J., Huang, J. C. (2008). Hot embossing of micro-lens array on bulk metallic glass. *Senors and Actuators A: Physical.*, vol. 141, no. 2, p. 422–431.

[3] Tran, N. K., Lam, Y. C., Yue, C. Y., Tan, M. J. (2010). Manufacturing of an aluminum alloy mold for micro-hot embossing of polymeric micro-devices. *Journal of Micromechanics and Microengineering*, vol. 20, no. 5, p. 055020.

[4] Daly, D. (2001). *Microlens arrays*. Taylor & Francis, London . New York.

[5] Trumper, D. L., Lu, X. (2007). Fast tool servos: advances in precision, acceleration, and bandwidth. In *Towards Synthesis of Micro-/Nano-systems*, Springer, p. 11–19.

[6] Brecher, C., Wetter, O. (2005). Manufacturing of free-form surfaces using a fast tool servo (FTS) and an online trajectory generator. In *Proceedings of ASPE winter topical meeting*.

[7] Chen, W.-C., Wu, T.-J., Wu, W.-J., Su, G.-D. J. (2013). Fabrication of inkjet-printed SU-8 photoresist microlenses using hydrophilic confinement. *Journal of Micromechanics and Microengineering*, vol. 23, no. 6, p. 065008.

[8] Fakhfouri, V., Cantale, N., Mermoud, G., Kim, J. Y., Boiko, D., Charbon, E., Martinoli, A., Brugger, J. (2008). Inkjet printing of SU-8 for polymer-based MEMS a case study for microlenses. In *Micro Electro Mechanical Systems, 2008. MEMS 2008. IEEE 21st International Conference on*, pp. 407–410.

[9] Lorber, B., Hsiao, W.-K., Hutchings, I. M., Martin, K. R. (2014). Adult rat retinal ganglion cells and glia can be printed by piezoelectric inkjet printing. *Biofabrication*, vol. 6, no. 1, p. 015001.

[10] Blessing, K., Vrie, R. van de (2013). *Print head, upgrade kit for a conventional inkjet printer, printer and method for printing optical structures*. Google Patents, US 8840235 B2.

[11] Biehl, S., Danzebrink, R., Oliveira, P., Aegerter, M. A. (1998). Refractive microlens fabrication by ink-jet process. *Journal of Sol-Gel Science and Technology*, vol. 13, no. 1–3, p. 177–182.

[12] Popovic, Z. D., Sprague, R. A., Connell, G. A. N. (1988). Technique for monolithic fabrication of microlens arrays. *Applied. Optics*, vol. 27, no. 7, p. 1281-1284.

[13] Roy, E., Voisin, B., Gravel, J.-F., Peytavi, R., Boudreau, D., Veres, T. (2009). Microlens array fabrication by enhanced thermal reflow process: Towards efficient collection of fluorescence light from microarrays. *Microelectronic Engineering*, vol. 86, no. 11, p. 2255–2261.

Validation of automated surface quality inspection for aluminum castings

Elvedin Trakić [a*], Jaka Pribošek [b], Bahrudin Šarić [a], Janez Diaci [b]

[(a)] University of Tuzla, Faculty of Mechanical Engineering, Univerzitetska 4, 75 000 Tuzla, Bosnia and Herzegovina.

[(b)] University of Ljubljana, Faculty of Mechanical Engineering, Aškerčeva 6, 1000 Ljubljana, Slovenia.

* Correspondence author:
E-mail: elvedin.trakic@untz.ba

Abstract

This paper addresses the problem of quality assurance in high-pressure die casting technology. Since current industrial practice of manual visual inspections is very subjective and depends entirely on the visual skills of the inspector, there is a reasonable motivation and need for new methods that could replace manual inspection techniques. This paper presents a methodology based on the 3D laser triangulation combined with unique algorithm for surface quality inspection. The inspection algorithm bases on human experiences gained in current manual inspection method. The measured point cloud is first aligned with the reference CAD model. Once aligned, the algorithm detects and characterizes surface errors. The experimental comparison of proposed methodology with manual inspection has shown the increase in surface defects detection rate, as well as increase in repeatability and reliability of surface inspection of aluminum castings.

1 Introduction

Continuously increasing expected precision of complex products in automotive industry requires adequate quality control. Until now, sole human visual inspection is employed for surface quality control during the manufacturing process. Subjective assessment of each individual operator, and confusion induced by possible surface irregularities often leads to unnecessary misclassification of the product. [1,2]. Such method of control is less adequate because of increased costs and inrealiable results due to subjective assessment. Deviations in terms of the functionality of the castings may be acceptable at certain locations approved by the end user who quantitatively specifies the permitted shapes, sizes and locations of such deviations. The diversity of such conditions often creates confusion in the process of product quality control. Due to the subjectivity of operators either disposal of products that meet the quality requirements or unwanted reclamations often arise. Therefore, our effort is to find a suitable alternative method, which will be cheaper and more reliable in the sense that it

will eliminate the subjectivity of results and ensure good repeatability. In addition to that, the method should be easily integrated in the production chain to avoid expensive laboratory measurements. This paper presents the methodology of automatic quality control of the aluminium castings based on the application of the active laser triangulation [3].

2 Methods

The automated characterization starts with the 3D shape measurement is based on laser triangulation technique, which measures point cloud of the casting surface. The pointcloud refers to the equidistant locations with respect to the measurement coordinate system. First step towards surface characterization is the alignment of the 3D model with the CAD model, to allow for surface quality estimation.

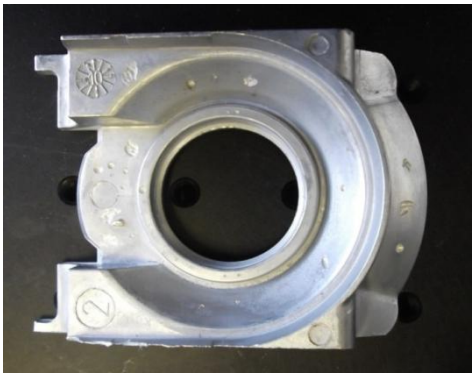

Figure 1. Photograph of the casting under inspection

The alignment is done with a two stage alignment process following coarse to fine paradigm. First the principal component analysis is employed to align the measured pointcloud fast and approximate manner, which is then precisely refined by iterative closest point method (ICP). [4],[5]. The combination of both processes allows for fast and precise alignment. Once the pointcloud is aligned to the CAD model, the surface deviation is estimated. The surface is then divided into several different regions of interests (ROI), which facilites the use of different regional dependant criteria for quality inspection. This follows an idea of human visual inspection. If all ROI meet the quality requirements, the product is qualified as good. The whole algorithm is depicted in Fig. 2 and shows the idea of systematically data reduction from 3D cloudpoint to final good/bad binary classification.

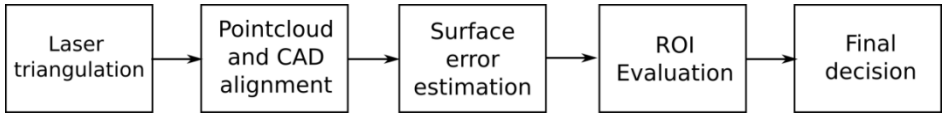

Figure 1. Concept of the method for automated classification of castings

The results of the automatic inspection method should follow either the criteria given by quality specification, or criteria of existing human visual inspection [6,7]. In our case, the criteria are established on the experience of human visual inspection. The parameters and criteria of automated inspection method are tuned empirically, until the required accuracy and compliance with expert inspection is obtained.

3 Experiments

Primary goal of the experiment is to validate the performance of the automatic inspection. In order to do that, 11 castings were exempted from the production process. Among those, 3 castings were non-compliant, where diversity of locations and shapes of surface irregularities represent a representative sample for assessing the impact of subjectivity of human visual inspection. In the experiment participate 4 operators, where two of them have gained years of experience in quality control (Operator 1 and Operator 4). Manual casting classification was carried out individually with all participants, and repeated three times at different time intervals. In addition to that, all 4 operator evaluated the castings together, forming an expert consensus, which represents the final human visual classification. All castings have been previously marked so that operators do not have insight into their previous classifications.

4 Results

Table 2 The outcomes of validation experiment (P = “PASS”, F = “FAIL”)

Sample	Operator 1			Operator 2			Operator 3			Operator 4			Consensus
	1	2	3	1	2	3	1	2	3	1	2	3	
1	P	P	P	P	P	P	P	F	P	P	P	P	P
2	P	P	P	P	P	P	P	P	P	P	P	P	P
3	P	P	P	P	P	F	P	F	P	P	P	P	P
4	P	P	P	P	P	P	P	P	P	P	P	P	P
5	P	P	P	P	P	F	F	P	P	P	P	P	P
6	P	P	P	P	P	P	F	P	P	P	F	P	P
7	P	P	P	P	P	P	F	P	P	P	P	P	P
8	F	F	F	F	F	F	F	F	P	F	P	F	F
9	P	P	P	P	P	P	F	F	F	P	P	P	P
10	F	F	F	F	F	F	F	F	F	F	F	F	F
11	F	F	F	F	F	F	F	F	F	F	F	F	F

5 Analysis and discussion

The conducted experiment has shown the subjective assessment of individual operators in the process of human visual inspection. We performed the analysis of variance in order to evaluate the experimental data. The analysis have shown significant deviation of individual operator compared to the consensus of all 4 operators. The assessments score and deviations of each individual operator is represented in the Fig.3.

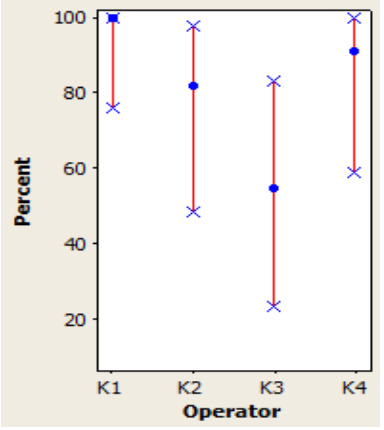

Figure 3. Analysis of variance

Next the automated inspection was employed. The performance of the automated inspection is controlled by multiple parameters of the algorithm carrying out the inspection and classification task. Parameters have been tuned on a large number of castings in an iterative manner until the outcome was satisfactorily similar to that of human visual inspection. We then validate the performance of tuned automatic inspection on a sample of 11 castings, previously characterized by expert operators (Figure 4). Additional iterative adjustment of parameters of the algorithm, disagreements automatic characterization improves in the exact characterization (sample 4,7,8 and 9).

Sample	Cosensus	Automatic Inspection
1	FAIL	FAIL
2	FAIL	FAIL
3	FAIL	FAIL
4	FAIL	PASS
5	PASS	PASS
6	FAIL	FAIL
7	PASS	FAIL
8	PASS	FAIL
9	FAIL	PASS
10	PASS	PASS
11	PASS	PASS

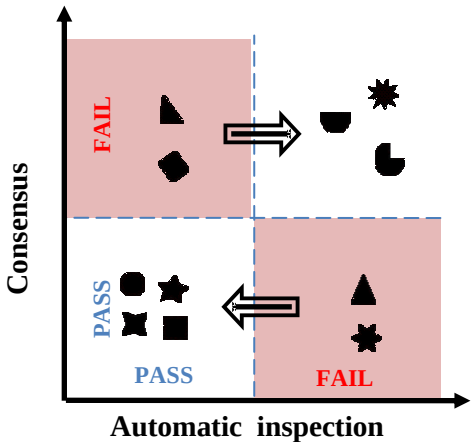

Figure 4. Setting the automatic selection criteria castings.

6 Conclusion

The experiment of subjectivity of human visual inspection was carried out. The experiments have shown major effect of subjective assessment of each individual operator which lowers the accuracy of the characterization and results in final misclassifications of the castings. Automated method based on laser triangulation was employed in order to eliminate the effect of human subjective assessment. The performance of the automated inspection is controlled by parameters, tuned empirically so the classification converges to that of human visual characterization. After the empirical tuning, validational experiment was carried out. Good agreement of automatic inspection with visual inspection methods on a set of 11 characteristic castings is obtained.

7 References

[1] Bračun, D., Jezeršek, M., Diaci, J. (2006). Triangulation model taking into account light sheet curvature. *Measurement Science & Technology*, vol.17, no.8, p. 2191- 2196.

[2] Muhič, M., Tušek, J., Kosel, F., Klobčar, D., Pleterski, M., (2010). Thermal fatigue cracking of die-casting dies. *Metalurgija* vol. 49, no. 1, p. 9–12.

[3] Bračun, D., Gruden, V., Možina, J. (2008). A method for surface quality assessment of die-castings based on laser triangulation. *Measurement Science & Technology*, vol. 19, no. 4, p. 1-8.

[4] Fitzgibbon, A. W. (2003). Robust registration of 2D and 3D point sets. *Image and Vision Computing*, vol. 21, p.1145–1153.

[5] Jolliffe, I.T. (2002). *Principal Component Analysis, Second Edition* , Springer.

[6] Bračun, D., Perdan, B., Diaci, J. (2011). Surface defect detection on power transmission belts using laser profilometry. *Strojni vestnik - Journal of Mechanical Engineering*, vol. 57, no. 3, p. 257-266.

[7] Trakić, E. (2014). *Primjena opto-mehatroničkih sistema za karakterizaciju proizvoda kompleksnih oblika*. Doctoral thesis. University of Tuzla, Faculty of Mecanical Engineering.

Quantitative risk assessment on transmission network for natural gas

Tom Bajcar [a*], Franc Cimerman [b], Brane Širok [a], Aljaž Osterman [a]

[(a)] University of Ljubljana, Faculty of Mechanical Engineering, Aškerčeva 6, 1000 Ljubljana, Slovenia.

[(b)] Plinovodi d.o.o., Cesta Ljubljanske brigade 11b, 1000 Ljubljana, Slovenia.

* Corresponding author:
E-mail: tom.bajcar@fs.uni-lj.si

Abstract

Increasing length of transmission pipelines for natural gas that also spread into urban areas has spawned the need for safety and assessment of risk, which is posed on environment by such a gas transmission network. In order to achieve reliable, safe enough and continuous operation of transmission system for natural gas, its influence on environment should be minimized. Apart from that, early recognition of less reliable parts of the system that endanger the operation of the gas network is desirable as well. Therefore, certain tools for risk assessment and risk management should be applied. In this way, the system operator is able to monitor continuously the operation of the system as well as to detect potential risks due to technical and operational issues or environmental influences. Such tools usually present a part of an integral system for safety management, which serves for safety management of employees and public, protection of urban, natural or industrial environment as well as for operational reliability of natural gas transmission network. Risk is usually assessed by special models, which should be developed in accordance with standards and legislation. Their main task is to model consequences of hazardous events, to predict the frequency of such events and to assess risk with the ability to incorporate different risk mitigation measures. Particularly important is the method of quantitative risk assessment that enables the magnitude of risk to be assessed as a numerical value.

1 Introduction

The age of existing natural gas networks is getting higher. At the same time, more and more new high pressure pipelines are introduced due to ever rising energy needs in EU countries. Accordingly, the risk that these systems pose on the environment in their vicinity rises as well. In order to keep the risk in acceptable levels, a system or model for risk assessment and risk management should be applied whenever new pipelines are laid close to existing inhabited buildings or vice versa (i.e. when new building are to be built close to existing pipelines or pipeline objects).

Risk is generally defined as a measure for likelihood and severity (injuries or harm) of an event. It can be therefore written as [1, 2]:

$$\text{Event risk} = \text{Event frequency} \times \text{Event consequences} \quad (1)$$

Individual risk is annual probability that a person in the vicinity of a hazardous object dies due to potential hazardous events on that object. On the other hand, societal risk represents the annual expected number of casualties due to hazardous events.

Safety results from the judgement of acceptability of risk: an activity is assessed as safe if the level of its risk is assessed as acceptable. General acceptability criterion (= upper acceptable margin) in many EU countries for individual risk due to natural gas network is $1 \cdot 10^{-6}$/year. Acceptable risk levels are usually provided by national legislation.

Risk assessment procedure generally consists of the following steps:

- determination of hazard (i.e. specific hazardous events that can occur on the system);
- determination of consequences of hazardous events;
- determination of frequency of hazardous events;
- evaluation of assessed risk.

If the assessed risk is too high, it should be reduced with the use of different additional risk mitigation measures or (rarely) by changing operational parameters ("what if" scenarios). The whole above procedure is then repeated until the acceptable risk level is reached.

A general concept of a model for individual risk assessment on transmission pipeline network for natural gas is presented below. It comprises quantified risk assessment (QRA) on pipelines and on other gas transmission objects (such as metering-regulation stations - MRS). The model is a result of broad European experiences as well as domestic (local) knowledge.

2 Risk analysis

Determination of event consequences

The most unwanted event on natural gas transmission network is the uncontrolled gas leak and ignition of escaped gas due to failures on the system. Consequences of such a hazardous event are usually heat radiation of burning gas jet (in unobstructed areas) and/or explosion of flammable mixture of natural gas and air (in obstructed areas); they both cause negative effects on inhabitants in the vicinity (injuries, casualties). Heat radiation of burning gas jet generally occurs in the case of pipeline failure, while explosions potentially happen in enclosed spaces (objects such as MRS).

Effects of heat radiation on people depend on heat flux density and time of exposure to heat radiation [3]. According to past experiences [2, 3], the exposure time of 20 s is

usually taken as an average time period for a person needed to find appropriate shelter. In this time period, the amount of heat flux density that surpasses 35 kW/m^2 is deemed as 100% lethal, while 9.84 kW/m^2 represents 1% lethality [2].

Radiation heat flux density and its consequences diminish with distance from the radiation source; consequences can have effect on the recipient (person) up to a certain distance r_h (Fig. 1). The distance r_h defines the effective length L of pipeline, within which a hazardous event (*HE*) can still cause detrimental effects on a person at a distance h from the pipeline.

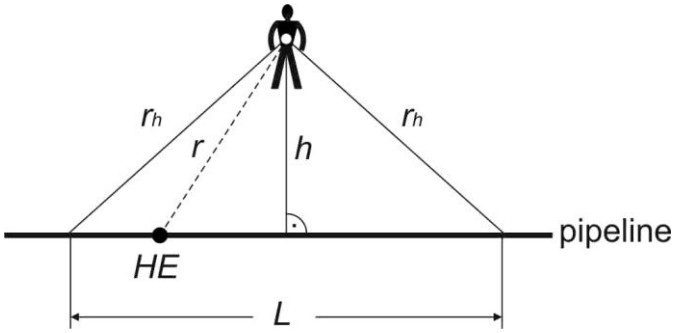

Figure 1: Effective pipeline length L, where an unwanted event (burning jet fire and its heat radiation) can still affect the recipient (person).

The length L rises together with the pipeline diameter and natural gas pressure. The amount of escaped natural gas from a damaged pipeline can be determined analitically or through numerical simulations using computational fluid dynamics (CFD) methods (Fig. 2).

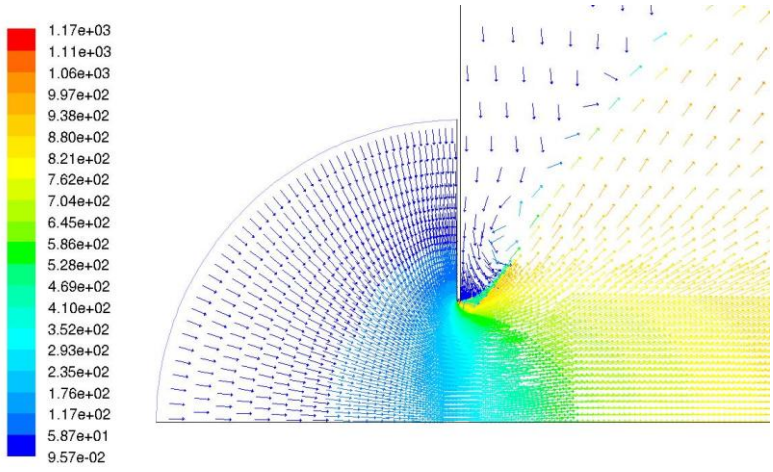

Figure 2: Numerical (CFD) simulation of velocity field of escaping natural gas through a hole (damage) in a high pressure gas pipeline.

Explosion of natural gas – air mixture occurs in obstructed (enclosed) space. Its effects (i.e. pressure waves) depend on the highest level of overpressure at the location of the recipient (person). There are many different approaches and models to assess the lethality of explosion; one of them is the so-called multi-energy method, where there are two boundary pressure levels: 0.3 bar or more (100% lethality if exposed) and 0.1 bar or lower (0% lethality) [3].

Consequences of explosion diminish as well with the distance from the explosion centre; their magnitude depends mainly on the amount of the explosive mixture (i.e. the size of the explosive cloud) and its combustion heat.

Determination of event frequencies

Hazardous event frequencies can generally be extracted from historical databases that contain information on already occurred past events [4, 5]. The event frequencies are affected by different risk sources that cause damage on natural gas transmission network. In the case of pipelines, these sources can be usually classified into one of the following groups: third-party interference (usually the risk source linked with the highest hazardous event frequencies [4]), construction/material defects, corrosion, ground movements, hot taps and others (such as lightning strike etc.) On the other hand, in enclosed secured gas installations (such as MRS) with the risk of explosion, the sources of risk comprise the inspection intervals of gas installations and the quality of ventilation [6].

When event consequences (Section 2.1) and event frequencies are determined, one can assess the risk on the selected section of the pipeline or pipeline object according to Eq. 1.

3 Risk mitigation measures

Mitigation of risk is needed whenever the assessed risk exceeds the acceptable value. In such cases, risk mitigation measures should be applied to chosen gas transmission network segments with unacceptable high risk. After that, the whole procedure of risk assessment should be repeated to see if the value of newly assessed risk lies within the acceptable range. Risk mitigation measures are usually applied in order to reduce the event frequencies rather than event consequences.

If the transmission pipelines are in question, the most used risk mitigation measures comprise the inspection enhancement (aerial and ground inspection, pipeline pigging), warning enhancement (buried warning tapes and surface line markers above the pipeline) and mechanical protection enhancement (increased pipe wall thickness and protective slabs) [5, 7].

While the mitigation of risk in closed installations (such as MRS) is possible by more frequent inspections, it is usually more efficient to enhance the ventilation in such objects; the consequence is lower probability of occurrence of explosive atmosphere [6]. If these measures are not enough, the risk levels can be further lowered by

installation of protective walls around the risky object. The function of these walls is to obstruct the propagation of pressure waves and thus to shorten the range of explosion consequences (Fig. 3).

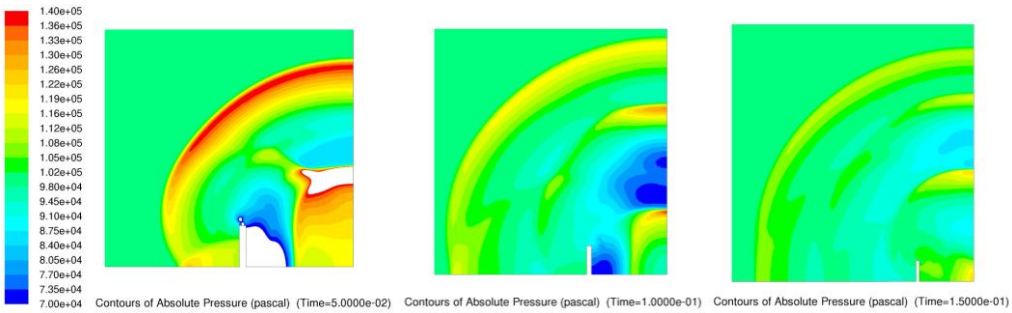

Figure 3: Propagation of pressure wave over protective wall (time interval between succesive images is 0.05 s).

4 Results

Following the above described steps the model can be able to assess individual risk due to transmission network for natural gas. With the appropriate input of all required parameters (together with pipeline coordinates and locations for particular gas installations, the final result can be seen in Fig. 4.

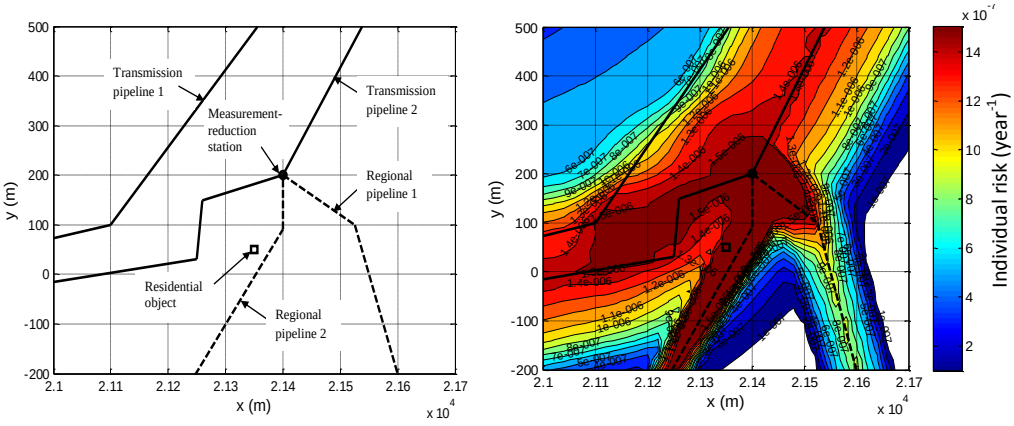

Figure 4: Presentation of individual risk due to natural gas transmission network on a specified location.

The nature of the model, as presented in Fig. 4, can serve for risk-mapping the whole desired area and can further be enhanced by connections with geographic information system (GIS).

5 Conclusions

The main benefits from the presented concept of a model that enables the risk assessment on the whole transmission network for natural gas can be presented as follows:.

- Ability of joint quantitative risk assessment on both, natural gas pipelines and natural gas installations (such as metering-reduction stations).
- Apart from operational and constructive parameters, the layout of the pipeline network also plays important role in the presented model.
- The model can show different iso-risk contours in ground projection, among others the one that represents acceptable risk margin.
- Quantification and evaluation of mitigation measures effects on risk.
- Ability to change gas network parameters („what-if" scenarios).
- Ability to produce risk maps in connection with GIS.

6 References

[1] IGEM – Institution of Gas Engineers and Managers (2008). *Steel Pipelines and Associated Installations for High pressure Gas Transmission, Recommendations on Transmission and Distribution Practice*. IGEM/TD/1 Edition 5, Loughborough.

[2] CPR 18E Purple Book (1999). *Guideline for Quantitative Risk Assessment, Committee for the Prevention of Disasters*, The Hague.

[3] CPR 14E Yellow Book (2005). *Methods for the calculation of physical effects, 3rd edition*, Committee for the Prevention of Disasters, The Hague.

[4] EGIG – European Gas pipeline Incident data Group (2011). *Gas Pipeline Incidents 8th Report 1970-2010*, Groningen.

[5] Mather J., Blackmore C., Petrie A., Treves C. (2001). An assessment of measures in use for gas pipelines to mitigate against damage caused by third party activity, Contract Research Report 372/2001, *Health and Safety Executive*.

[6] Bajcar, T., Cimerman, F., Širok, B. (2014). Model for quantitative risk assessment on naturally ventilated metering-regulation stations for natural gas. *Safety Science*, vol. 64, p. 50–59.

[7] Bajcar, T., Širok, B., Cimerman, F., Eberlinc, M. (2008). Quantification of impact of line markers on risk on transmission pipelines with natural gas. *Journal of loss prevention in process industry*, vol. 21, no. 6, p. 613-619.

»Jolt« - New criterium of safety in climbing

Anatolij Nikonov [a*], Stojan Burnik [b], Bojan Rotovnik [c], Igor Emri [a]

[(a)] University of Ljubljana, Faculty of Mechanical Engineering, Aškerčeva 6, 1000 Ljubljana, Slovenia.

[(b)] University of Ljubljana, Faculty of Sport, Gortanova 22, 1000 Ljubljana Slovenia.

[(c)] Planinska zveza Slovenije, Dvorakova 9, 1000 Ljubljana, Slovenia.

* Corresponding author:
E-mail: anatoly.nikonov@fs.uni-lj.si

Abstract

In-house developed experimental-numerical-analytical (ENA) methodology based on a simple non-standard falling weight experiment, was used for mechanical characterization of "dry" and "wet" climbing ropes. Analysis of the maximum impact force; the amount of dissipated energy; the stiffness of the rope; and the maximum value of the first derivative of the de-acceleration (jolt) showed that moisture significantly affects the functionality and durability of ropes. "Wet" ropes create larger maximum force, dissipate less energy, and generate larger retrieved energy that propels climbers in the opposite vertical direction. Properties of "wet" ropes are also more sensitive to number of repeated drops. It has been shown that for the safety of climbers the most indicative properties are dissipated energy and jolt (first derivative of climber de-acceleration).

1 Introduction

Quality of climbing ropes is determined by two parameters, i.e. climber safety and rope's durability [1]. Durability in this case does not mean just failure of a rope, but rather deterioration of its time-dependent response when exposed to an impact force. Both parameters are governed by time-dependent properties of the material from which ropes are manufactured.

The UIAA (Union Internationale des Associations d'Alpinisme) has established standard testing procedures to measure how ropes react to severe drops [2]. The standard says little about the durability of ropes, which is more difficult to define or assess with a simplified procedures. The experiments prescribed by the UIAA standard are not geared to analyze the time-dependent deformation process of the rope, which causes structural changes in the material and consequently affects the functionality and durability of the rope itself. This is particularly important when ropes are exposed to extreme weather conditions.

It is well known that humidity notably affects the characteristics of ropes, in particular those that are fabricated from polyamide (PA) fibers. "Wet" ropes become difficult to manage, bear fewer drops, and have less strength [3]. Cotugno et al. reviewed processes involved in absorption of water by polymeric yarns [4]. The plasticization effect of water causes reductions in elastic modulus and yield strength. This occurs by changing the mechanisms of yield and deformation, as well as cutting of polymer chains by hydrolysis. Nylon-6 absorbs large quantities of water, which causes significant changes in mechanical properties and a reduction in the polymer's glass transition temperature.

Water acts like a plasticizer, and it strongly modifies the mobility of the amorphous part of a PA material and shifts, similar as temperature [5], mechanical response functions and corresponding spectrums along the logarithmic time scale towards the "shorter" times. Thus moisture may drastically change the time-dependent properties of PA, and consequently hamper the safety of climbers.

Knowledge on the viscoelastic nature of materials is one of the main understandings required for determining new criteria for safer climbing ropes, i.e., smaller impact force, bigger dissipation energy, less stiffness, less elongation, smaller jolt, etc. However, there is relatively little known about the influence of time-dependent properties of polymeric materials on the mechanical behaviour of ropes. Therefore, more detailed experimental and analytical analysis of time-dependency of materials from which the ropes are made on their behaviour under impact loading is needed.

We have developed a new Experimental-Numerical-Analytical (ENA) methodology [6], which allows prediction of thirteen physical parameters describing dynamic behaviour of tested ropes, and consequently safety of climbers. All these parameters can be determined from a measured time-dependent (dynamic) response of ropes exposed to a falling-weight impulse loading.

2 Experimental work

Time-dependent response of a rope exposed to dynamic loading generated by a falling mass (deadweight) may be retrieved from the analysis of the force measured at the upper fixture of the rope. This force is transmitted through the rope and acts on the falling weight (mass), as schematically shown in Fig. 1a. In such experiments a mass, m, is dropped from an arbitrary height, $h \leq 2l_0$, where l_0 is the length of the tested rope. Details of experimental setup and measuring methodology are described elsewhere [7].

We have tested four "dry" and four "wet" specimens prepared from the same commercial rope. Tested rope was single rope made out of polyamide fibers. The length of all samples was the same, i.e. l_0. Diameter of the rope was 9.7 mm, and weight per meter was 63 g. Core of the rope consisted of nine 3-ply yarns. The set of "dry" ropes were then kept at room condition, whereas the "wet" samples were immersed in water at $26 \pm 2^{\circ}\mathrm{C}$ for 96 hours. Each rope was then exposed to 10

consecutive impact loadings (drops of deadweight) with the time interval of 5 minutes between each drop. Examples of the measured force for “dry” and “wet” samples during the first impact loading are shown in Fig. 1b.

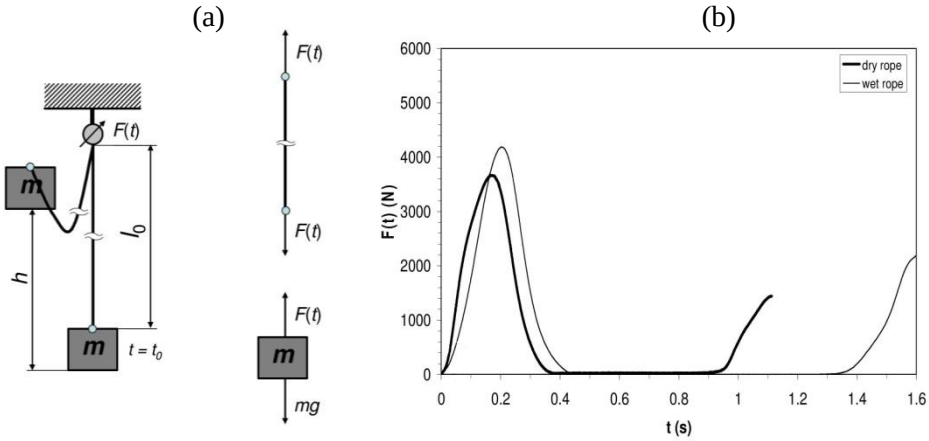

Figure 1. (a) Schematics of the rope exposed to the falling mass, and (b) an example of measured force as function of time for a “dry” and a “wet” rope during the first impact loading.

The equation of motion of the moving mass may be written as $m\ddot{s}(t) = mg - F(t)$, where $\ddot{s}(t)$ denotes the second derivative of the weight displacement that corresponds to the evolution of the rope deformation. Taking into account the initial conditions, $s(0) = 0$ and $\dot{s}(0) = \sqrt{2gh}$, the solution of the equation of motion gives the displacement of the weight as function of time. Knowing the force and the displacement of the weight, deformation energy of the rope may be calculated as function of time accordingly to the experimental-numerical-analytical (ENA) methodology presented in [6].

For each of the ten consecutive drops we analyze the maximum impact force, $F_{\max}$; the amount of dissipated energy, W_{dis}; the stiffness of the rope, k_{ini}, at $F(t) = mg$; and the maximum value of the first derivative of the de-acceleration, $j_{\max}$, commonly called jolt.

3 Results and discussion

The first important quantity is the maximum force $F_{\max}$ that is acting upon the climber during the loading cycle. This quantity is measured directly and is also prescribed by

the standard EN 892:2004 (see Ref. [2]). Fig. 2a shows comparison of $F_{\max}$ as function of number of drops for "dry" and "wet" ropes.

Dissipated energy, W_{dis}, is one of the most important and most desirable characteristics of climbing ropes. This is the energy that is "absorbed" by the rope during the loading cycle. There are two major mechanisms of energy dissipation. The first is Coulomb friction between the individual fibers, whereas the second is dissipation of energy due to the time-dependent (visco-elasto-plastic) behaviour of polymeric material (in our case polyamide) from which individual fibers are made. During rope deformation both mechanisms happen simultaneously. Comparison of "dry" and "wet" ropes as function of number of drops is shown in Fig. 2b.

All presented results are average values of measurements performed on four "dry" ropes and four "wet" ropes. Standard deviations, indicated in all figures, show good repeatability of experimental results. As expected, standard deviations for experiments on "wet" ropes are slightly larger than those for experiments on "dry" ropes. Nevertheless, the repeatability of measurements is still very good.

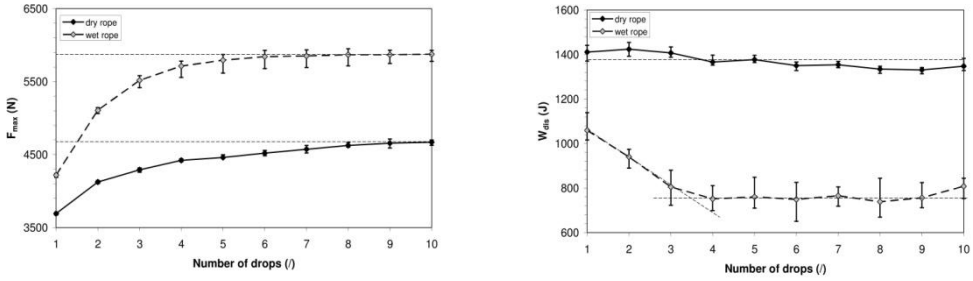

Figure 2. (a) Maximum force acting on "dry" and "wet" ropes (force acting on climbers), and (b) dissipated energy as functions of number of drops.

From the shown results we may observe that "dry" and "wet" ropes behave significantly different. The difference in $F_{\max}$ at the first drop is not so large, however, with the increased number of drops the maximum force for "wet" ropes increases much faster than that of "dry" ropes. In fact, already at the second impact loading the maximum force of "wet" ropes exceeds the maximum force that is reached with "dry" ropes after ten consecutive drops. Thus, one could as well say that the life-time of "wet" ropes is ten times shorter then that of "dry" ropes! For climbers this is definitely information that should be considered very seriously.

From Fig. 2b, showing rope's energy absorption capability, we may clearly observe huge difference between the "dry" and "wet" ropes. While W_{dis} of "dry" ropes does not change much with number of loading cycles (drops), the "wet" ropes after four drops literary lose potential of dissipating kinetic energy of a falling climber. Already at the fourth drop W_{dis} of "wet" ropes is almost half smaller than that of the

corresponding “dry” ropes. Hence, moisture has indeed tremendous effect on performance of climbing ropes. Thus, climbers must be especially cautious when climbing in “wet” conditions.

Another very important parameter that determines the quality of climbing ropes is a derivative of climber acceleration or de-acceleration, commonly called as jolt. From the experience in human space explorations and from car crash experiments it is known that for human beings the change of acceleration or de-acceleration, i.e., magnitude of jolt, is more dangerous than the magnitude of acceleration (inertial force) to which a body is exposed.

From some investigations it is known that maximum jolt should not exceed $j = 120\ g/s$. However, at present there are no unique tolerance limits for fall-arrest (de-)acceleration. Fig. 3a shows how jolt is changing with number of drops. We may see that “dry” ropes reach the critical value of $j = 120\ g/s$ only after 10 consecutive drops. On the other hand “wet” ropes reach the critical value already during the second drop. For climbers, particularly beginners, this is a very alarming finding, which requires further systematic analysis of this problem.

Stiffness was calculated as $k_{ini} = \left[dF(s)/ds \right]_{F=mg}$. Comparison of “wet” and “dry” ropes stiffness as function of number of drops is shown in Fig. 3b. As one would expect “dry” ropes are almost twice as stiff as “wet” ropes. For both ropes we observe that main changes of the stiffness happen during the first three loading cycles, and from then on it remains practically unchanged.

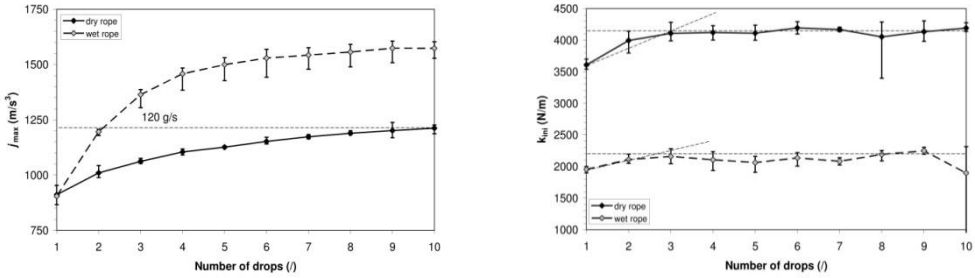

Figure 3. (a) Maximum jolt generated during the impact loading of “dry” and “wet” rope, and (b) stiffness of the “dry” and “wet” rope at the beginning of each impact loading at $F = mg$ as functions of number of drops.

4 Conclusions

Experimental analysis of “dry” and “wet” ropes exposed to an impact loading, and using ENA methodology, showed that moisture has a significant effect on the functionality and durability of ropes. In brief, “wet” ropes create larger maximum force and dissipate less energy. Using wet ropes can lead to the change in (de)acceleration

which exceeds the critical safety limit and endanger the user of the rope. These results also indicate that mechanical properties of ropes are governed mainly by the time dependency of the material, from which the rope is manufactured.

More particular findings may be summarized as follows:

(i) With the increased number of loading cycles the maximum force for "wet" ropes increases much faster than that of "dry" ropes. Already at the second loading the maximum force of "wet" ropes exceeds the maximum force that is reached with "dry" ropes after ten drops.

(ii) Dissipated energy of "dry" ropes does not change much with the number of loading cycles, whereas the "wet" ropes after four drops literary loose their potential of dissipating energy of a falling climber.

(iii) Examined "dry" ropes reach the critical jolt value of $j = 120\ g/s$ only after 10 consecutive drops, whereas "wet" ropes reach the critical value already during the second loading cycle.

(iv) Investigated "dry" ropes are almost twice as stiff as "wet" ropes. Main changes of stiffness happen during the first three loading cycles.

5 References

[1] Blackford, J.R. (2003). Materials in mountaineering. Jenkins, M., (Ed.) *Materials in sports equipment*, Cambridge, UK: Woodhead Publishing, p. 279-325.

[2] EN 892:2004 (2004). Mountaineering equipment – Dynamic mountaineering ropes – Safety requirements and test methods. European Standard.

[3] Cox, S.M., Fulsaas, K. (2003). *Mountaineering: the freedom of the hills*. Seattle: The mountaineers.

[4] Cotugno, S., Mensitieri, G., Musto, P., Nicolais, L. (2002). Water sorption and transport in polymers. *Italian Alpine Club Technical Committee*, Turin.

[5] Emri, I., Pavšek, V. (1992). On the influence of moisture on the mechanical properties of polymers. *Mater. forum (Rushcutters Bay)*, p. 123-131.

[6] Emri, I., Nikonov, A., Zupančič, B., Florjančič, U. (2008). Time-dependent behavior of ropes under impact loading – a dynamic analysis. *Sports Technology*, vol. 1, no. 4-5, p. 208-219.

[7] Nikonov, A., Saprunov, I., Zupančič, B., Emri, I. (2011). Influence of moisture on functional properties of climbing ropes. *International Journal of Impact Engineering*, vol. 38, p. 900-909.

Numerical simulation of the whiplash test for a front car seat according to ECE and Euro NCAP regulations

Andrej Škrlec [a], Jernej Klemenc [a*], Mirko Zupanc [b], Vili Malnarič [b]

[(a)] University of Ljubljana, Faculty of Mechanical Engineering, Aškerčeva 6, 1000 Ljubljana, Slovenia.

[(b)] TPV d.d., Kandijska cesta 60, 8000 Novo mesto, Slovenia.

* Corresponding author:
E-mail: jernej.klemenc@fs.uni-lj.si

Abstract

A numerical simulation of the whiplash test for the front car seat according to ECE and Euro NCAP regulations was performed using a finite element method. A purpose was to evaluate the car seat from a company TPV d.d according to Euro NCAP criteria using numerical simulation.

The simulations were performed using an explicit finite element method software Ls-Dyna with the boundary and initial conditions defined according to a EuroNCAP whiplash test. Loads on dummy (accelerations, shear and tensile forces in the dummy's neck area) and dynamics of the seat and head support in rear crash events are necessary information for the whiplash test and are presented together with a 3D model of a car seat and a crash-test dummy Hybrid III.

The simulations were performed in several stages: from the first stage, where only the main elements were included to the last stage where the fabric of the seat and the seat belt were included. In this manuscript the results from the last stage of simulations are presented.

1 Introduction

The Euro NCAP whiplash test is one of the R&D evaluations that is necessary for all of the forward facing front car seats. This procedure enables the manufacturer to dynamically test a motor vehicle seat and its head restraint assembly in order to assess the extent to which they reflect best practice in preventing soft tissue neck injuries [1].

Whiplash is the most commonly occurring injury in road vehicle crashes. In the Euro NCAP regulations [1] it is stated that that 10% of all whiplash injuries are long term and 1% of the whiplash injuries have permanent impairment. The whiplash injuries occur during rear impacts at high and low velocities. In light of this the Euro NCAP test consists of three sled tests simulating a variety of rear crash scenarios at a variety of ΔV magnitudes [1-2].

Our objective was to numerically simulate the Euro NCAP whiplash test for the new seat assembly from company TPV d.d. before the first prototype was built. This kind of numerical evaluations can effectively reduce costs and time for development of the new seat. Results from the simulations can be a basis for potential corrections, modifications and optimizations of the seat structure.

In the paper a finite element model of the seat assembly is first presented. This is followed by a brief summary of the whiplash assessment criteria from the Euro NCAP standard. At the end the results and conclusions are presented.

2 The model with boundary conditions

The finite element model of a car seat consists of a seat structure with deformable foam and fabric, one seatbelt, a deformable crash-test dummy Hybrid III and a supporting structure for the dummy's legs (Figure 1).

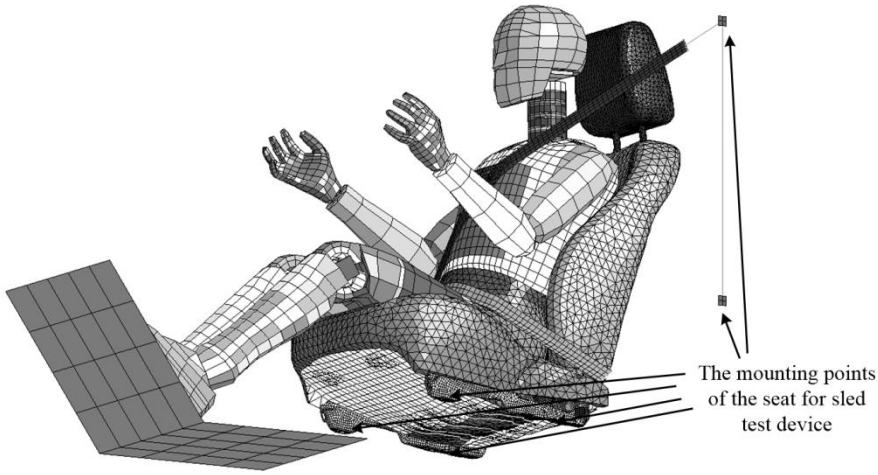

Figure 1. 3D model of the Hybrid III dummy with the seat.

The seat structure was modelled with four-node shell and eight-node solid finite elements, the seat foam was modelled with four-node tetrahedron finite elements and the seat fabric was modelled with four-node and three-node shell elements [3]. To simulate operation of the seatbelt we applied the seatbelt elements from LS-Dyna software, which were shell and beam elements with seatbelt properties [4]. The total numbers of finite elements is listed in the Table 1.

Table 1. Type of the applied finite elements.

Type of the element	Beam	Shell	Solid	Seatbelt
Total number	2644	54278	130772	94

Boundary conditions were applied according to the physical test which is described in Euro NCAP documents [1-2]. The first phase of the test is dummy positioning. First, the H-point of the seat should be determined. Then the dummy should be set into the seat with a proper torso and limbs posture. After setting the dummy, its H-point should be in the prescribed region of the H-point of the seat.

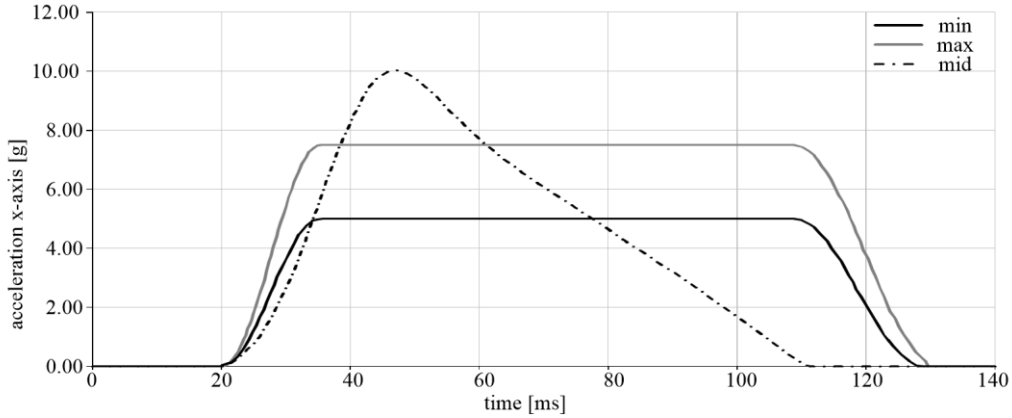

Figure 2. Three applied acceleration pulses.

The second phase is the whiplash test, where three different acceleration pulses (Figure 2) are applied to the test sled, on top of which the seat with a dummy is mounted. In order to perform the dynamic assessment of the seat according to Euro NCAP regulative, the results from all tests are included in whiplash assessment criteria. The criteria are briefly described in Section 3.

In the simulation we set the dummy to the position where the H-points of the seat and the dummy were coincident and posture of dummy's torso and limbs was as it is described in the Euro NCAP regulations [2]. Then we applied the accelerations to the mounting points (Figure 1).

3 Whiplash assessment criteria

There are seven whiplash assessment criteria, which are fully described in Euro NCAP protocol [1] for physical whiplash test. In this section only the essential points of the criteria are presented. In addition, it is also noted, which results were used and how we obtained them from the simulation.

- Head Restrain Contact Time:

  The contact time is defined as a time of the contact duration between the rear of the dummy's head and the head restrain. To obtain the time value, the T-HRC_{start} and T-HRC_{end} should be determined. The T-HRC_{start} is defined as the first contact, where subsequent continuous contact duration exceeds 40ms and the T-HRC_{end} is defined as the time where subsequent continuous loss of contact duration exceeds 40ms.

In the simulation this time points were measured indirectly through the contact forces between the head restraint and the dummy and are presented in Figure 3.

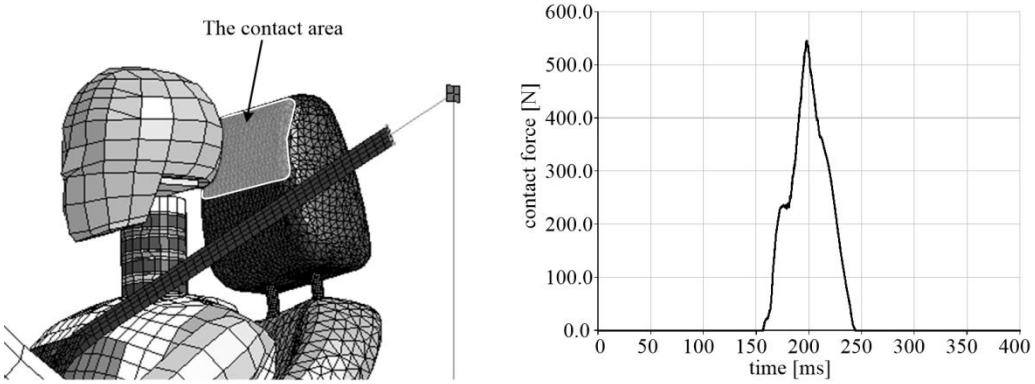

Figure 3. Contact force vs. time to detect contact time.

- T1 x-acceleration:

  BioRID, the dummy which should be used in whiplash test, is fitted with two accelerometers on the first thoracic vertebra (T1), one on either side. The data channels acquired from these accelerometers should be filtered and averaged.

  To obtain this data in the simulation, where we use Hybrid III dummy, the accelerations along x-axes for two nodes on either side of the lower neck (Figure 4) was recorded. The data were filtered to channel frequency class (CFC) 60 and then an average channel was produced from these filtered signals. The result is in Figure 4.

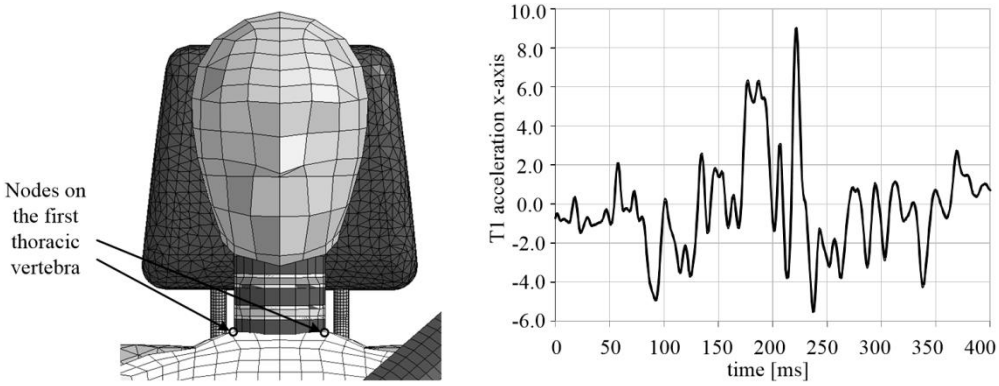

Figure 4. The averaged T1 acceleration for x-axis.

- Upper Neck Shear Force and Upper Neck Tension

  The loadcell on the upper side of the BioRID's neck records both tensile and shear forces. Positive tensile forces should be associated with pulling a head upwards and positive shear forces should be indicative of the head-rewards motion. This data should be filtered at CFC 1000.

  In the simulation we recorded stresses on the upper part of the dummy's neck. From the results of simulations the upper neck tension and shear forces are calculated by numerically integrating the corresponding components of element stress tensors over the neck cross section area. From these data the peak value was determined in the signal range from T-zero to T-HRC_{end}.

- Head Rebound Velocity:

  The head rebound velocity (in the horizontal/X direction) should be determined using target tracking with high speed cameras mounted on the test sled. The rebound velocity is usually generated due to the release of stored elastic energy within the seat structure, suspension and foam. The time of occurrence of peak rebound velocity should be the maximum horizontal component of head rebound velocity calculated between T=0 and 300ms.

  In the simulation this data were obtained by recording a relative velocity between a node on the dummy's head and a node on the sled structure. Recorded signal was filtered at CFC 30 and is presented in Figure 5.

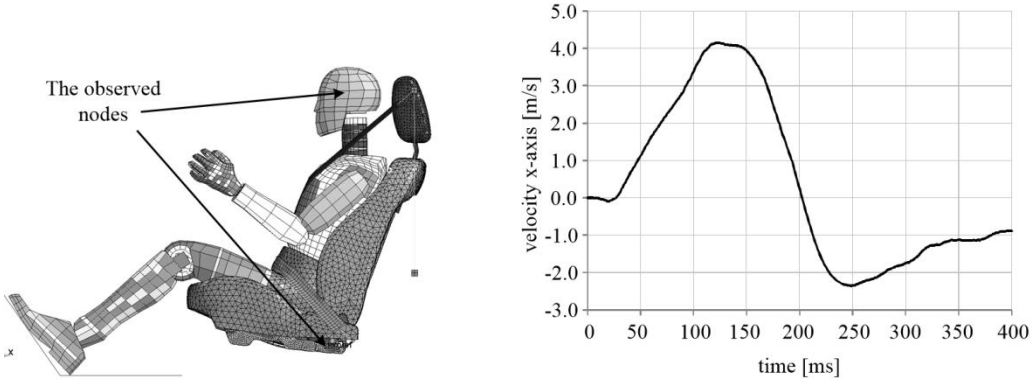

Figure 5. Relative velocity vs. time between presented nodes.

- NIC calculation

  The neck injury criterion (NIC) is based on the relative horizontal acceleration and velocity of the occipital joint relative to T1. To calculate NIC, two data channels are needed, which are the head x-acceleration and average T1 x-acceleration. The calculation is according to the following equation:

$$NIC(t) = 0.2 \cdot \gamma_x^{rel}(t) + \left[V_x^{rel}(t)\right]^2$$

(15)

where $\gamma_x^{rel}(t)$ and $V_x^{rel}(t)$ are relative x-acceleration and relative x-velocity between the head and T1, respectively. The relative x-velocity should be calculated by integrating the relative acceleration channel with respect to time, as follows:

$$V_x^{rel}(t) = \int_0^t \gamma_x^{rel}(\tau)\mathrm{d}\tau$$

(16)

For the head's acceleration in the simulation we observed a node in the centre of gravity of the head. The recorded signal was filtered at CFC 60 (Figure 6) and substracted from the previously calculated T1-acceleration.

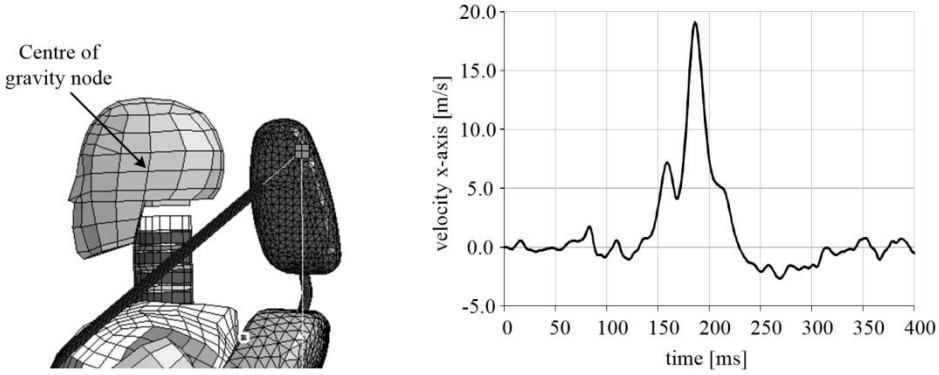

Figure 6. The acceleration for x-axis in the head's centre of gravity.

- Nkm criterion

  The Nkm criterion is based on a combination of moment and shear forces in the neck area using critical intercept values for the load and moment. Two channels are required to perform Nkm calculation, upper neck shear force and moment. Both signals should be filtered at CFC 600. The complete calculation of the Nkm criterion is written in Euro NCAP regulation [1].

- Seatback Dynamic Opening

  The Seatback Dynamic Opening is defined as the maximum change in angle between two lines achieved at any time during the test between the T zero position and T-HRC(end). The lines are defined using forward and rearward sled targets and lower and upper seatback targets. This criterion is used only for the maximum pulse acceleration.

In the simulation these lines were defined with nodes at approximate position where sled and seatback targets are defined (Figure 7).

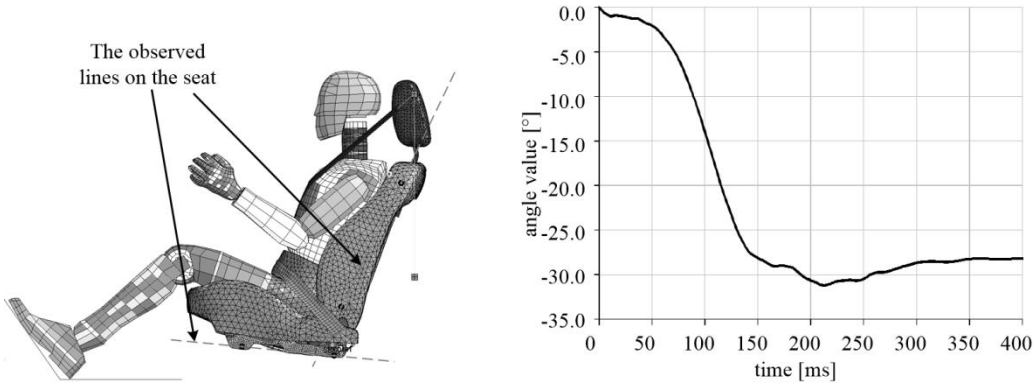

Figure 7. The change in angle between determined lines.

4 Simulations results for the minimum pulse acceleration

In the Figure 8 positions of the dummy and dynamic response of the seat at four different time steps are presented (t=0 ms, t=100 ms, t=200 ms, t=300 ms).

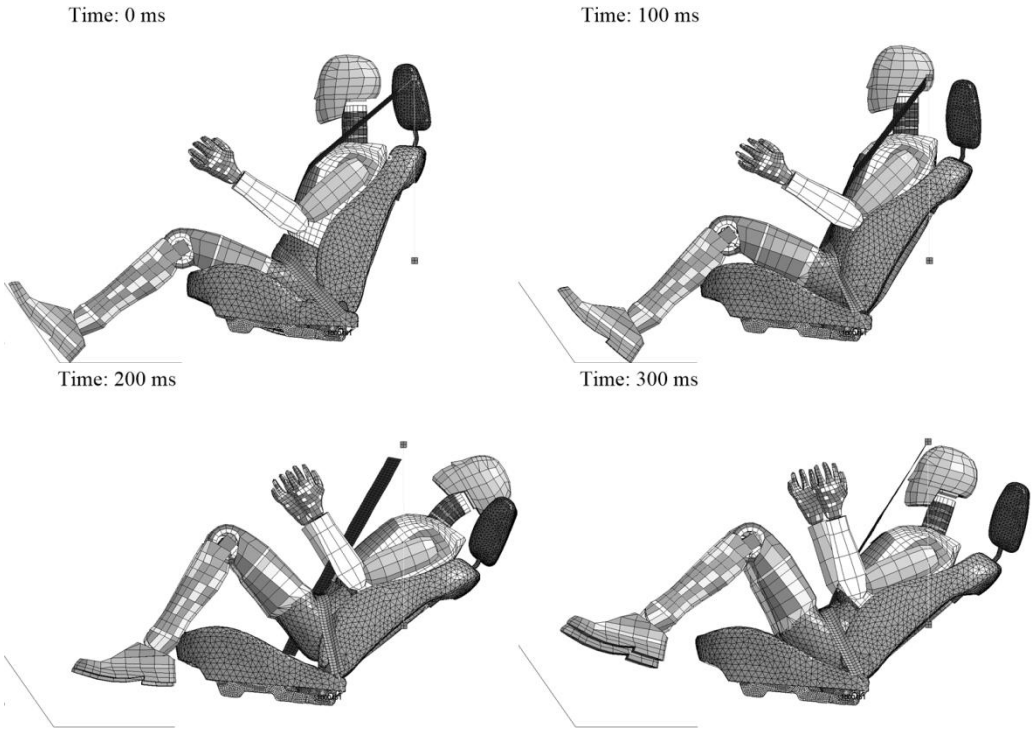

Figure 8: Dynamic response for four timesteps.

From all results we can see, that acceleration and velocity values are meaningful and in reasonable ranges. If we compare last figure with sequences of the Euro NCAP whiplash test video, we can say that displacement and the dynamic response of the seat are in the same order of magnitude that in our simulation. We can conclude that even if we did not use the appropriate dummy for whiplash test, the simulation results could be used as a good approximation.

5 Conclusions

In the manuscript the whiplash test simulation for the front car seat was presented that was performed according to the Euro NCAP regulations using an explicit finite element method. The aim of the project was to evaluate the new car seat before the prototype was build. This kind of numerical evaluation can reduce development time and costs of the new seat.

6 Acknowledgement

The authors would like to thank the TPV d.d. company for financial support of this research.

7 References

[1] Euro NCAP (2010). *The dynamic assessment of car seats for neck injury protection testing protocol*. Version 3.0.

[2] Euro NCAP (2010). *Assessement protocol – adult occupant protection*. Version 5.2.

[3] Hallquist, J.O (1998). LS-*DYNA Theoretical manual*. Livermore software technology corporation, Livermore, California.

[4] *LS-DYNA Keyword manual* (1998). Livermore software technology corporation, Livermore, California.

AKADEMIJA STROJNIŠTVA 2014

4. mednarodna konferenca strojnih inženirjev 2014

INŽENIRSTVO – Razvoj in inovacije za nova delovna mesta

LJUBLJANA, CANKARJEV DOM

23. OKTOBER 2014 OB 18^{00}

POKROVITELJI

ZLATI POKROVITELJ:

ENGINEERING TOMORROW

Danfoss

SREBRNI POKROVITELJ:

PETROL

Energija za življenje

BRONASTI POKROVITELJI:

arex development as a way of life

hidroinženiring

RENAULT REVOZ d.d.

FESTO

IMP d.d.

Plinovodi Povezani z energijo

gorenjegroup

Kambič metrology

HELLA

METRONIK

YASKAWA

K VSEBINI SO PRISPEVALI TUDI:

SAVSKE ELEKTRARNE LJUBLJANA d.o.o.

MESTNI MUZEJ IDRIJA MUZEJ ZA IDRIJSKO IN CERKLANSKO

TMS

- Kovaški muzej Kropa
- Muzej Železniki
- Društvo Rojaka Janeza Puha Juršinci
- Muzej in galerije mesta Ljubljane
- Klub prijateljev IMV

Gospodarska zbornica Slovenije

ZSIS

Univerza v Ljubljani Fakulteta za strojništvo

Univerza v Mariboru Fakulteta za strojništvo

ZVEZA STROJNIH INŽENIRJEV SLOVENIJE WWW.ZVEZA-ZSIS.SI

MAKING MODERN LIVING POSSIBLE

Danfoss

Prihranite energijo z uporabo Danfossovih izdelkov
Izboljšajte učinkovitost energetskih sistemov in bivajte udobneje

Danfoss Trata d.o.o. | Ulica Jožeta Jame 16 | 1210 Ljubljana Šentvid
e-mail: danfoss-trata@danfoss.com | www.danfoss.com


FESTO


Skupina TPV
25 let
Povezujemo
inovativne
rešitve.